Fakultät für Chemie

Lehrstuhl für Technische Chemie II

Aqueous phase dehydration of cyclohexanol on zeolite Beta

Aleksei Vjunov

Vollständiger Abdruck der von der Fakultät für Chemie der Technischen Universität München zur Erlangung des akademischen Grades eines Doktors der Naturwissenschaften (Dr. rer.nat.) genehmigten Dissertation.

Vorsitzender:	Univ.–Prof. Dr. Dr. h.c. Bernhard Rieger
Prüfer der Dissertation:	
	1. Univ.–Prof. Dr. Johannes A. Lercher
	2. Univ.–Prof. Dr. Reinhard Niessner
	3. Prof. Moniek Tromp, Ph.D. (Univ. Amsterdam Niederlande)

Die Dissertation wurde am 27.11.2014 bei der Technischen Universität München eingereicht und durch die Fakultät für Chemie am 07.01.2015 angenommen.

Acknowledgements

The presented thesis work would be impossible without the invaluable advice and support, technically, intellectually and personally from friends, colleagues and family.

First and foremost I would like to express my sincerest gratitude to my thesis advisor, Prof. Johannes A. Lercher, for the endless support throughout my Ph.D. with his patience and profound knowledge whilst allowing room for creativity and scientific expression. I deeply appreciate the trust Johannes offered as well as the invaluable discussions at times reaching far beyond the boundaries of the chemical world that have impacted both my scientific and personal growth.

I am utmost grateful to my supervisor Donald M. Camaioni for the excellent discussions and encouragement I received over the years. The high degree of attention to even the smallest details, which has lead to an in–depth understanding of the studied chemistry and thoroughness when examining approaches to solve complex scientific problems, have left a deep mark on my personality. I greatly acknowledge the time and effort Don has spent to enlighten me and direct toward becoming and independent and efficient researcher.

I would like to express a sincere gratitude to John L. Fulton, with whom I have shared not only the experience of conducting work and synchrotrons on different continents, but also the exciting path of data analysis and interpretation. John has introduced me to the field of experimental spectroscopy and broadened my horizons both in and outside the lab.

I am full of gratitude to my colleagues Miroslaw A. Derewinski, Jian Z. Hu, Sarah D. Burton, Ilke Arslan and Bruce W. Arey for the inspiring work on materials synthesis and characterization. The fruitful collaboration during my thesis work has not only resulted in impactful science, but also further stimulated my natural curiosity toward solving complex challenges in the chemical field.

Acknowledgements

I deeply appreciate the help of my lab mates Zizwe A. Chase, Hui Shi and Sebastian Prodinger who have always supported me during my stay at the Pacific Northwest National Laboratory. Finalizing my thesis work on time would not have been possible without their input, advice and sincere interest in both my personality and the chemistry I worked on. Life in the lab would have been much less comfortable and amenable, had my mates not have been as helpful and candid.

Finally, I am greatly indebted to my spouse Alena, parents, relatives and friends from whom I've been receiving endless support.

Aleksei Vjunov
December 2014

Abstract

An in–depth study of the mechanistic pathways, catalyst stability and active site performance for the aqueous phase cyclohexanol dehydration on zeolite Beta is reported. Dehydration, the rate–limiting reaction of the phenol hydrodeoxygenation (HDO) sequence, leads to the formation of cyclohexene and proceeds *via* the E1 elimination mechanism. This reaction is catalyzed by the Brønsted acid sites that are formed upon substitution of Si by Al in the HBEA framework. The distribution of zeolite active sites is for the first time quantitatively and independently determined by XAFS and NMR spectroscopic methods that allowed both monitoring Al location in as–synthesized zeolites and following post–synthetic modifications, e.g. selective removal of Al during zeolite steaming. Since the dehydration reaction is studied in aqueous phase, the impact of water on zeolite stability is also investigated. While the geometries of the Al sites are retained, complete framework degradation *via* selective hydrolysis of links between zeolite Si–tetrahedra is observed in aqueous medium. The catalytic performance of HBEA in aqueous medium is largely independent of the Al concentration and distribution in the framework, because the Brønsted acidic protons are present in the form of hydrated hydronium ions.

Kurzzusammenfassung

Der folgende Bericht beschreibt die Untersuchung der Reaktionswege, Katalysatorstabilität und Aktivität der aktiven Zentren für Cyclohexanol Dehydratisierung auf Zeolith Beta in wässrigem Medium. Die Dehydratisierung, die geschwindigkeitsbestimmende Reaktion der Phenol Hydrodeoxygenierungs (HDO) Sequenz, führt zur Bildung von Cyclohexen und folgt dem E1–Eliminierungsmechanismus. Die Reaktion wird mittels Brønsted Säurezentren katalysiert, welche durch Substitution von Si mit Al in der HBEA Struktur entstehen. Die Verteilung der aktiven Zentren im Zeolith wurde zum ersten Mal quantitativ und unabhängig voneinander mittels XAFS und NMR spektroskopischer Methoden bestimmt. Die entwickelte Methode ermöglicht sowohl die Analyse der synthetisierten

Zeolithe, als auch den Verlauf post–synthetischen Modifikationen des Materials, z.B. selektive Entfernung von Al mit heißem Wasserdampf. Da die Dehydratisierung in Wasser studiert wurde, muss auch der Einfluss der wässrigen Phase auf die Stabilität des Zeolithgitters untersucht werden. Obwohl die Geometrie der aktiven Zentren weitestgehend unverändert bleibt, wird vollständiger Abbau des Zeolithgitters über selektive T–O–T Gruppen Spaltung durch Hydrolyse der Si–Tetraeder in der Interwachstumsregion der HBEA Polymorphe in wässriger Phase beobachtet. Die katalytische Aktivität des Zeoliths im Wasser ist weitgehend unabhängig von der Al–Konzentration und Al–Verteilung im Gitter, da die Brønsted–sauren Protonen als wasserkoordinierte Hydroniumionen vorliegen.

Table of contents

Chapter 5

Chapter 6

Chapter 1

Introduction

1.1 Environmental background

Over the past century the Earth's climate system has been experiencing a steady rise of average temperatures described as global warming.[1] While the most prominent temperature increase is often attributed to the world's oceans, an increase in the average air temperatures has also been reported.[2] Although still debated, one of the dominant factors leading to global warming according to the Intergovernmental Panel on Climate change (IPCC) is the increasing concentration of green house gases in the atmosphere.[3] Although water vapor, methane and ozone form the major fraction of the greenhouse gases, the single most feared component is the carbon dioxide, which is emitted as the result of human activity including among others fossil fuel burning, cement production, agriculture and deforestation.[1]

The growing CO_2 emissions lead to a multitude of changes around the globe that vary in impact from region to region. One of the prominent problems is the accelerated melting of glaciers and polar caps that not only leads to the depletion of potable water supplies, but also results in rising sea levels. The retreat of the permafrost results in vast emissions of enormous quantities of methane stored in the arctic soil thus promoting global warming. Also, the modification of the precipitation patterns around the globe is promising a significant expansion of subtropical deserts and may lead to extreme weather events, such as heat waves and sever droughts.[4] Finally the acidification of the world's oceans leads to extinction of certain marine wildlife and may result in substantial depletion of fish stock raising the food security problems for millions around the globe.

Suggested human responses include the reduction of greenhouse gas emissions *via* introduction of energy–saving technologies, design of fuel–efficient vehicles and popularization of recycling efforts. In this respect the work on renewable fuels, e.g. biodiesel, become increasingly important, because of the zero net–carbon emissions of biomass–derived energy carriers compared to conventional fossil fuels.

1.2 Global energy demand

The steadily increasing living standards accompanied by the growth of the world's population inevitably lead to an increase in fuel consumption. While the extraction of

fossil fuels, such as oil and gas, has led to prosperity for a fraction of the world's nations in the past, the depletion of the easily–extractable resources poses imminent economical threats in the near future. The global competition on the fuel market and the uncertainty of the energy carrier cost causes social tensions and in several cases has led to long–lasting war conflicts that pose long–term security threats to millions of people. The emerging economies of the developing countries, particularly the Asian–pacific region, are the driving force of the world's energy need. The current and projected energy demand estimate by the ExxonMobil Oil Corporation[5] for the next two decades is shown in Figure 1.

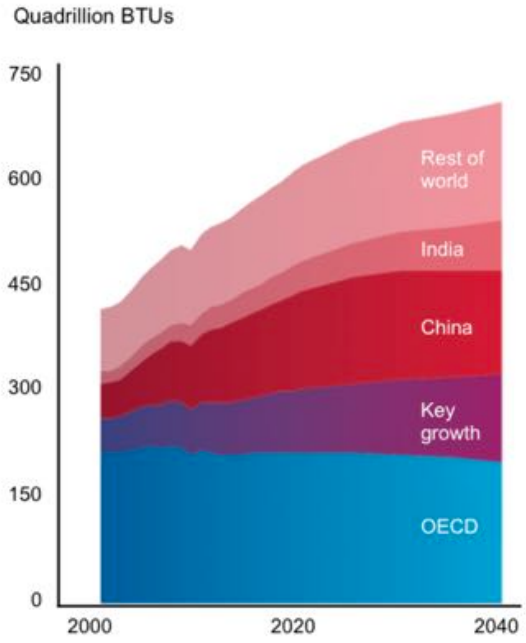

Figure 1. Global energy demand estimate until 2040 by the ExxonMobil Oil Corporation is shown.[5] *Mexico and Turkey are included in key growth.

While the introduction of advanced drilling and extraction technologies, such as hydraulic fracturing,[6] has made the fuel market more flexible, the impacts of these new approaches applied by the oil industry on the environment, particularly ground water contamination and the increase of seismic activity in the oil recovery region, remain unclear. Although there are a number of alternative energy sources, e.g. hydro–electric

power generation, that could potentially substitute burning fossil fuels, there is still no competitive (in respect to maximum range and fuel energy density) replacement for gasoline, diesel and jet fuel in the transportation sector. Because of rapid economic growth in the developing countries, the heavy–duty vehicle fleet is projected to become an increasingly important sector in the overall fuel consumption due to the low initial investment costs compared to the rail and geographic restrictions of the marine sector. The current and projected fuel consumption of the world's transportation sector is shown in Figure 2 and is based on the reported estimate by the ExxonMobil Oil Corporation.[5]

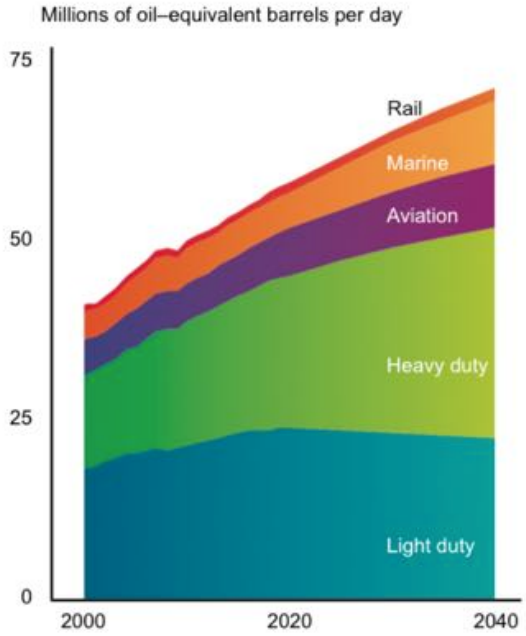

Figure 2. Transportation fuel demand estimate until 2040 by consumption sectors reported by ExxonMobil Oil Corporation is shown.[5]

A possible solution could be found in the nuclear power generation, a sustainable energy source that reduces carbon emissions.[7] Unfortunately, however, the large capital cost, unfavorable public opinion and complex waste management hinder the development of nuclear energy industry. Still, the abundant and relatively cheap[8] electricity generated at nuclear plants may substantially expand the electric vehicle (EV)

market. Currently, however, EV's are outside the financial reach of the majority of the world's population and are substantially limited in range, especially under harsh climate conditions.

Because green energy sources such as wind and solar are unreliable and climate–dependent, a possible solution for powering the transportation sector may be found in fuel production from biomass derived feeds. The abundance of biomass waste material produced in the lumber and food industries could not only satisfy a portion of the diesel demand, but also reduce energy input in waste management projects. The details on the potential biomass feedstock and its valorization strategies are provided in the sections below.

1.3 Biomass energy carriers

The term biomass includes among others also the waste from the agriculture and lumber industry, food residues as well as organic waste material.[9] Wood and plant–based materials are often specifically referred to as lignocellulosic biomass.[10] The main chemically relevant components of biomass can be arranged into five categories: lignin, cellulose, hemicellulose, starch and oils.[11] The first three are typically derived from plants and wood, which typically yields 35–50% cellulose, 20–35% hemicellulose and 5–30% lignin.[12] Cellulose consists of β–D–glucopyranose units linked *via* the β–glycosidic bonds[13] that may be hydrolytically deconstructed to form glucose, which is often suggested as a potential building block for fine chemical synthesis.[14,15] Unlike cellulose, the hemicellulose is largely amorphous exhibiting a very low degree of polymerization and can be hence hydrolyzed under significantly milder conditions. Also, because the structure of hemicellulose is not homogeneous and contains a variety of carbohydrates, e.g. pentoses and hexoses,[16] its conversion to fuels typically results in a range of hydrocarbon products. Lignin, which is the third major component of wood derived–biomass, is an amorphous polymer abundant with aromatic monomers (see Figure 3). Because lignin is not suitable for food production, is a cheap and readily available residue from the lumber industry and has a high (compared to other sources) energy content due to the relative high carbon density, it is considered a potential source

for diesel–range fuel production[17] in the scope of the current work and, is hence analyzed in greater detail in the sections below.

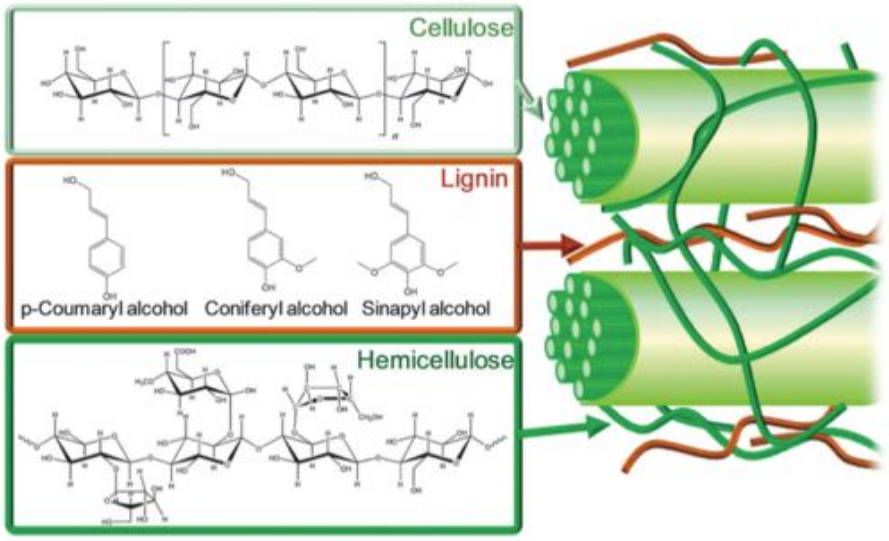

Figure 3. The structure of lignocellulosic biomass is shown schematically along with the major components (cellulose, lignin and hemicellulose) and the main building units for each component.[18]

1.4 Lignin

Although lignin is usually extracted from wood, it is also part of the plant cell walls as well as several algae types.[19] Lignin has two significant biological roles: 1) it participates in the carbon cycle by sequestering carbon dioxide into the tree tissue and 2) conducts water in plant stems due to substantially higher hydrophobicity than polysaccharides.[20] The composition of lignin can vary substantially depending on the source, e.g. the lignin derived from aspen predominantly consists of ~ 63% carbon, ~ 30% oxygen, ~ 6% hydrogen and 1% other elements.[21] Lignin is a highly branched aromatic polymer that is composed primarily of three monolignols: p–coumaryl alcohol, coniferyl alcohol and sinapyl alcohol.[22] The structure of lignin is shown schematically in Figure 4, and the three monolignols are also highlighted.

Overall, the individual building units in the lignin polymer are coupled as ethers or furans. The ether bonds can further be differentiated to better explain the complex C–O–C structure of lignin. Several main bonding patterns typically observed are the β–O–4 ether bonds forming up to 50% of monomer couplings as well as β–5 phenylcoumaran bonds responsible for approximately ~12% of monomer connections in lignin. Other bonds, such as the β–β' pinoresinol, diphenyl ether 4–O–5' and β–1' diphenyl methane are also often reported.

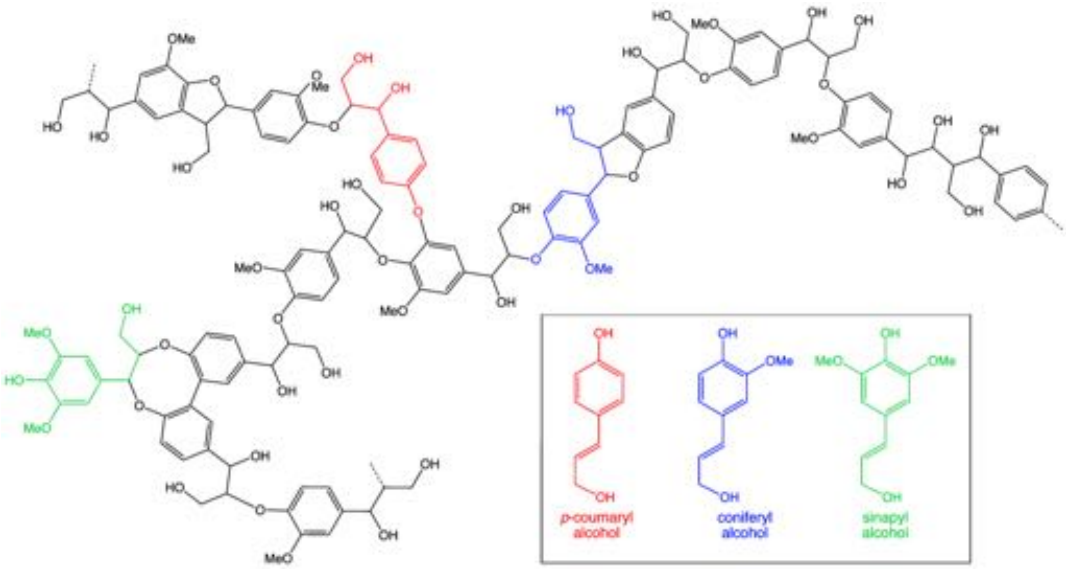

Figure 4. The structure of lignin is shown (adapted[23]) schematically along with the three monolignol units: p–coumaryl alcohol, coniferyl alcohol and sinapyl alcohol.

While lignin is primarily used as fuel for heat production through burning, a further industrial application is the use of sulfonated lignin as a dispersant in high performance cements.[24] Potentially, however, because lignin contains a high concentration of aromatic units in the structure, it may become an important source of elementary building blocks for fine chemical production. Most importantly, in respect to both industrial production volume and environmental impact, the catalytic conversion of lignin–derived phenolics to diesel–range fuels may lead to a sustainable and economically viable source of transportation fuel in the near future. Although

heterogeneous catalytic conversion of lignin is promising because the catalyst and products can be easily separated, the mass transfer of lignin to the catalytically active centers is substantially hindered.[25] This limitation could, however, be overcome by introducing a multi–step depolymerization sequence, which would allow deconstructing the branched lignin chains to oligomers suitable for existing catalytic systems. Current and perspective methods of lignin conversion are discussed in the section below.

1.5 Towards efficient methods of lignin conversion

The key to reducing the dependence on conventional fossil resources for the production of chemicals and liquid transportation fuels lies in the atom efficient transformation of biomass with a minimum use of hydrogen.[26] While lignin is widely abundant, there are two major complications associated with its application in fuel production: 1) the complexity of its chemical structure and 2) the dependence of quality on the lignin source (both biologically and geographically). Also, the long distance transportation of lignin is impractical due to the relatively low energy density (compared to conventional oil). A possible path to circumvent these limitations is to concentrate biomass thermally *via* pyrolysis[27] since the obtained bio–oil may provide an improved basis for long–haul transport and further processing, e.g. admixing bio–oil derived from different lignin sources to achieve a constant specification of the refinery feed.

Unfortunately, the product of lignin pyrolysis is a mixture of aqueous and oily phases that are difficult to characterize and stabilize.[28] While there are known catalytic approaches that lead to the enhancement of the pyrolysis efficiency, the advance of this technology is often hindered by marked coke deposition and the difficulty of controlling the chemistry at relatively high pyrolysis temperatures.[29] The pyrolysis of biomass also results in the formation of a large quantity of water contaminated with a range of organic components including formic and acetic acids as well as aldehydes and ketones.[30,31] While steam reforming could circumvent this problem, the formation of carbon oxides reduces the overall carbon yield to gasoline– and diesel–range products.[32]

An alternative to pyrolysis is found in the heterogeneously catalyzed lignin depolymerization in hydrogen–pressurized systems. Some examples of previous work in the field include the approach to deconstruct the polymeric lignin to monomer unit using

Ni catalyst, e.g. NiMo/γ–Al_2O_3.[33] The reaction occurs at hydrogen pressures of 40–70 bar at high temperatures, typically in the range of 320–380 ºC. These reactions can be performed also in aqueous media, which allows facile product separation upon reaction completion due to the formation of a tri–phasic (aqueous, organic and gaseous) system. While the aromatics as well as alkanes and alkenes form the much–desired organic phase that can be easily separated, the alcohol and light ethers are typically retained in the aqueous phase and can be further deoxygenated in subsequent reaction runs. Unfortunately, the high temperatures also lead to the formation of substantial amounts of light hydrocarbons as well as carbon monoxide and dioxide. The main limitation of this approach is, however, the high temperature and H_2 pressure necessary to convert lignin to aromatic products.

An alternative catalytic system using 5% Pd/C was demonstrated to successfully depolymerize lignin to the aromatic monomers at 200 ºC and hydrogen pressures as low as 35 bar.[34] This approach resulted in conversion level reaching as high as 90% with selectivity to dihydroguaiacyl alcohol, 4–propylguaiacol as well as a range of other ethers. Chase et al. have later studied the behavior of similar Pd/C catalysts using phenol as model compound representing the lignin–derived phenolic monomers and found that at reaction conditions mentioned above the supported Pd nanoparticles contain an elevated concentration of hydrogen, which was dissolved in the subsurface sites, that is then consumed to hydrogenate the aromatics.[35]

The most promising path forward currently is the conversion of lignin–derived phenols to transportation fuels, specifically diesel and jet fuels, as these are least amenable to being replaced by electrical–based power sources. The conversion of lignin is schematically shown in Figure 5 and consists of three major steps. First, the lignin polymer must be deconstructed *via* selective C–C and C–O bond cleavage to provide the fragments suitable for further processing. This step can be performed using supported metal catalysts, such as Pt, Pd, Ru, Cu and most notably Ni.[36,37,38] Using bimetallic catalysts allows efficient control of the selectivity and yields of individual hydrogenolysis products.[39]

Then the derived pool of oxofunctionalized monomers must undergo dehydrogenation/hydrogenation that leads to the saturation of both C=C and C=O bonds.

While in general the same supported catalysts used for polymer deconstruction are suitable as hydrogenation catalysts, different selectivity is observed depending on the chosen metal, support material, solvent and hydrogen pressure. As an example, Pt and Pd are most efficient for the hydrogenation of C=C bonds and the bimetallic catalysts such as RuSn are best suited for selective C=O hydrogenation.[40] The hydrogenation is typically also accompanied by the disproportionation reactions as well as coupled defunctionalization and reduction reactions. In recent reports supported Ni catalysts have been often proposed as efficient catalysts, especially for the hydrogenation step of lignin conversion. Lercher et al. have studied the aqueous phase upgrading of crude bio–oil components using a bifunctional Ni/HZSM5 catalyst that was capable of hydrodeoxygenating major components of the aromatic fraction following the hydrogenation–hydrolysis–dehydration–dehydroaromatization reaction sequence.[41]

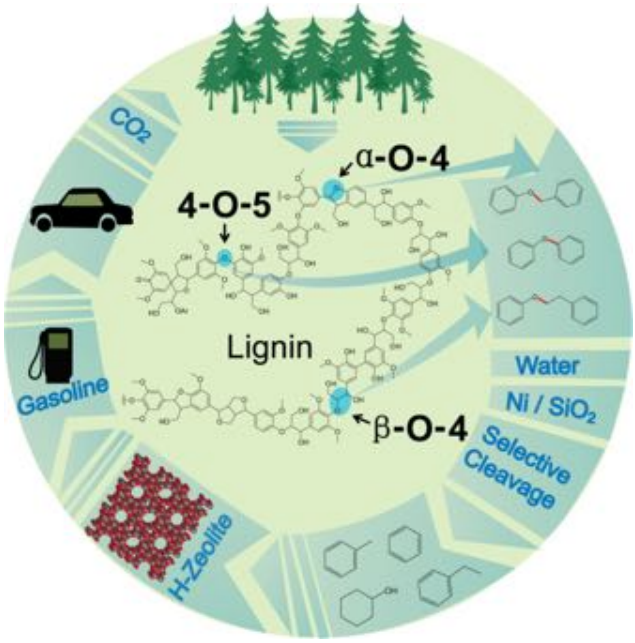

Figure 5. One of the possible cycles of lignin conversion to transportation fuels proposed by the Lercher group[42] is schematically shown.

Unfortunately, the Ni based catalysts still have a tendency to deactivation due to sintering and coke formation. The problem can at least in part be circumvented by alloying with Cu as was shown on the example of conversion of guaiacol,[43] a model compound from phenol hydrodeoxygenation. Albeit using the supported NiCu catalysts resulted in a subtle decrease of guaiacol conversion, the decreased coke deposition and low amount of gaseous products make this catalytic system promising for further studies.[43]

The cascade reactions discussed above also include the dehydration of secondary alcohols as part of the deoxygenation process. It would be most advantageous to perform this rate–limiting step of water removal from cycloalkanols in aqueous medium, because the abundance of water in the biomass feed makes it the solvent of choice for the catalytic lignin deconstruction sequence. The catalytic dehydration reactions that require a strong acid function are often performed using solid acid catalysts, e.g. zeolites.[44] The large pore size of zeolites such as HZSM–5 or HBEA also benefits C–C and C–O coupling reactions that can occur parallel to the dehydration reaction. Note that upon hydrogenation (discussed above) a final upgrading step is required in order to selectively rearrange the C–C bonds with the aim for the production of higher carbon number precursors to aliphatic and aromatic hydrocarbons. Because zeolites do not require hydrogen for C–C rearrangement and coupling reactions and are often chosen as support materials for metals used as hydrogenation catalysts (e.g. Ni), this class of materials becomes increasingly important for the overall biomass conversion sequence. To–date, however, neither a quantitative analysis of the zeolite active sites, their nature and distribution, nor an in–depth analysis of the zeolite integrity and performance in aqueous medium have been reported.

1.6 Catalytic conversion of lignin–derived phenols

Albeit lignin contains much less oxygen than cellulose, the relatively (~30%) high oxygen content in the lignin–derived bio–oils still requires performing the hydrodeoxygenation (HDO), the hydrogenolysis approach of removing oxygenates. The HDO is competitive with transalkylation, the dominant pathway strongly depends on the catalyst, both its metal and acid function.[45] As an example, in the case of guaiacol

conversion the demethylation toward the formation of catechol is dominant if the support material exhibits low acidity.[46] Hydrodeoxygenation is often preferred because it allows the retention of the carbon number in the final products without substantial loss of carbon as a result of light alcohol formation.[47] The HDO process requires substantial amounts of hydrogen for complete reduction to hydrocarbons[48] and typically proceeds in two[49] stages: initial removal of oxygenates capable of polymerization followed by the catalytic conversion of the lignin–derived phenols. In the past, a range of sulfided Mo–based catalysts was proposed for the different stages of HDO.[50,51] Unfortunately, these catalysts exhibit a strong tendency to incorporate sulfur into the HDO products, as well as to rapidly deactivate in the presence of high concentrations of water.[52,53] Lercher et al. have extensively studied the reductive upgrading of bio–oil and model compounds in aqueous medium using a combination of acid and metal catalysts. [54] The hydrodeoxygenation sequence of phenol conversion to alkanes proposed by Lercher et al. is schematically shown in Figure 6 and is briefly reviewed below.

The hydrodeoxygenation can be efficiently performed on dual functional catalysts that use the metal function for the hydrogenation reactions and perform the dehydration, hydrolysis and isomerization reactions using the acid functionality. The observed chemistry is controlled, at least in part, by the metal/acid site ratio. The hydrogenation of phenol on metals, such as Pt,[55] Pd[56] or Ni,[57] typically leads to a range of C_6–C_9 cycloalkanols. These secondary alcohols in turn must be dehydrated to form the corresponding olefins, e.g. cyclohexene. The dehydration reaction is typically two orders of magnitude slower than the hydrogenation step and requires high concentrations of strong Brønsted acid sites. Although mineral acids, such as H_3PO_4 or H_2SO_4, can lead to high olefin yields, the resulting high quantities of dilute aqueous acid waste make these catalysts unfavorable for industrial application. This problem is often addressed by using solid microporous materials, e.g. zeolites, that can be easily separated from the reaction and allow significant yields of dimer products formed *via* olefin alkylation reactions. Unlike in the case of mineral acids when the substantially diluted reactant concentrations in aqueous medium significantly reduce the rates of alkylation, the local increase of phenol and cycloalkanol concentrations in the zeolite pores leads to the enhancement of the alkylation rates. The olefins are alkylated to form the C–C coupling, e.g. coupling of

two cyclohexene molecules leading to the formation of cyclohexyl–cyclohexene, or C–O coupling, e.g. coupling of cyclohexanol and cyclohexene molecules leading to the formation of dicyclohexyl ether. However, the ether yields are typically low since the formation of ethers in aqueous medium is reversible[58,59] and in equilibrium with the corresponding cycloalkanol.

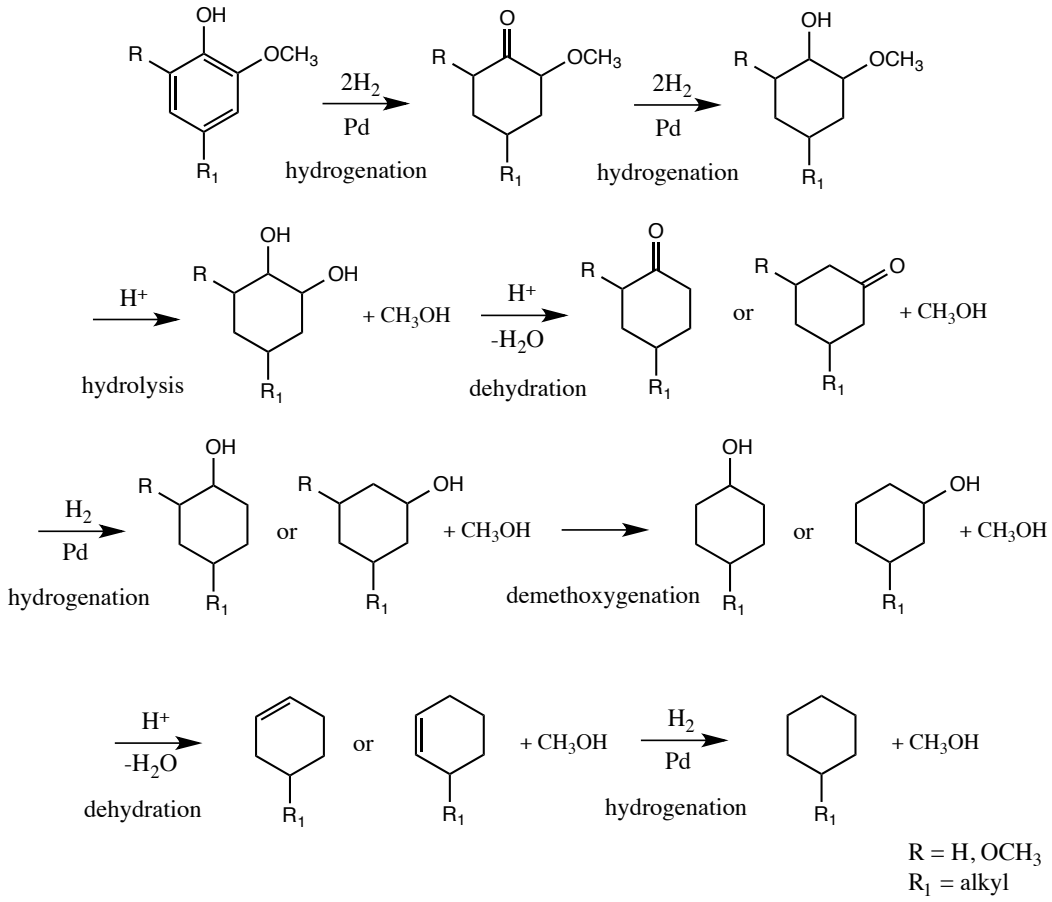

Figure 6. The individual steps of the phenol hydrodeoxygenation sequence resulting in alkane formation are schematically shown.

In the final step, the olefins are hydrogenated to obtain diesel–range alkanes.[60] Because the produced hydrocarbons have poor solubility in the aqueous reaction medium, the products can be easily separated from the reaction solution as an organic phase. While a direct, one pot, conversion of biomass derived molecules would be most

advantageous,[61] the dehydration step of the reaction cascade still poses significant complications and is rate–limiting for the reaction sequence. The possible pathways for water removal on acid catalysts and the potential mechanisms of this reaction are briefly reviewed in the section below.

1.7 Alcohol dehydration – the elimination reaction

The catalytic dehydration of alcohol is an example of the elimination reaction in which two substituents are removed from the reacting molecule.[62] The reaction can follow either a single– or a two–step mechanism, an E2 or an E1 elimination referring to the bimolecular and unimolecular reactions, respectively.

The E2 elimination mechanism, which includes a single transition state, and requires the C–O and β C–H bonds of an alcohol to be cleaved concertedly is shown schematically in Figure 7 using the example of a H_2SO_4 catalyzed reaction. The oxygen atom of the alcohol hydroxyl group donates two electrons to one of the sulfuric acid protons forming an alkyloxonium ion. The nucleophilic HSO_4^- anion then attacks one adjacent proton of the alcohol and the hydroxyl group leaves in a concerted process, leading to the formation of an olefin double bond and a water molecule. Because the E2 elimination mechanism leads to the formation of a π–bond, the two leaving groups, e.g. proton and hydroxyl, must be orientated antiperiplanar.

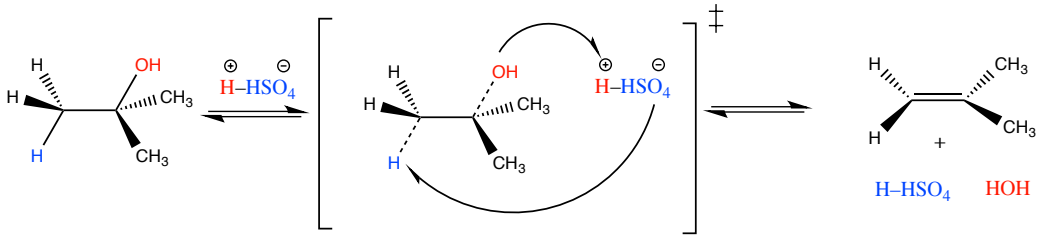

Figure 7. An example elimination reaction following the E2 mechanism is shown.

While the E2 elimination reaction on tertiary alcohols as well as sterically hindered secondary alcohols in mild acidic conditions can be achieved by using reagents such as phosphorous oxychloride ($POCl_3$), these reactions often require a base as solvent, e.g. pyridine.[63] An example of this chemistry is the dehydration of 2,4,4–trimethyl–2–

pentanol leading to the predominant formation of the less substituted double bond Hoffman product, which is favored due to steric hindrance of the protons of the methylene group. The alcohol elimination *via* the E2 mechanism can also be achieved when the alcohol is first converted to the corresponding sulfonate ester followed by the introduction of a base to the reaction.[63] This approach allows alcohol dehydration while avoiding possible rearrangement and/or double bond migration reactions that may occur in the presence of strong acids. Note, however, that due to the limited stability of tertiary sulfonate derivatives this reaction pathway is most efficient for primary and secondary alcohols. Unlike secondary alcohols, primary alcohols readily undergo dehydration following the E2 elimination mechanism, which is competitive with the S_N2 substitution and the product distribution (E2 vs. S_N2) is dependent on the reaction conditions.[62]

In the case of the unimolecular E1 elimination mechanism the alcohol is similarly protonated followed by water elimination leading to the formation of a carbenium ion as the reaction intermediate. In the next step the deprotonation of the carbenium ion leads to the formation of the olefin and closes the catalytic cycle. The individual steps of the E1 mechanism are schematically shown in Figure 8.

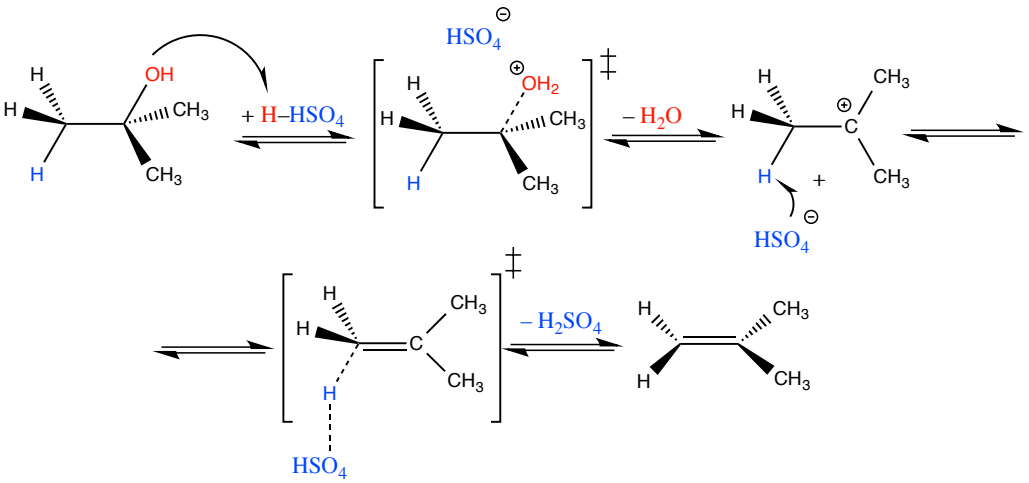

Figure 8. An example elimination reaction following the E1 mechanism is shown.

The elimination of water from alcohols leading to the formation of olefins is generally possible *via* the E1 mechanism when the hydroxyl–group becomes a good

leaving group, e.g. through protonation or coordination by a Lewis acid. A number of reagents, e.g. the Burgess–reagent, can be used in order to promote the E1 mechanism under mild reaction conditions.[64] The E1 elimination is favored for substrates that allow a facile formation of stable carbenium ions. While the reaction is competing with the S_N1 substitution, the elimination becomes more favorable with increasing temperature, because the latter exhibits strongly positive reaction entropy as the number of molecules is increased in the course of reaction. This leads to a lowered energy barrier for the transition state and an increase in reaction rate. The E1 elimination of water from tertiary alcohols is regioselective and typically leads to the Zaitsev product.

While the dehydration of primary alcohols in supercritical water has been suggested to be better explained by the E2 elimination mechanism,[65] the aqueous phase dehydration of secondary alcohols catalyzed by mineral acids was previously shown to generally proceed *via* the E1 mechanism.[66] Interestingly, in the absence of water, the zeolite catalyzed alcohol dehydration was shown to follow the E1–mechanistic pathway,[67] which comprises the formation of pore surface–bound alkoxide species and water in the rate determining step.[68] The dehydration product distribution depends in the size of the zeolite pores. Bhan et al. have shown that while in the case of HMOR, a medium size pore zeolite, ethanol dehydrates to form both ethylene and diethyl ether, only the ether is observed in the case of the large pore HMFI.[68] Also, the gas phase alcohol dehydration using zeolite[69] and polyoxometalate (POM)[70] catalysts was suggested to follow strictly the E1 elimination pathway. Iglesia et al. have also shown that in the case of POM clusters the elimination barrier is most affected by the degree of the alcohol substitution, because this directly impacts the stabilization of the formed carbenium ions.

The acidity of zeolite catalysts, which can be used among other also to perform water elimination from alcohols, is determined by the lattice composition[71] as well as pore shape and size which have been suggested to control jointly the activity and selectivity for catalytic gas phase reactions.[72] A fundamental study of the active centers, reaction intermediates and reaction dynamics/kinetics is critically needed to facilitate the development of catalysts for the practical conversion of biomass to energy–carrying

alkanes. More detail on zeolite catalysts as well as their synthesis and post–synthetic treatment procedures is provided in the section below.

1.8 On the nature of zeolites

Zeolites, microporous solid acids with a complex structure, are commonly used as sieves and catalysts for several important industrial processes.[73] The sieve properties of zeolites are due to the very regular pore structure of molecular dimensions defined by the ring size of the aperture that enables selective sorting of molecules based primarily on size.[74] The catalytic performance of the zeolites is based on the fact that this class of materials contains a substantial amount of voids that can solvate transition states and reactive intermediates.[75] Figure 9 shows the framework of a MFI–type zeolite, which is one of the commercially most important solid acids.

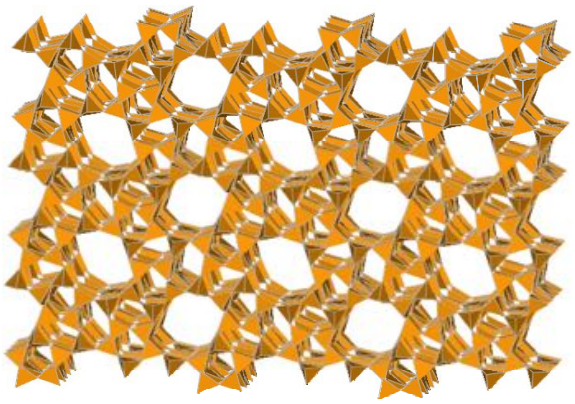

Figure 9. The unit cell of MFI zeolite is shown. The Si atoms are located in the centers of the tetrahedra, the O atoms (not shown) corner connect the tetrahedra.

While zeolites are abundant in nature and are mined in enormous quantities, the most important zeolites for industrial applications, e.g. oil refining, are produced synthetically. The typical synthetic pathway includes heating aqueous solutions of alumina or sodium aluminate and silica with sodium hydroxide. The procedure also requires the use of organic templating agents that direct the pore size and geometry.[76] The typical zeolite synthesis steps are schematically shown in Figure 10. The process is

typically divided into the following steps: 1) the coordination of silicates present in the synthesis gel on the structure directing agents (templates) *via* hydrogen bonding; 2) oligomerisation of silicates; 3) condensation of the template coordinated silicates leading to the formation of first stable crystalline domains; 4) formation of the zeolite particles *via* crystal growth.[77]

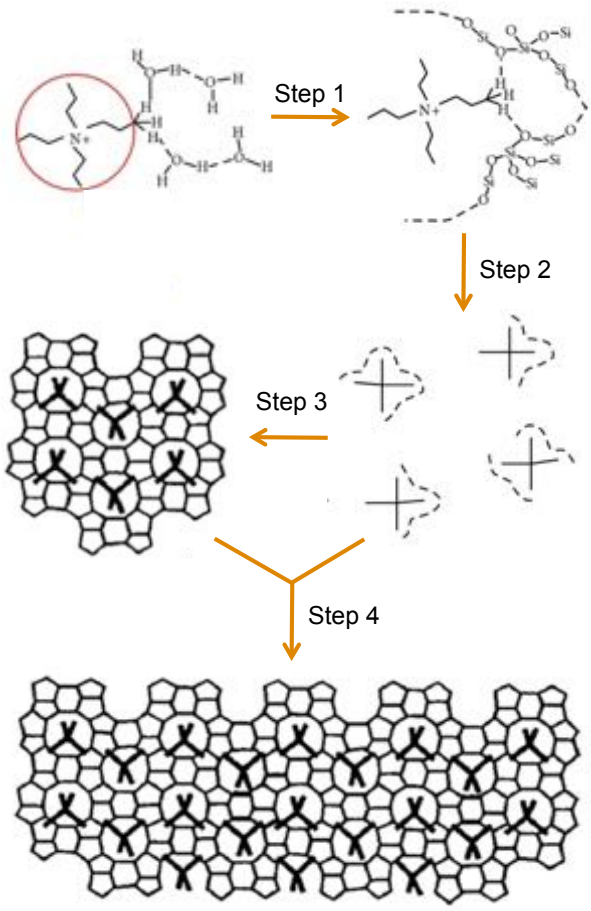

Figure 10. Schematic representation of the proposed individual steps of zeolite synthesis is shown. The scheme is adapted from work by Davis et al.[77] The steps are described in the text above and involve the coordination of template on the silicates (Step 1), oligomerisation (Step 2), formation of crystalline domains (Step 3) and particle formation *via* crystal growth (Step4).

Zeolite synthesis is typically performed in a strong alkali medium (pH > 13). The high concentration of hydroxyl groups is required to increase the solubility of the silicate and aluminate building blocks used in the synthesis. A possible means of OH^- substitution is the method proposed by Guth and Kessler[78] and involves a fluorine–based mineralization agent.[79] This approach allows zeolite synthesis in neutral or even slightly acidic medium and results in high heteroatom (B, Al, Fe, etc.) incorporation and relatively low defect–concentration in the final product.

The morphology of the zeolite often depends on the synthesis conditions as well as the chosen structure–directing agents (SDA), which are typically (except for MFI) required for high–silica zeolite synthesis.[80] The organic reagents, necessary for lattice charge compensation, however, are often observed in concentrations exceeding those required for framework charge compensation. This phenomenon has been attributed to processes occurring either in the gelation or the nucleation whereby the organic component organizes the oxide tetrahedra into certain geometric topologies around itself leading to the formation of primary building units of a particular zeolite framework.[81,82] Davis et al., however, suggested that the true role of the guest molecules is space filling, e.g., filling the forming hydrophobic zeolite voids in aqueous synthesis medium, that leads to an increase in the thermodynamic stability (meta–stability) of the framework.[80] Although not completely unambiguous, both explanations outlined above suggest that the nucleation process is affected and that the correct choice of SDA may define the formed zeolite pore shape, size and tortuosity.

The concentration of acid sites in the zeolite typically depends on the amounts of incorporated hetero–atoms, such as Al. The concentration of Al in the zeolite synthesis gel affects the final crystalline product composition and properties, e.g. the higher the Al concentration, the smaller is the resulting zeolite Si/Al ratio and particle size. Also, the Si/Al ratio of the zeolite is often lower than that of the gel leaving a partly unreacted siliceous solution.[83] The desired concentration of Al can be achieved either by variation of the concentration of Al species in the synthesis gel, or by post–synthetic zeolite treatment. The later typically involves steaming and acid leaching to decrease the Al concentration to desired level.[84] While industrial zeolites are often manufactured in pure

form, to–date there is no unambiguous method to accurately and quantitatively determine the distribution of Al T–sites, the zeolite active sites.

1.9 The catalytic activity of zeolites

Zeolites are used as catalyst in a range of industrially important chemical processes, such as linear paraffin isomerization,[85] butene alkylation[86] as well as cracking reactions.[87] The catalytic activity of zeolites is attributed to the framework Si substitution with tetrahedral coordinated Al atoms that form the Al tetrahedral sites (Al T–sites).[88] This substitution requires also a charge compensating cation, such as Na^+ or NH_4^+, however for catalytic applications most common is the H–form of a zeolite. The charge compensating protons can act as Brønsted acid centers in heterogeneous catalysis.[89] There have been reports suggesting that while zeolites with high Al concentration exhibit a high density of low strength acid sites, zeolites with high Si/Al ratios contain a low density of highly acidic sites.[90] As a note in passing, zeolites with high concentrations of Al are also prone to the formation of extra–framework Al (EFAL) species during post–synthetic treatment, such as calcination. The EFAL is typically responsible for Lewis acidity, the presence of which in conjunction with Brønsted acidity may have synergistic effects on the overall acid strength of the zeolite.[90] The acidity of zeolites is suggested dependent on the structure of the microporous material, e.g., for materials with similar chemical composition the acid site strength is higher in medium pore size zeolites when compared to the large pore zeolites.[91,92] There have also been examples showing that tailoring the strength of zeolite acid sites[93,94] can lead to different reaction mechanisms, e.g., as was previously demonstrated for isomerization reactions.[95]

The superior catalytic performance of microporous solid acids is at least in part explained by and attributed to the pore environment of acid sites, often referred to as confinement and nest effects,[96,97] which allow for a better stabilization of reaction intermediates and transition states.[98] An example of the improved stabilization was previously demonstrated for monomolecular cracking of light alkanes on H–MFI zeolite. The respective transition state energies decreased at a rate of approximately 12 kJ/mol per CH_2 group, which was attributed to the preferential stabilization of larger transition

states by van der Waals interactions.[99] The pore confinement causes enthalpic stabilization that prevails over the loss of entropy at moderate temperatures.[100,101] Interestingly, however, the activation barriers determined for the cracking reactions did not scale monotonically with the void size or adsorption energy when the study was performed on a range of zeolites with different ring–structures.[102] This inconsistency remains unclear and was tentatively attributed to the different Al distributions among the zeolite rings that vary in size and shape[103] and are likely responsible for the observed marked differences in transition state solvation and intermediate reactivity.

The behavior of the zeolite acid sites and their properties in gas–phase reaction conditions, however, may substantially differ from condensed–phase reactions. The filling of zeolite pores with liquid water may significantly decrease the differences in acidity and confinement observed for Al T–sites in the gas phase. Unfortunately, to–date there have been no studies exploring the relation between zeolite active site concentration and distribution and the catalytic performance in condensed phase. Currently the major limitation for such work is the absence of a technique that would allow unambiguously determining Al location among crystallographically different positions of the zeolite framework.

1.10 On the stability of zeolite frameworks

Since zeolites have a well–defined pore structure, high activity per site and reasonable price,[104] this class of materials is favorable for the conversion of biomass. The typical refining conditions, however, may pose substantial stability problems, especially in the presence of high concentrations of steam or liquid water.[105] Under steaming conditions[106,107] the zeolites typically undergo dealumination, selective removal of framework Al atoms, leading to the formation of octahedral Al species.[108] The Brønsted acid site concentration in a zeolite is typically decreased during the dealumination, however the overall acidity of the material can be compensated by the formation of Lewis acidity attributed to the EFAL species. The extraction of Al is also accompanied by the creation of vacancies in the Si–backbone of the microporous material that in severe cases may even result in pore collapse or may lead to modification of the acidic properties of the zeolite.[109] However, when studying the

impact of HBEA zeolite steaming (~750K, 100% steam) on the framework integrity, Maier et al. have observed the condensation of Si–OH groups leading to the formation of Q^4 Si ($Si–(OSi)_4$) that allowed stabilization of the lattice due to strain reduction.[110] The authors noted, however, that while the individual Si–nests may be cured as a result of Si migration, a certain concentration of Si–defects is preserved in the polymorph inter–growth region formed due to the polymorph stacking disorder in the HBEA framework.

While the impact of steaming was investigated in detail in the past,[111,112] the effects of liquid water on the zeolite framework and the exact mechanism of structural degradation in aqueous medium remain unclear. The to–date studies of zeolite stability performed in the condensed–phase have only shown general trends of Si–OH bond cleavage leading to removal of Si,[113,114] which appears to be the dominating pathway for the degradation of zeolite frameworks in aqueous media. The selective Si removal, or desilication, was previously achieved in condensed–phase *via* alkaline treatment, which was performed in order to introduce additional mesoporosity.[115] Interestingly, in zeolites with low Si/Al ratios the high concentration of framework Al prevented the removal of Si,[116] thus potentially protecting the siloxane bonds due to the formation of negative local lattice charges. Whether similar behavior (from a mechanistic point of view) will be observed in pure water remains unclear. Similarly, the integrity of Al T–sites in the presence of hot water and their ability to perform catalytic reactions as the zeolite framework is gradually degraded in aqueous medium remains unknown. Finally, the impacts of active site distribution and concentration in a zeolite on the catalytic activity during aqueous phase reactions have not been studied.

1.11 The scope of this thesis

The goal of this Ph.D. thesis is to study the aqueous phase dehydration of cyclohexanol on zeolite. The reaction is important because cycloalkanol dehydration is the rate–limiting step in the phenol hydrodeoxygenation (HDO) sequence. Specifically, the reaction mechanism is studied using in situ magic angle spinning (MAS) nuclear magnetic resonance (NMR) spectroscopy. This technique not only enables discriminating between different mechanisms of water elimination, but also allows

following the reactant and product distributions and provides insight regarding the adsorption of molecules on the catalyst surface. Because using isotope labeled reactants leads to quantitative NMR signal recovery, the initial rates of functional group migration in the reactants/products during cyclohexanol dehydration in liquid water could be directly related to the reaction mechanism, which is presented in detail in Chapter 2.

The dehydration of cycloalkanols is successfully performed using a solid acid, zeolite HBEA, in aqueous environment. The substitution of Si^{4+} by Al^{3+} in the tetrahedral (T) positions of the framework leads to the formation of the zeolite catalytically active sites (Al T–sites). In Chapter 3 an in–depth structure analysis of the HBEA catalysts is reported. The quantitative analysis using the combination of Al K–edge XAFS and ^{27}Al MAS NMR spectroscopies leads to the identification of the Al^{3+} lattice distribution in HBEA. The experimental EXAFS spectra are interpreted by invoking a linear combination fit of the molecular dynamics (MD) EXAFS derived for each T–site from the DFT modeled structure. Similarly, DFT NMR calculations of the chemical shift values of the 9 different T–sites of HBEA are performed in order to interpret the NMR spectra. It is determined that most of the Al^{3+} populates T–sites that are part of one or more 4–member framework rings. In contrast, different Al^{3+} distributions are found for the T–sites occupying only 5– and 6–member rings.

The ubiquitous presence of water in biomass requires that the rate–limiting dehydration reaction be performed in aqueous phase. Hence an in–depth study of the stability of the HBEA catalysts and the mechanism of structural degradation in aqueous medium is critically needed. There are two mechanisms describing zeolite lattice degradation in liquid water: 1) selective removal of Al from the lattice *via* dealumination and 2) Si–O–Si group hydrolysis leading to desilication. The latter follows either a selective hydrolysis in a mode similar to crack propagation in glass or *via* non–selective Si–OH group formation. In this work a three–step mechanism of zeolite framework degradation in liquid water is proposed using a range of spectroscopic techniques in combination with microscopy and theory. These findings are reported in Chapter 4. The integrity of zeolite active sites, Al T–sites, is also addressed, with experimental results indicating that the Al T–sites remain largely unaltered even as the zeolite framework is

substantially degraded. A modification of Al coordination is observed only after complete zeolite lattice deconstruction.

Since both the mechanism of the dehydration reaction and the nature of the catalyst active sites as well as their stability in water are successfully determined, the next step is to elucidate the synergy of the above–mentioned insights on the apparent catalytic performance. Chapter 5 addresses several main points in order to better understand and improve existing catalytic systems: 1) the effect of water on the catalytic performance of zeolites in respect to zeolite pore and active site integrity and 2) the influence of Al–concentration and distribution on the reaction turnover frequency (TOF). While results suggest that TOF is proportional to the concentration of strong Brønsted acid sites, it does not correlate with the Si/Al ratio, the concentration of tetrahedral Al or its distribution in the zeolite.

The final chapter, Chapter 6, summarizes the performed work as well as concludes the new insights and generalizes proposed future research toward efficient and sustainable catalytic performance of zeolites in aqueous medium.

REFERENCES

[1] *Warming of the climate system is unequivocal*, IPCC, Climate Change **2013**: The Physical Science Basis - Summary for Policymakers, Observed Changes in the Climate System, IPCC AR5 WG1 2013.

[2] H. Riebeek, *2010, Global Warming: Feature Articles"*. Earth Observatory, part of the EOS Project Science Office located at NASA Goddard Space Flight Center.

[3] IPCC, Synthesis Report, Attribution of climate change, in IPCC AR4 SYR **2007**.

[4] J. Lu, G. A. Vechhi, T. Reichler, *Geophys. Res. Lett.* **2007**, *34,* L06805.

[5] ExxonMobil Oil Corporation Energy outlook **2014**, http://corporate.exxonmobil.com/en/energy/energy–outlook

[6] P. A. Charlez, *Rock Mechanics: Petroleum Applications*. Paris: Editions Technip. **1997**, 239. ISBN 9782710805861.

[7] *U.S. Energy Legislation May Be 'Renaissance' for Nuclear Power,* **2005**, www.bloomberg.com

[8] NEA, IAEA: *Uranium 2007 – Resources, Production and Demand*, OECD Publishing **2008**, ISBN 978–92–64–04766–2.

[9] *Biorefineries – Industrial processes and products,* Ullmann's encyclopedia of industrial chemistry, **2005**, Vol. *4*. 101–133, Wiley–VCH, Weinheim.

[10] Biomass Energy Center, http://www.biomassenergycentre.org.uk

[11] E. M. Rubin, *Nature* **2008**, *454*, 841–845.

[12] P. Mäki-Arvela, B. Holmbom, T. Salmi, D. Y. Murzin, *Catal. Rev.* **2007**, *49*, 197–340.

[13] *Analytical methods in wood chemistry, pulping, and papermaking,* E. Sjöström, R. Alen **1999**, Springer-Verlag, Berlin Heidelburg.

[14] P. L. Dhepe, A. Fukuoka, *ChemSusChem* **2008**, *1*, 969–975.

[15] R. Rinaldi, F. Schueth, *ChemSusChem* **2009**, *2*, 1096–1107.

[16] *Biomass to renewable energy processes,* J. Cheng, **2010**, CRC Press, Boca Raton.

[17] G. W. Huber, S. Iborra, A. Corma, *Chem. Rev.* **2006**, *106*, 4044–4098.

[18] D. M. Alonso, S. G Wettstein, J. A. Dumesic, *Chem. Soc. Rev*. **2012**, *41*, 8075–8098.

[19] Pt. Martone, Jm. Estevez, F. Lu, K. Ruel, Mw. Denny, C. Somerville, J. Ralph, *Current biology* **2009***, 19*, 169–175.

[20] K.V. Sarkanen, C.H. Ludwig (eds.), *Lignins: Occurrence, Formation, Structure, and Reactions*. New York: Wiley Intersci. **1971**.

[21] H.–H. King, P. R. Solomon, E. Avni, R. W. Coughlin, *"Modeling Tar Composition in Lignin Pyrolysis". Symposium on Mathematical Modeling of Biomass Pyrolysis Phenomena,* Washington, D.C.*,* **1983**.

[22] K. Freudenberg, A.C. Nash **1968**. *Constitution and Biosynthesis of Lignin*. Berlin: Springer–Verlag.

[23] R. Whitwam, *Biodegradable waterproof coating created from plants*, **2014**, www.geek.com

[24] S. E. Lebo, J. D. Gargulak, T. J. McNally, *Kirk–Othmer Encyclopedia of Chemical Technology,* **2001**, John Wiley & Sons, Inc. ISBN 0–471–23896–1.

[25] A. L. Jongerius, P. C. A. Bruijnincx, B. M. Weckhuysen, *Green Chem*. **2013**, *15,* 3049.

[26] *Breaking the Chemical and Engineering Barriers to Lignocellulosic Biofuels: Next Generation Hydrocarbon Biorefineries*; DOE Workshop: Washington, D.C., **2007**.

[27] W. Mu, H. Ben, A. Ragauskas, Y. Deng, *Bioenerg. Res.* **2013**, *6*, 1183–1204.

[28] D. C. Elliott, *Energy & Fuels*, **2007**, *21*, 1792.

[29] T. R. Carlson, T. P Vispute, G. W. Huber, *ChemSusChem*, **2008**, *1(5)*, 397.

[30] R. Trane, S. Dahl, M. S. Skjøth-Rasmussen, A. D. Jensen, *Int. J. Hydrogen Energy* **2012**, *37*, 6447–6472.

[31] J. Sun, D. Mei, A. M. Karim, A. K. Datye, Y. Wang, *ChemCatChem*, **2013**, *5*, 1299.

[32] C. Liu, H. Wang, A. M. Karim, J. Sun, Y. Wang, *Chem. Soc. Rev.* **2014**, *43*, 7594.

[33] J. Horácek, F. Homola, I. Kubicková, D. Kubicka, *Catal. Today* **2012**, *179*, 191–198.

[34] K. M. Torr, D. J. van de Pas, E. Cazeils, I. D. Suckling, *Bioresour. Technol*. **2011**, *102*, 7608–7611.

[35] Z. A. Chase, J. L. Fulton, D. M. Camaioni, D. Mei, M. Balasubramanian, V.-T. Pham, C. Zhao, R. S. Weber, Y. Wang, J. A. Lercher, *J.Phys.Chem.C* **2013**, *117*, 17603–17612.

[36] J. Chaminand, L. a. Djakovitch, P. Gallezot, P. Marion, C. Pinel and C. Rosier, *Green Chem.*, **2004**, *6*, 359–361.

[37] D. G. Lahr, B. H. Shanks, *J. Catal*. **2005**, *232*, 386–394.

[38] T. Miyazawa, Y. Kusunoki, K. Kunimori, K. Tomishige, *J. Catal*. **2006**, *240*, 213–221.

[39] T. Jiang, Y. Zhou, S. Liang, H. Liu, B. Han, *Green Chem* **2009**, *11*, 1000–1006.

[40] S. G. Wettstein, J. Q. Bond, D. M. Alonso, H. N. Pham, A. K. Datye, J. A. Dumesic, *Appl. Catal. B*, **2012**, 321–329.

[41] C. Zhao, J. A. Lercher, *Angew. Chem. Int. Ed*. **2012**, *51*, 5935.

[42] J. He, *Selective cleavage of C–O bonds and hydrodeoxygenation of lignin fragment molecules* **2014**.

[43] M. V. Bykova, D. Y. Ermakov, V. V. Kaichev, O. A. Bulavchenko, A. A. Saraev, M. Y. Lebedev, V. A. Yakovlev, *Appl. Catal. B* **2012**, *113*, 296–307.

[44] A. Corma, H. Garcia, *Catal. Today* **1997**, *38*, 257–308.

[45] S. Sitthisa, D. E. Resasco, *Catal. Lett*. **2011**, *141*, 784–791.

[46] M. A. n. González-Borja, D. E. Resasco, *Energy Fuels*, **2011**, *25*, 4155–4162.

[47] E. Laurent, B. Delmon, *Appl. Catal. A* **1994**, *109*, 77–96.

[48] V. M. Roberts, V. Stein, T. Reiner, X. Li, A. A. Lemonidou, J. A. Lercher, *Eur. J. Chem.* **2011**, *17*, 5939.

[49] D. C. Elliott, A. Oasmaa, *Energ. Fuel*. **1991**, *5*, 102.

[50] D. C. Elliott, E. G. Baker, J. Piskorz, D. S. Scott, Y. Solantausta, *Energ. Fuel*. **1988**, *2*, 234.

[51] E. Furimsky, *Appl. Catal. A; General* **2000***, 199*, 147.

[52] E. Laurent, B. Delmon, *J. Catal*. **1994**, *146*, 281.

[53] E. Furimsky, F. E. Massoth, *Catal. Today* **1999**, *52*, 381.

[54] C. Zhao, Y. Kou, A. A. Lemonidou, X. Li, J. A. Lercher, *Angew. Chem. Int. Ed.* **2009**, *48,* 3987.

[55] D.–Y. Hong, S. J. Miller, P. K. Agrawal, C. W. Jones, *Chem. Commun.* **2010**, *46*, 1038–1040.

[56] C. Zhao, J. He, A. A. Lemonidou, X. Li, J. A. Lercher, *J. Catal.* **2011,** *280*, 8–16.

[57] C. Zhao, S. Kasakov, J. He, J. A. Lercher, *J. Catal*. **2012**, *296*, 12–23.

[58] S. R. Blaszkowski, R. A. van Santen, *J. Am. Chem. Soc.* **1996**, *118*, 5152 – 5153.

[59] X. Liang, A. Montoya, B. S. Haynes, *J. Phys. Chem. B* **2011**, *115*, 8199-8206.

[60] J. He, C. Zhao, J. A. Lercher, *J. Am. Chem. Soc.*, **2012**, *134*, 20768–20775.

[61] T. D. Matson, K. Barta, A. V. Iretskii, P. C. Ford, *J. Am. Chem. Soc.*, **2011**, *133*, 14090.

[62] J. March, *Advanced Organic Chemistry: Reactions, Mechanisms, and Structure* (3rd ed.), **1985**, New York: Wiley, ISBN 0–471–85472–7.

[63] W. Reusch, *Virtual Text of Organic Chemistry* **1999**, http://www2.chemistry.msu.edu

[64] R. Brückner, *Reaktionsmechanismen*, **2007**, 3rd edition, Spektrum, Germany, ISBN 978–3–8274–1579–0.

[65] X. Xu, C. De Almeida, M. J. Antal, *J. Supercrit. Fluids* **1990**, *3*, 228–232.

[66] F. Carey, R. Sundberg, *Advanced Organic Chemistry*, Springer US, **2007**, 473–577.

[67] a) P. A. Jacobs, M. Tielen, J. B. Uytterhoeven, *J. Catal*. **1977**, *50*, 98–108; b) S. J. Gentry, R. Rudham, *J. Chem. Soc. Faraday Trans. 1* **1974**, *70,* 1685–1692.

[68] H. Chiang, A. Bhan, *J. Catal.* **2010**, *271*, 251–261.

[69] A. Corma, H. Garcia, *Catal. Today* **1997**, *38*, 257–308.

[70] M. Janik, J. Macht, E. Inglesia, M. Neurock, *J. Phys. Chem. C* **2009**, *113*, 1872–1885.

[71] M. Brändle, J. Sauer, *J. Am. Chem. Soc*. **1998**, *120*, 1556–1570.

[72] D. E. Bryant, W. L. Kranich, *J. Catal*, **1967**, *8*, 8–13.

[73] J. Cejka, A. Corma, S. I. Zones, *Zeolites and Catalysis: Synthesis, Reactions and Applications*; Wiley, New York **2010**.

[74] V. J. Frilette, W.O. Haag, R. M. Lago, *J. Catal.* **1981**, *67*, 218.

[75] R. Gounder, R., E. Iglesia, *Chem. Commun*. **2013**, *49*, 3491−3509.

[76] C. S. Cundy, P. A. Cox, *Micropor. Mesopor. Mat.* **2005**, *82*, 1–78.

[77] S. L. Burkett, M. E. Davis, *J. Phys. Chem*. **1994**, *98*, 4647–4653.

[78] J. L. Guth, H. Kessler, R. Wey, *Stud. Surf. Sci. Catal*. **1986**, *28*, 3.

[79] E. M. Flanigen, R. L. Patton, *US. Patent* 4,073,864, **1978**.

[80] M. E. Davis, R. F. Lobo, *Chem. Mater*. **1992**, *4*, 756–768.

[81] B. M. Lok, T. R. Cannon, C. A. Messina, *Zeolites* **1983**, *3*, 282.

[82] E. M. Flanigen, R. L. Patton, S. T. Wilson, *Stud. Surf. Sci. Catal*. *1988*, *37*, 13–27.

[83] R. M. Barrer, *Stud. Surf. Sci. Catal*. **1985**, *24*, 1.

[84] S.P. Naik, A.S.T. Chiang, R.W. Thompson, *J. Phys. Chem. B* **2003**, *107*, 7006.

[85] S. V. Luis, E. Garcia-Verdugo, *Chemical reactions and processes under flow conditions*, **2010**, ISBN**:** 978–0–85404–192–3.

[86] A. Feller, J. A. Lercher, *Adv. Catal*. **2004**, *48*, 229–295.

[87] G. James. G., *The Chemistry and Technology of Petroleum* (4th ed.). CRC Press. Speight **2006**, ISBN 0–8493–9067–2.

[88] A. Corma, *J. Catal*. **2003**, *216*, 298–312.

[89] G. Ertl, H. Knoezinger, J. Weitkamp, *Handbook of heterogeneous catalysis,* VCH Verlagsgesellschaft **2008**, ISBN 978–35272–92127.

[90] A. Primo, H. Garcia, *Chem. Soc. Rev*. **2014**, *43*, 7548–7561.

[91] A. Corma, V. Fornes, M. T. Navarro, J. Perez Pariente, *J. Catal*. **1994**, *148*, 569–574.

[92] J. Huang, Y. Jiang, V. R. R. Marthala, A. Bressel, J. Frey, M. Hunger, *J. Catal*. **2009**, *263*, 277–283.

[93] N. S. Gnep, M. Guisnet, *Bull. Soc. Chim. Fr.* **1977**, *5*, 429.

[94] L. D. Fernandes, J. L. F. Monteiro, E. F. S. Aguiar, A. Corma, *J. Catal.* **1998**, *177*, 363.

[95] M. Guisnet, N. S. Grup, S. Morin, *Micropor. Mesorpor Mater*. **2000**, *35*, 47.

[96] E. G. Derouane, *J. Catal*. **1986**, *100*, 541.

[97] E. Kikuchi, H. Nahano, K. Shinomura, Y. Morita, *Sekiyu Gakkash*i **1985**, *28*, 210.

[98] M. J. Antal, M. Carlsson, X. Xu, D. G. M. Anderson, *Ind. Eng. Chem. Res*. **1998**, *37*, 3820–3829.

[99] A. J. Jones, S. I. Zones, E. Iglesia, *J. Phys. Chem. C* **2014**, *118*, 17787–17800.

[100] A. Bhan, R. Gounder, J. Macht, E. Iglesia, *J. Catal*. **2008**, *253*, 221−224.

[101] R. Gounder, E. Iglesia, *Angew. Chem. Int. Ed*. **2010**, *49*, 808−811.

[102] B. Xu, C. Sievers, S. B. Hong, R. Prins, J. A. van Bokhoven, *J. Catal*. **2006**, *244*, 163.

[103] J. Dedecek, Z. Sobalík, B. Wichterlova, *Catal. Rev*. **2012**, *54*, 135−223.

[104] *Zeolites and Catalysis: Synthesis, Reactions and Applications,* J. Cejka, A. Corma, S. I. Zones, Wiley: New York, 2010.

[105] R. M. Ravenelle, F. Schüβler, A. D'Amico, N. Danilina, J. A. van Bokhoven, J. A. Lercher, C. W. Jones, C. Sievers, *J. Phys. Chem. C* **2010**, *114*, 19582–19595.

[106] C. S. Triantafillidis, A. G. Vlessidis, L. Nalbandian, N. P. Evmiridis, *Micropor. Mesopor. Mater.* **2001**, *47*, 369–388.

[107] S. van Donk, A. H. Janssen, J. H. Bitter, K. P. de Jong, *Catal. Rev.–Sci. Eng*. **2003**, *45,* 297–319.

[108] J. Klinowski, *Proc. Nucl. Magn. Reson. Spectrosc*. **1984**, *16*, 237–309.

[109] C. S. Triantafillidis, A. G. Vlessidis, N. P. Evmiridis, *Ind. Eng. Chem. Res*. **2000**, *39*, 307–319.

[110] S. M. Maier, A. Jentys, J. A. Lercher, *J. Phys. Chem. C* **2011**, *115*, 8005–8013.

[111] D. W. Breck, E. M. Flanigen, *Molecular Sieves*, Society of the Chemical Industry: London, **1968**.

[112] R. Carvajal, P.–J. Chu, J. H. Lunsford, *J. Catal.* **1990**, *125*, 123–131.

[113] W. Lutz, W. Gessner, R. Bertram, I. Pitsch, R. Fricke, *Micropor. Mater*. **1997**, *12*, 131–139.

[114] T. Sano, Y. Nakajima, Z. B. Wang, Y. Kawakami, K. Soga, *Micropor. Mater*. **1997**, *12*, 71–77.

[115] M. Ogura, S. Y. Shinomiya, J. Tateno, Y. Nara, E. Kikuchi, M. Matsukata, *Chem. Lett*. **2000**, 882–883.

[116] D. P. Serrano, J. M. Escola, P. Pizarro, *Chem. Soc. Rev*. **2013**, *42*, 4004.

Chapter 2

Following solid acid catalyzed reactions by MAS NMR spectroscopy in liquid phase – zeolite catalyzed conversion of cyclohexanol in water

The aqueous dehydration of secondary alcohols was previously shown to be the rate–limiting step of the biomass–derived phenol hydrodeoxygenation (HDO) sequence. Thus, a fundamental study of the reaction dynamics/kinetics is critically needed to facilitate the development of catalysts for the practical conversion of biomass to energy–carrying alkanes. An *in–situ* study of cyclohexanol (a common cycloalkanol from phenol HDO) dehydration on HBEA in liquid water at elevated temperatures using a custom designed batch micro autoclave, which is used as a rotor for high–resolution magic angle spinning (MAS) NMR spectroscopy, is reported. NMR spectroscopy not only enables discriminating between different mechanisms of water elimination, but also allows following the reactant distribution between the mobile and the adsorbed phases during the reaction. The initial rates of functional group migration in the reactants/products during aqueous cyclohexanol dehydration on HBEA are better explained by the E1 mechanism.

2.1 Introduction

The efficient catalytic hydrodeoxygenation (HDO) of phenols over metals, such as Pt,[1] Pd[2] or Ni,[3] requires an acid function to catalyze dehydration of the intermediately formed cycloalkanols. Surprisingly, the rate of dehydration normalized to the concentration of protons is about two orders of magnitude higher in a zeolite than in aqueous solution of a mineral acid.[4] It is also remarkable that hydroalkylation of phenol on HBEA can occur in water, while other macroporous solid acids do not catalyze this reaction.[5] It can be speculated that zeolites achieve this by providing an environment (sometimes called confinement and nest effects),[6] which uniquely stabilizes the sorbed and transition states.[7] To better understand the catalysis substantial efforts were undertaken to monitor the state of the reacting molecules by spectroscopic methods. The information obtained potentially allows one not only to understand the mechanistic pathways, but provides also the basis to design new and improve existing zeolites with respect to activity and selectivity.

The dehydration of secondary alcohols in aqueous phase catalyzed by a mineral acid generally proceeds by the E1 mechanism.[8] Also, alcohol dehydration in the gas phase using polyoxometalate[9] and zeolite[10] catalysts has been suggested to follow strictly the E1 elimination pathway. The catalyst acidity determined by the zeolite lattice composition[11] and the pore size[12] jointly control activity and selectivity for catalytic gas phase reactions. In this work the mechanism of the reaction of aqueous cyclohexanol on zeolite HBEA is elucidated using magic angle spinning (MAS) nuclear magnetic resonance (NMR) spectroscopy, which enables simultaneous monitoring of the state of reactants, intermediates and products, providing mechanistic insight *via* following the variations in isotopomer concentrations during catalytic transformations.

2.2 Experimental methods

2.2.1 Reagents

Cyclohexanol (Sigma–Aldrich, 99%), Cyclohexene (Sigma–Aldrich, 99%, GC–grade), 1,3–dimethoxybenzene (Sigma–Aldrich, 99%), dichloromethane (Sigma–Aldrich, HPLC grade), sodium sulfate (Acros Organics, 99%, anhydrous), ^{13}C–labeled

cyclohexanol–1–^{13}C (Sigma–Aldrich, 99 atom % ^{13}C, phosphoric acid (Sigma–Aldrich, 85wt% in water). HBEA was obtained from Süd Chemie AG (Clariant) in hydrogen form.

2.2.2 Zeolite catalyst characterization

Table 1. Physical properties of HBEA 150 (Si/Al = 75) zeolite used in this work.

Si/Al (mol × mol^{-1})	75
Total surface area (m^2 × g^{-1})	684
Mesopore surface area (m^2 × g^{-1})	140
Micropore surface area (m^2 × g^{-1})	544
Pore volume (cm^3 × g^{-1})	0.43
Mesopore volume (cm^3 × g^{-1})	0.21
Micropore volume (cm^3 × g^{-1})	0.22
Acid site concentration (NH_3–TPD) (μmol × g^{-1})	203
Acid site concentration (pyridine–TPD) (μmol × g^{-1})	180
Brønsted acid site (BAS) concentration (μmol × g^{-1})	147
Lewis acid site (LAS) concentration (μmol × g^{-1})	33

The zeolite is thermally treated for 10 hours at 400 °C in air and then used as catalyst. Chemical analysis was measured by atomic absorption spectroscopy (AAS) on a UNICAM 939 AA–Spectrometer. The BET surface area, pore volumes, and pore size distributions were determined by N_2 adsorption–desorption isotherms measured at 77.3 K using a PMI automatic BET–Sorptometer. Temperature–programmed desorption (TPD) of ammonia was carried out under flow conditions. The catalysts were activated in He at 623 K for 1 h with a heating rate of 5 K/min from ambient temperature to 623 K. Ammonia was adsorbed by adding 10 vol.% to the He carrier gas (total flow 30 mL/min) at 373 K. The sample was purged with He for 2 h in order to remove physisorbed molecules. The sample was then heated in flowing He at a rate of 10 K/min from 373 to 1033 K for TPD–NH_3 and the species desorbing was detected by mass spectrometry (Balzers QME 200). For calibration of the method, a standard (Zeolite HZSM–5 with Si/Al = 45, acid site concentration = 360 μmol × g^{-1}) was used. The average particle size was determined with DLS (Brookhaven Instruments 90Plus) IR spectra of adsorbed pyridine were recorded with a Perkin–Elmer 2000 spectrometer operating at a resolution of 4 cm^{-1} and equipped with an in situ IR cell capable of handling the activation of the

sample at elevated temperatures and under controlled pressures was used. Before recording the IR spectra, the catalyst samples were activated in vacuum ($p = 10^{-6}$ mbar) at 673 K for 1 h. Then, the sample was equilibrated with 0.5 mbar of pyridine at 423 K and was evacuated at 423 K for 1 h, subsequently. Catalyst characterization data is provided in Table 1.

2.2.3 Kinetic measurements

2.2.3.1 NMR batch autoclave

While in situ MAS–NMR spectroscopy was previously used to study gas solid reactions in controlled environments,[13] following reactions in liquid phase during the formation of solids was the limit for studying reactions during the synthesis of zeolites.[14] It has not been possible, thus far, to monitor two and three phase reactions involving solids, gases and liquids at elevated temperatures and pressures.[15] To address this a micro autoclave that functions as MAS–NMR rotor suitable for pressures of up to 20 bar independent of the gas atmosphere and temperatures of up to 200 °C was constructed allowing mechanistic studies of most reactions in organic synthesis. The detailed design of the micro autoclave that can be repeatedly sealed is illustrated in Figure 1. The rotor can withstand spinning the sample at elevated temperature and pressure with the design yielding negligible ^{13}C–background signal. The reactor is also suitable for operation with exogeneous high–pressure gas using a loading chamber that allows sealing and opening of the rotor in a controlled atmosphere.[16] The lid of the micro autoclave and the valve adaptor to pressurize it, are removable. Operation at pressures exceeding 20 bars is possible with marginal gas leaking for up to 72 h.

NMR experiments were performed using a custom designed batch micro autoclave NMR reactor (Figure 1) on a 500 MHz wide bore NMR spectrometer equipped with a homemade 9.5 mm MAS probe.[17] A single pulse sequence with a 45º–pulse angle and high power proton decoupling was used. As example experiment: in–situ ^{13}C MAS NMR spectra were acquired as function of time while spinning the sample, a mixture of 22 mg HBEA150 and 120 μL of 0.33 M cyclohexanol–1–^{13}C in water at estimated 130 °C, at 2.4 kHz. A recycle delay of 5 s and an accumulation number of 256 scans was applied resulting in single spectrum acquisition times of approximately 0.29 hours. The

temperature in the micro autoclave was calibrated prior to the experiment using Pb(NO3)2.[18] To minimize conversion of cyclohexanol–1–^{13}C prior to a kinetic run, the temperature of the sample was raised to 130 °C in two steps, first to 80 °C, at which time spectrometer settings were checked, and then to the reaction temperature. The heat up time for this second step was approximately 5 min. In this way less than 2 % of cyclohexanol–1–^{13}C was converted prior to acquiring the first spectrum. To assure quantitative analysis of obtained ^{13}C–NMR spectra T1 for cyclohexanol and cyclohexene were measured at RT and reaction temperature.

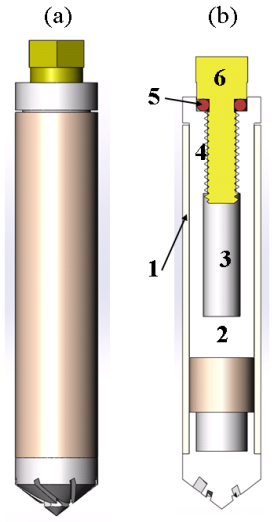

Figure 1. The 9.5 mm o.d. high temperature and high pressure MAS rotor is shown. (a) The fully assembled rotor; and (b) The various components, i.e., the zirconia rotor sleeve, 1, the ceramic insert made of materials such as Macor, 2, the sample cell space, 3, and thread, 4, O–ring, 5, and Torlon® screw, 6. The outside surface of the insert is fixed to the inner surface of the zirconia rotor sleeve by high temperature glue.

2.2.3.2 Parr batch autoclave

To complement the kinetic data obtained using the NMR batch autoclave the experiments were also repeated using a Parr 300 mL autoclave vessel. As an example of the batch autoclave experiment: 17.4 g HBEA150 and 80 mL 0.33 M cyclohexanol in water are placed in the 300 mL Hastelloy Parr reactor, heated to 160 °C and stirred

vigorously as temperature setting is reached. After a set time, the reactor is cooled with ice leading to a rapid cool down and reaction quench. Contents of reactor are extracted with dichloromethane and dried with sodium sulfate. The extract was analyzed on an Agilent 7890A GC equipped with HP–5MS 25–m 0.25–µm i.d. column, coupled with Agilent 5975C MS.

2.2.4 Theoretical methods

Periodic density functional calculations (DFT) were performed using the CP2K code.[19] Calculations employ a mixed Gaussian and plane wave basis sets. Core electrons were represented with norm–conserving Goedecker–Teter–Hutter pseudo–potentials[20] and the valence electron wave function was expanded in a double–zeta basis set with polarization functions[21] along with an auxiliary plane wave basis set with an energy cutoff of 360 eV. The generalized gradient approximation exchange–correlation functional of Perdew, Burke, and Enzerhof (PBE)[22] was used for all calculations. Each configuration was optimized with Broyden–Fletcher–Goldfarb–Shanno (BGFS) algorithm with SCF convergence criteria of 10^{-8} au. To compensate long–range van der Waals (VdW) interaction between adsorbate and zeolite, DFT–D3 scheme[23] with an empirical damped potential term was added into the energies obtained from exchange–correlation functional. Transition states for protonation, configuration transformation and dehydration steps in HBEA pore were located using IT–NEB method[24] with seven images between initial and final state.

2.3 Results and Discussion

2.3.1 The NMR batch micro autoclave results

Figure 2 shows the series of NMR spectra following the conversion of cyclohexanol with the assignment of individual ^{13}C–signals. After 23 hours reaction the following product distribution was observed: 36 % cyclohexene, 3 % dicyclohexyl ether and 1 % cyclohexyl–1–cyclohexene. The forward rate constant for cyclohexene formation was $k_f = 3.4\times10^{-5}$ s^{-1}, the turnover frequency (TOF) determined as the initial forward rate normalized by the concentration of Brønsted acid sites, TOF = 4.2×10^{-4} $mol_{cyclohexene}\cdot mol_{BAS}^{-1}\cdot s^{-1}$. At the start of the reaction, formation of cyclohexene and

dicyclohexyl ether is observed together with scrambling of the ^{13}C–label in the alicyclic ring. As the reaction progresses a secondary product, cyclohexyl–1–cyclohexene, is detected. At long reaction time quantification of products appearing in low concentration is hindered by the diversity of labeled products and long T1 for the carbon atoms without attached H atoms. However, ≥ 96 % of the ^{13}C could be accounted for as cyclohexanol and cyclohexene during the initial reaction stage (2 hours); the slight signal loss is attributed to low initial concentrations of dicyclohexyl ether and cyclohexyl–1–cyclohexene that would require a higher signal–to–noise ratio to measure accurately.

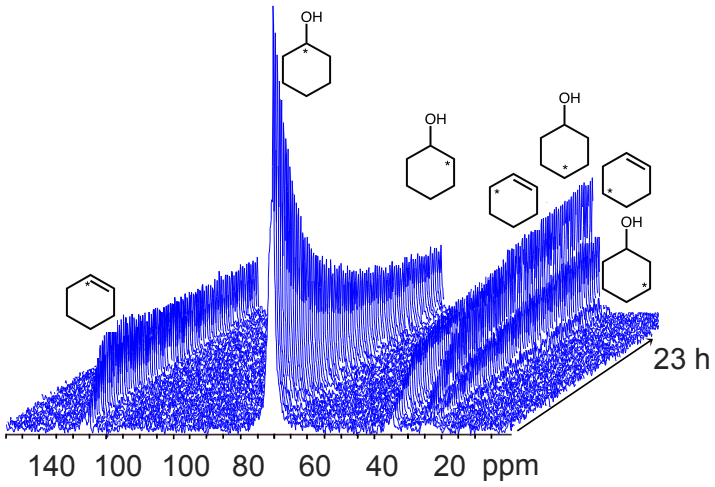

Figure 2. Stacked plot containing 80 MAS NMR spectra acquired data for a mixture of 22 mg HBEA150 and 120 µL of 0.33 M cyclohexanol–1–^{13}C at 130 °C in liquid water and as a function of time.

Initially cyclohexanol–1–^{13}C is observed as a narrow peak at about 70 ppm, corresponding to cyclohexanol–1–^{13}C in the aqueous phase, and a broad peak at about 70.8 ppm, which is attributed to cyclohexanol–1–^{13}C interacting with the zeolite. Using these two peaks it is estimated that about 50 % of the cyclohexanol present is initially adsorbed in the zeolite pores. A nearly identical value is observed for cyclohexene suggesting that the dispersion forces account for the largest fraction of the interaction energy.[25] Note that water fills the zeolite pores, while cyclohexanol occupies only up to 25 % of the pore volume during the reaction. Nevertheless, this corresponds to a

significant (20 fold) enhancement of the concentration of cyclohexanol compared to the aqueous phase. This exemplifies the potential to determine not only changes in concentrations, but also how it is possible to quantify the distribution between the adsorbed and the mobile phase at elevated pressures and temperatures.

2.3.2 Analysis of results from experiments using the MAS NMR micro autoclave rotor

Figure 2 shows a stack plot of *in situ* ^{13}C MAS NMR spectra that contains 80 individual spectra. Typically, very little of the cyclohexanol–1–^{13}C had converted prior to acquiring the first spectrum. For example, analysis of the run shown in Figure 3 and 4 found that 6 % conversion had occurred by the time the first spectrum was acquired (1024 s after starting acquisition). Extrapolating back in time to the start of acquisition, only about 1 % conversion had occurred during the set–up and heat–up times of this experiment.

The first and the 80^{th} spectrum in Figure 2 are compared in Figure 3. While initially only a single narrow peak is observed and assigned to cyclohexanol–^{13}C, after 23 h reaction at 130 °C (trace b in Figure 3) the primary reaction product is observed and identified as cyclohexene based on the characteristic double bond carbon peaks located at about 125 ppm (a narrow peak corresponding to the aqueous phase) and 126.6 ppm (a broad peak corresponding to those interacting with the catalyst surface). The isotope scrambling within both the reactants and the reaction products are observed as indicated in Figure 3. The peak assignments performed during analysis of individual spectra are based on the Spectral Database of Organic Compounds (SDBS).[26] Spin–lattice relaxation times (T1) measured for the peaks and their assignments are listed in Table 2. For the T1 measurements and the reaction kinetics, spectral deconvolution was performed first and then the integrated peak intensities for each of the reactants/products, both in the aqueous and the adsorbed phases, were obtained as a function of time.

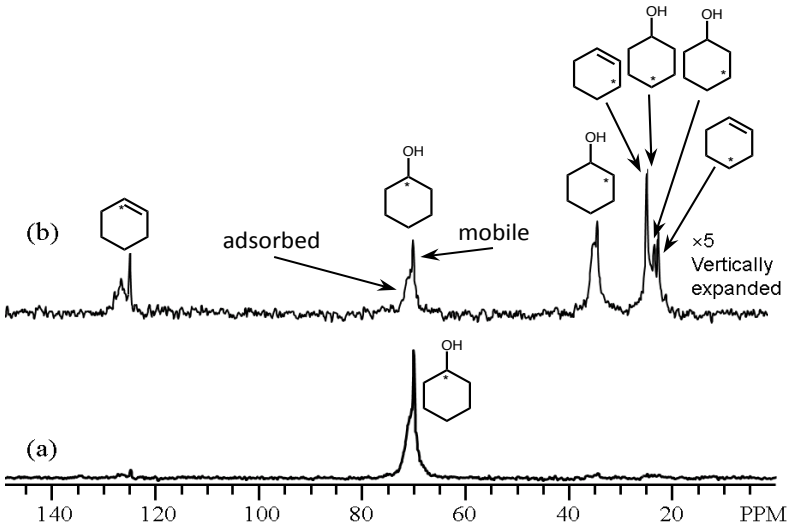

Figure 3. First (a) and 80th (b) *in situ* ^{13}C MAS NMR spectra obtained from Figure 2. The first and the 80th spectra acquired at the reaction temperature of 130 °C.

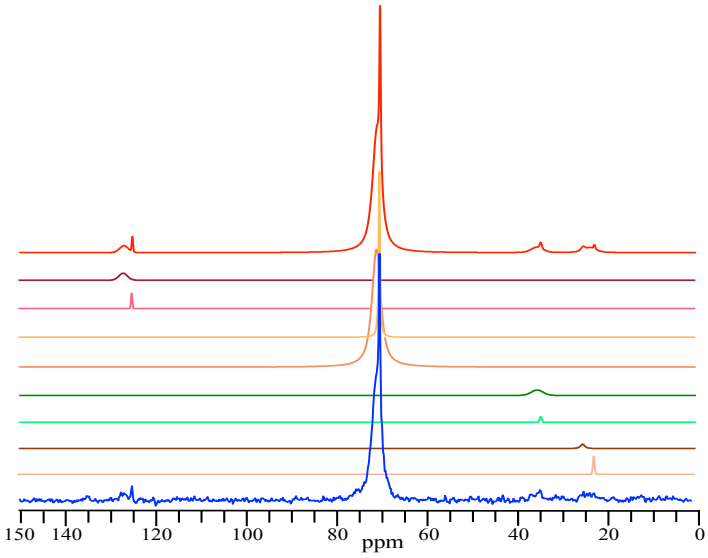

Figure 4. Example of ^{13}C MAS NMR spectrum deconvolution: measured (bottom blue), individual peaks (orange – purple) and fitted spectrum (top red).

Table 2. T1 values for carbon signals observed in MAS NMR measured at 130 °C.

NMR Shift (ppm)	T1 (s^{-1})	Assigned Structure	Phase
23.7	2.6 ± 0.3	cyclohexene–4–^{13}C + cyclohexanol–3–^{13}C	unresolved
25.1	0.6 ± 0.1	cyclohexene–3–^{13}C + cyclohexanol–4–^{13}C	unresolved
34.7	2.1 ± 0.5	cyclohexanol –2–^{13}C	mobile
35.1	0.78 ± 0.07		adsorbed
70.0	2.8 ± 0.4	cyclohexanol –1–^{13}C	mobile
70.8	0.7 ± 0.04		adsorbed
125.2	2.8 ± 0.4	cyclohexene–1–^{13}C	mobile
127.2	0.16 ± 0.02		adsorbed

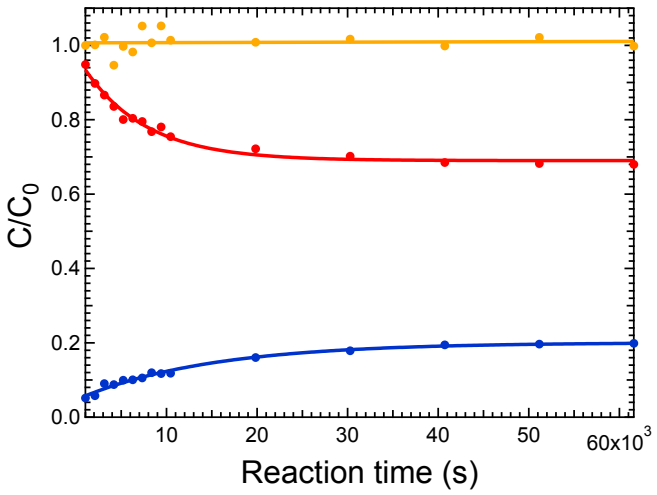

Figure 5. Cyclohexanol dehydration monitored by ^{13}C MAS NMR, internal standard (phenol) used. 27 mg HBEA + 123 µL 0.33 M cyclohexanol–1–^{13}C and 0.17 M phenol–1–^{13}C reacting at 130 °C. Cyclohexanol and cyclohexene concentrations are reported as fractions normalized to the initial concentration of alcohol in the reactor and phenol concentration is reported as fraction normalized to the initial concentration of phenol in the reactor. Only major products shown: cyclohexanol (red), cyclohexene (blue) and phenol (orange).

The distribution of products is based on the relative areas of ^{13}C–peaks normalized by the sum of ^{13}C–peaks present initially. To validate that the observed NMR signal intensity corresponds to the true compound amount in the rotor an additional experiment was performed using a mixture of 27 mg of HBEA150 and 123 µL of 0.33 M cyclohexanol–1–^{13}C and 0.17 M phenol–1–^{13}C were loaded in the NMR micro autoclave and heated to 130 °C while NMR spectra were acquired in situ as a function of time.

Table 3. Kinetic results for cyclohexanol dehydration catalyzed by HBEA and by phosphoric acid.

Entry	Reaction Conditions	Forward rate constant k_f,[a] s^{-1}	Intrinsic rate constant,[b] $L\ s^{-1}\ mol_{BAS}^{-1}$	TOF[c] $mol_{cyclohexene}\ mol_{BAS}^{-1}\ s^{-1}$
1	23.5 mg HBEA and 125 µL of 0.33 M cyclohexanol–1–^{13}C at 130 °C; NMR rotor autoclave	2.3×10^{-5}	1.5×10^{-3}	2.8×10^{-4}
2	22.0 mg HBEA and 120 µL of 0.33 M cyclohexanol–1–^{13}C at 130 °C; NMR rotor autoclave	3.4×10^{-5}	2.3×10^{-3}	4.2×10^{-4}
3	10.4 mg HBEA and 140 µL of 0.33 M cyclohexanol–1–^{13}C at 130 °C; NMR rotor autoclave	1.1×10^{-5}	1.6×10^{-3}	3.3×10^{-4}
4	27.0 mg HBEA and 123 µL of 0.33 M cyclohexanol–1–^{13}C and0.17 M phenol–1–^{13}C (internal standard) at 130°C; NMR rotor autoclave	1.5×10^{-5}	8.3×10^{-4}	1.5×10^{-4}
5	17.4g HBEA and 80 mL of 0.33 M cyclohexanol at 130 °C; stirred 300 mL batch reactor	6.1×10^{-5}	1.8×10^{-3}	6.1×10^{-4}
6	17.4g HBEA and 80 mL of 0.33 M cyclohexanol at 160 °C; stirred 300 mL batch reactor	1.0×10^{-3}	0.11	1.0×10^{-2}
7	177 µL of 0.33 M cyclohexanol–1–^{13}C and 0.9 M H_3PO_4 at 130 °C; NMR rotor autoclave	3.7×10^{-5}	5.1×10^{-5}	1.4×10^{-5}
8	80 mL of 0.33 M cyclohexanol and 0.9 M H_3PO_4 at 160 °C; stirred 300 mL batch reactor	3.8×10^{-4}	1.6×10^{-3}	1.4×10^{-4}

[a] Forward rate constant obtained from fitting reaction progress v. time data (see text) to reversible first order reaction rate law.

[b] Intrinsic rate constant calculated as $k_f \cdot vol_{reactor}/mol_{BAS}$, where BAS = Brønsted acid sites.

[c] Turnover frequency calculated as $k_f \cdot mol_{cyclohexol,t=0}/mol_{BAS}$.

As the phenol did not undergo alkylation or other reaction under these reaction conditions it serves as an internal standard. The time dependent concentrations of phenol, cyclohexanol and cyclohexene are shown in Figure 5. Note that cyclohexanol and cyclohexene are reported as fractions normalized to the initial concentration of alcohol in the reactor ($C_{cyclohexanol}/C_{0,cyclohexanol}$ and $C_{cyclohexene}/C_{0,cyclohexanol,}$ respectively) and phenol is reported as the fraction normalized to the initial concentration of phenol in the reactor ($C_{phenol}/C_{0,phenol}$). The fraction of carbon that is present as phenol–1–^{13}C is nearly constant during the experiment demonstrating that the NMR signal intensity remains constant during the measurements. The kinetic data for cyclohexanol dehydration reactions obtained in this study are summarized in Table 3.

2.3.3 NMR micro autoclave mass transport limitation estimate

In order to estimate the mass transport limitations that may occur during the reaction in the NMR micro autoclave the values for the Weisz–Prater criterion estimating the influence of pore diffusion on reaction rates[27] and the Thiele modulus describing the relationship between diffusion and reaction rate[28] were determined. Also, the values for Damkoehler I, estimating the ratio of reaction rate constant and the convective transport rate constant, and Damkoehler II, defined as the ratio of the chemical reaction rate to the mass transfer rate[29] were determined. Note that the obtained values listed in Table 4 are a conservative estimate using the diffusion coefficient (D_e) of cyclohexanol at room temperature (8.6×10^{-6} cm^2 s^{-1})[30] and the kinematic viscosity (ν) of water at room temperature (0.01 cm^2 s^{-1}).[31] The obtained values suggest there are no transport limitations for both the reactant transport in the bulk liquid phase and in the zeolite pore.

Table 4. Mass transport limitation estimates for the NMR micro autoclave reactor.

Weisz–Prater criterion	6.2×10^{-6}
Thiele modulus	8.8×10^{-4}
Damkoehler I	2.2×10^{-3}
Damkoehler II	3.4×10^{-10}

In addition to the estimates from dimensionless number, we are able to exclude the impact of external or internal diffusion limitations, as at the start of the reaction approximately 50 % of the alcohol is adsorbed in the zeolite pores corresponding to 5 cyclohexanol molecules per Brønsted acid site (see below) and, thus, local depletion of reactants is excluded up to moderate conversions.

2.3.4 Cyclohexanol adsorption on HBEA zeolite

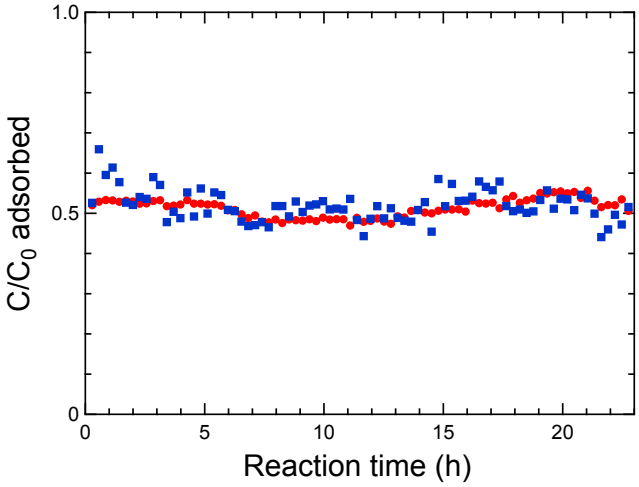

Figure 6. Fractions of cyclohexanol (red) and cyclohexene (blue) absorbed in the zeolite pore as measured by MAS NMR during reaction at 130 °C. Note: compound concentrations are reported as fractions normalized to the initial concentration of alcohol in the reactor. The results show that the zeolite adsorbs about 50 % of both cyclohexanol and cyclohexene.

From integration of the NMR peaks, the percentages of cyclohexanol and cyclohexene adsorbed by the zeolite during reaction at 130 °C were determined. It was found that approximately 50 % of the cyclohexanol is distributed in the zeolite (Figure 6). Note however, that the ratio of cyclohexanol to zeolite acid sites was purposefully set at 10:1. The NMR observations show a local concentration increase of cyclohexanol occurs in the zeolite pores, which can be then viewed as a separate micro–reactor. While one

cyclohexanol molecule is adsorbed on Brønsted acid site and a carbenium ion is formed, the next cyclohexanol molecule is already in the pore. Hence the cyclohexyl–cation can then either loose a proton to form cyclohexene, react with water to reform the cyclohexanol or undergo nucleophilic addition of cyclohexene leading to C–C bond coupling. Note that this information can be easily obtained by virtue of MAS NMR.

2.3.5 Catalysis by aqueous H_3PO_4

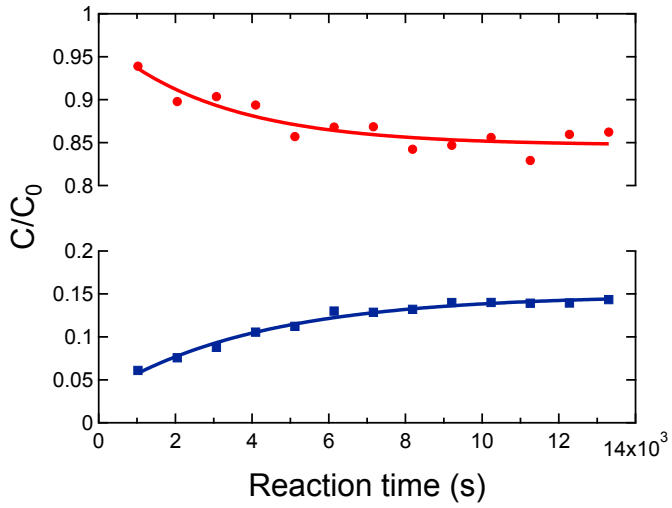

Figure 7. Kinetics for dehydration of cyclohexanol catalyzed by H_3PO_4 measured with the MAS NMR rotor autoclave, (red) cyclohexanol and (blue) cyclohexene. Conditions: 177 µL of 0.33 M cyclohexanol and 0.9 M phosphoric acid solution in water to 130 °C. Dicyclohexyl ether and cyclohexyl–1–cyclohexene, observed in the HBEA catalyzed reaction, were not observed. Note: compound concentrations are reported as fractions normalized to the initial concentration of alcohol in the reactor.

To compare HBEA with a homogeneous acid catalyst, the kinetics for reaction of cyclohexanol in aqueous H_3PO_4 using the MAS NMR autoclave rotor were measured. Results of an example experiment using a solution of 177 µL of 0.33 M cyclohexanol and 0.9 M phosphoric acid solution in water are shown in Figure 7. No C–C or C–O alkylation products were observed in this reaction. The analysis leads to $k_f = 3.7\times10^{-5}$ s^{-1}

and TOF = 1.4×10^{-5} $mol_{cyclohexene}\cdot mol_{BAS}^{-1}\cdot s^{-1}$. The rate constant for hydration of cyclohexene to cyclohexanol was determined at $k_{1r} = 2.1\times10^{-4}$ s^{-1}.

2.3.6 Results from experiments using a batch autoclave

The reaction was also studied under similar conditions in a 300 mL stirred (700 rpm) autoclave. As an example: 17.4 g HBEA150 and 80 mL 0.33 M cyclohexanol in water were placed in the reactor and heated to 160 °C. The reactor contents were stirred vigorously upon reaching the temperature setting. The conversion of cyclohexanol to cyclohexene was determined at 34 % in 1 h. In parallel with formation of cyclohexene, we observed conversion to dicyclohexyl ether (1.5 %) and to the C–C coupled product, cyclohexyl–1–cyclohexene (9 %). The TOF for alcohol conversion to olefin was determined at TOF = 1×10^{-2} $mol_{cyclohexene}\cdot mol_{BAS}^{-1}\cdot s^{-1}$. The Berkeley MadonnaTM[32] program for modeling and analysis of dynamic systems was used to analyze the results in Figure 8.

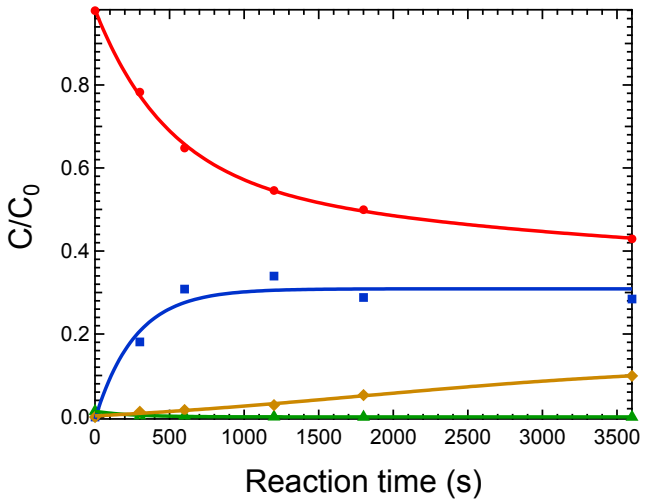

Figure 8. Product distribution for experiments performed in the 300 mL Parr batch autoclave. An example experiment: 17.4 g HBEA150 and 80 mL 0.33 M cyclohexanol in water heated to 160 °C for times up to 1 h; compound concentrations are normalized to the initial cyclohexanol concentration; cyclohexanol (red), cyclohexene (blue), dicyclohexyl ether (green) and cyclohexyl–1–cyclohexene are shown.

Equation 1. Reactions and differential rate equations used to fit the batch autoclave data.

1) Cyclohexanol (A) ⇌ Cyclohexene (B)

2) 2 Cyclohexanol ⇌ Dicyclohexyl ether (C)

3) 2 Cyclohexene → Cyclohexyl–1–cyclohexene (D)

$$dA/dt = -k_{1f}A + k_{1r}B - 2k_{2f}A^2 + k_{2r}C$$

$$dB/dt = k_{1f}A - k_{1r}B - 2k_{3f}B^2$$

$$dC/dt = k_{2f}A^2 - k_{2r}C$$

$$dD/dt = k_{3f}B^2$$

The model equations used to fit the experimental data are listed above (Equation 1). The dehydration of cyclohexanol and hydration of cyclohexene are modeled as pseudo first order reactions (water and proton concentrations are assumed to be constant). Formation of dicyclohexyl ether is modeled[33] as being pseudo second order in cyclohexanol. The reverse reaction is modeled as a pseudo first order process. Formation of cyclohexyl–1–cyclohexene is modeled as a reversible pseudo second order reaction. The reaction rate constant for olefin formation was determined as $k_{1f} = 1.0\times10^{-3}$ s^{-1}.

2.4 Alcohol dehydration mechanism in aqueous medium

2.4.1 Elimination reaction pathways

To determine which mechanism, E1 or E2, operates in the dehydration of cyclohexanol, the ^{13}C–label scrambling was analyzed and the initial rates of disappearance of cyclohexanol–1–^{13}C and the appearance of the differently labeled products were determined. A simplified kinetic model (discussed below) shows the E1–type elimination *via* carbenium–ions fully accounting for all initial rates, suggesting that the cyclohexyl cation undergoes 1,2–hydride shift competitive with rehydration and deprotonation.[34] The model shows that the rate of the 1,2–hydride shift approximately equals that of deprotonation and is approximately half the rate of the rehydration of cyclohexene (discussed in Figure 9, next section). As dehydration approaches equilibrium, the probability for electrophilic attack of cyclohexyl carbenium ion on cyclohexene to form cyclohexyl–1–cyclohexene increases. The cyclohexyl cation is concluded to be the central intermediate, which explains the reaction products, as well as

the rapid migration of the hydroxyl–group and double bond away from the ^{13}C–labeled carbon. An E2–type elimination kinetic model cannot account for these rates. The mechanism determined by virtue of in situ NMR analysis and proposed in this work is shown in Scheme 1.

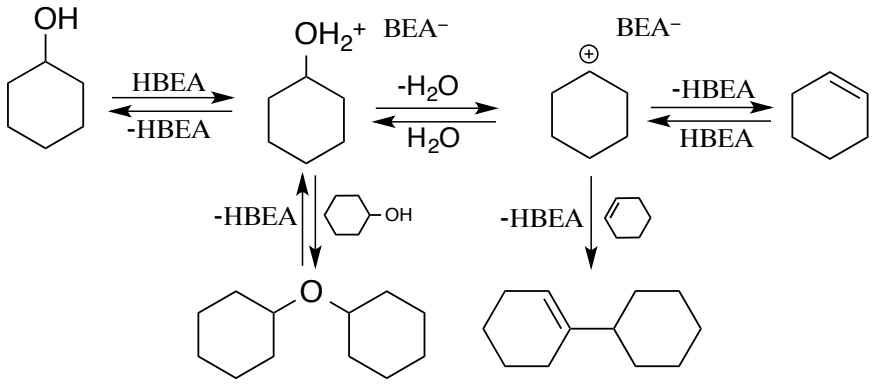

Scheme 1. Proposed reaction pathway of cyclohexanol reacting in water on HBEA.

In the absence of water, alcohol dehydration on zeolites has been suggested to proceed *via* the E1–mechanistic pathway,[35] with the formation of surface–bound alkoxide–species and water constituting the rate–determining step.[36] In contrast, a corresponding species was not observed in MAS–NMR (Zeolite^{+}–O^{-}R) in presence of larger concentrations of liquid water. In passing it should also be mentioned that such alkoxides have been suggested to be unstable even in the presence of gaseous water.[37]

The E2 mechanism, requiring the C–O and β C–H bonds to be cleaved concertedly, is not relevant in the present case. If this pathway were dominant, then the initial rate of disappearance of the starting cyclohexanol–1–^{13}C should equal the initial rate of appearance of cyclohexene. Since this step is reversible, the ^{13}C–scrambling would be explained by hydration of cyclohexene leading to equal probability for the label to be in either the 1– or 2–labeled position of cyclohexanol. However, the initial rate for disappearance of cyclohexanol–1–^{13}C is 2.5 times the initial rate of formation of cyclohexene–1–^{13}C. Furthermore, the initial rates for formation of cyclohexanol–2–^{13}C and cyclohexene–3–^{13}C are 0.2 and 0.1 times the initial rate of disappearance of

cyclohexanol–1–^{13}C, respectively. Thus, on the basis of these individual rates an E2–type elimination mechanism can be excluded.

Given that hydronium ions or Brønsted acid sites are the catalytically active species, it is important to compare the specific catalytic activity of Brønsted acid sites in zeolites with the activity of hydronium ions in acidic aqueous solutions. The comparison of the reactivity of zeolite HBEA with that of phosphoric acid at 160 °C shows under identical reaction conditions a TOF = 1×10^{-2} $mol_{cyclohexene}\cdot mol_{BAS}^{-1}\cdot s^{-1}$ for the zeolite and 1.4×10^{-4} $mol_{cyclohexene}\cdot mol_{BAS}^{-1}\cdot s^{-1}$ for H_3PO_4, i.e., the zeolite has over a 100 times higher turnover frequency (Table 3). Because the dehydration displays a first order dependence in cyclohexanol for the zeolite as well as the mineral acid, it is concluded that the acid site concentration interacting with cyclohexanol must be low. This raises the question, why the rate is substantially higher in the case of the zeolite. While the presence of sufficient water leads to hydronium ions in both cases, the environment of the zeolite pore is shown to stabilize the transition state such that the activation entropy for the dehydration is significantly higher in the case of the zeolite.[38] A further interpretation is beyond the scope of the present contribution. Note, however, that preliminary results of theoretical calculations indeed point to a stabilization of the hydroxonium ion transition state.

Because C–C coupling products are observed in the presence of zeolite, but not when catalyzed by aqueous H_3PO_4, it is concluded that also in this case the zeolite pores exert a specific influence stabilizing the transition state of the bimolecular reaction.[36]

These reaction pathways are in line with computational modeling (see Appendix) in the absence of water indicating that cyclohexanol adsorbs on Brønsted acid sites with a binding energy of 116 kJ/mol, which is significantly higher than binding energy of water (45 kJ/mol). Cyclohexanol is spontaneously protonated upon adsorption, with proton transfer being thermodynamically favored by 29 kJ/mol. Calculation shows that decomposition of the protonated cyclohexanol into cyclohexyl cation and water *via* C–O bond scission is an endothermic step and rate limiting with an activation barrier of 97 kJ/mol. After C–O bond scission a β–methylene proton of cyclohexyl–cation is transferred back to HBEA re–forming the zeolite hydroxyl–group and leads to cyclohexene, which is favored over the carbenium ion by 15 kJ/mol in the zeolite.

2.4.2 Kinetic model for the formation of ^{13}C–isotopomers

The E1–elimination mechanism is shown in Figure 9 and the corresponding differential rate equations as well as reaction rate constants are listed in the Appendix.

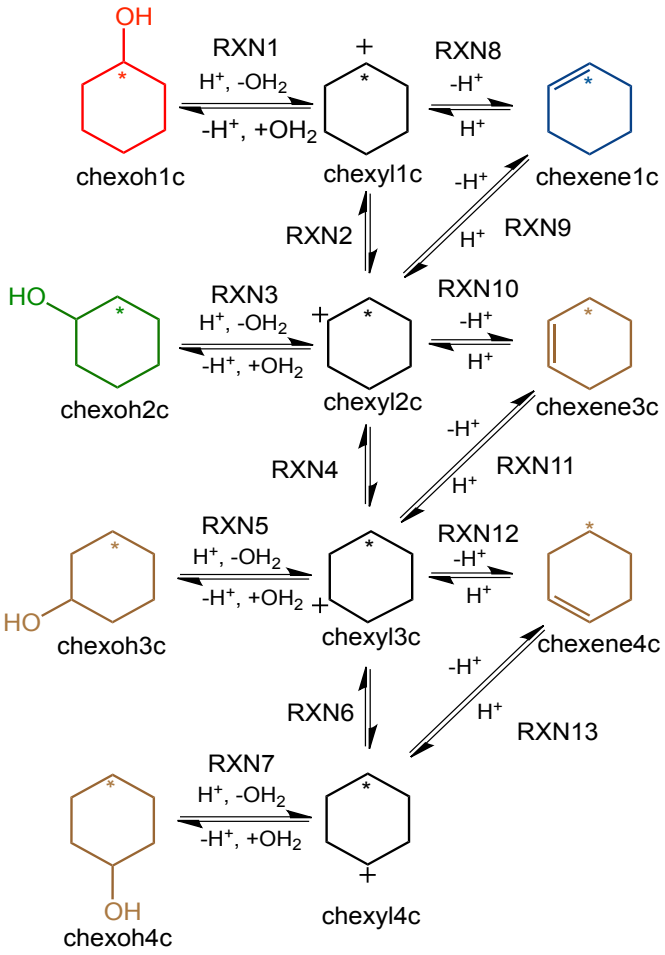

Figure 9. Reactions used to model the conversion of cyclohexanol–1–^{13}C catalyzed by HBEA zeolite in water. The model includes formation of the cyclohexyl cation and the 1,2–hydride shift reaction.

The 1,2–hydride shift reaction steps that would allow migration of the cationic site in competition with either deprotonation or hydration are also included in Figure 9. To simplify the kinetic model, the analysis is limited to the initial 6200 s (first six data points) of the reaction during which time the yields of dicyclohexyl ether and

cyclohexyl–1– cyclohexene are negligible. Therefore, only steps for the mechanism of dehydration that would account for isotope scrambling are included.

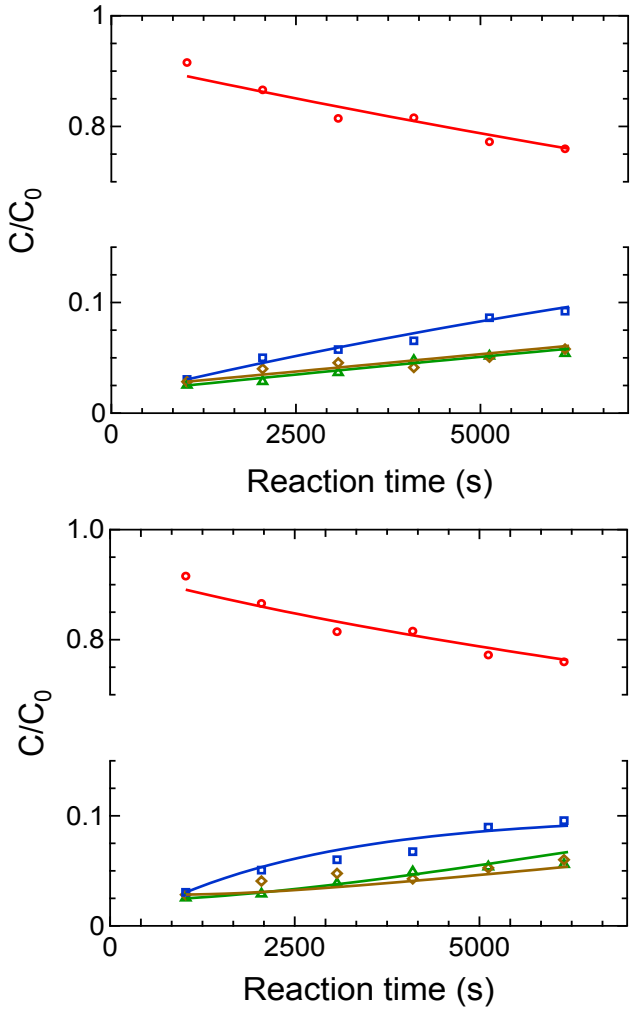

Figure 10. Comparison of plots showing the data for dehydration of cyclohexanol–^{13}C measured in the MAS NMR micro autoclave rotor at early times fitted to microkinetic models of the E1 and E2 mechanisms. The top plot shows the fit to the E1 mechanism and the bottom plot shows the fit to the E2 mechanism. (red) Cyclohexanol–1–^{13}C, (blue) cyclohexene–1–^{13}C, (green) cyclohexanol–2–^{13}C, and (brown) other isotopomers (cyclohexene–3–^{13}C and cyclohexene–4–^{13}C and cyclohexanol–3–^{13}C and cyclohexanol– 4–^{13}C). Conditions: 23.5 mg HBEA and 125 μL of 0.33 M cyclohexanol–1–^{13}C in liquid water heated to 130 °C. Note: compound concentrations are reported as fractions normalized to the initial concentration of cyclohexanol–1–^{13}C in the reactor.

Figure 10 (top) shows data for the dehydration of cyclohexanol measured in the MAS NMR micro autoclave rotor and the regression fit. The optimized rate constants for the E1 model are $k_{1f} = 5.06\times10^{-5}\ s^{-1}$, $k_{1r} = 2.45\ s^{-1}$, $k_{2f} = 1.43\ s^{-1}$, $k_{8f} = 3.09\times10^{-5}\ s^{-1}$, $k_{8r} = 1$ (assigned). The root mean square (RMS) deviation for the fit is 0.0231. Such a good fit could not be obtained without incorporation of 1,2–hydride shift steps in the model. The rate for formation of all cyclohexene isotopomers was determined by summing the individual isotopomers and fitting the data to the integrated rate law for a reversible reaction yielding $k_f = 2.3\times10^{-5}\ s^{-1}$ and $k_r = 3.1\times10^{-5}\ s^{-1}$, the TOF value was determined at $3\times10^{-4}\ mol_{cyclohexene}\cdot mol_{BAS}^{-1}\cdot s^{-1}$. The Figure 10 (bottom) also shows the fit to the E2 elimination mechanism, which requires a concerted scission of the C–O and β C–H bonds. To simulate the E2 mechanism, the following constraints are enforced in the model: $k_{2f} = 0$, $k_{1r} = 1$, $k_{8r} = 1$. This causes the cyclohexanol to disappear at the same rate as cyclohexene appears and scrambling only to occur *via* rehydration of cyclohexene. It leads to $k_{1f} = 6.0\times10^{-5}\ s^{-1}$ and $k_{8f} = 3.4\times10^{-4}\ s^{-1}$ and a RMS deviation for the fit, 0.0322, that is 40 % larger that the RMS deviation obtained when the E1 mechanism is simulated by letting k_{2f} and k_{1r} obtain optimum values. It can be seen in Figures 10 that the larger error is due to the E2 model predicting a too high of an initial rate for cyclohexene production.

2.5 Conclusions

The sorbed cyclohexanol is bound primarily *via* dispersion forces and is specifically adsorbed in the vicinity of the Brønsted acid sites in protonated form. Under present experimental conditions only approximately 5 % of cyclohexanol in the pores is adsorbed in the latter form. Water elimination follows an E1–mechanism forming a cyclohexyl carbenium ion, which either undergoes rapid 1,2–hydride shift or is re–hydrated, thus, scrambling the label in cyclohexanol. Transfer of the proton back to HBEA closes the catalytic cycle and leads to the primary product, cyclohexene. Alternatively, the cyclohexyl oxonium ion reacts with another cyclohexanol forming dicyclohexyl ether, in analogy to dimethyl ether formation. In approaching the equilibrium, the cyclohexyl carbenium ion also undergoes nucleophilic addition of cyclohexene leading to C–C coupling and formation of cyclohexyl–1–cyclohexene.

In this chapter the novel micro autoclave NMR rotor was demonstrated to allow kinetic and mechanistic studies of solid-liquid-gas and liquid-liquid-gas reactions at high temperatures and pressures to an unprecedented extent. The breadth and depths of mechanistic studies will only be limited by the sensitivity of the NMR spectrometer to differentiate the isotopomers of the reacting species.

2.6 Acknowledgements

Z. A. Chase and J. Sun (both from Washington State University) are acknowledged for pretreating the catalyst. C. F. Peden is acknowledged for his support in developing the NMR capability. This work was supported by the U. S. Department of Energy (DOE), Office of Basic Energy Sciences, Division of Chemical Sciences, Geosciences & Biosciences. All experiments were performed at the Environmental Molecular Sciences Laboratory, a national scientific user facility sponsored by the DOE's Office of Biological and Environmental Research located at Pacific Northwest National Laboratory (PNNL).

2.7 Appendix

2.7.1 Kinetic equations for the E1 elimination model used in the Berkeley MadonnaTM program to analyze the kinetics of ^{13}C–scrambling

The elementary reactions, differential equations and boundary conditions for the E1 elimination microkinetic model are listed below. The reaction scheme is diagrammed in Figure 9.

1) Cyclohexanol-1-^{13}C (A_1) ($+H^+$) ⇌ Cyclohexyl-1-^{13}C (I_1) ($+ H_2O$)
2) Cyclohexyl-1-^{13}C (I_1) ⇌ Cyclohexyl-2-^{13}C (I_2)
3) Cyclohexanol-2-^{13}C (A_2) ($+H^+$) ⇌ Cyclohexyl-2-^{13}C (I_2) ($+ H_2O$)
4) Cyclohexyl-2-^{13}C (I_2) ⇌ Cyclohexyl-3-^{13}C (I_3)
5) Cyclohexanol-3-^{13}C (A_3) ($+H^+$) ⇌ Cyclohexyl-3-^{13}C (I_3) ($+ H_2O$)
6) Cyclohexyl-3-^{13}C (I_3) ⇌ Cyclohexyl-4-^{13}C (I_4)
7) Cyclohexanol-4-^{13}C (A_4) ($+H^+$) ⇌ Cyclohexyl-4-^{13}C (I_4) ($+ H_2O$)
8) Cyclohexene-1-^{13}C (B_1) ($+H^+$) ⇌ Cyclohexyl-1-^{13}C (I_1)
9) Cyclohexene-1-^{13}C (B_1) ($+H^+$) ⇌ Cyclohexyl-2-^{13}C (I_2)
10) Cyclohexene-3-^{13}C (B_3) ($+H^+$) ⇌ Cyclohexyl-2-^{13}C (I_2)
11) Cyclohexene-3-^{13}C (B_3) ($+H^+$) ⇌ Cyclohexyl-3-^{13}C (I_3)
12) Cyclohexene-4-^{13}C (B_4) ($+H^+$) ⇌ Cyclohexyl-3-^{13}C (I_3)
13) Cyclohexene-4-^{13}C (B_4) ($+H^+$) ⇌ Cyclohexyl-4-^{13}C (I_4)

$dA_1/dt = – k_{1f} A_1 + k_{1r}I_1$
$dA_2/dt = – k_{3f}A_2 + 2k_{3r}I_2$
$dA_3/dt = – k_{5f}A_3 + 2k_{5r}I_3$
$dA_4/dt = – k_{7f}A_4 + k_{7r}I_4$
$dB_1/dt = – k_{8f}B_1 + 2k_{8r}I_1 – k_{9f}B_1 + 2k_{9r}I_2$
$dB_3/dt = – k_{10f}B_3 + 2k_{10r}I_2 – k_{11f}B_3 + 2k_{11r}I_3$
$dB_4/dt = – k_{12f}B_4 + 2k_{12r}I_3 – k_{13f}B_4 + 2k_{13r}I_4$
$dI_1/dt = – k_{1r}I_1 – 2k_{2f}I_1 – 2k_{8r}I_1 + k_{1f}A_1 + k_{8f}B_1 + k_{2r}I_2$
$dI_2/dt = 2k_{2f}I_1 – k_{2r}I_2 + k_{3f}A_2 – k_{3r}I_2 – k_{4f}I_2 + k_{4r}I_3 + k_{9f}B_1 – k_{9r}I_2 + k_{10f}B_3 – k_{10r}I_2$
$dI_3/dt = k_{4f}I_2 – k_{4r}I_3 + k_{5f}A_3 – k_{5r}I_3 – k_{6f}I_3 + 2k_{6r}I_4 + k_{11f}B_3 – k_{11r}I_3 + k_{12f}B_4 – k_{12r}I_3$
$dI_4/dt = k_{6f}I_3 – 2k_{6r}I_4 + k_{7f}A_4 – k_{7r}I_4 + k_{13f}B_4 – 2k_{13r}I_4$

Boundary conditions and constraints:
$[^{13}C]_{t0} = [A_1]_{t0} + [A_2]_{t0} + [A_3]_{t0} + [A_4]_{t0} + [B_1]_{t0} + [B_3]_{t0} + [B_4]_{t0}$
$[A_1]/[^{13}C]_{t0} = 0.891$
$[A_2]/[^{13}C]_{t0} = 0.0254$
$[A_3]/[^{13}C]_{t0} = 0.0143$
$[A_4]/[^{13}C]_{t0} = 0$
$[B_1]/[^{13}C]_{t0} = 0.0305$
$[B_3]/[^{13}C]_{t0} = 0.0143$
$[B_4]/[^{13}C]_{t0} = 0$
$[I_1]/[^{13}C]_{t0} = [I_4]/[^{13}C]_{t0} = 0$
$[I_2]/[^{13}C]_{t0} = [I_3]/[^{13}C]_{t0} = 2[I_1]/[^{13}C]_{t0}$

$k_{2r} = k_{4f} = k_{6f} = k_{2f}$
$k_{3f} = k_{5f} = k_{7f} = k_{1f}$
$k_{9f} = k_{10f} = k_{11f} = k_{12f} = k_{13f} = k_{8f}$
$k_{3r} = k_{5r} = k_{7r} = k_{1r}$
$k_{9r} = k_{10r} = k_{11r} = k_{12r} = k_{13r} = k_{8r}$

The differential equations and boundary conditions for the E1 elimination microkinetic model are listed below in a format for input to the Berkeley Madonna program. The reaction scheme with corresponding labels is diagrammed in Figure 9.

```
{ 1: chexol1c <--> chexyl1c }
   RXN1 = K1f*chexol1c - K1r*chexyl1c
   d/dt(chexol1c) = -RXN1
   d/dt(chexyl1c) = +RXN1-2*RXN2+2*RXN8

{ 2: chexyl1c <--> 1/2 chexyl2c }
   RXN2 = K2f*chexyl1c - K2r*chexyl2c/2
   d/dt(chexyl2c) = 2*(RXN2+RXN3-
RXN4+RXN9+RXN10)

{ 3: chexol2c <--> chexyl2c }
   RXN3 = 0.5*(K3f*chexol2c - K3r*chexyl2c)
   d/dt(chexol2c) = 2*(-RXN3)

{ 4: chexyl2c <--> chexyl3c }
   RXN4 = 0.5*(K4f*chexyl2c - K4r*chexyl3c)
   d/dt(chexyl3c) = 2*(RXN4+RXN5-
RXN6+RXN11+RXN12)

{ 5: chexol3c <--> chexyl3c }
   RXN5 = 0.5*(K5f*chexol3c - K5r*chexyl3c)
   d/dt(chexol3c) = 2*(-RXN5)

{ 6: 1/2 chexyl3c <--> chexyl4c }
   RXN6 = 0.5*K6f*chexyl3c - K6r*chexyl4c
   d/dt(chexyl4c) = +2*RXN6+RXN7+2*RXN13

{ 7: chexol4c <--> chexyl4c }
   RXN7 = K7f*chexol4c - K7r*chexyl4c
    d/dt(chexol4c) = -RXN7
```

```
{ 8: 1/2 chexene1c <--> chexyl1c }
   RXN8 = 0.5*K8f*chexene1c - K8r*chexyl1c
   d/dt(chexene1c) = 2*(-RXN8-RXN9)

{ 9: chexene1c <--> chexyl2c }
   RXN9 = 0.5*(K9f*chexene1c - K9r*chexyl2c)

{ 10: chexene3c <--> chexyl2c }
   RXN10 = 0.5*(K10f*chexene3c - K10r*chexyl2c)
   d/dt(chexene3c) = 2*(-RXN10-RXN11)

{ 11: chexene3c <--> chexyl3c }
   RXN11 = 0.5*(K11f*chexene3c - K11r*chexyl3c)

{ 12: chexene4c <--> chexyl3c }
   RXN12 = 0.5*(K12f*chexene4c - K12r*chexyl3c)
   d/dt(chexene4c) = 2*(-RXN12-RXN13)

{ 13: 1/2 chexene4c <--> chexyl4c }
   RXN13 = 0.5*K13f*chexene4c - K13r*chexyl4c

K1f = 5.060e-5      {cyclohexanol --> cyclohexyl
cation}
K1r = 2.454         {cyclohexyl --> cyclohexanol}
K2f = 1.429         {cyclohexyl 1,2-hydride shift}
K8f = 3.094e-5      {cyclohexene --> cyclohexyl
cation}
K8r = 1             {cyclohexyl cation -->
cyclohexene}

INIT chexol1c = 0.891          {[A1]/[13C]1024}
INIT chexol2c = 0.0254         {[A2]/[13C]1024}
INIT chexol3c = 0.0143         {[A3]/[13C]1024}
INIT chexol4c = 0              {[A4]/[13C]1024}
INIT chexene1c = 0.0305        {[B1]/[13C]1024}
INIT chexene3c = 0.0143        {[B3]/[13C]1024}
INIT chexene4c = 0             {[B4]/[13C]1024}
INIT(chexyl1c) = 0             {[I1]/[13C]1024}
INIT(chexyl2c) = 2*INIT(chexyl1c)
INIT(chexyl3c) = 2*INIT(chexyl1c)
INIT(chexyl4c) = INIT(chexyl1c)

{clump the species that give overlapping NMR peaks}
other=chexene3c+chexene4c+chexol3c+chexol4c

{clump isotopmers}
chexene=chexene1c+chexene3c+chexene4c
chexanol=chexol1c+chexol2c+chexol3c+chexol4c

K2r=K2f
K3f=K1f
K5f=K1f
K7f=K1f

K4f=K2f
K6f=K2f

K9f=K8f
K10f=K8f
K11f=K8f
K12f=K8f
K13f=K8f

K3r=K1r
K5r=K1r
K7r=K1r

K4r=K2r
K6r=K2r

K9r=K8r
K10r=K8r
K11r=K8r
K12r=K8r
K13r=K8r

METHOD STIFF
STARTTIME = 1024
STOPTIME = 6400
```

2.7.2 Computational modeling of the C–C and C–O alkylation products of the cyclohexanol dehydration in water

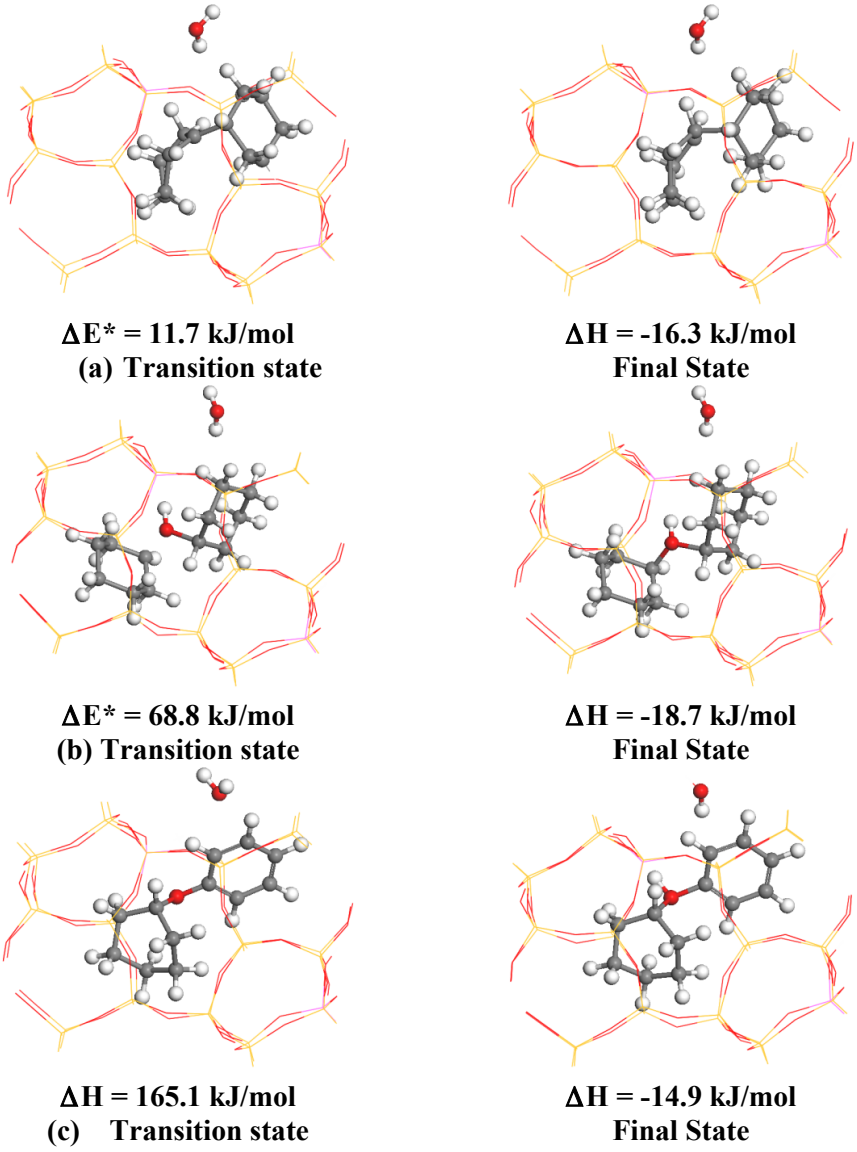

Figure A1. The calculated transition and final states for the C–C and C–O alkylation products of the cyclohexanol dehydration reaction on HBEA150.

REFERENCES

[1] D.–Y. Hong, S. J. Miller, P. K. Agrawal, C. W. Jones, *Chem. Commun.* **2010**, *46*, 1038–1040.

[2] C. Zhao, J. He, A. A. Lemonidou, X. Li, J. A. Lercher, *J. Catal.* **2011,** *280*, 8–16.

[3] C. Zhao, S. Kasakov, J. He, J. A. Lercher, *J. Catal*. **2012**, *296*, 12–23.

[4] C. Zhao, J. A. Lercher, *ChemCatChem* **2012**, *4*, 64.

[5] C. Zhao, D. M. Camaioni, J. A. Lercher, *J. Catal.* **2012**, *288*, 92–103; C. Zhao, W. Song, J. A. Lercher, *ACS Catal*. **2012**, *2*, 2714–2723.

[6] a) E. G. Derouane, *J. Catal*. **1986**, *100*, 541; b) E. Kikuchi, H. Nahano, K. Shinomura, Y. Morita, *Sekiyu Gakkashi* **1985**, *28*, 210.

[7] a) M. Brändle, J. Sauer, *J. Am. Chem. Soc*. **1998**, *120*, 1556–1570; b) M. J. Antal, M. Carlsson, X. Xu, D. G. M. Anderson, *Ind. Eng. Chem. Res*. **1998**, *37*, 3820–3829.

[8] F. Carey, R. Sundberg, in *Advanced Organic Chemistry*, Springer US, **2007**, pp. 473–577.

[9] M. Janik, J. Macht, E. Inglesia, M. Neurock, *J. Phys. Chem. C* **2009**, *113*, 1872–1885.

[10] A. Corma, H. Garcia, *Catal. Today* **1997**, *38*, 257–308.

[11] M. Brändle, J. Sauer, *J. Am. Chem. Soc*. **1998**, *120*, 1556–1570.

[12] Bryant, D.E.; Kranich, W.L., *J. Catal*, **1967**, *8*, 8–13.

[13] a) J. F. Haw, B. R. Richardson, I. S. Oshiro, N. D. Lazo, J. A. Speed, *J. Am. Chem. Soc*. **1989**, *111*, 2052–2058; b) W. Wang, J. Jiao, Y. Jiang, S. S. Ray, M. Hunger, *ChemPhysChem* **2005**, *6*, 1467–1469; c) J. Z. Hu, J. A. Sears, H. S. Mehta, J. J. Ford, J. H. Kwak, K. Zhu, Y. Wang, J. Liu, D. W. Hoyt, C. H. F. Peden, *Phys. Chem. Chem. Phys*. **2012**, *14*, 2137–2143; d) A. Aerts, C. E. A. Kirschhock, J. A. Martens, *Chem. Soc. Rev*. **2010**, *39*, 4626–4642; e) H. Ernst, D. Freude, T. Mildner, I. Wolf, *Solid State Nucl. Magn. Reson.* **1996**, *6*, 147–156.

[14] a) F. Taullele, M. Haouas, C. Gerardin, C. Estourned, T. Loiseau, G. Ferey, *Colloids and Surfaces A: Physicochemical and Engineering Aspects* **1999**, *158*, 299–311; b) O. B. Vistad, D. E. Akporiaye, F. Taulelle, K. P. Lillerud, *Chem. Mater*. **2003**, *15*, 1639–1649.

[15] F. Zaera, *Chem. Rev*. **2012**, *112*, 2920–2986.

[16] a) D. W. Hoyt, R. V. F. Turcu, J. A. Sears, K. M. Rosso, S. D. Burton, A. R. Felmy, J. Z. Hu, *J. Magn.Res*. **2011**, *212*, 378–385; b) R. V. F. Turcu, D. W. Hoyt, K. M. Rosso, J. A. Sears, J. S. Loring, A. R. Felmy, J. Z. Hu, *J. Magn. Res*. **2013**, *226*, 64–69.

[17] J. Z. Hu, J. A. Sears, H. S. Mehta, J. J. Ford, J. H. Kwak, K. Zhu, Y. Wang, J. Liu, D. W. Hoyt, C. H. F. Peden, *Phys. Chem. Chem. Phys.* **2012**, *14*, 2137–2143**.**

[18] T. Takahashi, H. Kawashima, H. Sugisawa, T. Baba, *Solid State Nucl. Magn, Reson*. **1999,** *15*, 119–123.

[19] S. Bandow, Y. Maruyama, X. X. Bi, R Ochoa, J. M. Holden, W. T. Lee, P. C. Eklund, *Mater. Sci. Eng.* **1995,** *A204*, 222.

[20] a) S. Goedecker, M. Teter, J. Hutter, *Phys. Rev. B* **1996,** *54*, 1703; b) C. Hartwigsen, S. Goedecker, J. Hutter, *Phys. Rev. B* **1998,** *58*, 3641; c) M. Krack, *Theor. Chem. Acc.* **2005,** *114*, 145.

[21] J. Van der Vondele, J. Hutter, *J. Chem. Phys.* **2007,** *127*, 114105.

[22] J. P. Perdew, K. Burke, M. Ernzerhof, *Phys. Rev. Lett.* **1996,** *77*, 3865.

[23] S. Grimme, J. Antony, S. Ehrlich, H. Krieg, *J. Chem. Phys.* **2010,** *132*, 154104.

[24] a) G. Henkelman, B. P. Uberuaga, H. Jonsson, *J. Chem. Phys.* **2000,** *113*, 9901; b) G. Mills, H. Jonsson, G. K. Schenter, *Surf. Science* **1995,** *324*, 305.

[25] a) F. Eder, M. Stockenhuber, J. A. Lercher, J. Phys. Chem. B **1997**, 101, 5414; b) B. de Moor, M. F. Reyniers, J. A. Lercher, G. Marin, J. Phys. Chem. C **2011**, *115*, 1204.

[26] Spectral Database of Organic Compounds, http://sdbs.riodb.aist.go.jp/sdbs/cgi–bin/cre_index.cgi

[27] P. B. Weisz, C. D. Prater, *Advances in Catalysis*. **1954**, *6*, 143.

[28] E. W. Thiele, *Ind. Eng. Chem*. **1939**, *31*, 916–920.

[29] M. Baerns, A. Behr, A Brehm, J. Gmehling, H. Hofmann, U. Onken, A. Renken, Technische Chemie, Wiley–VCH Verlag GmbH & Co. KGaA, ISBN 3–527–31000–2.

[30] GSI environmental, http://www.gsi–net.com/en/publications/gsi–chemical–database/single/153.html

[31] J. Kestin, M. Sokolov, W. A. Wakeham, *J. Phys. Chem. Ref. Data* **1978**, *7*, 941–948.

[32] R. Macey, G. Oster, Berkeley Madonna™, University of California, Berkeley, http://www.berkeleymadonna.com/

[33] a) S. R. Blaszkowski, R. A. van Santen, *J. Am. Chem. Soc.* **1996**, *118*, 5152 – 5153; b) S. Namuangruk, J. Meeprasert, P. Khemthong, K. Faungnawakij, *J. Phys. Chem. C* **2011**, *115*, 11649–11656; c) X. Liang, A. Montoya, B. S. Haynes, *J. Phys. Chem B* **2011**, *115*, 8199.

[34] T. S. Sorensen, S. M. Whitworth, *J. Am. Chem. Soc.* **1990**, *112*, 6647–6651.

[35] a) P. A. Jacobs, M. Tielen, J. B. Uytterhoeven, *J. Catal*. **1977**, *50*, 98–108; b) S. J. Gentry, R. Rudham, *J. Chem. Soc. Faraday Trans. 1* **1974**, *70,* 1685–1692.

[36] H. Chiang, A. Bhan, *J. Catal.* **2010**, *271*, 251–261.

[37] B. Hunger, S. Matysik, M. Heuchel, W. D. Einicke, *J. Therm. Anal. Cal.* **2001**, *64*, 1183.

[38] T. Maihom, P. Khongpracha, J. Sirijaraensre, J. Limtrakul, *Chem. Phys. Chem.* **2013**, *14*, 101–107.

Chapter 3

Quantitatively probing the Al distribution in zeolites

The degree of substitution of Si^{4+} by Al^{3+} in the oxygen–terminated tetrahedra (Al T–sites) of zeolites determines the concentration of ion–exchange and Brønsted acid sites. As the location of the tetrahedra and the associated subtle variations in bond angles influence the acid strength, quantitative information about Al T–sites in the framework is critical to rationalize catalytic properties and to design new catalysts. A quantitative analysis is reported that uses a combination of extended X–ray absorption fine structure (EXAFS) analysis and ^{27}Al MAS NMR spectroscopy supported by DFT–based molecular dynamics simulations. To discriminate individual Al atoms, sets of ab initio EXAFS spectra for various T–sites are generated from DFT–based molecular dynamics simulations allowing quantitative treatment of the EXAFS single– and multiple–photoelectron scattering processes out to 3–4 atom shells surrounding the Al absorption center. It is observed that identical zeolite types show dramatically different Al–distributions. A preference of Al for T–sites that are part of one or more 4–member rings in the framework over those T–sites that are part of only 5– and 6–member rings in an HBEA150 zeolite has been determined using this analysis.

3.1 Introduction

Zeolites are widely used as sorbents and catalysts, because their well–defined pore structure and adjustable acidity lead to high activity for a large variety of reactions.[1,2] The exceptional catalytic properties[3] are attributed to the combination of steric constraints and the specific properties of the active site, in particular of the Brønsted acid strength and concentration which is associated with the substitution of Al in the zeolite framework.[4,5]

It has been inferred from kinetic measurements that for a given zeolite framework, the specific substitution of Al atoms dramatically affects the catalytic activity.[6] It has also been proposed that the stability of zeolites with regard to dealumination, as well as acid strength, depends on the position of the Al T–sites in the zeolite structure.[7] Thus information about the location and stability of the Al T–sites in the zeolite framework is essential to understand the activity and availability of specific sites for catalysis. Such information also provides the basis to design new and improve existing zeolites with respect to activity and selectivity.

The location of Al in the zeolite lattice impacts the environment of the acid site, offering varying steric access for reacting molecules as well as subtle differences in acid strength due to variations in the bond angles of the tetrahedra.[8,9] More acute Al–O–Si bond angles have been postulated to induce higher acid strength.[10] Thus, the empirical relation between the Al–O–Si bond angle and the ^{27}Al NMR chemical shifts is frequently suggested as a means to locate Al in a zeolite lattice.[11,12]

^{27}Al Magic Angle Spinning (MAS) NMR has been extensively applied to study Al T–sites in zeolites allowing to differentiate tetrahedrally and octahedrally coordinated Al^{3+} at framework and extra–framework positions.[13] The analysis of Al T–site distribution, however, remains a difficult task especially for zeolites with a high number of crystallographically distinct framework positions.[14] The spectral resolution of the tetrahedral Al sites also suffers from line broadening[15] due to the quadrupolar character of Al.[16] This limitation has been partly overcome by quantitatively predicting ^{27}Al NMR chemical shifts using DFT[17,18] and hybrid approaches between quantum and molecular mechanics.[19,20] In this way parameters such as Al dilution level and the presence of silanol defect sites in the sample framework can be included to further improve accuracy

of the analysis.[21] While being internally consistent this approach has never been confirmed by an independent method.

An accurate method to determine the T–site distribution has been conceptually shown for relatively simple aluminosilicates using the X–ray standing wave (XSW) technique. van Bokhoven *et al.*[22] applied this XSW method to the analysis of a macroscopic single crystal of scolecite showing that all Al is selectively present in one of only two different Al T–sites.

As X–ray absorption spectroscopy (XAS) is conceptually sensitive to the local structure around zeolite T–sites, in this work a bold approach is taken using extended X–ray absorption spectroscopy (EXAFS) to derive the longer–range bond distances around Al T–sites, which is related to their average environment. In addition, the more traditional analysis of the region close to the absorption edge (XANES) is also utilized to derive information about the symmetry of the Al T–sites.[23,24] At this point it must be emphasized that the EXAFS analysis has the potential to accurately determine the nearby Al–O bond and Al–Si atom distances and their angular correlations up to a distance of approximately 3–4 atom shells beyond the central Al T–site. This potential, however, has not been used for quantitative zeolites analysis (other than for evaluating the first shell Al–O bond lengths),[25,26] because of the many factors limiting the data quality during acquisition of EXAFS spectra at low X–ray energies (1559 eV, Al K–edge) including achieving constant high X–ray flux at the sample, stable beam position, harmonic–free beam, stable sample detectors and finally properly accounting for the strong X–ray absorption by the sample in that energy region. The combination of a very high–flux undulator source, an improved X–ray monochromator, as well as an improved detector has allowed[27] the acquisition of high–quality spectra sufficient for a quantitative treatment of the higher–order scattering paths required to determine the zeolite structure.

Even with this progress quantitative evaluation of EXAFS remains challenging. The standard EXAFS analysis protocol involves selecting the most probable set of photoelectron scattering paths and then fitting their atom distances, disorder (Debye Waller factors or DWF) and coordination numbers (CN). This standard approach becomes intractable when considering that the multiple Al T–site occupancies lead to large numbers of fitted parameters, which exceed the information content of the

experimentally measured spectra. In order to circumvent this constraint, the structural parameters (bond distance, DWF and CN's) for each T–site were quantitatively determined from first principles calculations using ab–initio molecular dynamics simulation (DFT–MD). These calculated dynamical representations of the Al T–site structure then provide the input for calculating the molecular dynamics–EXAFS (MD–EXAFS) spectrum. [28] This represents an *ab initio* procedure for calculating the photoelectron single– and multiple–scattering pathways (~10^6) out to about 6 Å without the need for any adjustable parameters. As a note in passing, the generality of this approach, which provides a new opportunity for the evaluation of impurity locations in doped semiconductors[29] or ferromagnetic films,[30] must be emphasized.

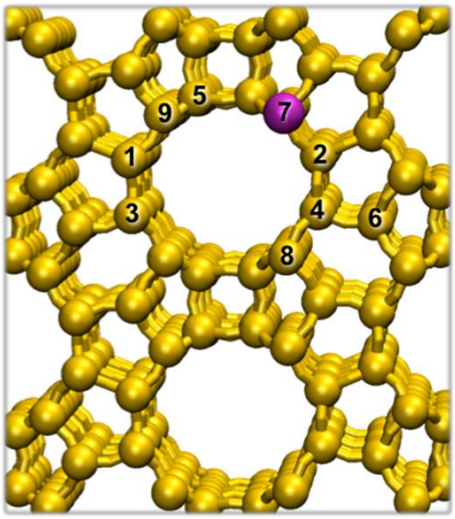

Figure 1. Representation of HBEA zeolite framework in the [0 1 0] axis with one of the nine different T–sites substituted by an Al^{3+} ion (purple). Oxygen atoms and the proton are not shown to emphasize ring structures containing 4, 5, 6 and 12 silicon atoms.

This chapter is limited to determining the Al distribution in zeolite Beta, a large–pore zeolite, which is central to many fine chemical reactions and petrochemical transformations.[31,32,33,34] Figure 1 provides a representation along the [0 1 0] axis for HBEA zeolite showing the primary catalytic channels represented as 6–7 Å diameter straight pores defined by the 12–member rings. The [0 1 0] axis has a nearly identical

structure that is likewise populated with a set of parallel, non–intersecting 6–7 Å pores. On the other hand, the [0 0 1] axis has slightly smaller 5–6 Å pores, which also form 12–member rings, that zigzag to alternately intersect the primary pores along both the [1 0 0] and the [0 1 0] axes. The structure contains 4–, 5– and 6–member rings forming the overall lattice with nine crystallographically different T–sites.

3.2 Experimental and theory methods

3.2.1 Sample description

HBEA25 (Si/Al = 12.5) and HBEA150 (Si/Al = 75), which was dealuminated *via* leaching, were received from Süd Chemie AG (Clariant) and HMOR (Si/Al = 45) from Zeolyst, all in hydrogen form. Both samples of zeolite Beta contain mixtures of two polymorphic forms A and B as described in more detail below. The samples were washed with deionized water, dried in vacuum at ambient temperature and then stored for more than 2 weeks under ambient temperature and humidity prior to measurement. $Na_2Al_2O_4$ (99.95% anhydrous) (tetrahedral–Al), $AlCl_3$ (99.999% anhydrous) and α–Al_2O_3 (99%) (octahedral–Al) were obtained from Sigma Aldrich and used without further processing.

The zeolite Beta contains two polymorphic forms, A and B.[35] The HBEA150 and HBEA25 samples used in this work contain a 50/50 mixture of the polymorphs A and B as was determined by comparing the measured XRD spectrum to literature references for zeolite beta.[36, 37] As both polymorphs A and B are constructed from identical centrosymmetric tertiary building units (TBU's),[38, 39] the local geometry is nearly identical for the two polymorph structures and thus the presence of a polymorph mixture does not affect (as is demonstrated in the sections below) the EXAFS and NMR analysis in this work. The similarity of the T–site structure of the two polymorphs was also demonstrated in earlier NMR and pair–distribution–function analysis.[40,41,42]

3.2.2 Al K–edge XAFS experimental methods

The Al K–edge XAFS measurements were conducted at the Phoenix I, elliptical undulator beamline at the Swiss Light Source (SLS) at the Paul Scherrer Institute. Energy calibration was achieved by setting inflection point of an Al foil spectrum to 1559.6 eV. The double–crystal monochromator employed a set of $KTiOPO_4$ (011) crystals to provide

an energy resolution of about 0.6 eV over a scan range for the Al K–edge from 1500 to 2150 eV, just below the P K–edge. Two Ni–coated mirrors were set at an angle of 1.45° to provide cutoff of higher harmonics. An unfocused 1.0 × 1.0–mm beam having a flux of approximately 10^9 photons/sec was used. The sample chamber pressure was maintained at approximately 2.5×10^{-4} mbar. Measurements were typically performed in fluorescence mode although several transmission measurements for individual samples were obtained in order to ascertain the magnitude of the self–absorption corrections. I_0 was measured as total electron yield signal taken from a 0.5 μm thin polyester foil, which was coated with 50 nm of Ni. This I_0 detector was held in a miniaturized vacuum (2.9×10^{-6} mbar) chamber, which is separated by a thin Kapton foil from the measurement chamber itself. The X–ray fluorescence was detected using a 4–element Vortex Si–drift diode detector. For transmission measurement a Si–diode was used.

ATHENA[43] software was used to remove the $\chi(k)$ oscillations from the background, and, in certain instances to apply (standard routines for) self–absorption correction of the XANES and XAFS spectra of the concentrated standard compounds. The linear combination fitting tools within ATHENA were used to evaluate of the Al T–site distributions based on MD–XAFS $\chi(k)$ spectra. Two different reference compounds α–Al_2O_3 and $Na_2Al_2O_4$ were also evaluated using the ARTEMIS[43] software package. Theoretical standards for these compounds were derived from FEFF9.[43]

During the background processing used to extract the $\chi(k)$ data from the background function, a Fourier filter cutoff distance, R_{bkg}, of 1.0 Å was used. It was found that the atomic background function, $\mu_0(E)$, contains strong multi–electron absorption edges at k = 5.3 $Å^{-1}$ due to the $KL_{II\&III}$ transition.[44] This transition is only observed for octahedral and not tetrahedral O–coordination symmetry about the Al T–site. The XAFS data were weighted by k^2, and truncated using a Hanning window with dk = 1.0 $Å^{-1}$ in the range of $1.5 < k < 8.0$ $Å^{-1}$. The value of the core hole factor was estimated at $S_0^2 = 1.0$ from fits to the two crystalline standards. The S_0^2 factor typically had an error of approximately 15%.

3.2.3 ^{27}Al MAS NMR

The Ultra–high field ^{27}Al MAS NMR experiments were performed on a Varian–Agilent Inova 63–mm wide–bore 850 MHz NMR–spectrometer. The main magnetic field

was 21.1 T and the corresponding ^{27}Al Larmor–frequency was 234.56 MHz. Experiments were performed using a commercial 3.2 mm pencil type MAS probe. In a typical experiment about 15 mg of sample powder were loaded in the rotor and measured at ambient temperature. The HBEA samples were stored under ambient humidity leading to a hydrated surface that is expected to contain Al tetrahedra that have minimal distortions and that have the maximum ^{27}Al MAS NMR spectral resolution.[45] A single pulse sequence with a pulse length of 2.0 μs, corresponding to a pulse angle of 45°, was selected for acquiring each ^{27}Al MAS NMR spectrum with a recycle time of 1 s and total accumulation of 5000 scans. The spectra were acquired at a sample spinning rate of 20 kHz ± 2 Hz and were referenced to 1.5 M $Al(NO_3)_3$ in H_2O (0 ppm) using the center of the octahedral peak of solid γ–Al_2O_3 (at 13.8 ppm) as a secondary reference. The measurement uncertainty is estimated to be ±0.1 ppm.

For quantitative measurements the weights of samples loaded into the MAS rotor were recorded and four spectra were acquired to check the stability of the spectrometer. The matching and tuning conditions of the RF circuit of the NMR probe were set using a network analyzer. All other experimental conditions were kept identical for all analyzed samples. In this way, the absolute peak areas normalized to the spectrometer standard were proportional to the Al in the sample. The spectra were analyzed using the MestreNova 8.1 software package.

3.2.4 Density functional theory (DFT) and Molecular Dynamics (MD) simulations

The CP2K program package[46] was used to perform periodic DFT structure optimizations and MD simulations. To obtain structures of the different Al T–sites in HBEA (see Figure 2), a single unit cell of the BEA crystal[47] was modified by substituting an Al for a single Si atom to form a negatively charged $[Si_{63}O_{128}Al_1]^-$ cell. While the presence of Al pairs (Al–O–Si–O–Al) was reported to affect the accuracy of Al chemical shift calculations,[48] such pairs were shown to be absent by ^{29}Si NMR (discussed in the results section), justifying the selected unit cell model. For the acid form of the structure a proton was placed on one of the O atoms neighboring the Al T–site to compensate the negative charge. The structures were optimized using the periodic DFT method with a

mixed Gaussian and plane wave basis set. Core electrons were represented with norm–conserving Goedecker–Teter–Hutter pseudopotentials,[49] and the valence electron wave function was expanded in a double–zeta basis set with polarization functions[50] along with an auxiliary plane wave basis set with an energy cutoff of 360 eV. The generalized gradient approximation exchange–correlation functional of Perdew, Burke, and Enzerhof (PBE)[51] was used for all calculations. Structure optimizations used the Broyden–Fletcher–Goldfarb–Shanno (BGFS) algorithm with SCF convergence criteria of 1.0×10^{-8} au. This process was repeated for each of the nine different T–sites labeled in Figure 2. The experimental lattice parameters (12.6614 × 12.6614 × 26.4061 $Å^3$) were used.[52]

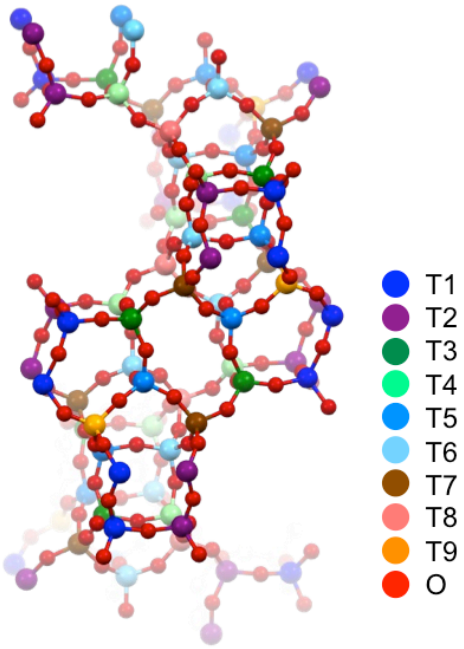

Figure 2. $[Si_{63}O_{128}Al_1]^{-1}$ structure with labeled T–sites is shown to demonstrate the 9 possible Al positions in HBEA. Parts of the unit cell demonstrating 5– and 6–member rings are shown as inset structures for simplicity. Color–coding is reported in the legend.

3.2.5 MD EXAFS

MD EXAFS was used to simulate the EXAFS spectra of the Al T–sites. Initially the nine different DFT optimized $[Si_{63}O_{128}Al_1]^-$ crystal structures were used to calculate a full set of EXAFS spectra from the ab initio scattering theory (FEFF9) by applying approximate global disorder parameters, σ^2, corresponding to 300 K (see Appendix).

Using this initial screening method, the nine T–sites were grouped into three sets, each set or group giving rise to uniquely different features in the predicted EXAFS. The sets were assigned as follows: Set A (T1, T2, T5, T6), Set B (T3, T4) and Set C (T7, T8, T9). The Al T–sites within each of these sets were found to have nearly identical EXAFS spectra.

Based on this assignment the full MD trajectories at 300 K were calculated for three representative T–sites: T1, T3 and T7 corresponding to sets A, B and C, respectively. For each MD calculation the system was equilibrated at a constant temperature of 300 K for 10 ps with a Nosé–Hoover chain thermostat in the canonical ensemble.[53] These MD trajectories were then used to generate the MD–EXAFS spectra. The MD–EXAFS method has been described in detail previously.[54] Briefly, for each of the 10^4 snapshots from the MD trajectory, a set of atom positions was used to calculate a full set of scattering (single and multiple scattering) paths for all atoms within 6 Å of the Al T–site. This step generated 10^3 scattering paths for each snapshot of the trajectory. This process was repeated for all of the snapshots of the trajectory. In the final step, an ensemble average of these $\sim 10^7$ scattering paths was generated and compared directly to the experimental spectra. This approach has lead to a quantitative treatment of all photoelectron single and multiple scattering paths generating an EXAFS spectrum that captures all the structural details inherent in the MD simulation including the bond lengths, bond angles, vibrational disorder and local symmetry about the Al T–site.

Finally, the MD–XAFS spectra (one for each of sets A, B and C) based on the DFT method are obtained. These spectra capture a high–level representation of the structure at the Al T–sites and are used as reference spectra to determine the Al T–site distribution in the HBEA150 and HBEA25 samples through linear combination fitting to the experimentally observed EXAFS, the fractional occupancies being the coefficients for the least squares fit to the k–weighted $\chi(k)$ data.

3.2.6 XANES calculations with Time–Dependent (TD) DFT

XANES calculations were performed at the Al K–edge for the T–sites considered in the NMR and EXAFS analysis using a TDDFT–based restricted excitation window as implemented in the NWChem quantum chemistry program.[55,56] This approach involves

defining a model subspace of single excitations from the relevant core orbitals and is a valid ansatz because core excitation energies are well separated from pure valence–valence excitations.

For each Al T–site conformation the Sapporo–QZP–2012 [57] all electron basis set was used for the single absorbing Al T–site and the nearest O atoms. The Si and O atoms further away were represented with the Stuttgart RLC ECPs.[58] The exchange–correlation was treated with the BHLYP functional.[59] All calculated spectra were Lorentzian broadened by 1 eV and shifted by +16.8 eV to match the experimental spectrum.

3.2.7 DFT NMR calculations

The NMR calculations (DFT–NMR) for the HBEA Al T–sites were performed using the NWChem software package.[55] The T–sites were modeled in the dissociated state as $[Al–(O–Si–OH)_4]^-$ ions. The structures of the ions were derived from the DFT optimized crystal structures by cutting and terminating O–Si bonds with hydrogens while maintaining the bond directions. The O–H–bond length was set to 0.96Å in all cases. This size of a cluster has been shown to be appropriate for zeolite ^{27}Al chemical shift calculations.[19] The cluster charge was set to "–1" to compensate for the dissociated Brønsted acidic proton. The calculations used the B3LYP (Becke 3–parameter Lee–Yang–Parr exchange correlation functional).[59,60] The shielding property for a single Al^{3+} atom populating the DFT optimized HBEA unit cell was calculated using the 6–311+G** basis set[61] applied for the Al, O, Si and H atoms. Note that the zeolite Si/Al ratio was shown to have no effect on the absolute MAS NMR peak shift values[62], provided that there are no Al pairs (Al–O–Si–O–Al).[48] Thus the DFT NMR can be calculated using identical structures for both HBEA150 and HBEA25. The NMR chemical shifts are referenced to aqueous Al^{3+} solution. However, the absolute chemical shielding tensor for this reference cannot be accurately determined by calculation, since the disordered aqueous structure of the Al^{3+} standard solution is difficult to model. In the least squares fitting procedure, the absolute chemical shift tensor for the reference was optimized while the NMR linewidth and shape (Voigt function) for each T–site were assumed to be same. This procedure provided an absolute chemical shielding tensor of 572.4 ppm for aqueous Al^{3+}. As a further point of reference HMOR zeolite, which is chemically and structurally

similar to HBEA, is calculated to have a chemical shift that is within 1 ppm of its measured value.

3.3 Results and discussion

3.3.1 Evaluation of α–Al_2O_3 and $Na_2Al_2O_4$ as crystalline standards

In general, a comprehensive EXAFS evaluation of Al K–edge spectra has only rarely been used to evaluate structure beyond the first Al–O shell. In order to demonstrate the sensitivity of EXAFS to the structure beyond the first Al–O shell, crystalline samples of α–Al_2O_3 and $Na_2Al_2O_4$ were evaluated in detail using the same MD–EXAFS methodology that is used to evaluate Al T–site distribution in the zeolites. Both of these compounds contain only one type of Al site. The analysis begins with their crystallographic structure,[63, 64] which is the starting input for generating the MD–trajectories. There are no adjustable parameters used to generate the respective MD–EXAFS spectrum that is then compared directly to the experimental one. The MD–EXAFS spectra for the two standards validate the method that is subsequently applied to the analysis of the more complex local structure of the $[Al–O_4]^-$ tetrahedra in the zeolite.

Figures 3a and 3b show the $k^2\,\chi(k)$ plot for α–Al_2O_3 and the imaginary Fourier transform of this function in the form of the Img[$\Box(R)$] plot. The MD–EXAFS spectrum reproduces all the relevant features of both $\chi(k)$ and it does an excellent job of reproducing the position and amplitudes of the peaks in the Img[$\Box(R)$] over the full range from 1 to about 5 Å. It is worthwhile to note that for α–Al_2O_3, there is a strong multi–electron absorption edge at about k = 5.3 $Å^{-1}$ due to the $KL_{II\&III}$ transition (Figure 3a). The amplitude of this multi–electron edge represents about 50% of the amplitude of the EXAFS oscillations in this region. Fourier transform of this feature may result in some high frequency ripples in the Img[$\Box(R)$] plots, although it appears to have a relatively minor effect on the location and amplitude of the main spectral features. This multi–electron edge appears to be much weaker for Al tetrahedral sites (e.g., zeolites). ΔSCF calculations for α–Al_2O_3 and $Na_2Al_2O_4$ predict the multi–electron edges at 115.81 eV and 115.86 eV from their respective K–edges. These are consistent with our experimental findings of 112.5 and 111.5 eV, respectively.

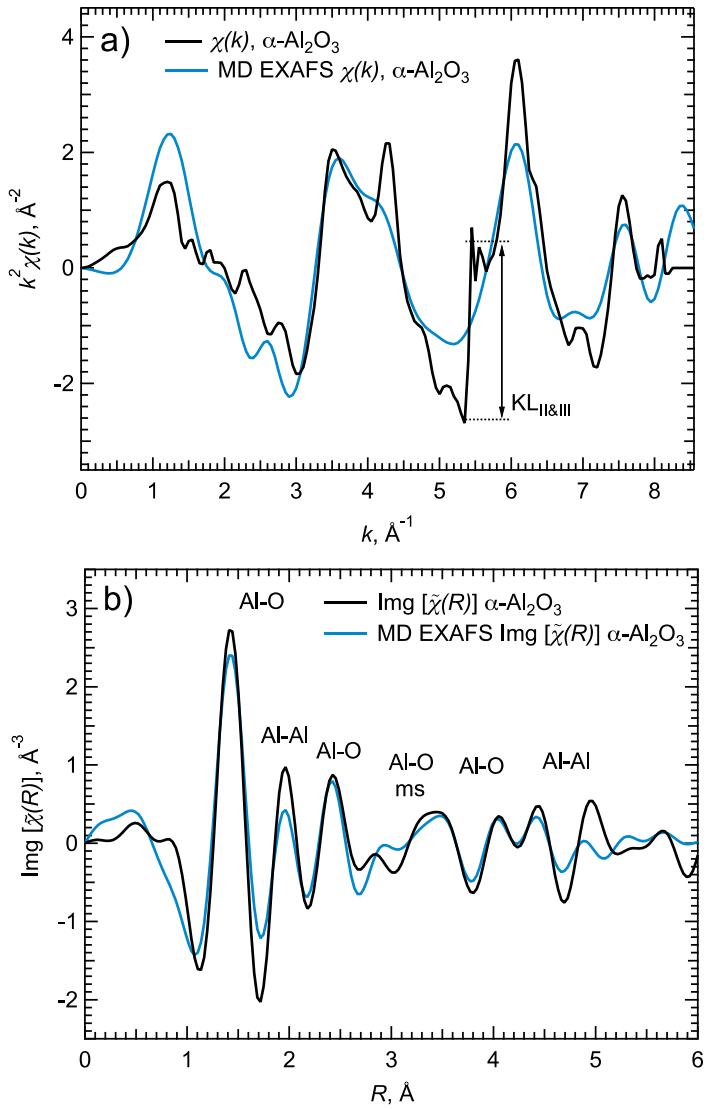

Figure 3. EXAFS k^2–weighted a) $\chi(k)$ and b) Img[$\tilde{\chi}(R)$] plots for α–alumina comparing experimental to MD EXAFS spectra that use only the initial configuration from the crystallographic data.

The same overall analysis procedure was applied to $Na_2Al_2O_4$ as shown in Figure 4. Again, all the relevant features of both $\chi(k)$ and Img[$\tilde{\chi}(R)$] are captured by MD–EXAFS. There is a small phase mismatch in the Img[$\tilde{\chi}(R)$] plot in the region around 2.5 to 3 Å. Subsequent XRD analysis showed the existence of about 15 % of the hydrate, $Na_4Al_4O_8 \cdot 5H_2O$, in the sample and this may be the cause of the shifting of the Al–Al and

Al–Na peaks to slightly longer distances in the experimental spectrum. Notably, the tetrahedrally coordinated $Na_2Al_2O_4$ shows only a small feature at the position of the $KL_{II\&III}$ transition at $k = 5.3$ Å^{-1}.

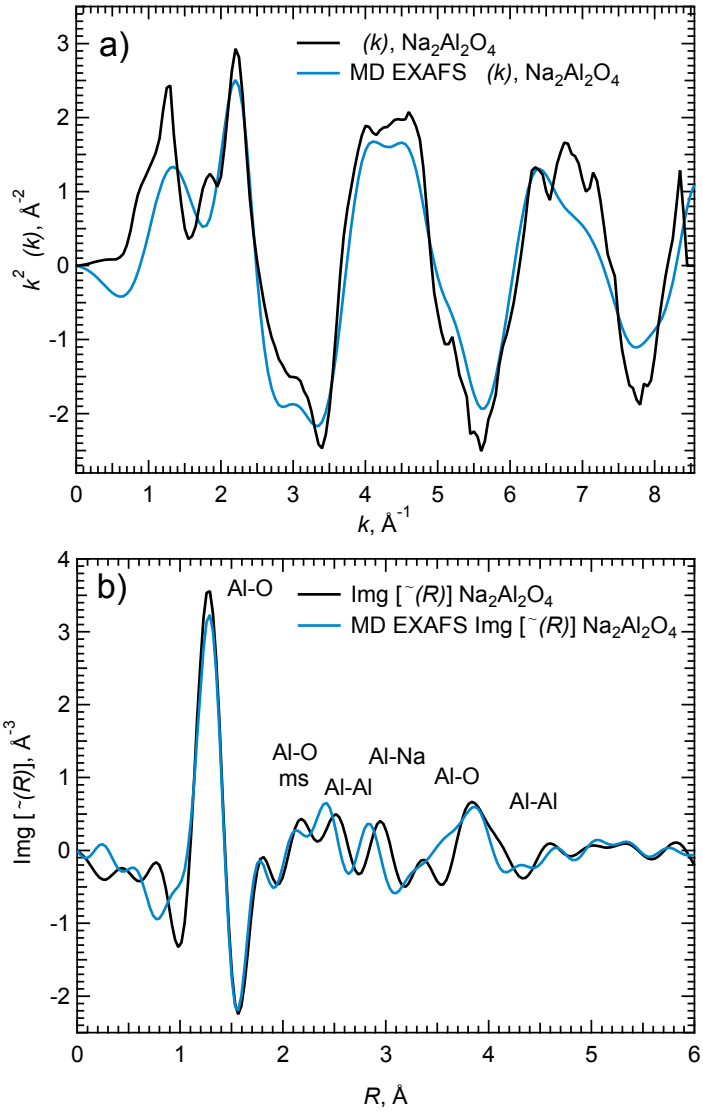

Figure 4. EXAFS k^2–weighted a) $\chi(k)$ and b) Img[$\tilde{}$$(R)$] plots for $Na_2Al_2O_4$ comparing experimental to MD EXAFS spectra that use only the initial configuration from the crystallographic data.

The ability to successfully define the features in the Img[$\chi(R)$] data from 1 to about 5 Å establishes the distance–range sensitivity for both the experimental and simulated Al EXAFS measurements and provides justification to apply these methods to the characterization of the zeolite structure.

3.3.2 Zeolite Beta polymorphs

Zeolite Beta is composed of polymorphs A, B and C.[65] The composition of HBEA150 and HBEA25 is studied by analyzing the powder X–ray diffraction (PXRD) patterns (Figure 5a) and comparing to the literature references.[66, 67] The composition was determined as a 50/50 mixture of polymorphs A and B. It is emphasized that both polymorphs are constructed from the same centrosymmetric tertiary building units that are arranged in layers.[39,41] As these are long–range structural features, the EXAFS analysis that probes only the local geometry about the target atom is not affected by the presence of the two polymorphs. To demonstrate this, we have calculated the DFT EXAFS for the 9 T–sites of the all–siliceous zeolite Beta using the two different (A and B) polymorph structures.[38] As shown in the Img[$\chi(R)$] plot in Figure 5b the two polymorphs are very similar from the EXAFS point of view. Note that the T–sites in polymorph A and polymorph B are compared based on their geometric position in the framework in such a way that the T–sites shown in identical colors in Figure 5b represent structurally equivalent conformations. It is likely, that after the published crystallographic structures are optimized using MD simulation, that minor observed differences would be even further reduced. 100 % pure phases of A and B have not yet been synthesized, their structures have been extrapolated from the refinement of the 50/50 mixture in zeolite Beta so there remain uncertainties in the refined atomic positions. The equivalency of A and B is supported by previous NMR studies and pair distribution function (PDF) measurements that are reported below. The results demonstrate the strong similarity of the T–sites in the two different polymorphs.

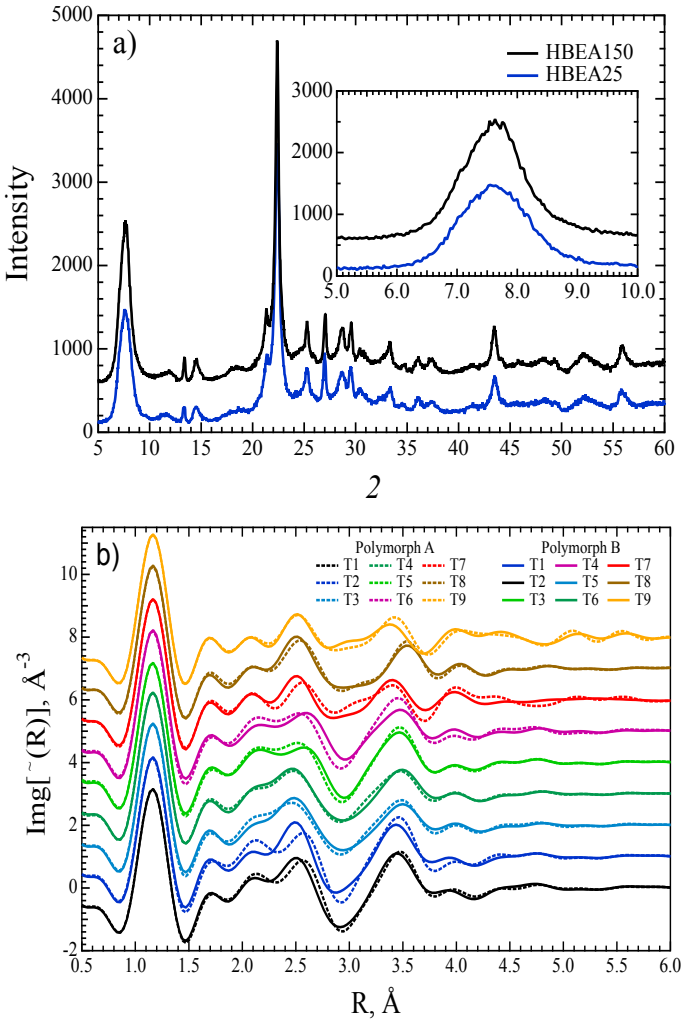

Figure 5. The XRD patterns for HBEA150 and HBEA25 (a) and the calculated DFT EXAFS Img[□(*R*)] plot (b) for the nine T–sites of the all–siliceous Polymorph A and Polymorph B of zeolite Beta. The color–coding is reported in the legend. The standard σ^2 (disorder) parameter was set to 0.003 for all Al T–sites. The position of these peaks is mostly independent of the choice of the disorder parameter.

Previous reports on ^{29}Si NMR studies of zeolite Beta (50 % polymorph mixture)[68,69] show the existence of 9 distinct NMR signals. In addition the T–site degeneracy (2 of 9 T–sites having degeneracy of ½ times of the other 7) is captured in these NMR spectra. This strongly suggests that the local T–site environment between "A" and "B"

polymorphs are nearly identical in their local structure from an NMR spectroscopy point of view.

A recent pair distribution function (pdf) analysis from a co–refinement of both X–ray and neutron scattering data [70] shows that the total pair distribution functions for polymorphs A and B are nearly identical up to about 4.5 Å, and thereafter, there are only small differences (see Figure 6). The pdf spectra were collected for the HBEA150 at the Advanced Photon Source, Sector 11 ID C (Argonne National Laboratory). Figure 6 compares the HBEA150 to this earlier published data for zeolite Beta. It is found that HBEA150 is in quantitative agreement over the full R–range. These pdfs contain the local structural information from all tetrahedral sites in polymorph A and B. Importantly, the region of these pdfs up to about 5 Å is the same region sampled by EXAFS.

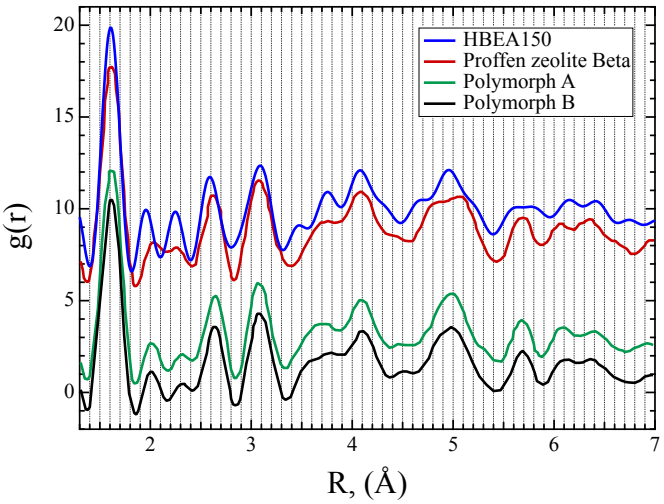

Figure 6. The PDF spectrum of HBEA150 used in this study is compared to prior measurements by Proffen *et al.* for zeolite Beta and their refinement of the two polymorphs A and B.[70] The HBEA150 spectrum was taken at somewhat higher spatial resolution, however, it reproduces the earlier reported structure nearly quantitatively. Polymorphs A and B have nearly the same structure up to about 6 Å.

The use of XRD crystal parameters for polymorph "A" and "B" has allowed determining the atomic structure and atom distances about the specific T–sites in the framework. The section below provides an example of statistics comparing T–site 3 to 7.

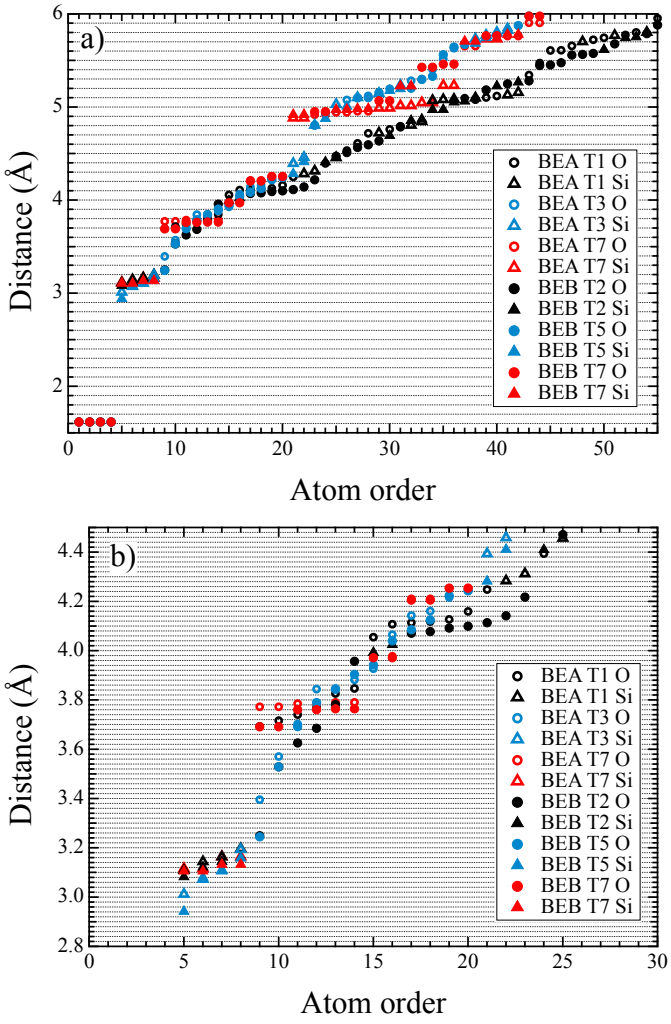

Figure 7. The Si–O and Si–Si bond distances are shown in a) and enlarged for the 2.8 – 4.5 Å region in b). The respective t–site coding is reported in the legend.

First, the absolute average distance deviation (AAD) between the atoms surrounding T–sites 3 and 7 were calculated. In EXAFS, the region of sensitivity for detecting T–site structure is the range from about 2.5 to 4.5 Å. For the 16 atoms that lie within this range, the AAD between T–site 3 and 7 is 0.17 Å ± 0.16. In contrast the AAD between polymorph A and B for this same set of atoms is 0.029 Å ± 0.02. In other words, the differences in the polymorph distances are only about 15 % of the distance differences between the different T–sites. Hence the dominant structure differences occur as a result

of the local T–site geometry and not as a result of differences between polymorphs. This result is elucidated in further detail by the plots in Figure 7.

3.3.3 DFT optimized Al T–site model

A single BEA unit cell contains 64 T–sites. Substituting one Al for Si corresponds to Si/Al ratio of 63 corresponding by definition to HBEA126, which is a satisfactory model for the experimental sample HBEA150 (Si/Al = 75) that on average has less than one Al^{3+} per unit cell, each separated by multiple shells of Si T–sites. The model is also representative of the Al T–sites within HBEA25 (Si/Al = 12.5), provided Al–O–Si–O–Al pairs are excluded in either case. To exclude the possibility of Al–O–Si–O–Al pairs in the studied HBEA samples, ^{29}Si MAS NMR spectra were obtained (see Figure 8). Note that at least three peaks are observed indicative of tetrahedral Si^{4+} in different environments.[68,69] The signals between –110 and –115 ppm are attributed to sites with Si^{4+} ions bonded to four oxygens which are in turn bonded to Si^{4+} ions, $Si(OSi)_4$ sites. The signal at –103 ppm corresponds to a $Si(OSi)_3OAl$ site in which one second shell Si^{4+} ion is substituted by an Al^{3+} ion.[71,72] The signal for $Si(OSi)_2(OAl)_2$ site, which shows up at –98 ppm,[73] if present, is weak (0.6 % and 2.4 % total Si for HBEA150 and HBEA25, respectively). At this level, the frequency of Al–O–Si–O–Al pairs in the HBEA samples is too low to affect the Al distribution analysis.

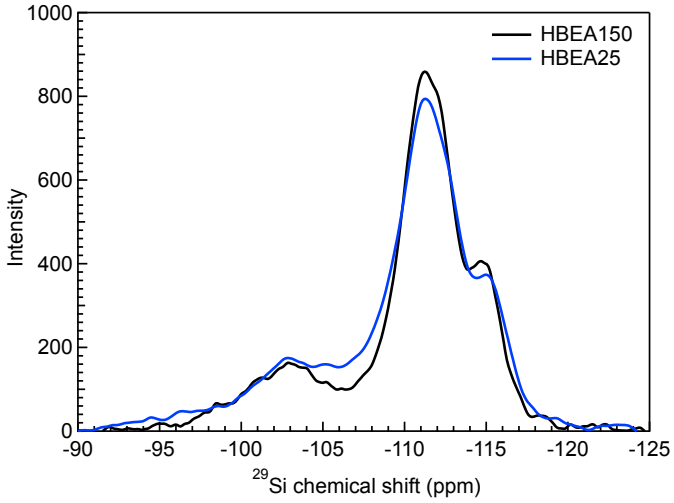

Figure 8. ^{29}Si MAS NMR spectra of HBEA150 (black) and HBEA25 (red).

3.3.4 Evaluating the position of the Brønsted acidic proton about the Al T–site

In water–free HBEA zeolites, the negative charge at the Al T–site is balanced by a proton bonded to one of the bridging O atoms (Al–OH–Si). However, in the presence of adsorbed water this proton exists as a hydronium ion (e.g., $(H_2O)_n \cdot H_3O^+$) that resides locally in the zeolite pore paired with the AlO_4^- T–site. Therefore, structures of protonated and unprotonated T–sites were calculated to determine how the structures differed and whether EXAFS could distinguish the differences. The DFT optimized Al–O bond distances are summarized in Table 1 for the nine T–sites in their protonated and unprotonated states. In general, the four first–shell Al–O bond distances are nearly identical in the unprotonated state. (It should be noted that this first–shell T–site similarity does extend to the higher O and Si shell distances that provide the basis for discriminating the T–site occupancy by EXAFS). When a proton is bonded to one of the bridging O atoms, that Al–O bond is elongated to about 1.92 Å versus about 1.70 Å for the remaining three Al–O bonds. As shown in the analysis of α–Al_2O_3 and $Na_2Al_2O_4$ above, the EXAFS measurements have a spatial resolution of approximately 0.15 Å (for k_{max} = 8 Å^{-1}). For this reason it is possible to differentiate the protonated from the "un–protonated" state of the Al T–sites. This was firmly established by performing MD–EXAFS simulations on protonated and unprotonated T–sites.

Figure 9 shows the Img[$\chi(R)$] plots for the experimentally measured spectrum for HBEA150 and the simulated spectra for a protonated and unprotonated T–site. Since the first shell Al–O distances are nearly the same in the nine different HBEA T–sites, only the T1 site is shown. For comparison, the EXAFS spectrum for tetrahedral $Na_2Al_2O_4$ is included. Figure 9 shows that the experimental spectrum for HBEA150 in the region between 1 and 1.75 Å is in quantitative agreement with the simulated value for the unprotonated site. The HBEA150 EXAFS spectrum is also seen to be similar to the tetrahedral $Na_2Al_2O_4$ where the four Al–O bond lengths are also equivalent. Though not shown, similar observations were made for HBEA25. Thus, it is concluded that for both HBEA150 and HBEA25 the T–sites are dissociated under measurement conditions, their negative charges being balanced by hydronium ions, and for this reason subsequent analyses will be based on the T–site structures in the dissociated (unprotonated) state. Note that while the EXAFS measurements were made on the samples in vacuum, the

ambient room temperature conditions were not sufficient to dehydrate hydronium ions.[74,75] The section that follows moves to a comprehensive analysis of the variation of longer–range Al–O and Al–Si distance at various T–sites beyond the first shell Al–O distances.

Table 1. Calculated Al–O bond distances (Å) for unprotonated and protonated Al T–sites in HBEA zeolite from periodic DFT optimized structures. [a]

T–site	Unprotonated	Protonated	
	O_3Al–O	$(HO)O_2Al$–O	O_3Al–OH, Å
T1	1.74	1.70	1.92
T2	1.72	1.70	1.91
T3	1.73	1.71	1.87
T4	1.72	1.71	1.88
T5	1.72	1.70	1.89
T6	1.73	1.71	1.89
T7	1.74	1.70	1.96
T8	1.74	1.70	1.94
T9	1.73	1.69	1.94

[a] The Al–O distances are averages of 4 values for the unprotonated site and 3 values for the protonated site, both averages having a standard deviations of 0.02 Å.

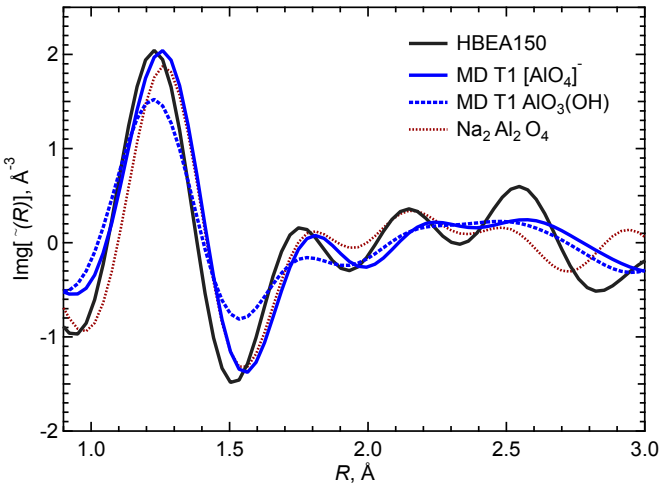

Figure 9. Img[~(*R*)] plot comparing the experimental HBEA150 spectrum (black), with MD–EXAFS spectra for the T1 site in the $[AlO_4]^-$ (solid blue) and $AlO_3(OH)$ (dashed blue) configurations, and the experimental spectrum for $Na_2Al_2O_4$ (dashed red).

3.3.5 Evaluating the distribution of Al^{3+} among HBEA T–sites from MD–EXAFS analysis

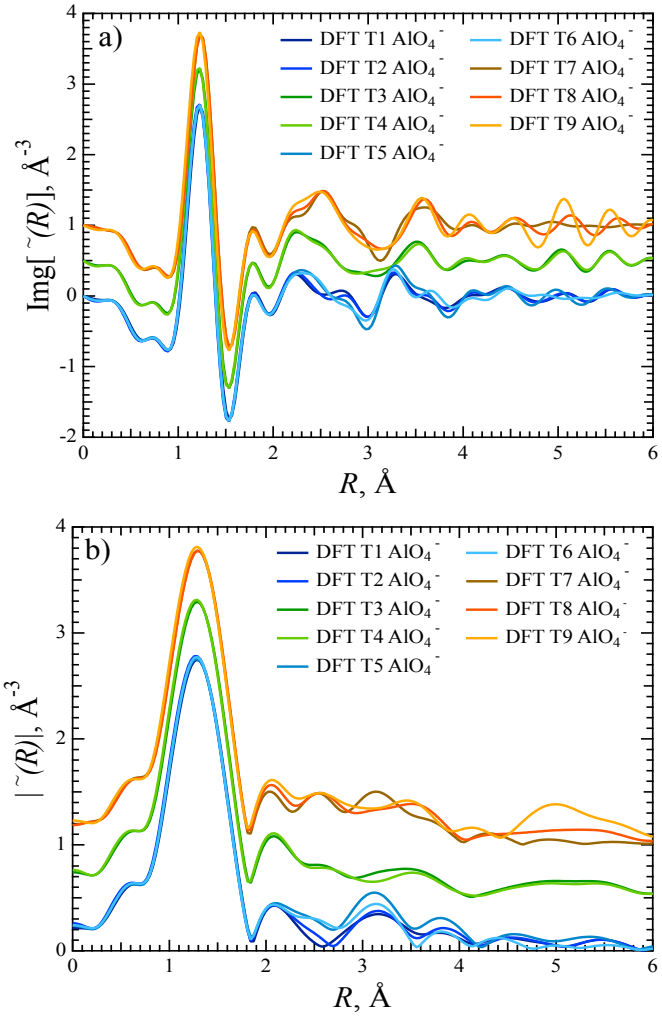

Figure 10. DFT optimized AlO_4^- EXAFS Img[$\tilde{\chi}(R)$] plot (a) and $|\tilde{\chi}(R)|$ plot (b) plots for the nine T–sites of HBEA. The color–coding is reported in the legend. The standard σ^2 (disorder) parameter was set to 0.003 for all Al T–sites. The T–sites are grouped as Set A (T1, T2, T5, T6), Set B (T3, T4) and Set C (T7, T8, T9). The groupings are based primarily on the positions of the various scattering peaks in the range from 2 to 5 Å. The position of these peaks is mostly independent of the choice of the disorder parameter.

HBEA zeolite contains 9 different T–sites that could be populated with Al atoms. The distribution of Al–Si and Al–O bond lengths (probed by EXAFS) within a given T–site can be correlated with the number of shared 4, 5, or 6 member rings (Figure 1) at that T–site. Based on this premise, a DFT–based EXAFS spectrum was calculated for each of the nine T–sites and it was found that they could be grouped into three sets, Set A (T1, T2, T5, T6), Set B (T3, T4) and Set C (T7, T8, T9), by way of the similarity of their EXAFS spectra (Figure 10).

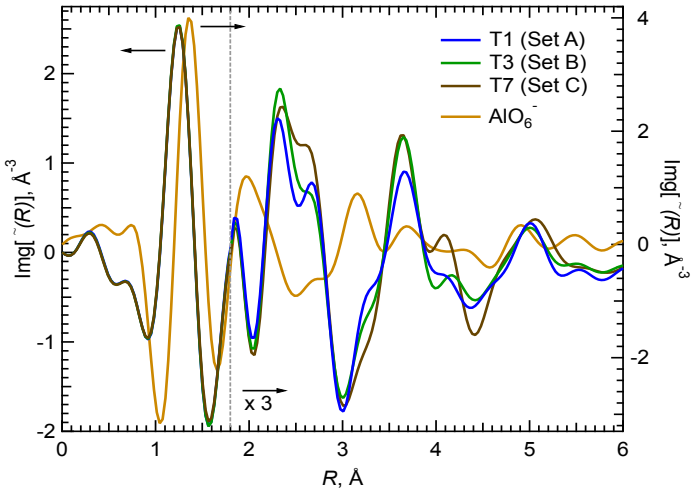

Figure 11. Img[~(*R*)] plots of the calculated MD–EXAFS spectra for sites T1 (blue), T3 (green) and T7 (brown) representing T site sets A, B, C, respectively. T1, T3, and T7 are rescaled beyond 1.8 Å as shown while the AlO_6^- spectrum is not. The AlO_6^- spectrum is from an experimentally measured aqueous Al^{3+}.

Subsequently, full MD trajectories at 300 K were calculated for one representative T–site from each set (T1, T3 and T7 from sets A, B and C, respectively) and these trajectories were in turn used to simulate the EXAFS spectra of the T–sites using the MD–EXAFS method. Figure 11 shows the full MD–EXAFS spectra generated for T–sites T1, T3 and T7. Note the significant spectral differences in the region from $2 < R < 5.5$ Å owing to the different arrangements of Si and second shell O atoms around the different Al T–sites. HBEA zeolites often contain small percentages of extra–framework AlO_6^- (octahedral) as an impurity. This species can be approximated by aqueous Al^{3+}, which would have nearly the same first–shell Al–O bond distances and symmetry. The spectrum

of aqueous Al^{3+} is shown in Figure 6 for comparison. The features for aqueous Al^{3+} are dominated by single and multiple scattering peaks (e.g. peak at 3.2 Å) from only the first shell O's.

To provide an understanding the structural similarities and differences between these sites and the groups they represent the Al–Si and Al–O radial distribution functions, g(r), generated from the MD trajectories of the three Al T–sites are compared in Figure 12. Both $g(r)_{Al–O}$ and $g(r)_{Al–Si}$ are shown because although the EXAFS backscattering signal from O is not nearly as strong as for Si, the signal still contributes significantly to the total EXAFS spectra and the contributions are distinct from those for Si. Peaks in the g(r) plots at $g(r)_{Al–O}$ = 1.75 Å and $g(r)_{Al–Si}$ = 3.15 Å are due to the nearest–neighbor O and Si atoms about each Al. When the Al T–site is protonated multiple peaks appear at these distances as shown in Figure 12 for the Al T1–site (the dashed purple line). In the $g(r)_{Al–O}$ plot two distinct peaks are seen, one intense peak for the three unprotonated oxygens bonded to Al appears at $g(r)_{Al–O}$ = 1.7 Å and one of lower intensity for the protonated O appears at $g(r)_{Al–O}$ = 1.95 Å. In the $g(r)_{Al–Si}$ plot, two peaks appear at $g(r)_{Al–Si}$ = 3.1 and 3.25 Å and a shoulder is evident at 3.45 Å. This analysis shows that the protonation state can be definitively determined from EXAFS measurements of the first shell Al–O and Al–Si distances.

When the Al T–site is unprotonated (the expected experimental state), there is very little difference in the Al–O and Al–Si first shell distances between the three different structural sets A, B and C. Hence EXAFS cannot differentiate the structure based solely upon the first shell Al–O and Al–Si distances. In contrast there are distinguishable differences in the second–shell Al–O and Al–Si distances. In sets A, B and C the Al T–sites share different combinations of 4, 5 and 6 member Al–O–$(Si–O)_{n–1}$ rings. The T–sites in sets A and B contain at least one 4–member ring. The second–shell Al–Si distances for these 4–member rings occurs at a distance of 4.5 Å. Set C contains no 4–member rings such that $g(r)_{Al–Si}$ shows a peak at a somewhat greater distance of ~5 Å for both 5– and 6–member rings. Although not nearly as distinct as for the 4–member rings, the atom distances for the 5–member rings are somewhat shorter than for 6–member rings. Analysis of the $g(r)_{Al–O}$ plot shows similar trends. The distributions of second shell Al–O distances for sets A and B appear at shorter distances than for set C. All three

structural sets of A, B, and C contain a component from a near linear arrangement of Al–O–Si–O–Si atoms leading to distinct peaks in the second–shell distances at $g(r)_{Al–O}$ = 4.2 – 4.4 Å and $g(r)_{Al–Si}$ = 5.8 Å.

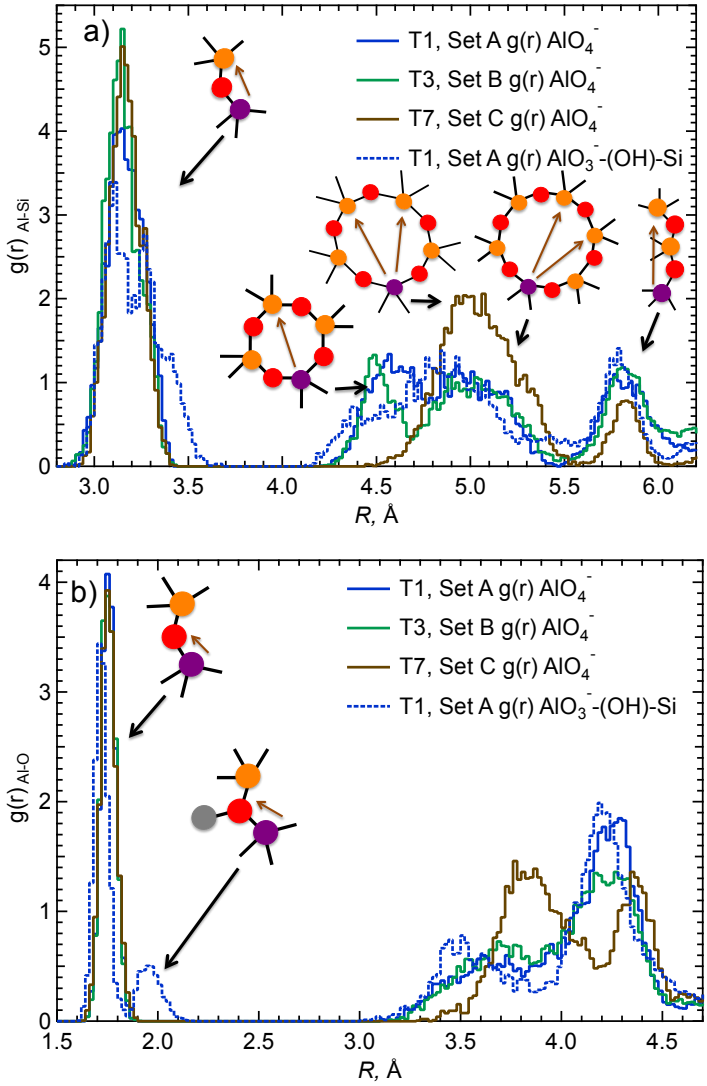

Figure 12. Calculated g(r) plots for Al–Si (a) and Al–O (b) atom pairs for the AlO_4^- structures of T1, T3, T7 and the AlO_3^-–(OH)–Si structure of T1. The color–coding is reported in the legend. The corresponding unique structural features providing information about the framework are shown as schemes, Al (purple), O (red), Si (orange), H (grey) atoms. Note: pore structures are schematic and bond distances for these structures are illustrated not to scale.

Thus, the differences in the distribution of Al–Si and Al–O distances revealed in the g(r) plots provide understanding of how the EXAFS data may discriminate between the different structural sets. In addition, EXAFS multiple scattering signals depend upon the angular correlations of the nearby Si and O atoms thereby further improving the structural resolution of bond lengths and symmetry. These multiple scattering features cannot be represented in the standard g(r) plots, but they are quantitatively represented in the calculated MD–EXAFS spectra.

The measured HBEA150 and HBEA25 $\chi(k)$ data were fit as a linear combination of the full MD–EXAFS spectra (Figure 11 T–sites T1, T3 and T7) to determine the Al T–site occupancy of each zeolite. Since both zeolites contain small fractions of octahedrally coordinated Al present as extra–framework Al^{3+}, the measured spectrum of aqueous $Al(H_2O)_6^{3+}$ was used as a reference for octahedral Al (see Appendix). The presence of octahedral Al is clearly differentiated by both its unique EXAFS structure and by its near–zero chemical shift in NMR.

Figure 13 and Figure 14 show the resulting analysis for HBEA150 and HBEA25 zeolites, respectively. The T–site occupancies in HBEA150 and HBEA25 as determined by EXAFS (and by MAS NMR as will be shown below) are shown in Table 2. It should again be emphasized, that the three MD–XAFS spectra (for set A, B, C) were generated from DFT methods without the need for any adjustable parameters. The percent occupancy was derived from fitting of four spectra (three T–sites and one AlO_6^- site) using only three parameters representing the fractions of each component.

The results show that HBEA150 and HBEA25 have distinctly different distributions of Al T–sites. In the HBEA150, the sites are 70 % populated by set A and 20 % by set B whereas in HBEA25 the sites are nearly equally populated by sets A and C. While the best EXAFS fit suggests no sites of set C are present in HBEA150 and no sites of set B sites are in HBEA25, we note that the estimated uncertainties for both spectroscopic techniques are 10 % of total Al in the sample (Table 2). Hence the uncertainties do not completely exclude the population of Set C and Set B to a minor extent in HBEA150 and HBEA25, respectively. Note that neither Al distributions correlate well with that expected from the relative thermodynamic stability of the T–sites (see Appendix).

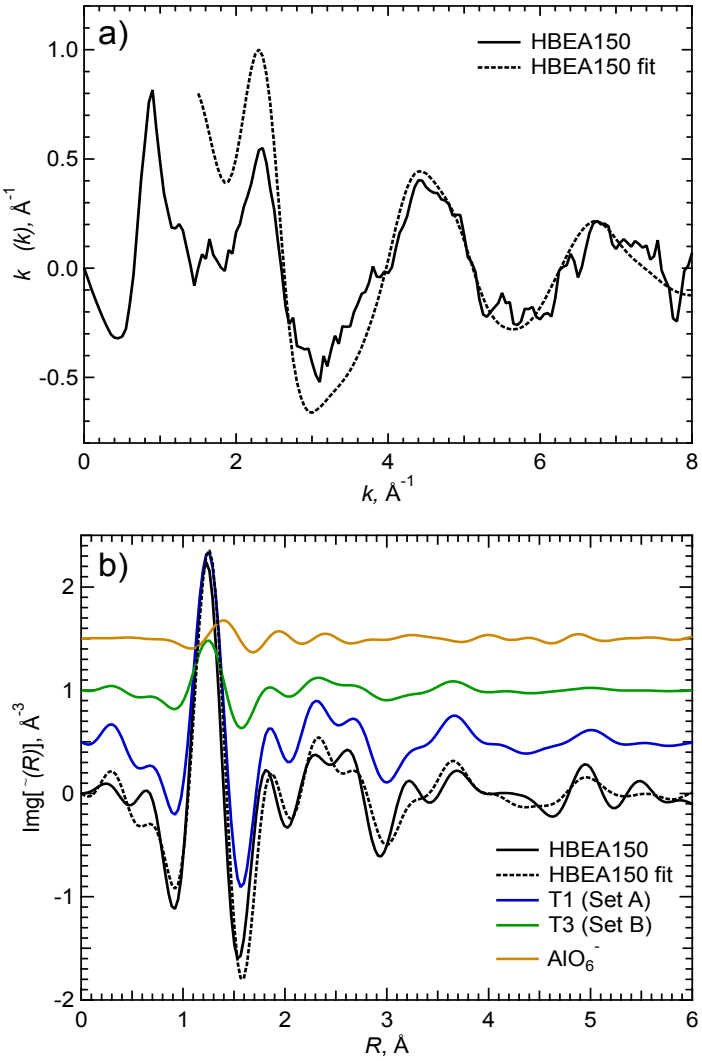

Figure 13. EXAFS *k*–weighted *χ(k)* plot (a) for experimental HBEA150 and simulated using a linear combination of MD EXAFS for Al T–site sets A and B, respectively, and a measured aqueous $Al(H_2O)_6^{3+}$ EXAFS for octahedral Al; Img[~(*R*)] plot (b) for experimental (solid black) and simulated (dotted black) HBEA150 with the calculated component spectra for T–sites T1 (Set A, blue) and T3 (Set B, green) and AlO_6^-(octahedral sites, gold).

The probabilities of Al to populate the different sites based on the degeneracies and the DFT energies of the 9 unprotonated sites are listed in Appendix in Table A3 and graphically depicted in Figure A3. Sites T7 and T8 are thermodynamically the most

favored sites (probabilities of 0.87 and 0.12, respectively). Members of set C, both T7 and T8, are located in 6–member rings that are connected to the large 12–member ring in the [1 0 0] and [0 1 0] planes. However, these two sites never occur in the same 6–member ring.

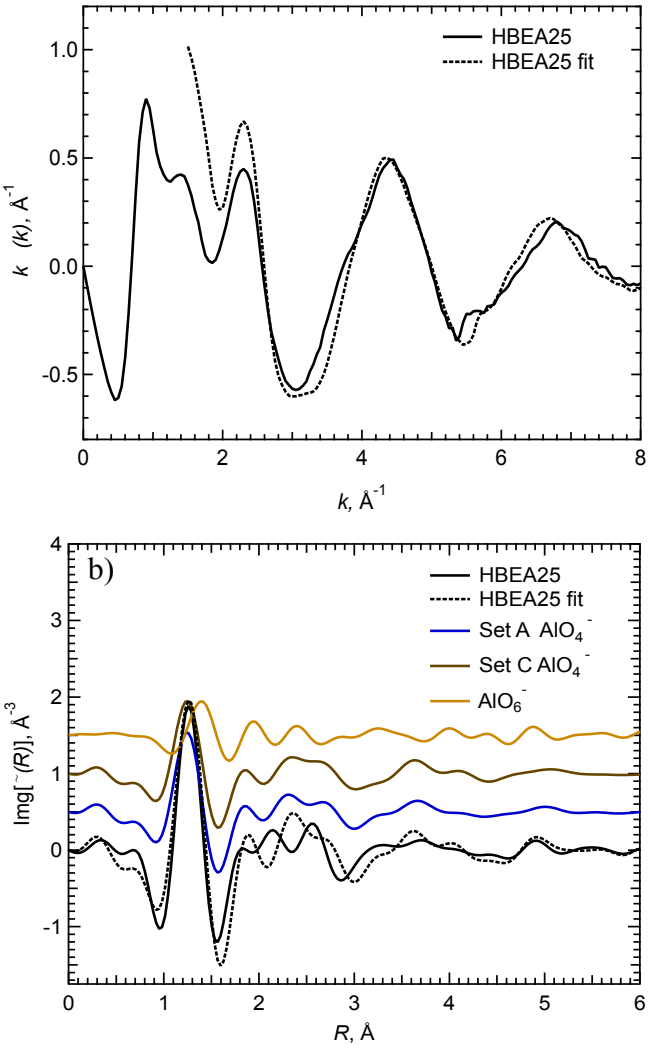

Figure 14. EXAFS *k*–weighted $\chi(k)$ plot (a) for experimental HBEA25 and simulated using a linear combination of MD EXAFS for Sets A and C of Al T–sites and a measured aqueous $Al(H_2O)_6^{3+}$ EXAFS for octahedral Al; Img[$\tilde{\chi}(R)$] plot (b) for experimental and simulated HBEA25 (black) with the calculated component spectra for T–sites A (T1, blue) and C (T7, brown) and octahedral sites (gold).

From the EXAFS analysis, approximately 50 % of the tetrahedral Al in HBEA25 may occupy site T7, but in HBEA150 the best EXAFS fit suggests that the T7–sites are not occupied by Al (within analysis accuracy). The EXAFS analysis shows that Set A sites (T1, T2, T5, T6) in both HBEA150 and HBEA25 samples are occupied by Al to significant extents although their thermodynamic probabilities of being occupied total to less than 0.1 %. The T3 and T4 sites (Set B), have similarly low probabilities of being occupied, yet the analysis of the best fit to the EXAFS spectra suggests that 19 % of the tetrahedral Al in the HBEA150 sample is located in these sites. Therefore, the differences in Al^{3+} distributions from thermodynamic equilibrium suggest that the distributions are controlled by kinetic factors, which are unique to the methods in which the two zeolites were synthesized, and the dealumination procedure, which may lead to selective removal of Al from certain T–sites of HBEA.

Table 2. Al T–site occupancies of HBEA150 and HBEA25 as determined from EXAFS and NMR spectra. The two zeolites not only vary in Al content, but also in Al T–site distribution. Site occupancies are derived from fitting of experimental EXAFS and NMR spectra to their respective sets of theoretical standards.

HBEA150	Occupancy [a]		HBEA150
EXAFS Grouped (T–sites)	*via* EXAFS	*via* NMR	NMR T–sites (fraction)
Set A (1, 2, 5, 6)	0.72	0.73	1 (0.53), 2 (0.20), 5+6 (0)
Set B (3, 4)	0.19 [b]	0	3 (0), 4 (0)
Set C (7, 8, 9)	0.0	0.23	7 (0.13), 8 (0), 9 (0.10)
AlO_6^- (octahedral)	0.09	0.04	AlO_6^- (octahedral)
HBEA25	Occupancy [a]		HBEA25
EXAFS Grouped (T–sites)	*via* EXAFS	*via* NMR	NMR T–sites (fraction)
Set A (1, 2, 5, 6)	0.41	0.41	1 (0.10), 2 (0.31), 5+6 (0)
Set B (3, 4)	0.0	0.0	3 (0), 4 (0)
Set C (7, 8, 9)	0.38	0.36	7 (0.26), 8 (0), 9 (0.10)
AlO_6^- (octahedral)	0.21	0.23	AlO_6^- (octahedral)

[a] The estimated errors are ±10 % by EXAFS and ±10 % by NMR; [b] Fit accuracy does not exclude population of set C sites instead of set B.

3.3.6 Evaluating the occupancy of Al T–sites from the NMR analysis

The ^{27}Al MAS 850 MHz NMR spectra of HBEA 150 and HBEA25 are shown in Figure 15. The chemical shifts are in agreement with chemical shift values reported for

HBEA previously.[76,77] The differences in the relative intensities and the slight offset of the HBEA150 NMR spectrum compared to HBEA25 (~ 0.3 ppm down field) indicate that the zeolites have substantially different distributions of Al^{3+}. The peaks at ~ 0 ppm are typical of extra–framework octahedral Al. From integration of the spectra, 23 % of the Al in HBEA25 and 4 % in HBEA150 occupy octahedral environments. These amounts are consistent with the EXAFS analysis (Table 2), which yielded 21 and 9 %, respectively. The peaks at ~ 54 and ~ 57 ppm are attributed to tetrahedral Al in the zeolite framework. The presence of other Al species, e.g. extra–framework tetrahedral Al, which would give rise to signals at ~ 30 – 45 ppm,[78,79] is excluded based of the MAS NMR spectra. These findings are consistent with the EXAFS results, which showed that Al does not populate some T–sites.

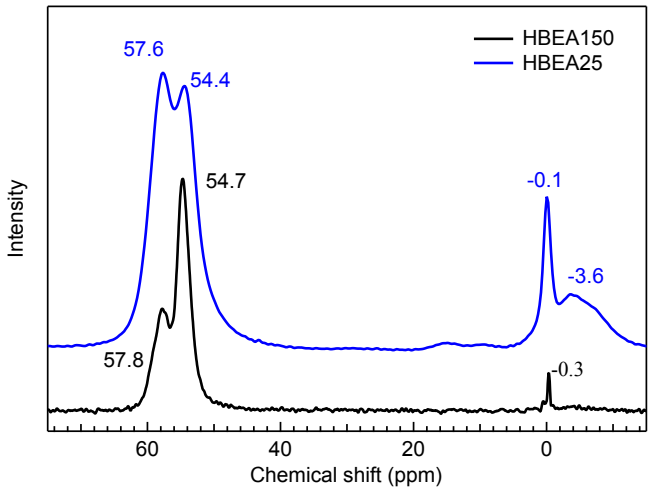

Figure 15. ^{27}Al MAS NMR spectra measured for HBEA150 (black) and HBEA25 (blue). The intensity of HBEA25 spectrum was scaled (0.33) for better visualization.

3.3.7 ^{27}Al DFT NMR calculations

In the past there were reports of a useful relationship between the ^{27}Al NMR chemical shift of the tetrahedral site to the mean Al–O–Si bond.[80,81]

$$_{Al} = 0.50\ _{avg} + 132 \qquad (1)$$

Where $_{avg}$ is the average of four Al–O–Si angles at each T–site. Based on the calculated Al–O–Si bond angles from the DFT optimized structures the chemical shifts

according to Equation 1 are shown in Figure 16. For comparison to this empirical model, the DFT–NMR calculations of ^{27}Al chemical shifts for Al in the framework were performed based on DFT–optimized crystal structures for all potential Al positions referenced to the isotropic chemical shift of aqueous Al^{3+}. The MAS NMR shielding calculation results as well as corresponding bond angles for each T–site are shown in Table 3. The DFT–NMR values are also plotted in Figure 16. Note that the empirical bond angle model (Equation 1) mostly captures the trends of the chemical shift versus T–site. However the overall span of the shifts is significantly smaller and there is some reordering of the series for certain T–sites (especially T7). The chemical shifts calculated from DFT suggest that perhaps there is a significant error in the simple average bond angle relationship (Equation 1). A similar level of error is also observed in fitting Equation 1 to the original set of 17 crystalline standards.[80] The chemical shift is thus suggested dependent upon more complete representation of the local structure than solely the average bond angle.

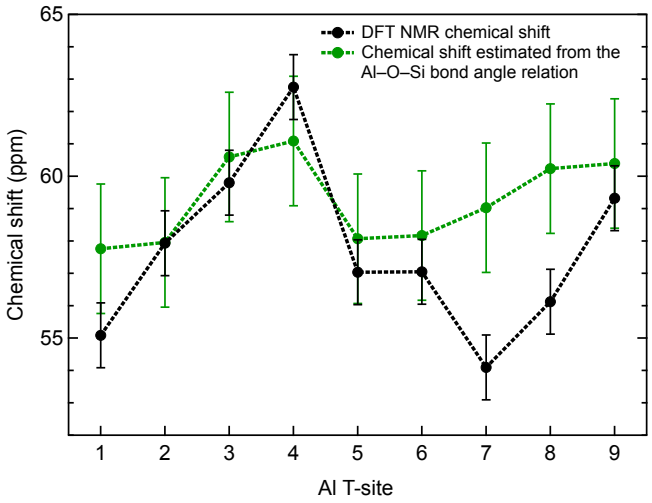

Figure 16. The calculated NMR chemical shifts for tetrahedral $^{27}Al^{3+}$ using the empiric model (green) and DFT NMR (black) are shown.

DFT–NMR calculations of ^{27}Al chemical shifts were performed to assign the T–sites that contribute to the observed peaks. The chemical shifts calculated for the 9 different T–sites are shown graphically in Figure 17 on expanded plots of the NMR resonances for

tetrahedral Al in the HBEA150 and HBEA25 samples. The calculated chemical shifts span from 52.9 to 61.5 ppm.

The DFT–NMR chemical shifts are used to simulate the experimental spectra and through a least square fitting procedure determine the relative Al occupancy at each T–site. The fitting of DFT NMR to the experimental ^{27}Al NMR spectra is performed completely independent of the EXAFS analysis and is not constrained in any way by the amounts of Al in the different T–site sets determined in the EXAFS analysis. To limit the number of parameters used in the fitting procedure, the NMR linewidth and shape (Voigt function) for each T–site were assumed to be identical. As shown in Figure 17a and 17b, both the HBEA150 and HBEA25 spectra can be represented as a combination of four peaks assigned to T1, T2, T7 and T9. The best fit is obtained allowing a +1.2 ppm offset of the experimental data to the calculated chemical shifts (Table 3).

Table 3. Calculated ^{27}Al NMR chemical shifts as well as Al–Si–O angles for 9 potential Al T–site positions.

T–site	Average Al–O–Si angle (°)	Predicted NMR chemical shifts (ppm) based on Al–O–Si angle relation	Calculated ^{27}Al MAS NMR isotropic chemical shift for Al–$(O–Si–OH)_4^-$	^{27}Al NMR chemical shift (ppm) for Al–O–Si–O–H	^{27}Al NMR chemical shift (ppm) for Al–O–Si–O–H offset by +1.2 ppm
1	148.5	57.76	517.5	53.9	55.1
2	148.1	57.95375	514.7	56.7	57.9
3	142.8	60.59625	512.8	58.6	59.8
4	141.8	61.0875	509.9	61.5	62.7
5	147.9	58.07	515.5	55.8	57.0
6	147.7	58.16625	515.6	55.8	57.0
7	145.9	59.02875	518.5	52.9	54.1
8	143.5	60.235	516.5	54.9	56.1
9	143.2	60.395	513.3	58.1	59.3

The incorporation of additional peaks into the fitting procedure did not lead to an improvement of the DFT NMR fit to the experimental data. The Al T–site occupancies determined by DFT–NMR are listed in Table 2 and they are summed into the same sets of T–sites (A, B, C) that were defined by the MD–EXAFS analysis. The agreement with EXAFS on the distribution of Al among these sets of T–sites is good for both HBEA150 and HBEA25 within the experimental uncertainty. While EXAFS suggest Set B sites rather than C (from NMR), the low concentration of these sites combined with the

analysis accuracy reported in Table 2 do not exclude the population of Set C sites in HBEA150. Consistent with observations from the EXAFS analysis, the Al^{3+} distribution in HBEA25 (from NMR) is found to be significantly different from the HBEA150.

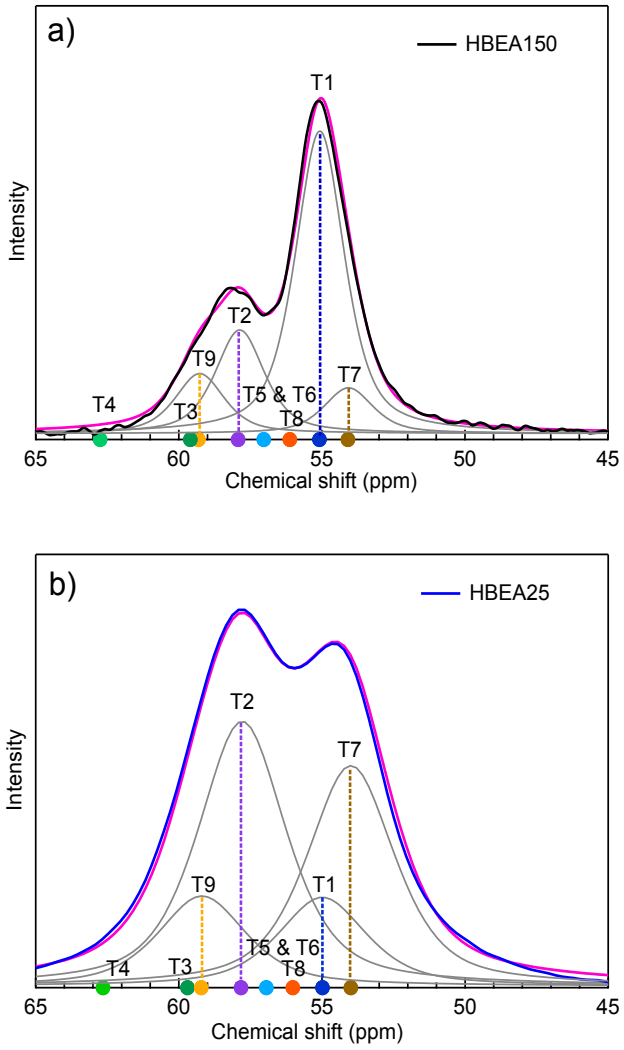

Figure 17. The calculated ^{27}Al MAS NMR chemical shifts for the tetrahedral Al based on the DFT optimized T–site structures for the measured HBEA150 (a) and HBEA25 (b). Fitted NMR peaks are shown in grey, the fit spectrum is shown in magenta. Note: the T5– and T6– signals overlap. DFT NMR peak intensity is based on fitting results.

Note that the NMR data then leads to a further refinement of the EXAFS–derived information with respect to the T–site occupancy. For HBEA150, the occupancy of T4 by Al can be excluded with high confidence as the calculated DFT–NMR peak position is too far down field to contribute significantly to the observed spectrum, see Figure 17a. While the Al occupancy of T3, T5, T6 and T8 cannot be excluded completely; the NMR suggests that the population of these T–sites is least probable. Similarly, for HBEA25, Al occupancy of T3, T4, T5, T6, and T8 is suggested unlikely. These refinements are reflected in the NMR distributions reported in Table 2. Hence, the combination of EXAFS and NMR analysis allowed a more quantitative determination of the Al distribution among T–sites than either would have permitted alone.

Although not the primary focus of this study, the analysis provides new insight to the HBEA zeolite synthesis demonstrating the potential to aid in understanding how synthesis methods affect Al distributions and ultimately to guide efforts to optimize catalytic efficiency. Both HBEA25 and HBEA150 are synthesized hydrothermally using templating agents. Note that HBEA150 was obtained from a parent zeolite (Si/Al ratio similar to that of HBEA25) that was dealuminated by steaming and leaching steps to achieve the high Si/Al ratio of 75. Although it appears that the post–processing steps cause selective removal of Al from T2 and T7 sites in the framework, the description of the dealumination mechanism is incomplete at this point and requires a more comprehensive evaluation of the relation between zeolite synthesis methods and Al distribution.

3.3.8 Al XANES analysis and TDDFT Al XANES calculations

XANES spectra primarily represent core– to valence–state electronic transitions that, with the aid of theory, provide a sensitive probe of the bonding and structure in the vicinity of the target atom. While a quantitative analysis of the XANES region is beyond the scope of this study, the TDDFT calculations of the near edge spectra qualitatively confirm the conclusions deduced from the combination of EXAFS and NMR methods. In Figure 18, XANES spectra for HBEA150 and HBEA25 are compared to their respective theoretical calculations using TDDFT theory.

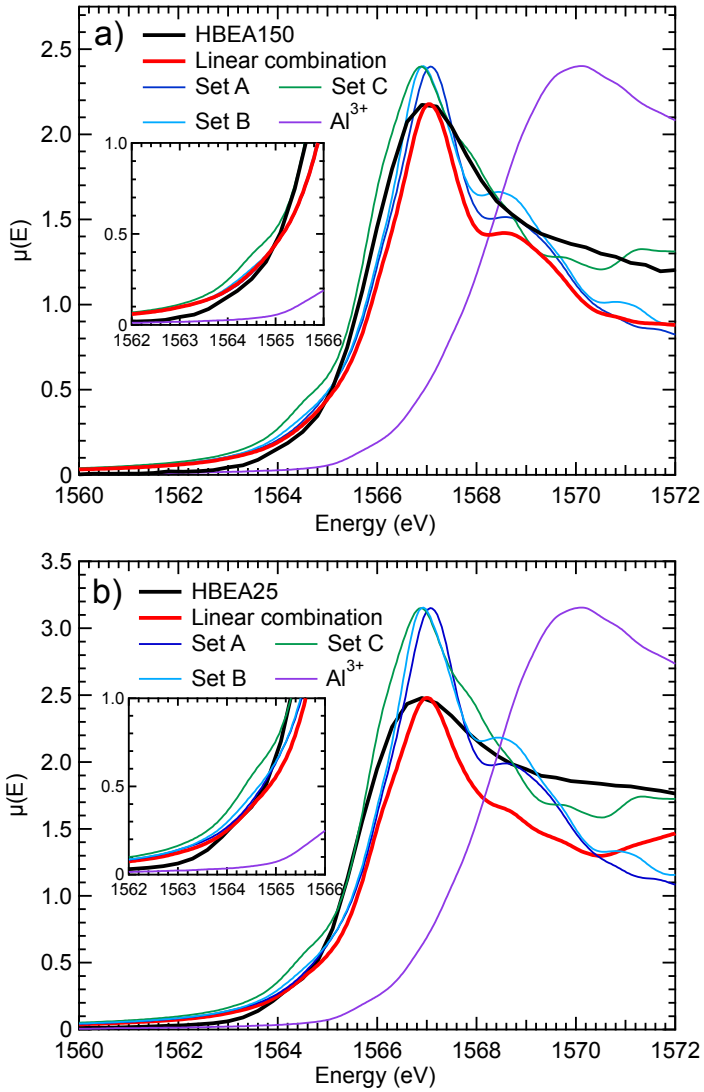

Figure 18. XANES normalized μ(E) plots for the experimental HBEA150 (a) and HBEA25 (b). The EXAFS weighted linear combination of Set A, Set B and octahedral Al (HBEA150) and Set A, Set C and octahedral Al (HBEA25) are shown in red. The TDDFT calculated signals, Set A (T1, T2, T5, T6) (dark blue), Set B (T3, T4) (light blue) and Set C (T7, T8, T9) (green), are also shown. The octahedral Al signal is shown in cyan. Note: the intensity of the measured Al^{3+} spectrum was scaled to the HBEA150 for comparison.

Initially, the XANES spectra for the complete set of nine T–sites were calculated and compared. The findings (see Figure 19) show that the XANES spectra for the T–sites can be grouped with high confidence into the same three sets (Sets A, B, C) that are used for the EXAFS analysis. As a result, Figure 18 shows the spectra for Sets A, B and C that were obtained by averaging the XANES spectra for T–sites (T1, T2, T5, T6), (T3, T4) and (T7, T8, T9), respectively.

Although there are significant differences in the spectral features of these three sets, they are insufficiently unique to determine the distribution of Al^{3+} at the same level as achieved by combining EXAFS and NMR data. For this reason, a representative spectrum was generated using the site occupancies derived from the EXAFS measurement. This linear combination of Sets A, B and C is shown Figure 18 (red lines). The linear combinations also include small contributions from octahedral Al (an experimental aqueous Al^{3+} spectrum is used to represent the octahedral Al fraction).

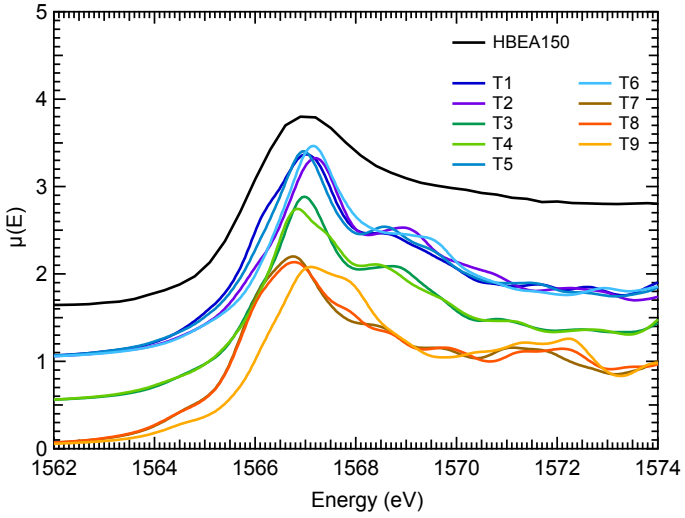

Figure 19. XANES plots for HBEA150 and DFT optimized AlO_4^- calculated for individual Al T–sites, the color–coding is reported in the legend.

The XANES calculations lead to an assignment of the electronic transitions for the HBEA spectra in the range of ~1560 eV to ~1568 eV. The feature at ~1564.5 eV, which is prominent in Set C but also present in Sets A and B, is attributed to excitations from

the Al 1s to a mixture of O 3p, Al 3p and Al 3d states. The prominent feature at ~1567 eV is attributed to excitations from Al 1s to a mixture of O 3p, Al 3p states. The deviation from experiment beyond ~1568 eV is tentatively interpreted as multiple excitation effects, which are not included within the linear–response formulation of TDDFT and hence not captured. Previous studies[56, 82, 83] have shown, however, that TDDFT calculations of XANES are very reliable up to ~10 eV from the rising edge, where single excitations are dominant. Overall, the linear combination of the TDDFT XANES spectra qualitatively predicts the features of the experimental HBEA150 and HBEA25 spectra supporting the Al^{3+} distribution derived using the EXAFS and NMR spectroscopy methods.

3.4 Conclusions

An unprecedented level of structural detail regarding the distribution of Al^{3+} in the HBEA zeolite framework has been attained through a combination of X–ray absorption and NMR spectroscopies supported by ab initio computational models that enable quantitative analysis of the spectral data. The excellent quality of Al EXAFS allowed analysis of scattering from atoms up to 6 Å apart from the absorbing Al T–site and enabled the quantification of both framework and extra–framework Al^{3+}. The identical first shell Al–O bond distances led us to conclude that hydronium ions are formed at all Al T–sites to compensate the lattice charges. The population of T–sites with Al in HBEA150 and HBEA25 does not follow the population predicted by the thermodynamic stability of Al T–sites. This strongly suggests that the incorporation of Al into the zeolite lattice during hydrothermal synthesis is controlled by kinetics and primarily determined by the organic base functioning as a template constituent. The differences in the distribution of Al T–sites in HBEA150 and HBEA25 are attributed to the zeolite synthesis and post–synthetic treatment conditions. While the details of post–synthetic treatment, e.g. dealumination, are not explored at present, the analysis using a combination of EXAFS, NMR and theory demonstrates the potential to analyze zeolite active sites in a depth and detail, which were not available hitherto.

3.5 Acknowledgements

Al XAFS measurements were performed at the Swiss Light Source, Paul Scherrer Institute, Villigen, Switzerland. This work was supported by the U. S. Department of Energy (DOE), Office of Basic Energy Sciences, Division of Chemical Sciences, Geosciences & Biosciences.

3.6 Appendix

3.6.1 Al EXAFS data fitting for α–alumina and sodium aluminate

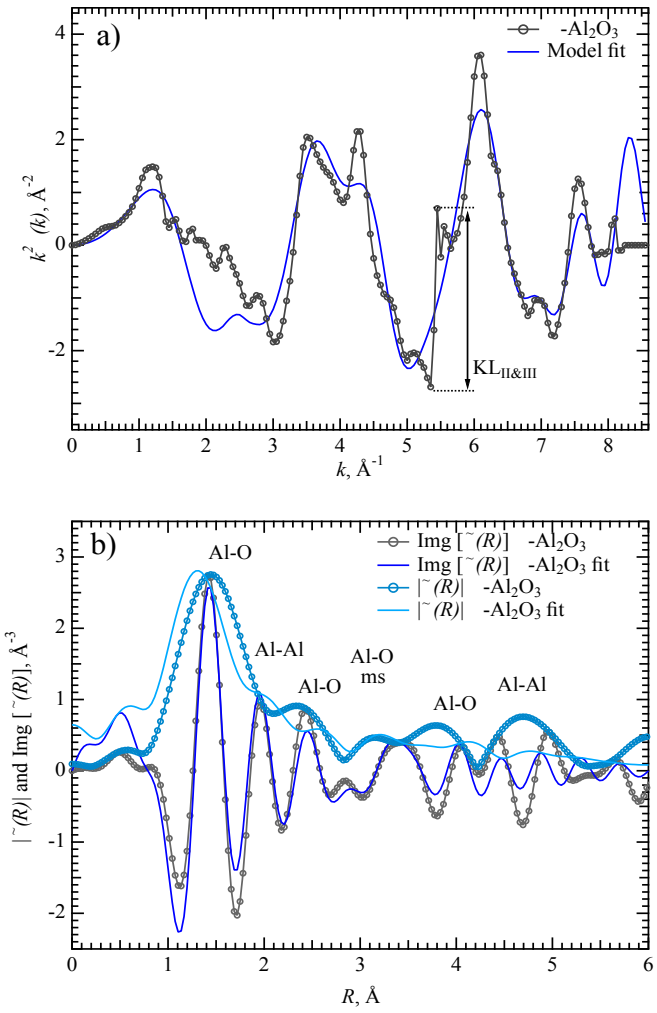

Figure A1. EXAFS k^2–weighted $\chi(k)$ (a) and $|\tilde{\chi}(R)|$ and Img$[\tilde{\chi}(R)]$ (b) plots for α–alumina with simple model fits starting from crystallographic data.

In addition to MD–EXAFS results reported in the main document, the experimental spectra for α–Al_2O_3 and $Na_2Al_2O_4$ were also fit using conventional EXAFS scattering path analysis. Figures A1 a) and b) show the $k^2\,\chi(k)$ plot for α–Al_2O_3 and the magnitude and imaginary Fourier transforms of this function in the form of $|\Box(R)|$ and Img[$\Box(R)$] plots, respectively. Fitting demonstrates that conventional EXAFS analysis can also be used to describe the main features in the experimental spectra. A structural model using scattering paths derived from known crystal structure, fits all relevant features of both $\chi(k)$ and $\Box(R)$. This model includes Al–O single scattering paths for the 2nd and 4th shells and Al–Al scattering paths for the 3rd and 5th shells in order to fit features in $|\Box(R)|$ up to 5.5 Å (Figure A1). Fitted parameters including bond distances for a combination of Al–O and Al–Al single and multiple scattering paths are shown in Table A1.

Table A1. Scattering paths used for fitting to the α–alumina standard. The number (between atoms) indicates the scattering angle. An EXAFS fit is applied that uses a simple linear expansion model applied to the set of Al–O or Al–Al crystallographic distances. The Debye–Waller factors (DWF) for all paths used in the fitting are reported.

#	Path	Fitted distances (Å)	DWF	Scattering path	Crystallographic distances (Å)
1	Al – 180° – O	1.81±0.020	0.0005	single	1.855
2	Al – 180° – O	1.92±0.021	0.0005	single	1.972
3	Al – 180° – Al	2.62±0.024	0.003	single	2.655
4	Al – 180° – Al	2.76±0.025	0.003	single	2.792
5	Al – 180° – Al	3.18±0.029	0.003	single	3.219
6	Al – 180° – O	3.22±0.036	0.002 (set)	single	3.222
7	Al – 180° – O	3.34±0.037	0.004 (set)	single	3.429
8	Al – 180° – Al	3.45±0.032	0.008	single	3.499
9	Al – 180° – O	3.46±0.038	0.004 (set)	single	3.559
10	Al – 180° – O – 180° – Al – 180° – O – 180° – Al	3.61±0.040	0.002	multiple	3.710
11	Al – 180° – O	3.76±0.042	0.01	single	3.865
12	Al – 180° – O – 180° – Al – 180° – O – 180° – Al	3.84±0.042	0.002	multiple	3.943
13	Al – 180° – O	4.05±0.045	0.01	single	4.162
14	Al – 180° – O	4.26±0.047	0.01	single	4.377
15	Al – 180° – O	4.55±0.050	0.01	single	4.677
16	Al – 180° – Al	4.70±0.043	0 (set)	single	4.760
17	Al – 180° – Al	5.06±0.067	0 (set)	single	5.129
18	Al – 180° – Al	5.38±0.071	0 (set)	single	5.450

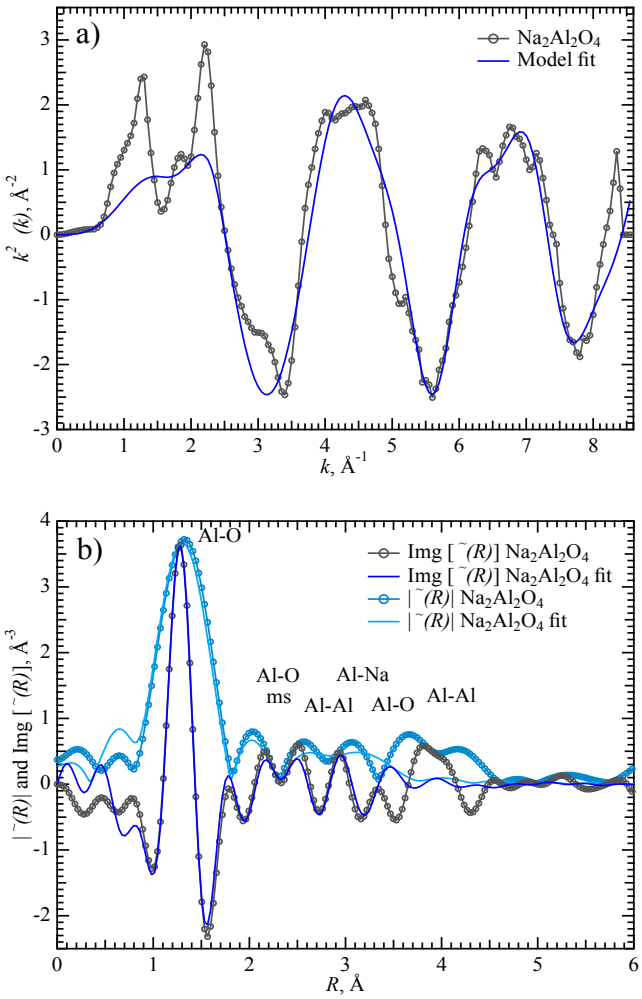

Figure A2. EXAFS k^2–weighted $\chi(k)$ (a) and $|\tilde{\chi}(R)|$ and Img[$\tilde{\chi}(R)$] (b) plots for $Na_2Al_2O_4$ with simple model fits starting from crystallographic data.

The same overall analysis procedure was applied to $Na_2Al_2O_4$ as shown in Figure A2. All relevant features of both $\chi(k)$ and $|\tilde{\chi}(R)|$ are captured in the model. The first shell Al–O bond distances were determined to be 1.76 Å, which is in excellent agreement with the crystallographic value (1.76Å).[84] The fitted bond distances are shown in Table A2 for sodium aluminate.

Table A2. Scattering paths used for fitting to the α–alumina standard. The number (between atoms) indicates the scattering angle. An EXAFS fit is applied that uses a simple linear expansion model applied to the set of Al–O or Al–Al crystallographic distances. The Debye–Waller factors (DWF) for all paths used in the fitting are reported.

#	Path	Fitted distances (Å)	DWF	Scattering path	Crystallographic distances (Å)
1	Al – 180° – O	1.75±0.0012	0.0002	single	1.759
2	Al – 180° – Na	3.19±0 (set)	0.03	single	3.191
3	Al – 180° – Al	3.25±0.092	0.01	single	3.215
4	Al – 180° – Na	3.37±0 (set)	0.05	single	3.369
5	Al – 180° – O	3.49±0.0024	0.0002	single	3.517
6	Al – 180° – O	3.69±0.0025	0.0002	single	3.722
7	Al – 180° – O	3.88±0.0027	0.0002	single	3.905

3.6.2 EXAFS measurements of $Al^{3+}(H_2O)_6$

The measurements were performed in a liquid cell equipped with 1.5 mm diameter 800 nm thick CVD diamond X–ray windows (Applied Diamond, Inc. Wilmington, DE). The cell design is shown in Figure A3. A similar cell using SiN_3 windows and has been reported in detail in the past.[85] An aqueous 2 M $AlCl_3$ solution was used to perform EXAFS measurements in transmission mode wherein the sample chamber was held at 800 mbar He.

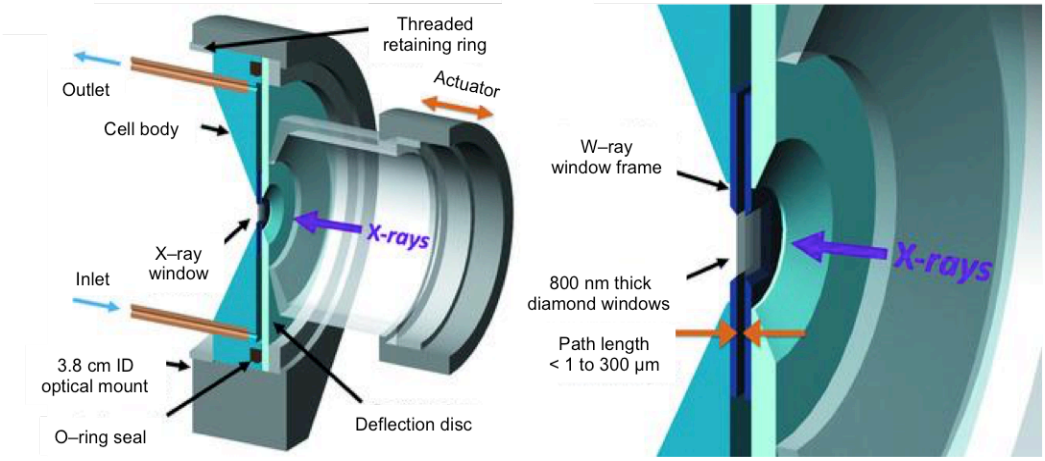

Figure A3. The EXAFS liquid cell used in this work for Al^{3+} measurements in water is shown. The design is based on the cell developed by Fulton et al.[85]

3.6.3 HBEA T–site thermodynamic stability calculation

The thermodynamic stability of the nine HBEA T–sites as well as the Boltzmann probabilities of Al to populate the sites as function of temperature are listed in Table A3 and graphically depicted in Figure A4. The probabilities of occupying the sites are equivalent to the equilibrium distribution since the internal entropies and zero point energies of the various Al T–sites are expected to be similar.

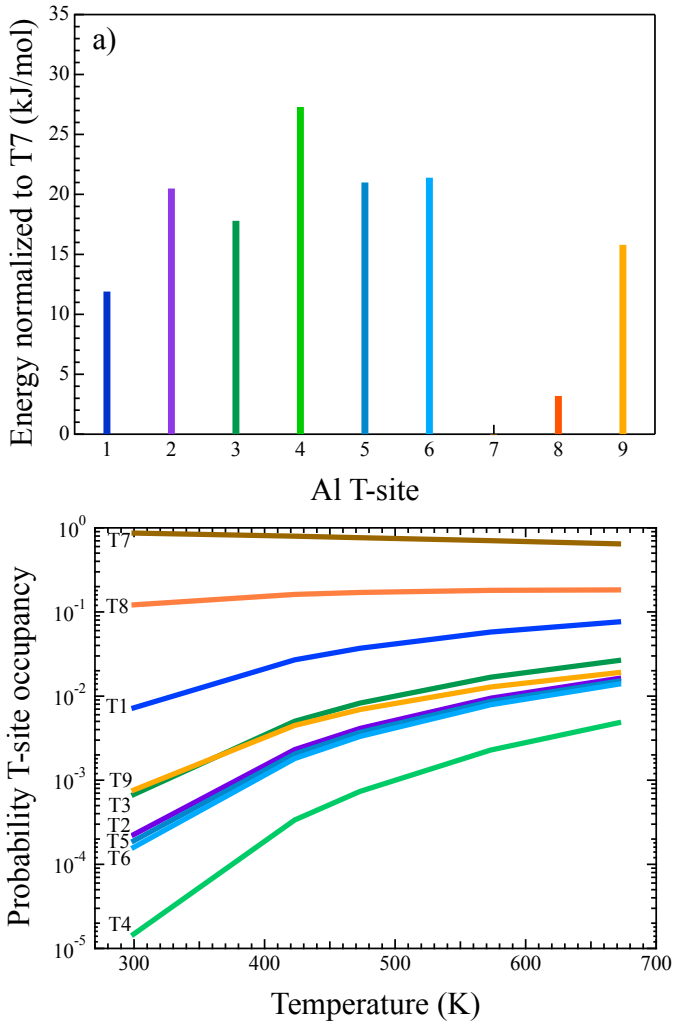

Figure A4. Calculated relative thermodynamic stability of individual Al T–sites (a) and the T–site occupancy probability for different temperatures (b) are shown. The color–coding is reported in the legend.

Table A3. The relative energies of the T–sites calculated by DFT and the probability of Al distribution among T–sites are shown. Note: the degeneracy is derived based on atom population in the unit cell of the BEA crystal.

HBEA T–site	Energy (hartree)	Energy normalized to T7 (kJ/mol)	Degeneracy
T1	–2312.059399	11.9	8
T2	–2312.056111	20.5	8
T3	–2312.057151	17.8	8
T4	–2312.053532	27.3	8
T5	–2312.055950	21.0	8
T6	–2312.055784	21.4	8
T7	–2312.063932	0.0	8
T8	–2312.062726	3.2	4
T9	–2312.057925	15.8	4

HBEA T–site	Probability				
	298	423 K	473 K	573 K	673 K
T1	7.13E–03	2.70E–02	3.71E–02	5.78E–02	7.67E–02
T2	2.19E–04	2.32E–03	4.13E–03	9.45E–03	1.64E–02
T3	6.59E–04	5.04E–03	8.27E–03	1.68E–02	2.67E–02
T4	1.42E–05	3.38E–04	7.38E–04	2.28E–03	4.89E–03
T5	1.84E–04	2.05E–03	3.71E–03	8.64E–03	1.52E–02
T6	1.55E–04	1.81E–03	3.32E–03	7.89E–03	1.41E–02
T7	8.70E–01	7.95E–01	7.65E–01	7.03E–01	6.44E–01
T8	1.21E–01	1.62E–01	1.71E–01	1.81E–01	1.83E–01
T9	7.47E–04	4.49E–03	6.93E–03	1.28E–02	1.92E–02

3.6.4 DFT NMR calculations supplemental

Table A4. Average first shell Al – O bond distances, O – O atom distances and O – Al – O angles for the 9 T–sites of HBEA. The atoms are labeled in accordance with the crystallographic reference.

T1				
Distance O–O	**Distance (Å)**	**O–Al–O angles (°)**	**Distance Al–O**	**Distance (Å)**
O94–O93	2.84312	110.0633	Al–O94	1.72386
O94–O89	2.76244	106.0856	Al–O188	1.73961
O94–O188	2.86498	111.6239	Al–O93	1.74558
O93–O89	2.87633	111.5498	Al–O89	1.73314
O93–O188	2.79928	106.8721		
O89–O188	2.85707	110.7143		
T2				
Distance O–O	**Distance (Å)**	**O–Al–O angles (°)**	**Distance Al–O**	**Distance (Å)**
O93–O91	2.89337	113.3576	Al–O91	1.72325
O93–O189	2.81247	108.6766	Al–O95	1.71126
O93–O95	2.82369	109.8306	Al–O93	1.73934
O91–O189	2.76613	106.8013	Al–O189	1.72225
O91–O95	2.78067	108.1181		
O189–O95	2.81248	109.9941		

T3

Distance O–O	Distance (Å)	O–Al–O angles (°)	Distance Al–O	Distance (Å)
O82–O148	2.83954	109.4104	Al–O82	1.73878
O82–O150	2.81146	108.8308	Al–O148	1.74024
O82–O149	2.85793	111.6097	Al–O150	1.71823
O148–O150	2.83913	110.3529	Al–O149	1.71642
O148–O149	2.81597	109.1035		
O150–O149	2.77017	107.5178		

T4

Distance O–O	Distance (Å)	O–Al–O angles (°)	Distance Al–O	Distance (Å)
O85–O151	2.85812	112.1994	Al–O85	1.7296
O85–O152	2.80846	109.4533	Al–O151	1.71386
O85–O148	2.81638	108.7672	Al–O152	1.7104
O151–O152	2.7116	104.7228	Al–O148	1.73486
O151–O148	2.8617	112.152		
O152–O148	2.81266	109.4473		

T5

Distance O–O	Distance (Å)	O–Al–O angles (°)	Distance Al–O	Distance (Å)
O153–O149	2.82277	109.5793	Al–O153	1.74
O153–O154	2.80382	108.4398	Al–O149	1.71482
O153–O188	2.87486	111.2404	Al–O154	1.71605
O149–O188	2.80063	108.1617	Al–O188	1.74335
O149–O154	2.74319	106.1763		
O188–O154	2.88622	113.0861		

T6

Distance O–O	Distance (Å)	O–Al–O angles (°)	Distance Al–O	Distance (Å)
O151–O153	2.88293	112.5771	Al–O151	1.72084
O151–O155	2.7689	107.2465	Al–O153	1.74483
O151–O189	2.77844	107.2106	Al–O155	1.71822
O153–O189	2.83677	109.4068	Al–O189	1.73085
O153–O155	2.81118	108.535		
O155–O189	2.8576	111.8923		

T7

Distance O–O	Distance (Å)	O–Al–O angles (°)	Distance Al–O	Distance (Å)
O158–O83	2.87119	110.4222	Al–O158	1.74677
O158–O94	2.78954	106.8219	Al–O83	1.74931
O158–O169	2.87554	111.4085	Al–O94	1.7274
O83–O169	2.84003	109.2423	Al–O169	1.73391
O83–O94	2.8713	111.3514		
O94–O169	2.7923	107.5528		

T8

Distance O–O	Distance (Å)	O–Al–O angles (°)	Distance Al–O	Distance (Å)
O161–O84	2.88082	110.7239	Al–O161	1.75228
O161–O90	2.89878	112.2637	Al–O84	1.74914
O161–O170	2.81449	108.1705	Al–O90	1.73886
O84–O170	2.83927	109.7232	Al–O170	1.72281
O84–O90	2.82977	108.4434		
O90–O170	2.79069	107.446		

T9				
Distance O–O	**Distance (Å)**	**O–Al–O angles (°)**	**Distance Al–O**	**Distance (Å)**
O167–O92	2.76762	107.2083	Al–O167	1.71858
O167–O87	2.84203	110.7091	Al–O92	1.71973
O167–O162	2.82798	109.8806	Al–O87	1.73597
O92–O162	2.84438	110.7782	Al–O162	1.73625
O92–O87	2.78762	107.5433		
O87–O162	2.85542	110.6435		

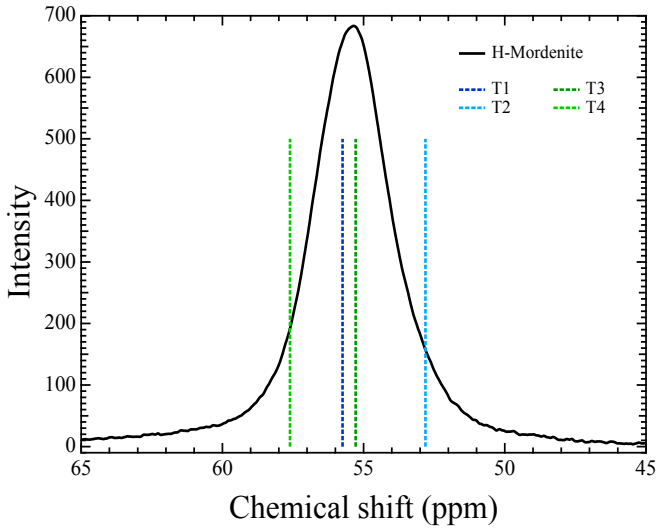

Figure A5. Measured ^{27}Al MAS NMR spectrum (tetrahedral Al signal range) as well as chemical shifts calculated for the 4 T–sites of H–Mordenite reference are shown. The color–coding is reported in the legend. Note: DFT NMR chemical shifts must be offset by –0.9 ppm in order to best match the experimental spectrum.

The ^{27}Al NMR calculations were performed using NWChem software package, the shielding property for the target Al T–site was determined for a DFT optimized Al–cluster. 6–311+G** basis set was used for all atoms. The determined isotropic chemical shift values are compared to H–Mordenite (H–MOR), see Figure A4 and Table A5. Note that the experimental value for H–MOR chemical shift is in very good agreement with previous reports.[80] The single signal in MAS NMR is explained by the nature of the samples. HMOR sample is a naturally occurring zeolite with Al T–sites distributed predominantly amongst T1 and T3 sites, which as shown in Figure A5, cannot be distinguished in NMR. The calculated chemical shift, however, assumes all four T–sites are equally probable in the framework (average calculated chemical shift is centered on

the experimental NMR peak). The T–site atom coordinates for the Al–[O–Si–$(OH)_3]_4^-$ cluster used in ^{27}Al NMR calculations for HBEA and the T–site atom coordinates Al–[O–Si–$(OH)_3]_4^-$ cluster used in ^{27}Al NMR calculations for HMOR were reported by Vjunov et al. in the supporting information in *J. Am. Chem. Soc.* **2014**, *136*, 8296–8306.

Table A5. Calculated ^{27}Al NMR chemical shifts for the 4 Al T–site positions of H–Mordenite. Note that the average calculated chemical shift is +0.9 ppm larger than the experimental value. This offset is within the accuracy of the DFT NMT calculations.

T–site	^{27}Al NMR isotropic chemical shift for Al–O–Si–O–H	^{27}Al calculated NMR chemical shifts (ppm) for Al–O–Si–O–H	Measured ^{27}Al MAS NMR chemical shift (ppm)
1	515.7	56.7	55.4
2	518.6	53.8	
3	516.1	56.2	
4	513.8	58.6	
		Average: 56.3 ± 2.0	

REFERENCES

[1] S. Feast, J. A. Lercher, *Stud. Surf. Sci. Catal.* **1996**, *102*, 363.

[2] J. A. Lercher, A. Jentys, A. Brait, *Molecular Sieves – Science and Technology* **2008**, *6*, 153.

[3] M. E. Davis, *Acc. Chem. Res.* **1993**, *26*, 111–115.

[4] A. Bhan, E. Iglesia, *Acc. Chem. Res.* **2008**, *41*, 559–567.

[5] D. E. De Vos, M. Dams, B. F. Sels, P. A. Jacobs, *Chem. Rev*. **2002**, *102*, 3615–3640.

[6] R. Gounder, E. Iglesia, *J. Am. Chem. Soc*. **2009**, *131*, 1958–1971.

[7] R. A. Beyerlein, C. Choi–Feng, J. B. Hall, B. J. Huggins, G. J. Ray, *Top. Catal.* **1997**, *4*, 27–42.

[8] M. Sierka, U. Eichler, J. Datka, J. Sauer, *J. Phys. Chem. B* **1998**, *102*, 6397–6404.

[9] J. Sauer, U. Eichler, U. Meier, A. Schäfer, M. von Arnim, R. Ahlrichs, *Chem. Phys. Lett*. **1999**, *308*, 147–154.

[10] N. Katada, K. Suzuki, T. Noda, G. Sastre, M. Niwa, *J. Phys. Chem. C* **2009**, *113*, 19208–19217.

[11] E. Lippmaa, A. Samoson, M. Mägi, *J. Am. Chem. Soc.* **1986,** *108,* 1730.

[12] J. A. van Bokhoven, D. C. Koningsberger, P. Kunkeler, H. van Bekkum, A. P. M. Kentgens, *J. Am. Chem. Soc*. **2000**, *122*, 12842.

[13] J. Kannelopoulos, A. Unger, W. Schwieger, D. Freude, *J. Catal*. **2006**, *237*, 416–425.

[14] J. Dedecek, Z. Sobalik, B. Wichterlova, *Cat. Rev. Sci. Eng*. **2012**, *54*, 135–223.

[15] H. Kraus, R Prins, A. P. M. Kentgens, *J. Phys. Chem.* **1996,** *100,* 16336.

[16] S. Sklenak, J. Dedecek, C. Li, B. Wichterlova, V. Gabova, M. Sierka, J. Sauer, *Phys. Chem. Chem. Phys.* **2009**, *11*, 1237–1247.

[17] Z. Yu, A. Zheng, Q. Wang, L. Chen, J. Xu, J. –P. Amoureux, F. Deng, *Angew. Chem. Int. Ed.* **2010**, *49*, 8657–8661.

[18] J. Dedecek, M. J. Lucero, C. Li, F. Gao, P. Klein, M. Urbanova, Z. Tvaruzkova, P. Sazama, S. Sklenak, *J. Phys. Chem. C* **2011**, *115*, 11056–11064.

[19] S. Sklenak, J. Dedecek, C. Li, B. Wichterlova, V. Gabova, M. Sierka, J. Sauer, *Angew. Chem. Int. Ed*. **2007**, *46*, 7286–7289.

[20] S. Sklenak, J. Dedecek, C. Li, B. Wichterlova, V. Gabova, M. Sierka, J. Sauer, *Phys. Chem. Chem. Phys*. **2009**, *11*, 1237–1247.

[21] J. Dedecek, S. Sklenak, C. Li, F. Gao, J. Brus, Q. Zhu, T. Tatsumi, *J. Phys. Chem. C* **2009**, *113*, 14454–14466.

[22] J. A. van Bokhoven, T.–L. Lee, M. Drakopoulos, C. Lamberti, S. Thieβ, J. Zegenhagen, *Nat. Mater*. **2008**, *7*, 551.

[23] J. A. van Bokhoven, D. C. Koningsberger, P. Kunkeler, H. van Bekkum, *J. Catal*. **2002**, *211*, 540–547.

[24] D. Manuel, D. Cabaret, C. Brouder, P. Sainctavit, A. Bordage, N. Trcera, *Phys. Rev. B* **2012**, *85***,** 224108.

[25] I. J. Drake, Y. Zhang, M. K. Gilles, C. N. T. Liu, P. Nachimuthu, R. C. C. Perera, H. Wakita, A. T. Bell, *J. Phys. Chem. B* **2006**, *110,* 11665–11676.

[26] J. A. van Bokhoven, Ad M. J. van der Eerden, R. Prins, *J. Am. Chem. Soc.* **2004**, *126*, 4506–4507.

[27] A.–M. Flank, G. Cauchon, P. Lagarde, S. Bac, M. Janousch, R. Wetter, J.–M. Dubuisson, M. Idir, F. Langlois, T. Moreno, D. Vantelon, *Nucl. Instrum. Meth. Phys. Res. B* **2006**, *246*, 269–274.

[28] B. J. Palmer, D. M. Pfund, J. L. Fulton, *J. Phys. Chem*. **1996**, *100*, 13393–13398.

[29] Y. Amit, H. Eshet, A. Faust, A. Patllola, E. Rabani, U. Banin, A. I. Frenkel, *J. Phys. Chem. C* **2013**, *117*, 13688−1369.

[30] Y. Matsumoto, M. Murakami, T. Shono, T. Hasegawa, T. Fukumura, M. Kawasaki, P. Ahmet, T. Chikyow, S. Koshihara, H. Koinuma, *Science* **2001***, 291*, 854–856.

[31] A. Chica, A. Corma, *J. Catal*. **1999**, *187*, 167–176.

[32] I. Rodriguez, M. J. Climent, S. Iborra, V. Fornds, A. Corma, *J. Catal*. **2000**, *192*, 441–447.

[33] C. Zhao, Y. Kou, A. A. Lemonidou, X. Li, J. A. Lercher, *Chem. Commun.* **2010**, *46*, 412–414.

[34] C. Zhao, D. M. Camaioni, J. A. Lercher, *J. Catal.* **2012***, 288*, 92–103.

[35] A. Corma, M. Moliner, A. Cantín, M. J. Díaz–Cabañas, J. L. Jordá, D. Zhang, J. Sun, K. Jansson, S. Hovmöller, X. Zou, *Chem. Mater.* **2008,** *20,* 3218–3223.

[36] J. M. Newsam, M. M. J. Treacy, W. T. Koetsier, C. B. de Gruyter, *Proc. R. Soc. Lond. A* **1988**, *420*, 375–405.

[37] T. Willhammar, X. Zhou, *Z. Kristallogr*. **2013**, *228*, 11–27.

[38] A. Andersen, N. Govind, L. Subramanian, *Mol. Simul*. **2008**, *34*, 1025–1039.

[39] P. A. Wright, W. Zhou, J. Perez–Pariente, M. Arranz, *J. Am. Chem. Soc.* **2005**, *127*, 494–495.

[40] M. A. Cambior, A. Corma, S. Valencia, *Chem. Comm*. **1996**, 2365–2366.

[41] M. M. J. Treacy, J. M. Newsam, *Nature* **1988**, *332*, 249–251.

[42] M. M. Martinez–Iñesta, I. Peral, T. Proffen, R. F. Lobo, Micropor. *Mesopor. Mater*. **2005**, *77*, 55–66.

[43] a) B. Ravel, M. Newville, *J. Synchrotron Radiat.* **2005**, *12*, 537; b) M. Newville, *Ibid.* **2001**, *8*, 322.

[44] J. L. Fulton, M. Balasubramanian, *J. Am. Chem. Soc*. **2010**, *132*, 12597–12604.

[45] J. Jiao, J. Kanellopoulos, W. Wang, S. S. Ray, H. Foerster, D. Freude, M. Hunger, *Phys. Chem. Chem. Phys.* **2005**, *7*, 3221 –3226.

[46] a) CP2K open source Molecular Dynamics Program, http://www.CP2K.org/; b) J. VandeVondele, M. Krack, F. Mohamed, M. Parrinello, T. Chassaing, J. Hutter, *Comput. Phys. Commun.* **2005,** *167*, 103.

[47] International Zeolite Association, Framework structure database.

http://izasc–mirror.la.asu.edu/fmi/xsl/IZA–SC/ft.xsl

[48] J. Dedecek, S. Sklenak, C. Li, B. Wichterlova, V. Gabova, J. Brus, M. Sierka, J. Sauer, *J. Phys. Chem. C* **2009**, *113*, 1447–1458.

[49] S. Goedecker, M. Teter, J. Hutter, *Phys. Rev. B* **1996,** *54*, 1703.

[50] J. VandeVondele, J. Hutter, *J. Chem. Phys.* **2007,** *127*, 114105.

[51] J. P. Perdew, K. Burke, M. Ernzerhof, *Phys. Rev. Lett.* **1996,** *77*, 3865.

[52] J. B. Higgins, R. B. LaPierre, J. L. Schlenker, A. C. Rohrman, J. D. Wood, G. T. Kerr, W. J. Rohrbaugh, *Zeolites* **1988**, *8*, 446–452.

[53] J. VandeVondele, U. Rothlisberger, *J. Phys. Chem. B* **2002,** *106*, 203.

[54] J. L. Fulton, E. J. Bylaska, S. Bogatko, M. Balasubramanian, E. Cauët, G. K. Schenter, J. H. Weare, *J. Phys Chem. Lett*. **2012**, *3*, 2588.

[55] M. Valiev, E. J. Bylaska, N. Govind, K. Kowalski, T. P. Straatsma, H. J. J. Van Dam, D. Wang, J. Nieplocha, E. Apra, T. L. Windus, and W. A. de Jong, *Computer Physics Communications* **2010**, *181*, 1477.

[56] K. Lopata, B. E. Van Kuiken, M. Khalil, and N. Govind, *J. Chem. Theory Comput.* **2012**, *8*, 3284.

[57] *Sapporo Segmented Gaussian Basis Sets*. http://setani.sci.hokudai.ac.jp/sapporo (accessed June **2013**)

[58] *EMSL Basis Set Exchange*. https://bse.pnl.gov/bse/portal (accessed June **2013**)

[59] A. D. Becke, *J. Chem. Phys.* **1993**, *98*, 1372–77.

[60] C. Lee, W. Yang, R. G. Parr, Phys. *Rev. B* **1988**, *37*, 785.

[61] A. D. McLean, G. S. Chandler, *J. Chem. Phys.* **1980**, *72,* 5639–5648.

[62] O. H. Han, C.–S. Kim, S. B. Hong, *Angew. Chem. Int. Ed*. **2002**, *41*, 469–472.

[63] J. Lewis, D. Schwarzenbach, H. D. Flack, *Acta Cryst. A* **1982**, *38*, 733.

[64] J. A. Kaduk, S. Pei, *J. Solid State Chem.* **1995***, 115*, 126–139.

[65] A. Corma, M. Moliner, A. Cantín, M. J. Díaz–Cabañas, J. L. Jordá, D. Zhang, J. Sun, K. Jansson, S. Hovmöller, X. Zou, *Chem. Mater.* **2008,** *20,* 3218–3223.

[66] J. M. Newsam, M. M. J. Treacy, W. T. Koetsier, C. B. de Gruyter, *Proc. R. Soc. Lond. A* **1988**, *420*, 375–405.

[67] T. Willhammar, X. Zhou, *Z. Kristallogr*. **2013**, *228*, 11–27.

[68] C A. Fyfe, H. Strobl, G. T. Kokotailo, C. T. Pasztor, G. E. Barlow, S. Bradley, *Zeolites* **1988**, *8*, 132–136.

[69] M. A. Camblor, A. Corma, S. Valencia, *Chem. Comm*. **1996**, 2365–2366.

[70] M. M. Martinez–Iñesta, I. Peral, T. Proffen, R. F. Lobo, *Micropor*. *Mesopor. Mater*. **2005**, *77*, 55–66.

[71] L. Čapek, J. Dědeček, B. Wichterlová, *J. Catal*. **2004**, *227*, 352–366.

[72] J. Pérez–Pariente, J. Sanz, J. Fornés, A. Corma, *J. Catal*. **1990**, *124,* 217.

[73] A. Fyfe, Y. Feng, H. Grondey, G.T. Kokotailo, H. Gies, *Chem. Rev.* **1991**, *91,* 1525.

[74] J. Huang, Y. Jiang, V. R. R. Marthala, B. Thomas, E. Romanov, M. Hunger, *J. Phys. Chem. C* **2008**, *112,* 3811–3818.

[75] Y. Jiang, J. Huang, W. Dai, M. Hunger, *Sol. State Nucl. Mag. Res*. **2011**, *39*, 116–141.

[76] J. A. van Bokhoven, A. M. J. van der Berden, D. C. Koningsberger, *J. Am. Chem. Soc*. **2003**, *125*, 7435–7442.

[77] S. M. Maier, A. Jentys, J. A Lercher, *J. Phys. Chem. C* **2011**, *115*, 8005–8011.

[78] F. Deng, Y. Yue, C. Ye, *J. Phys. Chem. B* **1998**, *102*, 5252–5256.

[79] M. Hunger, G. Engelhardt, J. Weitkamp, *Microporous Mater*. **1995**, *3*, 497.

[80] E. Lippmaa, A. Samoson, M. Mägi, *J. Am. Chem. Soc.* **1986,** *108,* 1730.

[81] J.A. van Bokhoven, A.M.J. van der Berden, D.C. Koningsbeger, *J. Am. Chem. Soc*. **2003**, *125*, 7435–7442.

[82] B. E. Van Kuiken, M. Valiev, S. L. Daifuku, C. Bannan, M. L. Strader, H. Cho, N. Huse, R. W. Schoenlein, N. Govind, M. Khalil, *J. Phys. Chem. A* **2013**, *117*, 4444.

[83] Y. Zhang, J. D. Biggs, D. Healion, N. Govind, S. Mukamel, J. Chem. Phys. 2012, *137*, 194306.

[84] J. A. Kaduk, S. Pei, *J. Solid State Chem.* **1995***, 115*, 126–139.

[85] J. L. Fulton, M. Balasubramanian, V.–T. Pham, G. S. Deverman, *J. Synchrotron Rad*. **2012**, *19*, 949–953.

Chapter 4

The impact of aqueous medium on zeolite framework degradation

Understanding the zeolite framework stability in aqueous phase is crucial to develop stable catalysts. Al K–edge, extended X–ray absorption fine structure and ^{27}Al MAS NMR spectroscopies in combination with DFT calculations have been used to monitor both qualitative and quantitative structural changes of two well–characterized samples with BEA structure. The effects of various properties on stability were explored, including Al concentration, Al distribution, particle size and structural defects. As the samples were degraded by treatment in hot liquid water, the local structure about the Al T–site remained mostly intact, including the Al–O–Si angles and bond distances, while the nano–scale crystalline structure as measured by XRD and TEM was disrupted. The combined data suggest a three–step mechanism in which, initially, the HBEA framework crystallinity decreases *via* hydrolysis of T–O bonds along polymorph stacking faults and inter–grain boundaries in a mode similar to crack propagation in glass. With prolonged exposure, amorphization occurs *via* hydrolysis of surface Si–OH groups propagating inward through the zeolite lattice. In parallel, cracks propagate within the crystalline micro–domains along paths through specific T–O–T groups.

4.1 Introduction

Zeolites, tectosilicates with solid acid properties, are widely used as catalysts and cation exchangers.[1] The catalytic activity is attributed to the framework substitution of tetrahedrally coordinated Si with Al (Al T–sites). The remarkable catalytic properties are often attributed to the pore environment of the acid sites that stabilize transition states better than more open solid acids.[2] Recently, zeolites have been used as preferred solid acid for the conversion of bio–derived intermediates of algal or lignocellosic biomass, such as hydroalkylation [3] and hydrodeoxygenation (HDO)[4] of phenols. These transformations are conducted in hot liquid water, which is a favorable solvent for the upgrading of bio–oils.[5] It has been reported, however, that some zeolites rapidly degrade under such conditions.[6] Similarly, zeolites partially dissolve and if the liquid reaction medium is basic.[7] Sano et al. showed that the stability of ZSM–5 in liquid water is affected by the concentration of framework Al.[8] Increasing concentrations of Al in HY–zeolite have been also associated with increased stability in hot (150 °C) water.[6] In addition the nature and concentration of extra–framework (EF) Al species (i.e., EFAl and charge compensating cations) were reported to influence zeolite stability in water.[9] It has been speculated that EFAl species interact with terminal Si–OH groups and Si–O–Si functional groups near the surface, protecting them against the attack by OH^- anions.[10]

The reasons why Al T–sites stabilize the zeolite lattice have not been elucidated. Studying the effects of hot liquid water on Y–zeolites, Sievers et al. observed the formation of an amorphous Al phase, which retained tetrahedral coordination even upon removal from the lattice.[6] Previous observations suggest that depending on the treatment conditions the zeolite framework Si–O–Si groups may be cleaved selectively such that only few, but not all pores collapse.[6] The structural changes induced by water were attributed to the hydrolysis of terminal Si–O–Si–OH groups,[11] creating a defect, which propagated inward throughout the zeolite lattice.[12]

The relation between these complex transformations and the zeolite framework structural strains and defects as well as selective substitutions leading to different stabilities of tectosilicates in water remains unclear. As the solubility of silica in water is significant at elevated temperatures, variations in the stability of materials must be kinetically determined, and, hence, will depend on the bond stability and the potential of water or other agents to interact with the atoms constituting the bonds forming the zeolite lattice. To stabilize zeolites it will be,

therefore, of utmost importance to atomistically describe and understand the transformations, finding ways to block the dynamic process of silica dissolution and the consequential breakdown of the zeolite lattice.

In order to understand these processes on an atomistic level we combine Al extended X–ray absorption fine structure (EXAFS) analysis and ^{27}Al magic angle spinning (MAS) nuclear magnetic resonance (NMR) spectroscopy to follow Al siting as a function of the exposure to liquid water. The combination[13] of techniques allows to speciate the location and concentration of Al in the HBEA lattice. This approach has been successfully used here, augmented with STEM, to show that HBEA is degraded in water *via* a three–step mechanism: 1) hydrolysis of T–O bonds along polymorph stacking faults and intergrain boundaries in a mode similar to crack propagation in glass, 2) amorphization by hydrolysis of surface Si–OH groups propagating inward through the zeolite lattice, and 3) crack propagation within the crystalline micro–domains along paths through specific T–O–T groups. Features in the mechanism should be common to other types of zeolites.

4.2 Experimental methods

4.2.1 Sample preparation

HBEA150 (Si/Al = 75) and HBEA25 (Si/Al = 12) were received from Süd Chemie AG (Clariant) in H–form. An example of typical sample preparation *via* hot liquid water treatment: 1 g zeolite and 80 mL deionized water are sealed in a 300 mL Hastelloy PARR autoclave reactor and heated for 48 h at 160 and 300 °C while stirred at 600 rpm. The reactor is cooled using ice and the samples are centrifuged and dried in vacuum for 24 h prior to storing. Full zeolite pore hydration at ambient conditions is performed prior to analysis. The BET surface area was determined using N_2 on a Micromeritics ASAP 2020. The total concentration of acid sites was determined using Temperature–programmed desorption (TPD) of ammonia. The catalysts were activated in vacuum at 450 °C for 1 h at a heating rate of 10 °C min^{-1} from ambient temperature to 450 °C. Ammonia was adsorbed and equilibrated (1 mbar, 100 °C) for 1 h. Subsequently, the sample was outgassed for 2 h to remove physisorbed molecules. The sample was then heated at a rate of 10 °C min^{-1} from 100 to 800 °C. The desorbing species were detected by mass spectrometry (Pfeiffer Prisma QME 200). For calibration of the method, a standard (Zeolite HZSM–5 with Si/Al = 45, acid site concentration = 360 μmol g^{-1}) was used. $AlCl_3$ (99.99%

anhydrous) was obtained from Sigma Aldrich and used without further processing. The list of samples and respective treatments and characterization results are shown in Table 1.

Table 1. Studied HBEA zeolite samples with the corresponding BET and TPD characterization data.

Zeolite	Si/Al ratio*	Pore volume [cm^3/g]	Mesopores [cm^3/g]	Micropores [cm^3/g]	Acid site concentration [µmol/g]
HBEA150 untreated	75	0.48	0.29	0.18	142
HBEA150 160 °C H_2O 3 h	74	0.48	0.34	0.14	137
HBEA150 160 °C H_2O 48 h	66	0.46	0.38	0.08	148
HBEA150 300 °C H_2O 48 h	65	0.18	0.15	0.03	22
HBEA25 untreated	12	0.51	0.38	0.13	456
HBEA25 160 °C H_2O 48 h	11	0.56	0.48	0.08	478
HBEA25 300 °C H_2O 48 h	11	0.16	0.13	0.03	102

* Si/Al ratios are determined from element analysis

4.2.2 Al K–edge XAFS

The Al K–edge XAFS experimental as well as analysis methods including DFT and MD calculations are reported in sections 3.2.2, 3.2.4 and 3.2.5.

4.2.3 ^{27}Al MAS NMR

The ^{27}Al MAS NMR experimental as well as analysis methods including DFT calculations are reported in sections 3.2.3 and 3.2.7.

4.2.4 X–ray diffraction (XRD)

XRD patterns were collected on a Rigaku Mini Flex II bench top X–ray diffractometer using a Cu–Kα radiation of 0.154056 nm (30 kV and 15 mA). Experiments were performed on a rotating powder sample holder in a 2θ range of 5º to 60º with a step size of 0.02 °/s. All measurements were performed under ambient conditions.

4.2.5 ^{29}Si MAS NMR

The single pulse (SP) and cross–polarization (CP) ^{29}Si MAS NMR experiments were performed using a Varian Inova 89–mm wide–bore 300 MHz NMR spectrometer and a 5 mm HXY MAS Chemagnetics style probe. The following parameters for the cross–polarization pulse sequence were used: the H90 was set to 3.5 μsec, the contact time was 1 ms and the decoupling field of 62.5 KHz was applied for 10 ms during the acquisition time. The spinning speed was set to 5 KHz. The ^{29}Si DFT NMR calculations were performed following the procedure described section 3.2.7. using the all–siliceous BEA crystal structure.

4.2.6 Helium ion microscopy (HIM)

HIM images were obtained using 35 keV He ions with 0.1 pA beam current at normal incidence. Secondary electrons were detected using an Everhart–Thornley detector. For HIM imaging, a very thin layer of carbon (<1 nm) was coated using a carbon sputter deposition system as the samples were completely insulating. The instrument resolution was 0.35 nm.

4.2.7 Scanning transmission electron microscopy (STEM)

The high–resolution STEM images were acquired on an aberration–corrected 300 kV FEI Titan microscope at the Environmental Molecular Sciences Laboratory (EMSL) at the Pacific Northwest National Laboratory (PNNL). The zeolite samples were infiltrated in the LR White acrylic resin (Electron Microscopy Sciences, Hatfield, PA), and polymerized at 60 ºC for 24 h. The embedded material was sectioned to a 50 nm thickness on Leica ultramicrotome (Ultracut E) using a Diatome diamond knife. The material sections were placed on holey carbon Cu grids for STEM imaging.

4.3 Results and discussion

4.3.1 Zeolite beta structure

Zeolite H–Beta (HBEA) has a three–dimensional network containing 4–, 5–, 6– and 12–member rings.[14] The primary channels accessible to polyatomic molecules are 6−7 Å in diameter defined by the 12–member rings. The zeolite structure is composed of an intergrowth of polymorphs A, B and C. The studied HBEA consists of two of these polymorphs, A and B, as determined by XRD.[15,16] Both polymorphs are constructed from the same centrosymmetric

tertiary building units arranged in layers.[14] While the polymorph intergrowth does not significantly affect the pores in [100] and [010] directions, pores in the [001] axis are slightly tortuous due to faults caused by one–dimensional stacking disorders of the periodic building units. The HBEA unit cell contains nine crystallographically different T–sites, which may be populated by Al.

4.3.2 Structural changes in water

The impact of exposing the zeolite to liquid water at 160° and 300 °C was explored for two samples, varying in the concentration of Al in the lattice (HBEA150 and HBEA25). The impact of water was explored macroscopically using X–ray diffraction (XRD) to characterize the material crystallinity at coherent length scales greater than ~ 5 nm; Helium ion microscopy (HIM) probed the macroscopic structure while scanning transmission electron microscopy (STEM) was used to probe the internal particle structure. BET analysis provided qualitative information about the pore size distribution spanning the range from ~ 0.5 to ~ 50 nm. Finally, the local molecular structure around the Al and Si atoms was probed using the combination of EXAFS and NMR techniques.

4.3.3 Macroscopic Structure from Helium Ion Microscopy (HIM)

The images in Figure 1a and 1b portray the initial state of HBEA150 and HBEA25. The average particle sizes for the features are approximately 220 – 250 nm and 50 – 75 nm for HBEA150 and HBEA25, respectively. In general, the smaller particle size of the HBEA25 would make it more prone to processes related to Ostwald ripening[17] and sintering[18] minimizing the free surface energy.

Figure 2 presents higher resolution HIM images of the HBEA150 structure. Figure 2a shows that an individual particle consists of stacked layers or terraces of much smaller crystallites. The individual terrace heights are smaller than 10 nm. The shape of the particles suggests that during formation the in–plane growth rate is faster than the perpendicular growth rate.[19] New crystallites nucleate at and grow from the top layer of the stack. The lattice structure of these nucleated crystallites can be oriented either coherently or incoherently with respect to the base layers.[20] Incoherent placement leads to lattice mismatch; wherein the localized defect sites form an array

of mesopores due to the intersection of partially formed pores having Si–OH termination (or "silanol nests").

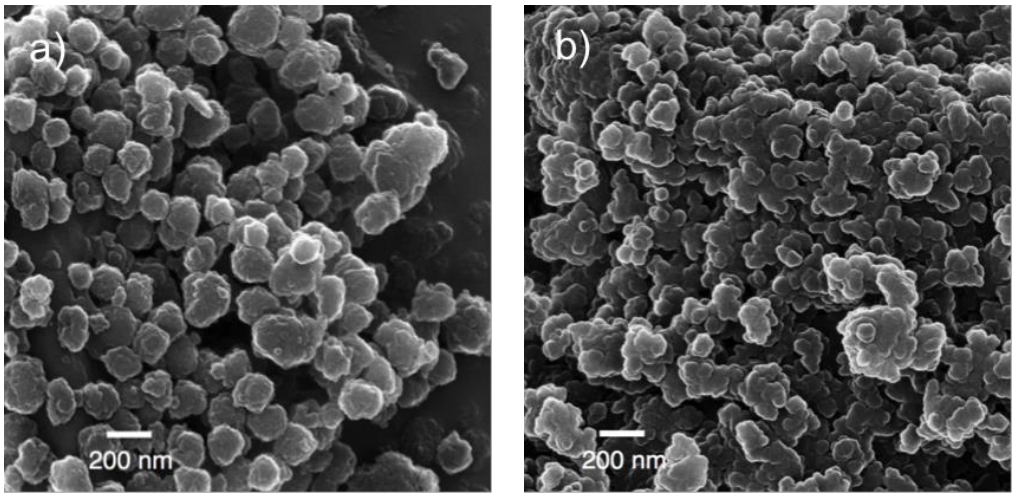

Figure 1. HIM images of the (a) HBEA150 and (b) HBEA25 untreated zeolites samples.

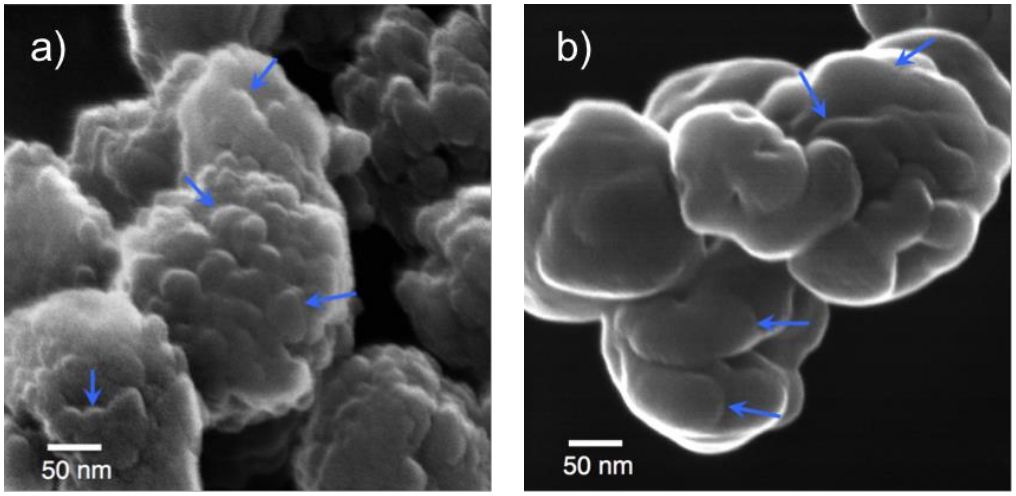

Figure 2. HIM images for the a) undertreated HBEA150 and b) HBEA150 treated in water for 48 h at 300 ºC are shown. The arrows indicate regions of overlapping terraces that are an inherent part of the HBEA starting structure. In b), the particles have no crystallinity as measured by XRD.

Figure 2b shows an image of the HBEA150 after hydrothermal treatment at 300 °C for 48 h. Features smaller than 20 nm have been eliminated from the surfaces of the particles. Since the loss in mass was marginal, the process leading to the loss of these features is thought to follow an Ostwald ripening–like mechanism.[17] The macroscopic features of the original zeolite structure are retained even though the crystallinity (see XRD data) was macroscopically destroyed after treatment. In other words, the macroscopic features of original terraces have been retained even when the initial zeolite crystallinity (XRD) no longer existed after treatment in water. Small crystalline domains were, however, retained (STEM results).

4.3.4 XRD analysis of crystallinity

XRD measurements for both HBEA150 and HBEA25 parent and treated samples are shown in Figures 3a and 3b, respectively. The observed reflections are consistent with the known structure of zeolite H–beta. For HBEA150, the diffraction peaks persist upon water treatment at 160 °C for 48 h, but disappear upon treatment at 300 °C for 48 h. The overall reduction in the XRD peak amplitudes is associated with several factors including (a) formation of a separate amorphous phase, (b) the reduction in the crystalline domain size below the Scherrer broadening limit and (c) lattice distortions (shown in STEM, Figure 5). While the HBEA150 and lattice was stable up to 48 h at 160 °C in liquid water (Figure 4a), significant degradation of the HBEA25 was observed under these conditions (Figure 4b). After treatment at 300 ºC the XRD crystallinity of HBEA150 and HBEA25 was lost. If crystal structure and mutual alignment of the micro–domains remained unaffected by the exposure to water, the disappearance of peaks in the XRD would imply that crystalline domains must be smaller than ~ 5 nm. As shown and discussed in the STEM section below, because crystalline micro–domains larger than 5 nm were observed (HBEA150 treated in water at 300 ºC for 48 h, STEM Figure 5c), the absence of XRD diffraction peaks is concluded to be caused by lattice distortions and subtle changes in orientations of micro–domains.

In the case of HBEA25 at 300 °C, an additional mechanism was observed by the appearance of a new set of diffraction peaks (Figure 4b, 300 ºC 48 h H_2O sample). The higher Al content of HBEA25 induced (Figure 4b) presumably the formation of halloysite [21] or a related aluminosilicate clay material.[22] The measured Al–O bond distance (as discussed in the EXAFS section below) is, however, somewhat shorter than expected for clays.[23] The formation of the

new phase is consistent with the appearance of dihedrally oriented plate–like particles in the HIM images (see Appendix) of HBEA25 treated at 300 °C.

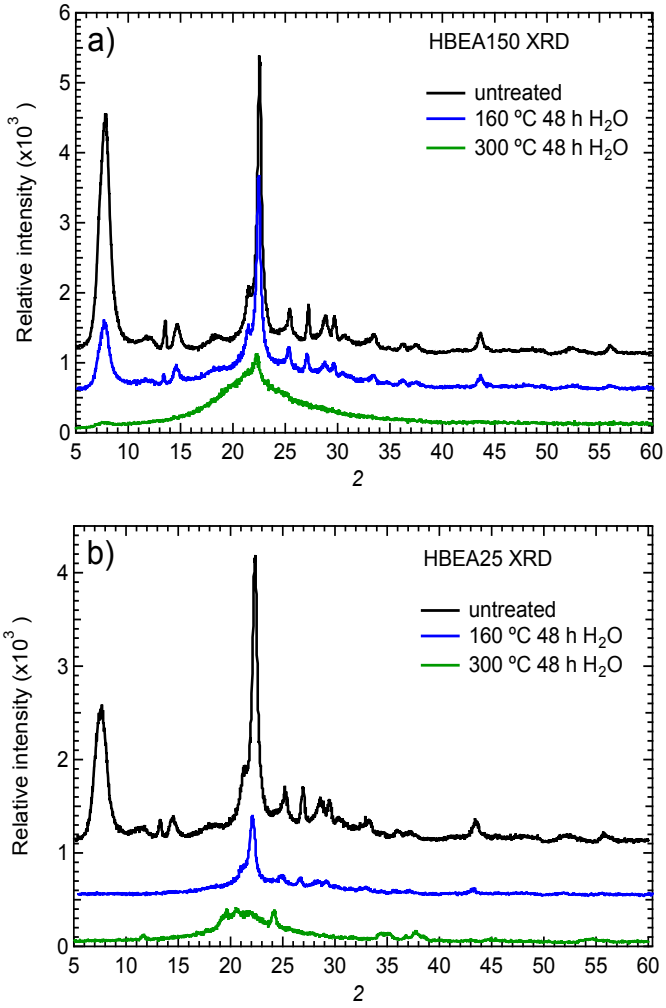

Figure 3. XRD patterns collected for a) HBEA150 and b) HBEA25. The untreated (black), 160 ºC 48 h water treated (blue) and 300 ºC 48 h water treated (green) samples are shown.

As shown in Figure 3 and expanded in Figure 4, the XRD peak at $2\Theta = 7.7$ was most affected by the hot liquid water. The intensity of the reflection decreased already after 3 h at 160 °C and was observed at ~ 25 % intensity compared to the parent zeolite after 48 h 160 °C. Because the studied HBEA samples consisted of approximately 50/50 mixture of polymorph A and B, the

origin of the features in the powder diffraction pattern must be discussed in more detail. For BEA (polymorph A) the $2\Theta = 7.7$ reflection results predominantly from the [010] plane. The reduction in reflection intensity indicates modifications occurring in the [010] plane of BEA, i.e., at T3 & T7 and T4 & T8 bridges selectively prior to the more general 12–member ring pore collapse (see Appendix).

For BEB (polymorph B) the $2\Theta = 7.7$ reflection results from both the [110] and the [11–1] planes. Both planes bisect the same T–site pairs in case of polymorph A and polymorph B. The full list of reflections for BEA and BEB polymorphs are shown in the Appendix.

We suggest that if framework decomposition along other planes of the unit cell were occurring in the initial phase of the hydrolysis, the intensity of either of the two XRD peaks would have changed with respect to the untreated sample, because the fraction of coherent structure due to polymorph A and to polymorph B would change in that case.

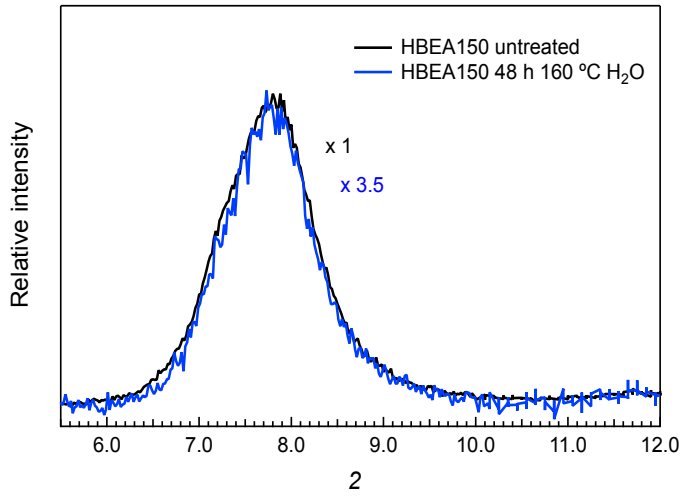

Figure 4. XRD pattern in the region of $2\Theta = 7.7°$ for the parent (black) and 48 h 160 ºC water treated (blue) HBEA150 is shown. The XRD feature intensities are scaled to the parent sample. The scaling factor is shown on the plot and is color–coded to match the samples.

In Figure 4, the XRD pattern ($2\Theta = 5 – 12°$) for the starting HBEA150 is compared to the sample treated for 48 h at 160 °C. The XRD pattern of the treated and the fresh sample are presented at the same intensities. The shapes of the peaks are identical, including the shoulder at

~ 2Θ = 7.2° which is directly related to the ratio of BEA and BEB. Therefore, water treatment is concluded not alter the ratio of the polymorphs.

4.3.5 Nanoscale Structure from STEM

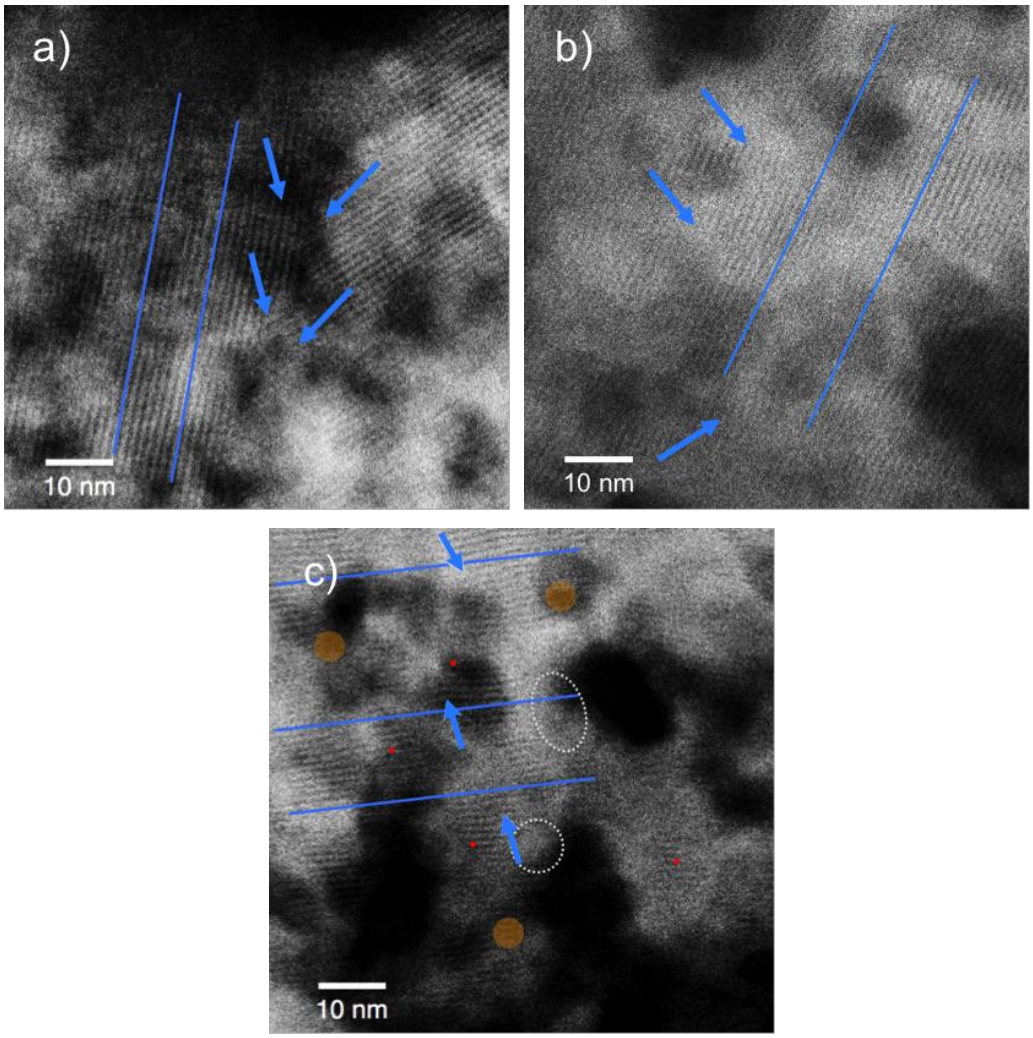

Figure 5. STEM images for a) HBEA150 treated in water for 3 h at 160 ºC, b) HBEA150 treated in water for 48 h at 160 ºC and c) HBEA150 treated in water for 48 h at 300 ºC are shown. In b) and c) arrows indicate regions where original large crystal lattice has been distorted by formation of nearby amorphous domains. White dashed circles indicate possible amorphous regions. For reference, in c) the red circles show the maximum size domain for sensitivity of the Al EXAFS measurements, the orange circles show the minimum domain size detected by XRD.

Figure 5 shows STEM images of three specimens of water treated HBEA150, after treatment at 160 °C for 3 h, after treatment at 160 ºC for 48 h and after treatment at 300 °C for 48 h. Since the samples were prepared by microtome cutting (Experimental section), the images show cross sections of zeolite particles rather than external surfaces. An image of the sample treated for 3 h at 160 °C is shown in Figure 5a, which indicates that this sample is almost unchanged from the parent HBEA150 (not shown). The image in Figure 5a shows intersecting crystallites having uniform and extended structure (shown with arrows). While the zeolite structure remains largely intact and is formed from large crystalline domains after the treatment at 160 ºC for 48 h, minor distortions of the crystal structure occurred. These distortions are observed as slight bending of the diffraction fringes in several positions as shown with arrows in Figure 5b. The sample treated at 300 °C for 48 h (Figure 5c) had undergone substantial structural changes. It appears that what was originally one large crystallite has been reduced to 10 or more individual micro–domains that remain roughly aligned to the original lattice. The large crystal domains of the starting material have been reduced to regions of approximately 10 – 20 nm in part due to the formation of inclusions of small amorphous domains. As shown by the arrows in Figure 5c, the lattice lines are substantially in distorted. The breakup of the crystallites size and the lattice distortions on this scale would marginalize the longer–range coherence characteristic of the original and the 3-h 160 ºC treated specimens and necessary for the XRD reflections. Thus, the STEM shows residual crystallinity despite the lack of long distance order.

4.3.6 Micropore and mesopore distribution

The micropore and mesopore surface area of the HBEA150 and HBEA25 parent and treated samples as a function of pore size is shown in Figures 6a and 6b. Pore sizes in the range from 0.4 to 20 nm are most important, because this region encompasses the most prominent variations in pore volumes. For a complete analysis see appendix. For water treated HBEA150 3 h and 48 h 160 ºC samples the specific surface area increased for mesopores above 5 nm diameter, predominantly at the expense of the micropores that have a diameter of ~ 0.8 nm (Figure 6).

While some of the water-treated samples do not show microporosity, the STEM images show the presence of significant domains of crystallinity that should have retained the microporous structure. Because hot liquid water exposure led to a substantial decrease in the BET surface area (Figure 6), which is most significant for the 48 h 300 °C water treated samples, we conclude that

the crystalline domains must be sealed either by an amorphous capping layer (likely SiO_2) on the particle exterior or by localized pore blockage.

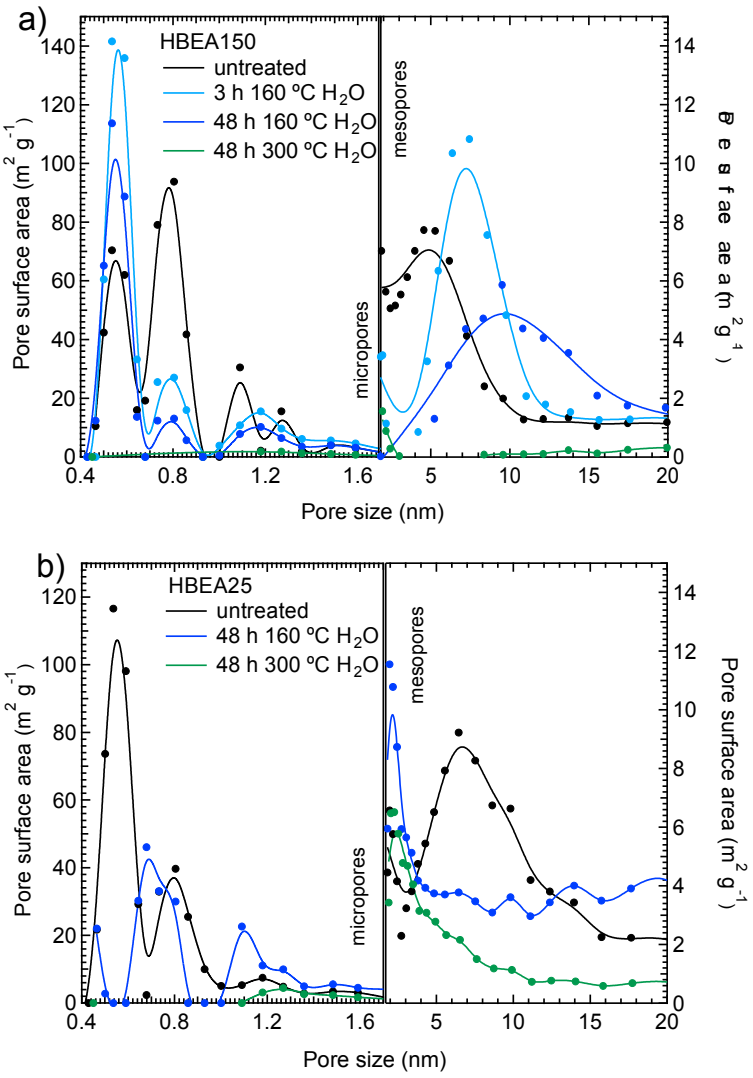

Figure 6. Relative pore size distributions for micropores (0.4 – 1.7 nm) and mesopores (1.7 – 20 nm) of a) HBEA150 and b) HBEA25. The untreated zeolite is shown in black, the 48 h 160 ºC water treated sample in blue and the 48 h 300 ºC sample is shown in green. The 3 h 160 ºC water treated HBEA150 is shown in a) in light blue. A spline if fitted through the data points for better visualization.

The acid site concentration of the 48 h 160 ºC water treated samples was very similar to that of the parent material suggesting that neither the Si/Al ratio nor the Al T–site geometry was significantly changed during water treatment. However, the acidity was nearly completely lost for the 48 h 300 ºC water treated samples due to complete framework degradation and the formation of a new Al–oxide phase.

4.3.7 Al T–site structure from Al EXAFS analysis

The Al EXAFS Img[$\tilde{\chi}(R)$] plots for HBEA150 and HBEA25 samples are shown in Figures 7a and 7b, respectively. The detailed principles of the HBEA Al–distribution analysis are reported in Chapter 3. Briefly, the nine different T–sites of HBEA are grouped in sets based on T–site similarity from an EXAFS point of view. T1–, T2–, T5–, and T6–sites are referred to as Set A, T3– and T4– as Set B and T7–, T8– and T9– as Set C in the analysis below. Note that unlike for Set A and Set B, T–sites in Set C never occupy four–member rings in the HBEA framework. MD EXAFS spectra are then calculated for a representative T–site of each Set and are used to fit experimental data. Fractions of Al that populates each set of T–sites are reported for all samples in Table 2. Al distribution analysis accuracy is ±10 % of total Al in HBEA.

The Al EXAFS showed that HBEA150 and HBEA25 have distinctly different Al T–site distributions. In HBEA150, the best EXAFS fit suggests that 70 % of T–sites are populated by Set A sites and 30 % of T–sites by Set B sites. In contrast, in HBEA25 the sites are nearly equally populated by Sets A and C representing approximately 40 % of total Al content each. Note that there are no Set C T–sites present in HBEA150 and no Set B T–sites in HBEA25. The octahedral Al content is determined at 9 % and 21 % for HBEA150 and HBEA25, respectively.

EXAFS indicates that hot liquid water treatment leads to almost no modification (within analysis accuracy) of the zeolite Al T–site geometry. The Set A T–site concentration was mostly unchanged for the HBEA150 sample treated at 160 °C for 48 h indicating that the local Al structure remained largely intact after partial loss of long–range order. Even after treatment at 300 ºC for 48 h, the Al geometry still resembles that of the untreated HBEA150, the first shell Al–O bond is elongated by only 0.02 Å and the Al–Si distance by 0.04 Å. These small changes are tentatively attributed to a combination of two factors: 1) the long–range structural changes in the zeolite framework induced by hydrolysis of T–O–T groups remote to Al as well as 2) a minor increase in octahedral Al concentration in the sample (Table 2).

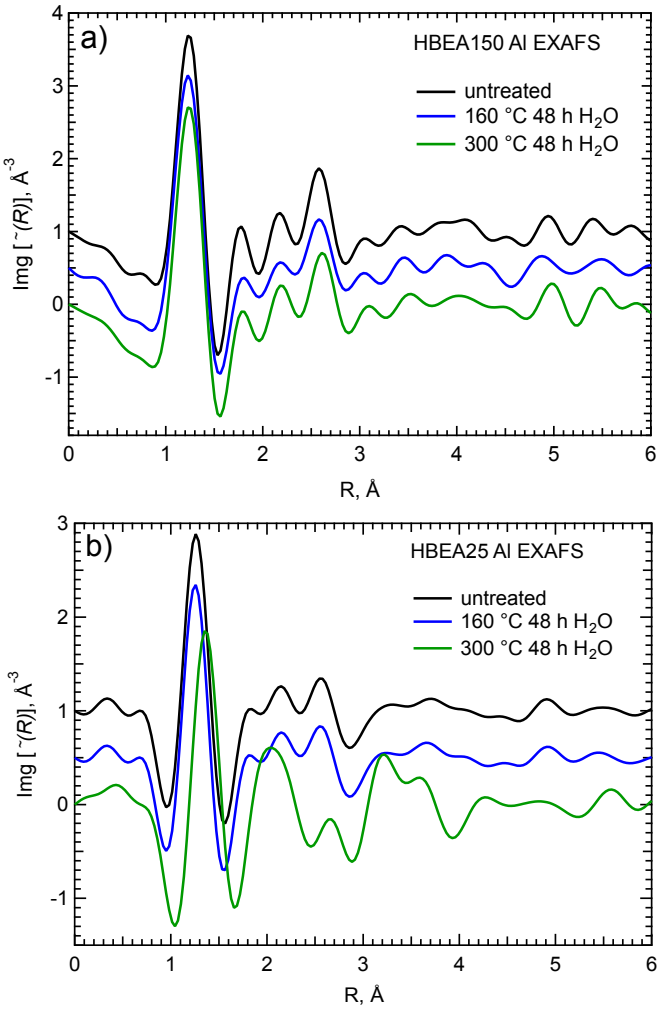

Figure 7. The EXAFS $\mathbf{Img}[\tilde{\chi}(\boldsymbol{R})]$ spectra for a) HBEA150 and b) HBEA25 are shown. The untreated (black), the 160 ºC 48 h water treated (blue) and 300 ºC 48 h water treated (green) samples are shown. Note that with the exception of HBEA25 300 ºC 48 h water treated sample there is almost no modification of the tetrahedral Al T–site structure for the HBEA samples.

The 48 h 160 ºC water treated HBEA25 zeolite sample demonstrates a moderate intensity change in the EXAFS spectrum at longer distances from the Al atom, when compared to the untreated material. An apparent slight increase in concentration of Set A T–sites is noted. This transformation occurs at the expense of the Set C T–sites (decrease by 11%). Because octahedral Al did not increase in concentration and the total Al– concentration was identical to that of the

parent zeolite, the minor changes in T–site distribution are attributed to the changes in the Si–O backbone of the zeolite framework. Since the Al–O and Al–Si atom distances for different Al T–sites are affected by the local Al environment, the linear combination fitting of the experimental EXAFS treats these modifications as an apparent increase or decrease of an Al T–site set concentration.

Unlike in the case of HBEA150, the EXAFS spectrum of the 300 ºC 48 h water treated HBEA25 sample shows a significant phase shift (see Figure 7b) translating to the first shell Al–O bond distance being elongated by 0.1 Å indicating octahedral Al coordination. The formation of octahedral Al occurred at the expense of both Set A and Set C Al T–sites. The Img$[\tilde{\chi}(R)]$ of the 48 h 300 ºC water treated HBEA25 strongly suggests that the Al T–sites undergo irreversible structural changes, which are attributed to zeolite framework degradation. MD EXAFS fitting results for both HBEA150 and HBEA25 as well as ^{27}Al MAS NMR results (discussed below) are summarized in Table 2.

The EXAFS results suggest that the Al T–site geometry remains largely unchanged after water treatment. The Al coordination sphere of the treated samples (Figure 7) is nearly identical to that of the parent zeolite out to the limit of EXAFS sensitivity, ~ 6 Å, (with the exception of 300 ºC 48 h water treated HBEA25). Thus, we conclude that framework domains around the Al T–sites out to a sphere of at least 12 Å in diameter are largely unaffected during T–O–T hydrolysis in water and Al is not selectively removed from the framework.

4.3.8 Al T–site environment from ^{27}Al MAS NMR

^{27}Al MAS NMR spectra for the untreated and water treated samples of HBEA150 and HBEA25 are shown in Figures 8a and 8b, respectively. Both parent zeolites show two main peaks at ~ 54 and ~ 57 ppm, which, however, exhibit different relative intensity. The HBEA150 peaks have different relative intensities of 7:3, respectively. The two peaks in HBEA25 have nearly equal intensities. The peaks observed at ~ 0 ppm are typical of extra–framework octahedral Al.[24] The fractions of tetrahedral (contributions from two peaks grouped similar to the EXAFS T–site Sets) and octahedral Al determined from NMR are reported in Table 2.

While in the case of the 48 h 160 ºC water treated HBEA25 sample the fractions of tetrahedral Al were determined to be almost identical to the parent zeolite, the NMR suggests an approximately 10 % increase of the octahedral Al concentration in the 48 h 160 ºC water treated

HBEA150. The relative intensities of the peaks attributable to tetrahedral Al were also changed: in the HBEA150, the relative intensity of the peak at ~ 54 ppm decreased and the peak at ~ 57 ppm increased. Similar changes occurred in HBEA25 treated sample (relative intensity of ~ 54–ppm peak decreased and the ~ 57–ppm peak increased), but to a lesser degree.

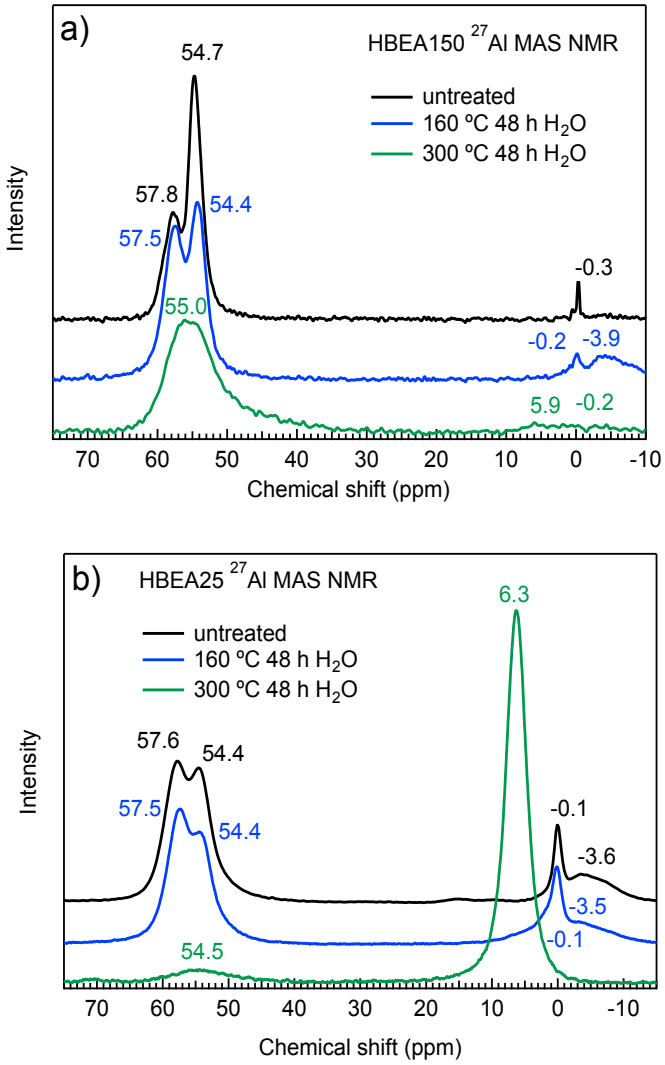

Figure 8. The ^{27}Al MAS NMR spectra for a) HBEA150 and b) HBEA25 samples are shown. The untreated (black), the 160 ºC 48 h water treated (blue) and the 300 ºC 48 h water treated (green) samples are shown. The tetrahedral Al coordination is largely retained in all cases except for the HBEA25 300 ºC 48 h sample, in which nearly all Al is present in octahedral coordination. Note: the signal intensity in MAS NMR is normalized to sample weight.

Table 2. The distribution of tetrahedral (T–sites) and octahedral Al determined for the parent and water treated HBEA150 and HBEA25 samples. The Al T–site distributions are reported as sets: Set A (T1, T2, T5&T6), Set B (T3, T4) and Set C (T7, T8, T9).

Sample	Al EXAFS [a]				^{27}Al NMR [a]			
	Tetrahedral Al			Octahedral Al^{3+}	Tetrahedral Al			Octahedral Al^{3+}
	Set A	Set B	Set C		Set A	Set B	Set C	
HBEA150 untreated	0.72	0.19 [b]	0	0.09	T1 (0.53), T2 (0.20), T5&T6 (0)	T3 (0), T4 (0)	T7 (0.13), T8 (0), T9 (0.10)	0.04
HBEA150 160 °C H_2O 48 h	0.82	0	0.08	0.10	T1 (0.27), T2 (0.29), T5&T6 (0)	T3 (0), T4 (0)	T7 (0.18), T8 (0), T9 (0.10)	0.16
HBEA150 300 °C H_2O 48 h	0.73	0	0.14	0.13	(0.92) [b]			0.08
HBEA25 untreated	0.41	0	0.38	0.21	T1 (0.10), T2 (0.31), T5&T6 (0)	T3 (0), T4 (0)	T7 (0.26), T8 (0), T9 (0.10)	0.23
HBEA25 160 °C H_2O 48 h	0.54	0	0.26	0.20	T1 (0.06), T2 (0.41), T5&T6 (0)	T3 (0), T4 (0)	T7 (0.27), T8 (0), T9 (0.02)	0.24
HBEA25 300 °C H_2O 48 h	0.15 [c]			0.85	(0.09) [c]			0.91

[a] The estimated errors are ±10 % by EXAFS and ±10 % by NMR.
[b] Fit accuracy does not exclude population of set C sites instead of set B.
[c] The distribution of tetrahedral Al T–sites could not be unambiguously deconvoluted.

While these changes might be taken to indicate transformation of the T–sites, an alternative explanation would be that a fraction of the T–sites, which give rise to the ~ 54–ppm peak, are selectively transformed into octahedral Al. Because the water treatment leads to a decrease in Si/Al ratio in the sample, the increased Al concentration results in an apparent increase of intensity for the 57–ppm peak.

In the first interpretation, the Al T–sites would have undergone a rearrangement with the neighboring Si T–sites, breaking and then reforming several Si–O and Al–O bonds to switch with a Si atom moving from a T–site in a 4–member (Set A) ring to a T–site in a 6–member ring (Set C). Such a transformation seems improbable and is also contradicted by the EXAFS analysis suggesting that the water treatment at 160 °C increased the fraction of Set A sites and decreased the fraction of Set C (or Set B due to analysis accuracy limitations) sites.

In the second interpretation, the observed change in NMR peak intensity for the 48 h 160 ºC water treated samples is attributed to modification of Al coordination for a fraction of Al T–sites caused by Al–O–Si hydrolysis. Note that the Si/Al ratios for both HBEA150 and HBEA25

decrease after aging in water. The framework degradation explains the ~ 10 % increase of the octahedral Al signal in the 48 h 160 ºC water treated HBEA150. Because of the higher initial Al concentration in HBEA25 this effect is less obvious for the water treated HBEA25 sample. The slight increase in octahedral Al concentration also explains the differences observed between the Al EXAFS spectra of the parent and treated zeolites (both HBEA150 and HBEA25). Note that the EXAFS analysis is affected by subtle structural changes induced by the T–O–T group hydrolysis in the vicinity of the Al T–sites. Although the short–range geometry around the Al atom is largely retained, the NMR chemical shift is sensitive to nonlocal structural details extending into the higher shells of the Al T–site.[25] Unlike in the case of Al rearrangement, the hydrolysis of the Si–O–Si and Al–O–Si must also lead to an increase in Si–OH concentration in the framework, which is observed in the cross–polarization ^{29}Si NMR, Figure 10.

In the case of the 48 h 300 ºC water treated HBEA150 sample only the distribution of tetrahedral– and octahedral–coordinated Al were determined because attempts to deconvolute the broadened peaks gave ambiguous results. The formation of a new Al phase is indicated by a signal at ~ 45 ppm, which is attributed to extra–framework tetrahedral Al^{3+}.[26] The observations lead us to conclude that the zeolite framework experiences significant damage prior to the removal (and change in coordination) of a significant amount of the framework tetrahedral Al atoms. A substantial transition of tetrahedral Al to 6–coordination suggesting irreversible lattice degradation was observed only in the case of the 300 ºC 48 h water treated HBEA25 sample, but not the HBEA150 sample, suggesting that stability in water is inversely correlated with Al concentration.

4.3.9 Si T–site environment from ^{29}Si MAS NMR

Let us now turn to the ^{29}Si MAS NMR. The ^{29}Si NMR spectra for HBEA150 and HBEA25 samples are shown in Figures 9a and 9b, respectively. At least four peaks are attributed to tetrahedral Si in different environments.[27,28] Signal intensity at –98 ppm, which is typically assigned to Q^2 Si corresponding to Si atoms located between Al–pairs in an Al–O–Si–O–Al pattern,[29] account for 0.6 % and 2.4 % of total Si intensity for HBEA 150 and HBEA25, respectively. Therefore Al–pairs, if present, are not considered affecting the quantitative analysis.

The peak intensity in the region from –108 to –115 ppm is assigned to $Si(OSi)_4$ species,[30] the peak at –103 ppm is assigned to the $Si(OSi)_3OAl$ species.[31] Note that a slight decrease in Si Q^4

and an increase in Si Q^3 signal intensity are observed. As the EXAFS results suggest that the Al T–site geometry remains largely unaltered, we suggest the increase in SP ^{29}Si NMR signal intensity between –101 and –107 ppm is attributed to the formation of Si–OH defects.[32] The peak at ~ –90 ppm in the HBEA25 sample treated for 48 h at 300 °C is attributed to the $Si(OAl)_3OSi$,[33] which is formed after substantial framework degradation.

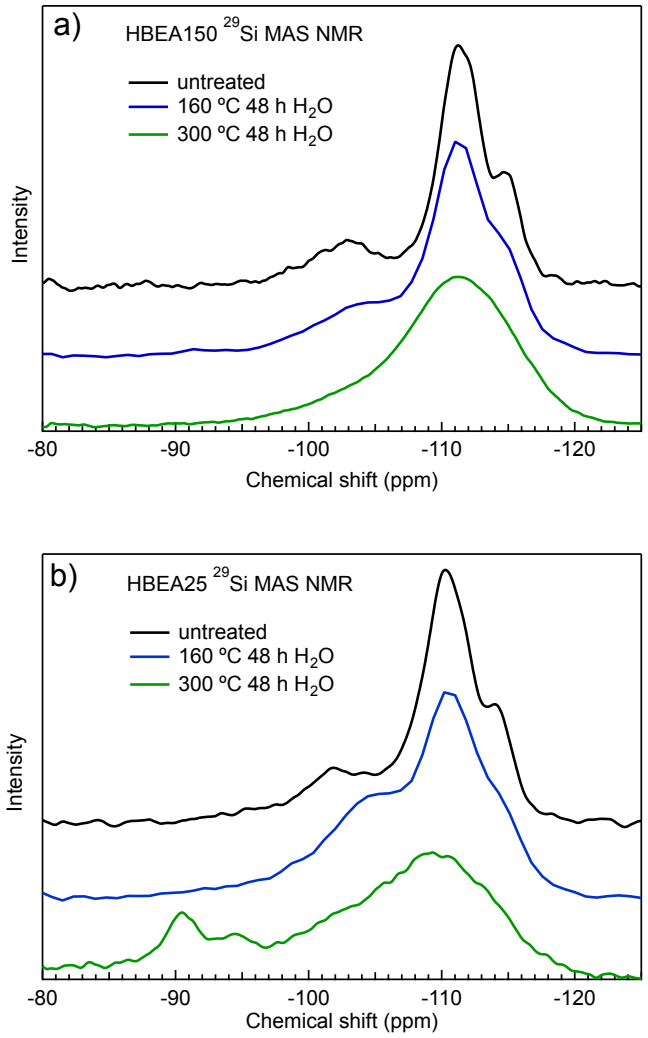

Figure 9. The ^{29}Si MAS NMR spectra for a) HBEA150 and b) HBEA25 samples are shown. The untreated (black), the 160 ºC 48 h water treated (blue) and the 300 ºC 48 h water treated (green) samples are shown. Line broadening indicates the changes occurring in the Si–environment. Note: the signal intensity in MAS NMR is normalized to sample weight.

4.3.10 Selective bond cleavage and Si–OH group formation determined from single pulse and cross–polarization ^{29}Si MAS NMR

Since the HBEA150 samples have demonstrated relatively high stability during water treatment, this zeolite is chosen for the in–depth mechanistic study of the initial steps of zeolite degradation in aqueous medium. Using quantitative single pulse (SP) NMR, the concentrations of Si with different coordination (i.e., Si Q^4 ($Si(OSi)_4$) and Si Q^3 ($Si(OSi)_3OAl$))[31] were evaluated. The SP ^{29}Si NMR spectra of the parent and 48 h 160 ºC water treated HBEA150 are shown in Figure 10a.

Table 3. The calculated ^{29}Si DFT NMR chemical shift values for the 9 Si T–sites of BEA. The average first Si shell Si–Si atom distances and the average Si–O–Si angles are also shown.

Si T–site	Chemical shift (ppm)*	Average Si–Si distance (Å)	Average Si–O–Si angle (º)
1	–113.04	3.11	151.23
2	–113.37	3.11	151.75
3	–109.71	3.08	147.08
4	–109.92	3.09	147.33
5	–115.30	3.13	153.46
6	–113.94	3.12	152.11
7	–113.07	3.11	149.90
8	–112.79	3.11	149.55
9	–112.55	3.11	149.47

* Isotropic chemical shifts are referenced to TMS.

The Si Q^4 ^{29}Si DFT NMR chemical shift values were calculated for the nine Si T–sites of HBEA (Table 3 and shown as vertical lines in Figure 10a). All T–sites contribute to one relatively broad peak with a maximum at –111.5 ppm. The T3– and T4–sites are calculated to both have a chemical shift of –109 ppm. The T5–sites are assigned to the distinct signal (shoulder) at –115 ppm. All other T–sites have chemical shift values approximately at –113 ppm. After water treatment the broad peak at –111.5 ppm slightly decreased. Assuming that T atoms with the Si Q^4 SP NMR chemical shift closest to this main peak contribute most to the intensity decrease, we speculate that primarily T1, T2, T7, T8, and T9 were converted from Si Q^4 to Si Q^3 coordination. The intensity of the Si Q^4 signal of T3–, T4–, T5– and T6–sites hardly changed.

While intensity variations of T3 and T4 are difficult to analyze (possible compensation of a decrease in intensity due to the signal intensity increase in the Si Q^3 region) T5– and T6– sites appear to remain constant throughout the experiments.

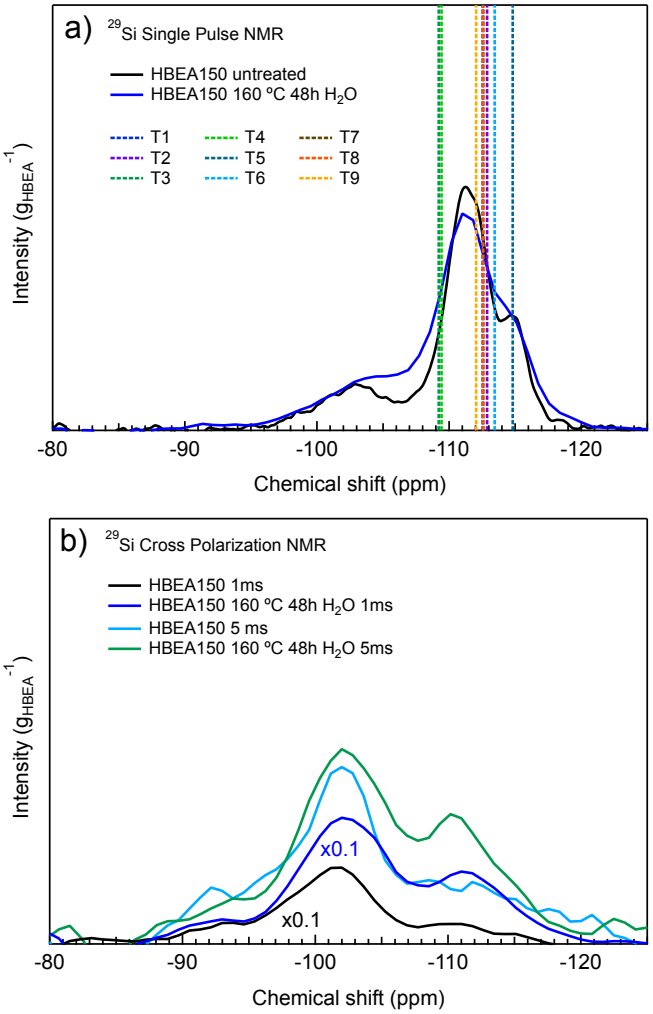

Figure 10. Measured ^{29}Si MAS NMR a) single pulse (SP) and b) cross–polarization (CP) spectra for untreated and 48 h 160 ºC water treated HBEA150 samples are shown. The intensity is normalized to sample weight. The CP spectra are acquired with two different (1.0 and 5.0 ms) contact times. The color–coding is reported in the legend. The CP NMR scaling is reported in the plot where applicable. The calculated Si Q^4 ^{29}Si DFT NMR shift values for the 9 T–sites of HBEA are shown in a) as vertical bars. Note, the chemical shift values for some of the T–sites are very similar and the bars in the plot overlap; the exact values are reported in Table 3.

Cross–polarization (CP) ^{29}Si NMR was used to qualitatively probe T atoms in proximity to H, i.e., Si–OH groups and bridging OH–groups, primarily up to a distance of approximately 3.3 Å.[34] The ^{29}Si CP NMR spectra measured at contact times of 1 and 5 ms are shown for the parent and 48 h 160 ºC water treated HBEA150 samples in Figure 10b. The preferential enhancement of signals from ^{29}Si atoms nearer to the protons (–OH) was obtained using the shorter (1 ms) contact time. The peaks from –110 to –114 ppm are characteristic for the Si Q^4 sites of the intact lattice. The large peak at –103 ppm is assigned to the Si(OAl)$(OSi)_3$ site.[31] The low intensity in this region is attributed to the low concentration of Al in HBEA150 (Table 1). The Si Q^3 [Si$(OSi)_3$OH] atoms are assigned the CP NMR signal at –106 ppm,[31] which increased in the 160 ºC 48 h water treated HBEA150 sample indicating the increased concentration of Si–OH groups within the lattice structure.[35] The chemical shift region between approximately –90 and –105 ppm is characteristic of neighboring Si–OH groups in geminal [Si$(OH)_2(OSi)_2$] and vicinal [$(OSi)_3$Si–OH HO–Si$(OSi)_3$] structure, respectively.[36] The absence of a strong signal at –90 ppm,[37,38] which is attributed to the Si Q^2 [Si$(OH)_2(OSi)_2$] excludes the presence of geminal Si–OH groups in both the parent and water treated samples. The shoulder in the CP NMR at –100 ppm is attributed to the formation of surface Si–OH groups.[39]

In Figure 10b (spectra acquired with 1 ms contact time), the intensity of Si Q^4 T3– and Si T4–sites increased after water treatment suggesting the presence of OH–groups at next nearest Si neighbors to the probed T–site. Similarly, increase of the intensity of the Si Q^4 T1–, T2–, T7–, T8– and T9– signal points to an increase in the concentrations of OH–groups at next nearest Si neighbors of these T–sites. The impact of cleaving individual Si–O–Si bonds *via* hydrolysis leads to either generation of Si Q^3 signal intensity or to increasing Si Q^4 intensity through the presence of Si–OH groups at next nearest T atoms, precluding further analysis of the intensity variations.

The ^{29}Si NMR spectra acquired at longer contact time (5 ms) demonstrate increased intensity in the Si Q^4 region, especially for the water treated sample. While the Q^4 Si atoms do not have OH–groups in the first coordination sphere, the longer contact time allows detection of H that are located further than ~ 3.3 Å from the Si atom,[40] e.g. in the second or higher shells of the NMR target Si atom.

The nine T–sites of HBEA are shown in Figure 11 on the example of polymorph A. The T–site connectivity (with respect to next nearest neighbors) is identical between polymorphs A and B. As shown in Figure 11, the T3– and T7–sites as well as T4– and T8–sites form T–O–T pairs

located in the 6–member rings connecting the large pores (and forming the wall of the 12–member ring pores of the perpendicular channel). The T5– and T6–sites connect the T3 & T7 and T4 & T8 T–O–T pairs and are also part of the 6–member rings of the HBEA framework. The hydrolysis of the T3–O–T7 pair would not lead to a change in the intensity of the Si Q^4 T5–site in the ^{29}Si SP NMR spectrum, which corresponds to experimental observation. Similarly, the ^{29}Si SP NMR intensity of the Si T6–site would remain unaltered, if the T4–O–T8 is cleaved and two Si–OH groups are formed. Note that T1, T2, T7, T8 and T9 decreased in intensity in the ^{29}Si SP MAS NMR spectrum suggesting possible cleavage at these sites. Thus, we conclude that the Si–O bond hydrolysis does not occur at the Si T5– and T6–sites.

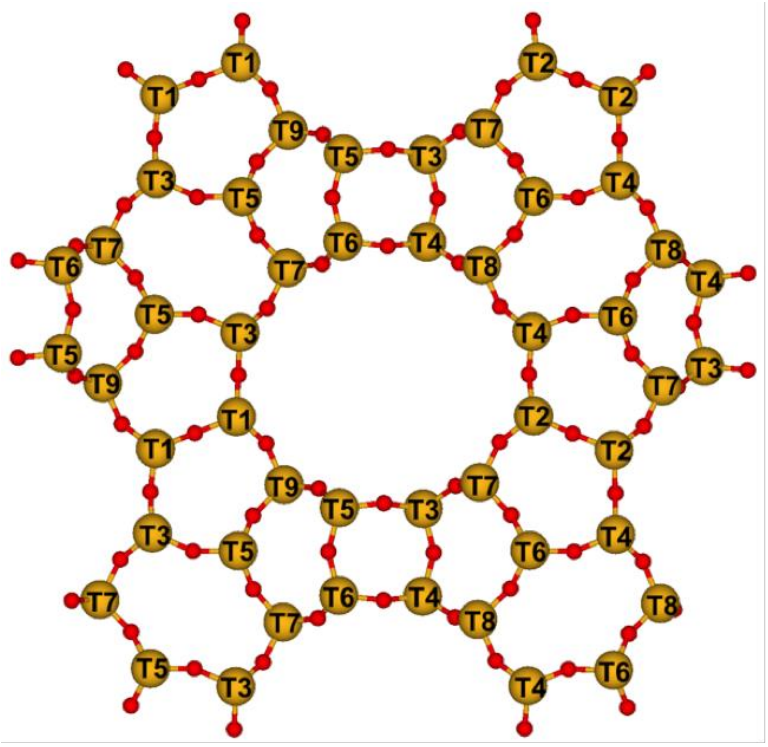

Figure 11. The 9 different T–sites of HBEA shown on the example of polymorph A. Si is shown in yellow and O is shown in red. Note that only a section of the unit cell is shown in the [010] projection for better visualization.

Figure 12 shows the H–beta polymorph intergrowth region of the all–siliceous BEA and BEB unit cells, which are schematically shown along the [010] plane for BEA and along the [110]

plane for BEB. Because XRD suggests that the crystal is cleaved along the [010] of polymorph A and [110] plane of polymorph B and ^{29}Si SP NMR suggests that the Si T5 and T6 are not affected by water, we conclude that hydrolysis breaks preferentially the T3–O–T7 and T4–O–T8 bridges.

The formation of crack–like cleavage patterns in the zeolite framework along specific polymorph planes results in a higher concentration of surface Si–OH groups. These have been suggested to be responsible for further strengthening interactions between the framework surface and adsorbate molecules.[35] The increasing concentration of Si–OH defect sites, thus, facilitates further T–O–T bond hydrolysis. The pK_W of water, 14.0 at RT, decreases to 11.6 at 150 °C and 11.3 at 200 °C respectively,[41] hence the increase in the concentration of ions in hot liquid water may further accelerates the hydrolysis.

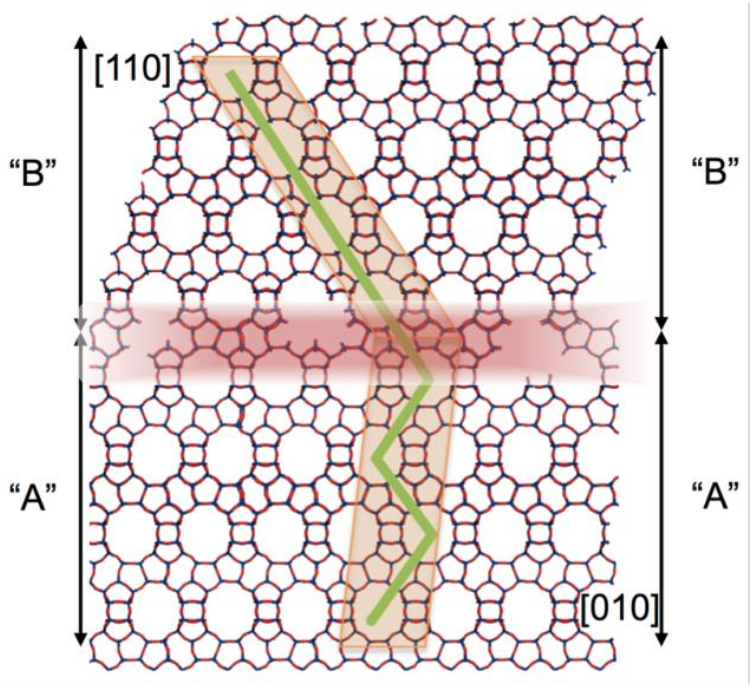

Figure 12. The polymorph inter–growth region of the all–siliceous BEA and BEB unit cells is shown in pink. The [010] plane of BEA and the [110] plane of BEB are highlighted in orange. The suggested selective bond cleavage along the respective polymorph planes is schematically shown in green. The cleavage exhibits a crack–like pattern propagating through the 6–member rings connecting the 12–member ring pores of H–beta *via* T3–O–T7 and T4–O–T8 bridge hydrolysis under Si Q^3 ($Si(OSi)_3OH$) formation. Si (blue) and O (red) are shown as sticks.

4.3.11 Mechanism of HBEA hydrothermal decomposition

The above results allow us to conclude that the HBEA framework decomposes in hot water *via* hydrolysis of T–O–T groups. While the STEM and XRD results suggest that crystallinity is readily degraded by hydrothermal treatment, Al EXAFS and ^{27}Al NMR show that changes in the direct Al coordination occur more slowly. Having demonstrated that the Al T–sites are kinetically stable links in the zeolite framework during hydrothermal treatment, let us discuss the pathway by which the zeolite lattice is degraded. Figure 13 shows a brief summary of the proposed zeolite degradation stages in water. Three parallel reaction pathways are hypothesized to occur.

1. Si–OH group formation and deconstruction

Si–OH groups form first at the boundaries of crystal domains. The rate depends on the temperature, and the concentration of H_3O^+ ions in the aqueous phase.[42,43] As the first Si–O bond is cleaved, two silanol–groups are formed resulting in a lattice defect. This bond cleavage can potentially continue until a Si atom is removed from the framework and a silanol–nest is formed. There are two possible patterns: 1) zeolite fragmentation *via* hydrolysis of the T–O–T groups similar to crack propagation in glass[44, 45] initiated at the silanol–nests and 2) structural degradation promoted at multiple silanol–nests simultaneously leading to the collapse of the zeolite pore structure.

The rate of crack propagation in glass exponentially depends on the applied stress,[46] which in turn can be affected by the presence of reactive species and the rate at which these species are delivered to the tip of the crack.[47] Previous crack growth and fatigue models have shown that the Si–O tetrahedra, which are inert to water at ambient conditions, are easily cleaved when under substantial stress such as encountered at the tip of the crack.[48] The high accessibility of strained T–O–T bonds leads us to hypothesize that the T–O–T cleavage in zeolite occurs primarily at inter–crystalline planes, preferentially first between two regions that do not share a coherent crystal lattice. Separation of crystalline domains in HBEA leads to loss of XRD intensity at 2Θ = 7.7 (primarily due to polymorph A and B separation). It also increases the mesopore volume. Note that the formation of a silyloxylated surface agrees well with the increase of ^{29}Si CP NMR signal intensity in the 48 h 160 ºC water treated HBEA150.

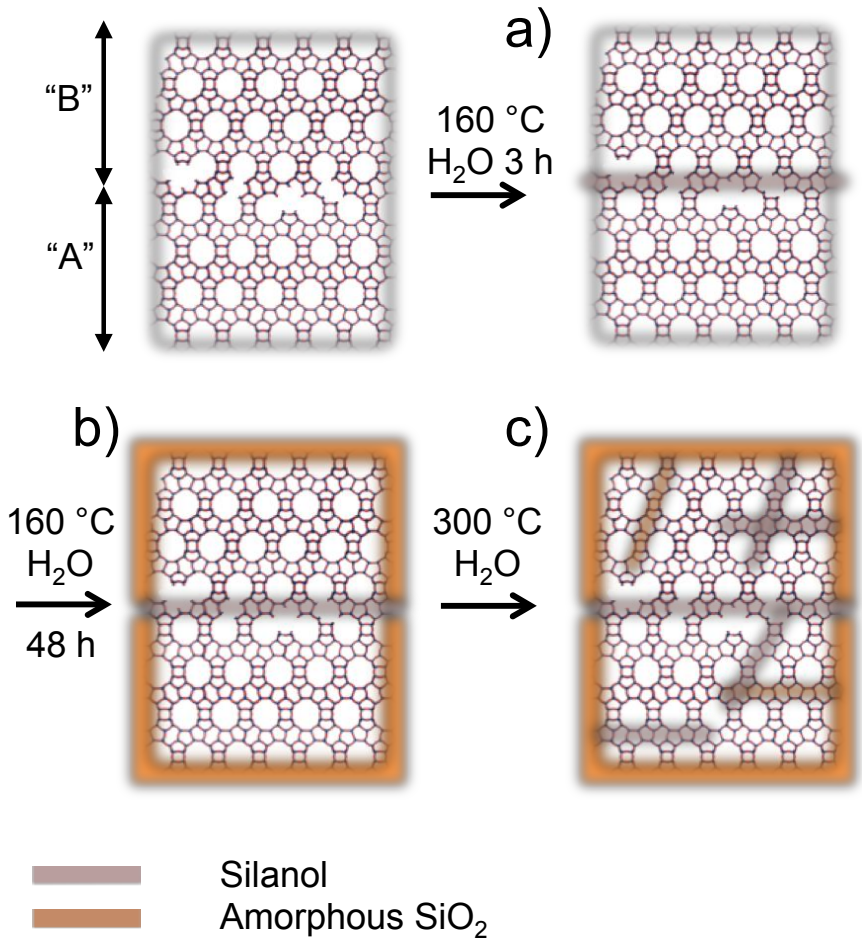

Figure 13. The suggested pathway for zeolite degradation in hot liquid water showing a) the framework hydrolysis along the polymorph inter–growth region between two different crystallites, b) the formation of amorphous silica cap on the single crystal surface and c) the T–O–T group hydrolysis prior to complete framework degradation to an amorphous material. Formed Si–OH groups are marked pink and the amorphous silica regions are marked orange. Note: the amorphous regions are schematically shown.

2. Ostwald ripening and amorphous silica

The exterior surface modifications of zeolite particles observed in HIM images occur through a process related to Ostwald–ripening accompanied by reactive diffusion, which occurs in the presence of a liquid phase. Under hot liquid water treatment conditions the most stable phase appears to be an amorphous, non–porous SiO_2 layer, which blankets intact crystalline volume.

Note the smoothing of the particle surface in HIM images (Figure 2b) in absence of changes in the XRD patterns or Al EXAFS spectra. In the case of large zeolite crystals, HBEA150 retains a certain degree of crystallinity even after water treatment at 300 ºC for 48 h. While these larger crystallites are most stable against degradation, the Brønsted acid sites, which should be present (the geometry of the active Al T–sites is retained), are inaccessible, which is in line with the drastic reduction of the micropore volume.

3. Breakdown of zeolite H–beta pore structure

Finally, at higher temperatures (300 °C) there is a slow internal decomposition by nucleation and hydrothermal growth of amorphous domains within the crystal lattice.

After outlining the three routes to degradation let us discuss differences between zeolite samples that lead to variations in the stability against water. Experimentally it is observed that the HBEA150 zeolite sample is more stable in hot liquid water than the Al–rich HBEA25. As the geometry of the Al T–sites is determined to remain unaltered after water treatment, the difference in stability must be caused by effects that are more subtle than the mere concentration of Al in the lattice.

The first striking difference is the population of Al in the lattice of the two samples. In HBEA25 in contrast to HBEA150 much less Al populates T1 and T2 (Set A) sites. These T–sites are located in the four–member rings which have the smallest average T–O–T angles and are therefore, the most labile. The presence of Al in such rings may introduce a stabilizing effect on the local zeolite structure the presence of water, preventing hydrolysis. Note that the crack propagation through the T3–O–T7 and T4–O–T8 bridges (see Figure 12) is the path that requires the minimum number of cleaved bonds. Remarkably, although HBEA25 contains almost 40 % of Al in the T7–positions, these do not markedly improve the overall zeolite stability in water.

The second difference may be related to the larger particle size of HBEA150. The smaller crystals of HBEA25 and the associated higher concentration of inter–grain boundaries (and as a consequence a much larger number of inter–crystalline defect sites) offers more options to initiate the hydrolytic processes, which are further accelerated by the deconstruction of the larger inter–grown particles into nano–crystallites.

The third factor is related to the significantly higher concentration of silanol–nests in HBEA25 compared to HBEA150. Both the concentration of surface terminal Si–OH groups as well as Si–OH nests that act as sites from which hydrolysis propagates.

In contrast to these three factors, hydrophobicity (differences in the concentration of water in the pores) may only influence the zeolite degradation, if the rate of hydrolysis is limited by the availability of water in the nano–domains where hydrolysis occurs. In the present case water is assumed to be present in excess and be equilibrated and, thus, is expected to have the same chemical potential independent of macroscopic differences.

4.4 Conclusions

The impact of liquid water on Brønsted acidic zeolites with H–beta structure has been analyzed as an example to elucidate the principal factors governing zeolite stability. The zeolite structural degradation in aqueous medium occurs primarily *via* gradual hydrolysis of T–O–T bonds and Si–OH group formation. It is initiated in the form of selective attack at the strained Si–O bonds and Si–OH groups at positions where lattice mismatch allows for this chemistry. The process spreads similar to crack formation and propagation in glass, ultimately leading to lattice deconstruction of larger polycrystalline zeolite particles along the polymorph or single crystal inter–growth faults into smaller crystalline blocks. These smaller crystalline domains form amorphous silica outer–shells resulting from progressive hydrolysis of T–O–T bonds on the external surface of the crystalline domains. Finally selective hydrolysis of T3–O–T7 and T4–O–T8 bridges leads to gradual zeolite sample amorphization. While the nano–scale crystalline structure as measured by XRD and STEM was disrupted, the local structure about the Al T–site remained mostly intact, including the Al–O–Si angles and bond distances.

While the specific impact of lattice structures is beyond the scope of the present contribution, it is obvious that local strain and the specific substitution will greatly impact the hydrothermal stability of zeolite structures. Thus, enhancing the quality of materials (absence of Si–OH groups), their surface modification to eliminate Si–OH groups, and mitigating local stress through selective incorporation are hypothesized to be the key to future stable zeolite materials.

4.5 Acknowledgements

B. W. Arey (PNNL) is acknowledged for HIM measurements, T. Huthwelker for support during Al XAFS measurements at the Swiss Light Source (PSI, Switzerland) and M. Y. Hu (PNNL) for support during NMR experiments. This work was supported by the U. S. Department of Energy (DOE), Office of Basic Energy Sciences, Division of Chemical Sciences, Geosciences & Biosciences.

4.6 Appendix

4.6.1 Powder X–Ray Diffraction data

During hot liquid water treatment the temperature has a severe impact on the zeolite stability. Figure A1 shows the structural degradation of HBEA150 treated for 3 h at 250 °C. The calculated XRD patterns for the all–siliceous BEA and BEB polymorphs are shown in Figure A2, the observed reflection as well as the corresponding Miller indexes are shown in Table A1.

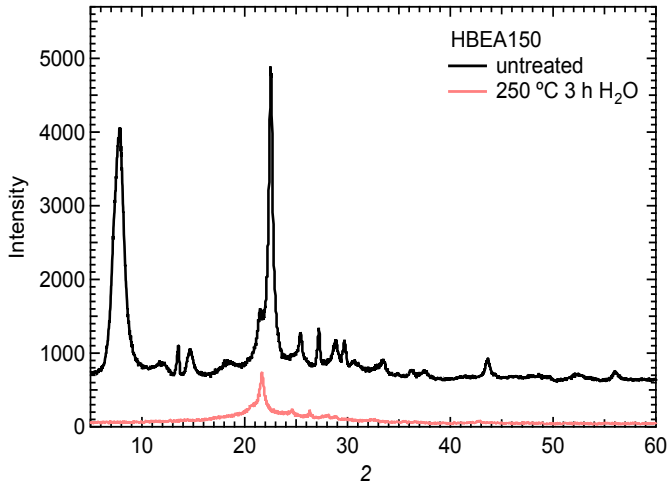

Figure A1. XRD pattern of HBEA150 untreated (black) and treated in water at 250 °C for 3 h (red).

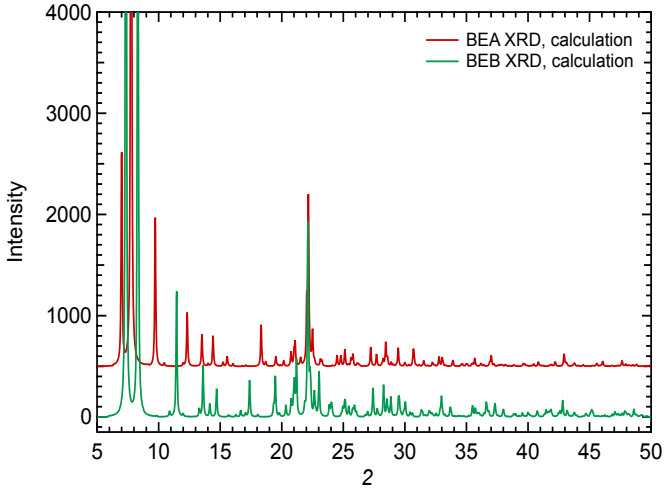

Figure A2. Calculated XRD patterns for BEA (red) and BEB (green) polymorphs of HBEA.

Table A1. Assignment of calculated XRD reflections to the unit cell planes of the BEA and BEB polymorphs of zeolite Beta.

BEA 2θ	BEA Miller index (h,k,l)	BEB 2θ	BEB Miller index (h,k,l)
7.05	1,0,0	7.40	1,1,0
7.75	1,0,1	8.40	1,1,–1
9.76	1,0,2	13.60	0,0,2
12.35	1,0,3	14.70	2,2,0
13.54	0,0,4	17.40	1,1,2
14.39	2,0,1	19.45	1,1,–3
18.39	1,0,5	21.00	3,3,–1
21.08	3,0,0	21.22	2,2,–3
22.02	2,0,5	22.12	3,3,0
22.14	3,0,2	22.30	4,2,–1
22.52	3,1,1	22.56	4,2,–2
25.15	3,0,4	23.00	2,2,2
27.21	0,0,8	27.40	0,0,4
28.45	4,0,1	28.26	4,4,–1
29.44	3,0,6	28.88	2,2,3
30.71	0,0,9	29.54	3,3,–4

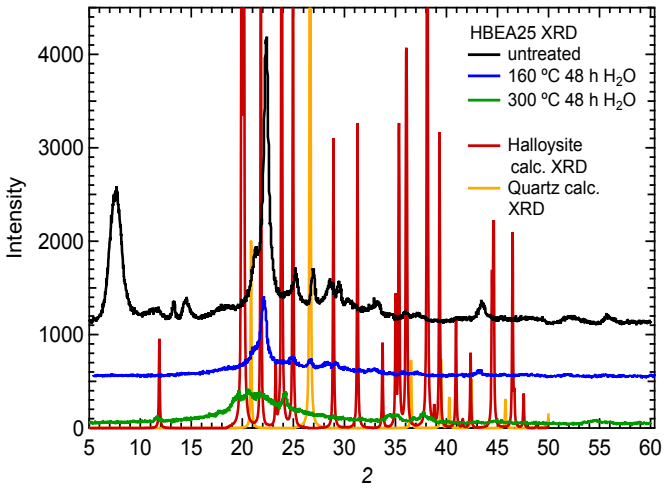

Figure A3. The XRD patterns measured for parent (black), 160 ºC 48 h water treated (blue) and 300 ºC 48 h water treated (green) HBEA25 zeolite, calculated XRD for quartz, crystalline SiO_2, (orange) and for halloysite, an aluminosilicate clay material, (red) also shown.

Although Si–solubility in hot water is substantial to allow Si–removal under formation of quartz, the possible dissolution–precipitation does not yield this crystalline SiO_2 form (Figure A3). The 48 h 300 °C hot water treated sample shows residual crystallinity, which is attributed to clay–like materials. Halloysite,[49] $Al_2Si_2O_5(OH)_4$, is the closest match to the measured XRD pattern, however a mixture of similar aluminosilicate clay materials is also possible.

4.6.2 Mircopore and mesopore surface area

The micropore and mesopore surface area was determined from BET surface area measurements using N_2 as probe molecule. The distribution of material pore sizes (up to 200 nm) with the corresponding surface areas is shown in Figure A4 a) & A4 b) for HBEA150 and HBEA25, respectively.

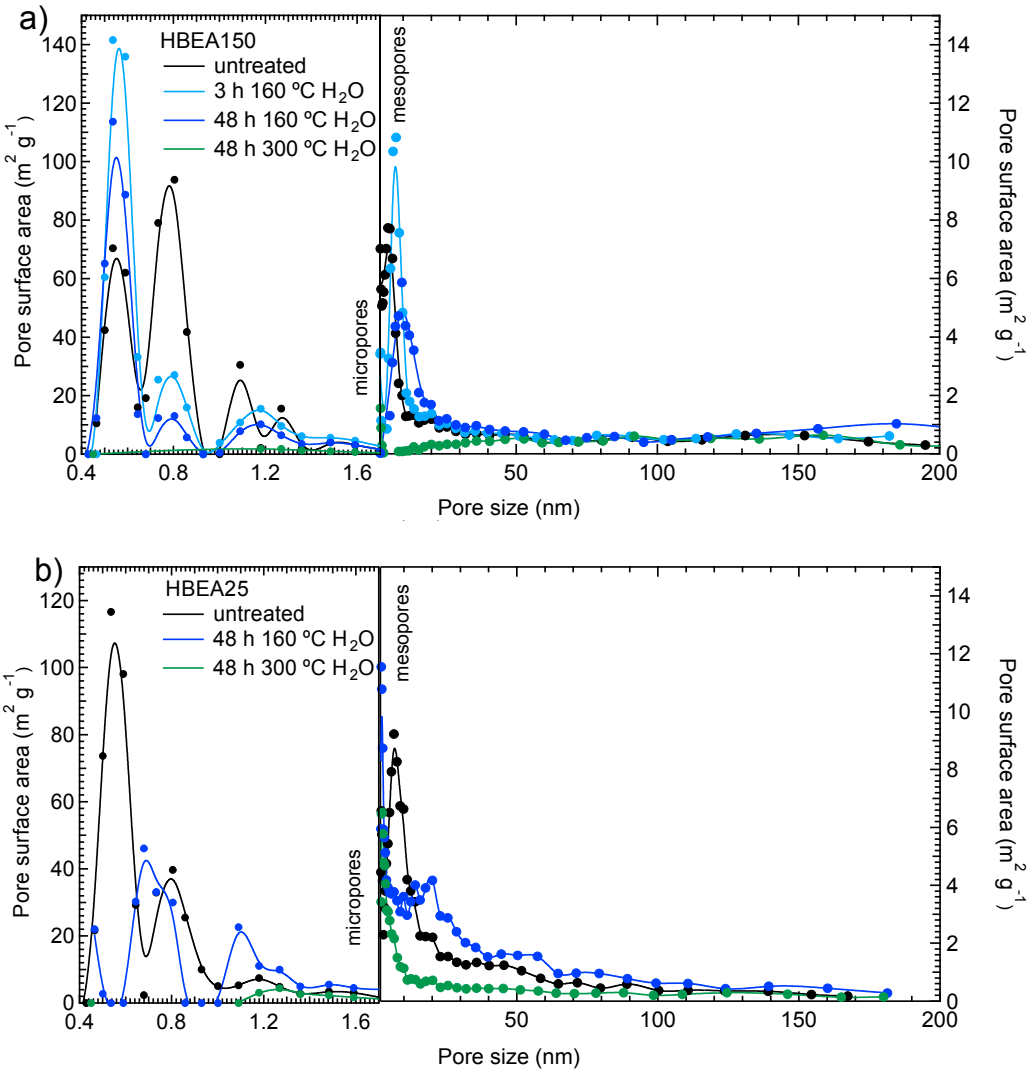

Figure A4. The distribution of zeolite HBEA150 in a) and HBEA25 in b) pore size in nm and the respective surface area are shown. Splice lines are fitted for better visualization. The untreated zeolite (black), the 48 h 160 ºC water treated (blue) and 48 h 300 ºC water treated (green) are shown. The 3 h 160 ºC water treated HBEA150 is shown in light blue in A4 a).

4.6.3 Mircopore and mesopore volume

The micropore and mesopore volume was determined from BET measurements using N_2 as probe molecule. The distribution of material pore sizes (up to 200 nm) with corresponding pore volumes is shown in Figure A5 a) & A5 b) for HBEA150 and HBEA25, respectively.

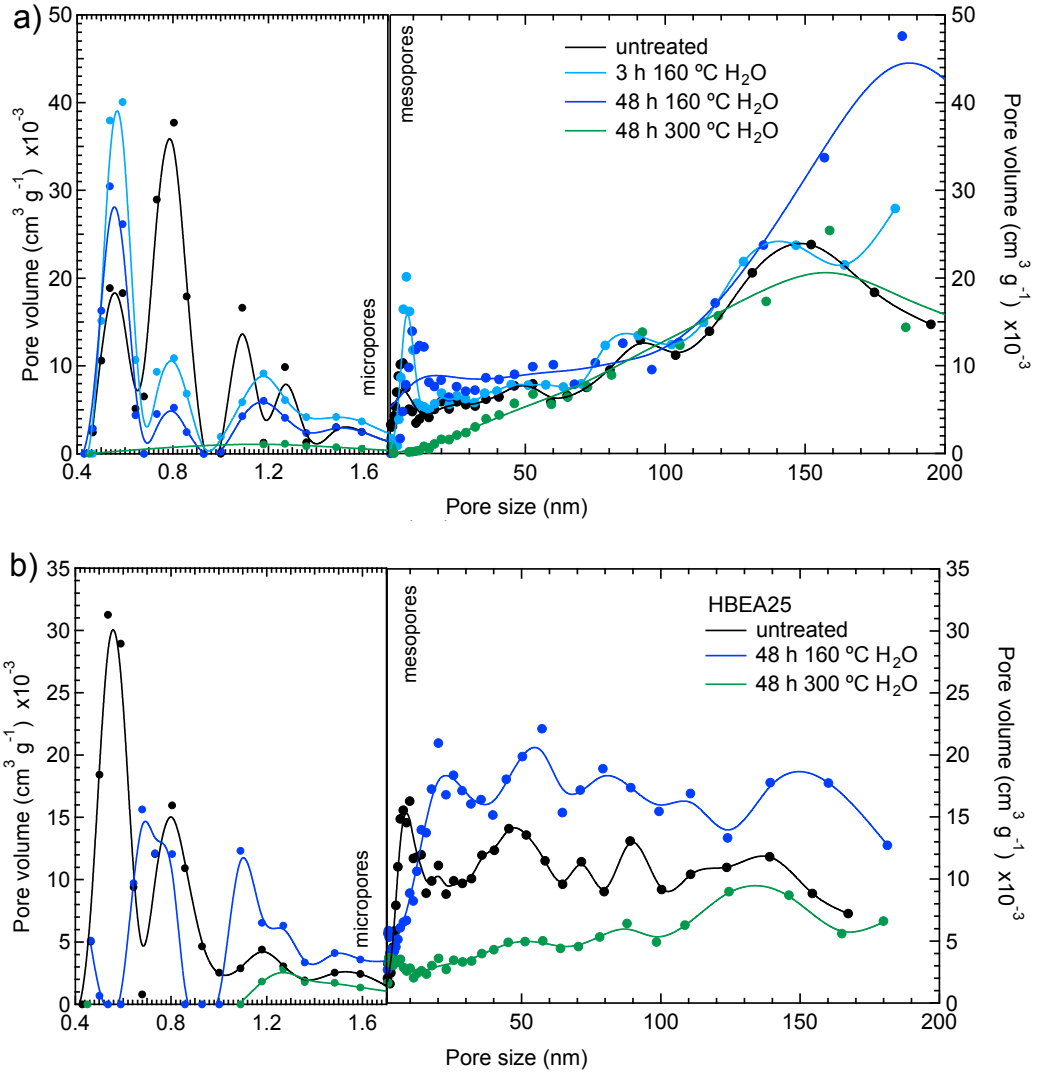

Figure A5. The distribution of zeolite HBEA150 in a) and HBEA25 in b) pore size in nm and the respective pore volume are shown. Splice lines are fitted for better visualization. The untreated zeolite (black), the 48 h 160 ºC water treated (blue) and 48 h 300 ºC water treated (green) are shown. The 3 h 160 ºC water treated HBEA150 is shown in light blue in A5 a).

4.6.4 Scanning transmission electron microscopy (STEM)

STEM images for the HBEA150 parent, 3 h 160 °C and 48 h 160 °C samples are shown in Figure A6.

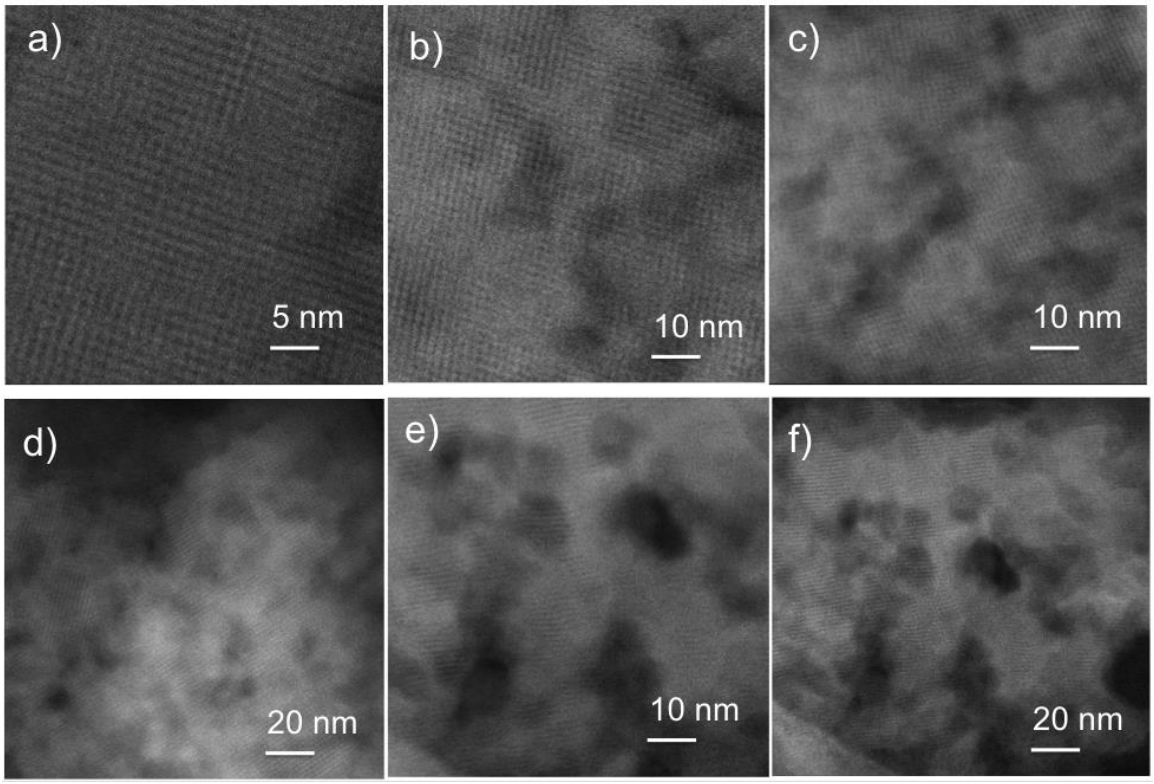

Figure A6. STEM images for the HBEA150 untreated (a & b), 3 h 160 ºC water treated (c & d) and 48 h 160 ºC water treated (e & f) samples. The magnification is reported in the individual images.

4.6.5 Helium Ion Microscopy (HIM)

HIM images for the parent and treated HBEA150 and HBEA25 are shown in Figures A7 and A8, respectively.

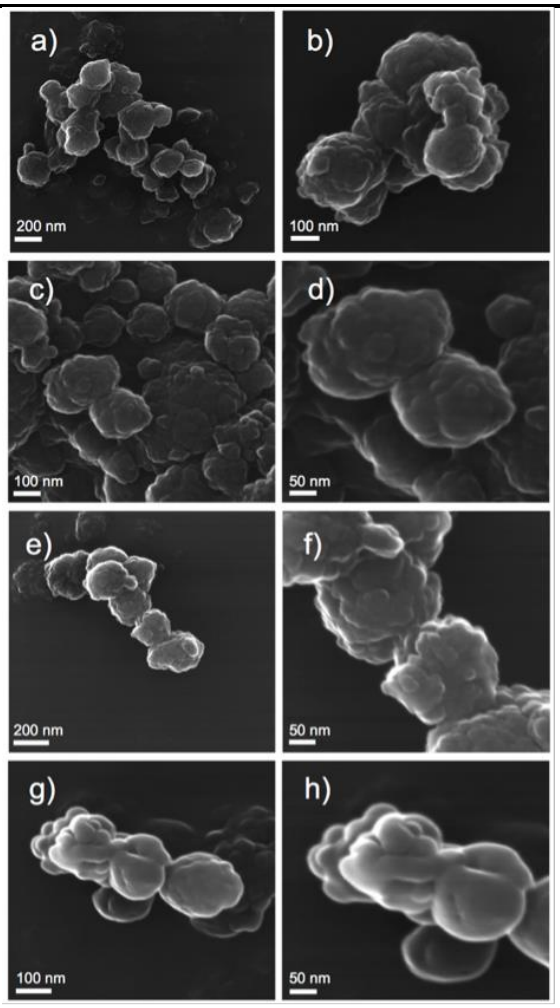

Figure A7. HIM images of the untreated (a & b) and the 3 h 160 °C (c & d), 48 h 160 °C (e & f) and 48 h 300 °C (g – h) hot liquid water treated HBEA150 samples. The magnification is reported in the plots.

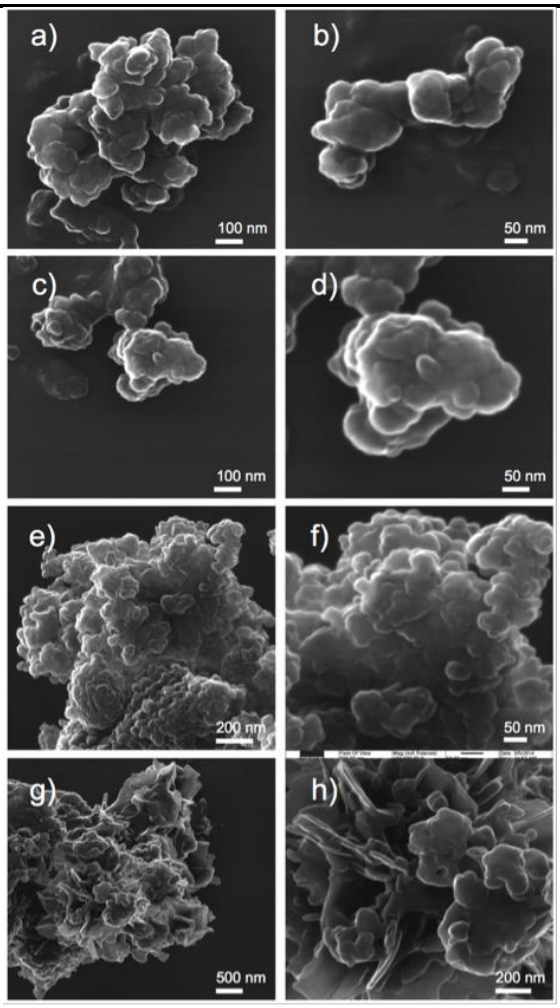

Figure A8. HIM images of the untreated (a & b) and the 3 h 160 °C (c & d), 48 h 160 °C (e & f) and 48 h 300 °C (g – h) hot liquid water treated HBEA25 samples. The magnification is reported in the plots.

4.6.6 Al EXAFS fitting calculations and error estimates

The fitting procedure is described in detail in *J. Am. Chem. Soc.* 2014, *136*, 8296–8306. The analysis is based on data fitting with calculated reference spectra in k–space. The quality of fits is reported in Tables A2–A5 below. Note that the R–space error is estimated using the T–site fractions determined from k–space fitting. T–site distribution could not be determined for the HBEA25 48 h 300 ºC sample due to substantial framework degradation in water.

Table A2. EXAFS fitting results for the parent HBEA150 sample.

Fitted combination	Set A (fraction)	Set B (fraction)	Set C (fraction)	Al^{3+} octahedral fraction	χ^2 k = 1.5–8	Reduced χ^2 k = 1.5–8
A+B+C+Al^{3+}	0.72	0.19	0	0.09	5.941	0.0464
A+B+Al^{3+}	0.74	0.17	N/A	0.09	5.941	0.0461
A+C+Al^{3+}	0.89	N/A	0.03	0.08	5.943	0.0461
B+C+Al^{3+}	N/A	0.89	0	0.11	5.982	0.0464
A+Al^{3+}	0.92	N/A	N/A	0.08	5.943	0.0457
B+Al^{3+}	N/A	0.89	N/A	0.11	5.982	0.046
C+Al^{3+}	N/A	N/A	0.86	0.14	6.191	0.0476

Fitted combination	χ^2 R = 1.5–6 Å	χ^2 R = 1.5–5.5 Å	χ^2 R = 2–4 Å	χ^2 R = 0.5–2 Å
A+B+C+Al^{3+}	3.64	3.60	1.22	4.81
A+B+Al^{3+}	3.63	3.59	1.21	4.81
A+C+Al^{3+}	3.58	3.54	1.17	4.67
B+C+Al^{3+}	4.10	4.06	1.63	5.14
A+Al^{3+}	3.58	3.53	1.16	4.67
B+Al^{3+}	4.10	4.06	1.63	5.14
C+Al^{3+}	3.79	3.74	2.03	2.84

Table A3. EXAFS fitting results for the 48 h 160 ºC water treated HBEA150 sample.

Fitted combination	Set A (fraction)	Set B (fraction)	Set C (fraction)	Al^{3+} octahedral fraction	χ^2 k = 1.5–8	Reduced χ^2 k = 1.5–8
A+B+C+Al^{3+}	0.82	0	0.078	0.1	5.29676	0.0413809
A+B+Al^{3+}	0.91	0	N/A	0.09	5.29893	0.041077
A+C+Al^{3+}	0.82	N/A	0.08	0.1	5.29676	0.0410601
B+C+Al^{3+}	N/A	0.82	0.06	0.12	5.36224	0.0415678
A+Al^{3+}	0.91	N/A	N/A	0.09	5.29893	0.040761

B+Al^{3+}	N/A	0.88	N/A	0.12	5.36314	0.0412549
C+Al^{3+}	N/A	N/A	0.84	0.16	5.50794	0.0423687

Fitted combination	χ^2 R = 1.5–6 Å	χ^2 R = 1.5–5.5 Å	χ^2 R = 2–4 Å	χ^2 R = 0.5–2 Å
A+B+C+Al^{3+}	3.617	3.547	1.848	11.005
A+B+Al^{3+}	3.602	3.533	1.851	10.831
A+C+Al^{3+}	3.617	3.547	1.848	11.005
B+C+Al^{3+}	3.657	3.585	1.839	11.745
A+Al^{3+}	3.602	3.533	1.851	10.831
B+Al^{3+}	3.642	3.570	1.838	11.626
C+Al^{3+}	4.099	4.019	1.991	13.211

Table A4. EXAFS fitting results for the 48 h 300 ºC water treated HBEA150 sample.

Fitted combination	Set A (fraction)	Set B (fraction)	Set C (fraction)	Al^{3+} octahedral fraction	χ^2 k = 1.5–8	Reduced χ^2 k = 1.5–8
A+B+C+Al^{3+}	0.73	0	0.14	0.13	4.8467	0.0378648
A+B+Al^{3+}	0.88	0	N/A	0.12	4.85378	0.0376261
A+C+Al^{3+}	0.73	N/A	0.14	0.13	4.8467	0.0375713
B+C+Al^{3+}	N/A	0.71	0.14	0.15	4.9054	0.0383234
A+Al^{3+}	0.88	N/A	N/A	0.12	4.85378	0.0373368
B+Al^{3+}	N/A	0.86	N/A	0.14	4.91047	0.0377728
C+Al^{3+}	N/A	N/A	0.82	0.18	5.01465	0.0385743

Fitted combination	χ^2 R = 1.5–6 Å	χ^2 R = 1.5–5.5 Å	χ^2 R = 2–4 Å	χ^2 R = 0.5–2 Å
A+B+C+Al^{3+}	4.01	3.97	1.87	10.12
A+B+Al^{3+}	3.96	3.91	1.87	9.81
A+C+Al^{3+}	4.01	3.97	1.87	10.12
B+C+Al^{3+}	4.24	4.19	2.01	10.75
A+Al^{3+}	3.96	3.91	1.87	9.82
B+Al^{3+}	4.21	4.16	2.02	10.56
C+Al^{3+}	4.59	4.54	2.02	12.04

Table A5. EXAFS fitting results for the parent HBEA25 sample.

Fitted combination	Set A (fraction)	Set B (fraction)	Set C (fraction)	Al^{3+} octahedral fraction	χ^2 k = 1.5–8	Reduced χ^2 k = 1.5–8
A+B+C+Al^{3+}	0.409	0	0.375	0.216	4.183	0.0327

A+B+Al^{3+}	0.464	0.336	N/A	0.2	4.225	0.0330
A+C+Al^{3+}	0.409	N/A	0.375	0.216	4.183	0.0327
B+C+Al^{3+}	N/A	0.379	0.393	0.228	4.204	0.0328
A+Al^{3+}	0.809	N/A	N/A	0.191	4.234	0.0326
B+Al^{3+}	N/A	0.787	N/A	0.213	4.241	0.0326
C+Al^{3+}	N/A	N/A	0.756	0.244	4.236	0.0326

Fitted combination	χ^2 R = 1.5–6 Å	χ^2 R = 1.5–5.5 Å	χ^2 R = 2–4 Å	χ^2 R = 0.5–2 Å
A+B+C+Al^{3+}	1.29	1.28	0.91	2.61
A+B+Al^{3+}	1.27	1.27	0.94	2.55
A+C+Al^{3+}	1.29	1.28	0.91	2.61
B+C+Al^{3+}	1.42	1.41	1.01	2.68
A+Al^{3+}	1.21	1.21	0.90	2.52
B+Al^{3+}	1.43	1.42	1.07	2.60
C+Al^{3+}	1.52	1.52	1.01	2.81

Table A6. EXAFS fitting results for the 48 h 160 ºC water treated HBEA25 sample.

Fitted combination	Set A (fraction)	Set B (fraction)	Set C (fraction)	Al^{3+} octahedral fraction	χ^2 k = 1.5–8	Reduced χ^2 k = 1.5–8
A+B+C+Al^{3+}	0.54	0	0.26	0.20	4.678	0.0365
A+B+Al^{3+}	0.50	0.32	N/A	0.18	4.695	0.0367
A+C+Al^{3+}	0.54	N/A	0.26	0.20	4.678	0.0365
B+C+Al^{3+}	N/A	0.56	0.23	0.21	4.701	0.0367
A+Al^{3+}	0.82	N/A	N/A	0.18	4.703	0.0362
B+Al^{3+}	N/A	0.80	N/A	0.20	4.714	0.0363
C+Al^{3+}	N/A	N/A	0.77	0.23	4.770	0.0367

Fitted combination	χ^2 R = 1.5–6 Å	χ^2 R = 1.5–5.5 Å	χ^2 R = 2–4 Å	χ^2 R = 0.5–2 Å
A+B+C+Al^{3+}	1.35	1.34	0.88	3.16
A+B+Al^{3+}	1.33	1.32	0.90	3.09
A+C+Al^{3+}	1.35	1.34	0.88	3.16
B+C+Al^{3+}	1.48	1.46	0.97	3.27
A+Al^{3+}	1.30	1.29	0.88	3.04
B+Al^{3+}	1.47	1.45	1.00	3.19
C+Al^{3+}	1.65	1.64	1.00	3.53

4.6.7 ^{27}Al MAS NMR measurements and ^{27}Al DFT NMR calculations

The fitting procedure is described in detail in *J. Am. Chem. Soc.* **2014**, *136*, 8296–8306. Figure A9 shows the DFT NMR fits to the experimental NMR spectra.

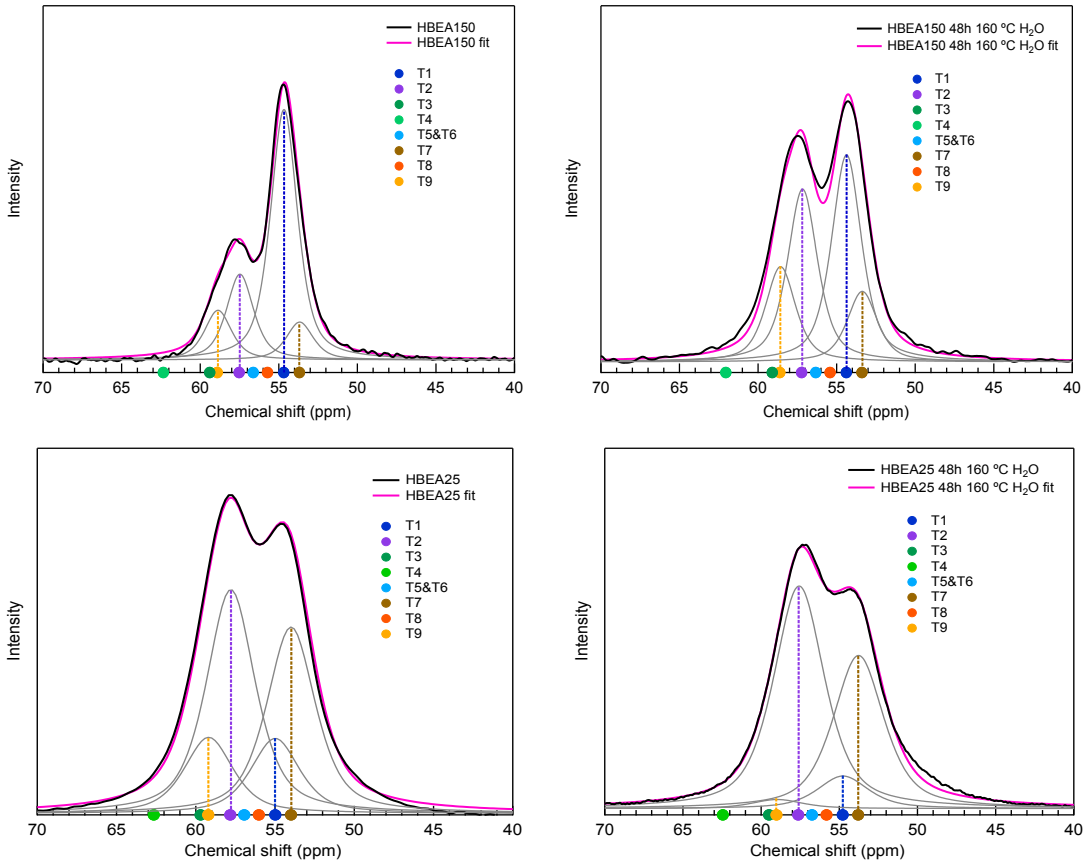

Figure A9. Measured ^{27}Al MAS NMR spectra for the parent and 48 h 160 ºC water treated HBEA150 and HBEA25 samples are shown in black. The DFT NMR fit is shown in magenta with individual fitted peaks shown in grey. The calculated Al T–site DFT NMR chemical shifts for HBEA are shown as markers. The T–site color–coding is reported in the legend of the plots.

4.6.8 ^{29}Si MAS NMR measurements and ^{29}Si DFT NMR calculations

The Si T–site ^{29}Si DFT NMR chemical shifts were calculated for [Si–(O–Si–OH)$_4$] clusters. The cluster charge was set to neutral (zero). The structures of the ions were derived from the DFT optimized crystal structures by cutting and terminating O–Si bonds with hydrogen atoms while maintaining the bond vectors. The O–H bond length was set to 0.96 Å in all cases. The obtained values were offset by –2.5 ppm to match the experimental chemical shift range. The relative T–site chemical shift differences, however, are retained. The alignment is performed based on two criteria: 1) the experimentally observed shoulder at –115 ppm is matched by the closest calculated value (in this case Si T5–site) and 2) the measured NMR spectrum is fitted with three peaks representing groups of T–sites based on DFT NMR values. The following grouping was applied for the Si T–sites: Set D (T3, T4), Set E (T1, T2, T7, T8, T9) and Set F (T5, T6). The sites T5 and T6 are grouped due to their unique position in the 6 membered rings of the zeolite framework. In the final step a least square fitting procedure for the three peaks to the experimental spectrum leads to the assignment of spectral features to certain T–site groups. This approach is necessary to interpret the single–pulse (SP) and cross–polarization (CP) ^{29}Si NMR results in section 4.3.10.

Table A7 T–site atom coordinates used in Si–[O–Si–$(OH)_3]_4^-$ cluster ^{29}Si NMR calculations for HBEA.

Geometry T1	Geometry T2	Geometry T3
Si 0.0000 0.0000 0.0000	Si 0.0000 0.0000 0.0000	Si 0.0000 0.0000 0.0000
O -0.0139 1.5979 0.1807	O –0.0050 –1.5992 0.1781	O 0.9196 –0.7933 1.0553
O -0.8981 -0.6809 1.1496	O –0.5861 0.3865 –1.4481	O 0.6164 –0.1427 –1.4795
O -0.5950 -0.3865 -1.4455	O –0.9146 0.6758 1.1391	O –0.0442 1.5575 0.4033
O 1.5133 -0.5419 0.1100	O 1.5070 0.5545 0.1309	O –1.4969 –0.5912 0.0262
Si 3.0102 0.0493 0.0838	Si 3.0077 –0.0278 0.0969	Si –3.0102 –0.0493 –0.0838
Si -2.3521 -0.8198 1.8278	Si –2.3622 0.8855 1.8095	Si 2.3672 –0.8501 1.7597
Si -1.1899 0.0000 -2.8909	Si –1.1723 0.0000 –2.8962	Si –0.0114 3.1201 0.0157
Si -0.0088 3.1972 0.0026	Si 0.0088 –3.1972 –0.0026	Si 0.5861 0.0467 –3.0769
O 2.9660 1.6068 0.4871	O 2.9748 –1.5904 0.4844	O –3.0241 1.5487 0.0969
O -3.4877 -0.6430 0.7018	O –3.5029 0.7832 0.6782	O 3.5079 –0.6101 0.6494
O -1.1760 1.5979 -3.0716	O –1.1672 –1.5992 –3.0742	O 0.6114 3.3134 –1.4533
O 3.6267 -0.0935 -1.3957	O 3.6304 0.1655 –1.3721	O –0.7124 –0.6922 –3.6765
O -2.5289 0.3158 2.9538	O –0.5861 –3.5837 –1.4481	O 2.4696 0.2905 2.8909
O -0.5950 3.5837 -1.4455	O –2.6022 –0.2552 2.9197	O 0.5381 1.6131 –3.4487
O 1.4982 3.7517 0.1336	O 1.5222 –3.7391 0.1074	O –3.6052 –0.4358 –1.5293
O -2.7032 -0.5419 -3.0009	O –2.6793 0.5545 –3.0271	O –1.5121 3.7024 0.0498
O -0.2918 -0.6809 -4.0405	O –0.2577 0.6758 –4.0353	O –3.9083 –0.7301 1.0658
O -0.9234 3.8730 1.1417	O –0.8893 –3.8780 1.1470	O 0.8994 3.8944 1.0920
O 3.9298 -0.7440 1.1391	O 3.9185 0.7466 1.1731	O 1.9138 –0.6101 –3.7079
O -2.4910 -2.2738 2.5060	O –2.4190 2.3331 2.5139	O 2.5769 –2.2978 2.4301
O 2.2978 -0.6430 -3.5927	O 2.3306 0.7832 –3.5744	Si –3.0190 3.1479 –0.0812
Si 2.9988 3.1694 0.0995	Si 3.0190 –3.1479 0.0812	Si 0.6000 3.1732 –3.0585
Si -1.1811 3.1972 -2.8935	Si –1.1811 –3.1972 –2.8935	Si 4.8355 0.0467 0.0183
Si 3.5963 0.0960 -2.9931	Si 3.6191 0.0253 –2.9773	O 2.5656 2.9167 2.8857
Si -4.7863 0.0960 0.1021	Si –4.7913 0.0253 0.0812	Si 2.3672 4.0334 1.7440
O -2.6110 2.9420 2.9224	O –2.5201 –2.8814 2.9512	Si 3.2275 1.5790 3.4880
Si 1.1621 -0.8198 -4.7187	Si 1.1899 0.8855 –4.7056	O 4.8052 –0.1427 –1.5790
O -4.7383 1.6624 0.4740	O –4.7294 –1.5348 0.4714	Si –4.2001 –0.0493 –2.9747
O -4.8166 -0.0935 -1.4952	Si –2.3432 –4.0170 1.8252	O 4.8835 1.6131 0.3902
Si -2.3710 4.0827 1.8121	O –4.8027 0.1655 –1.5240	O 3.4839 3.8351 0.6023
Si -3.2679 1.6144 3.5534	Si –3.2591 –1.5828 3.5508	Si –1.8481 –0.8691 –4.8025
O 3.6216 3.3626 -1.3695	O 3.6355 –3.2906 –1.3983	O –3.6052 3.5344 –1.5293
Si -4.2001 0.0493 -2.9747	O 3.5572 –1.5348 –3.3675	O –3.3020 –0.7301 –4.1243
O 3.5483 1.6624 -3.3649	Si –4.1799 –0.0278 –2.9931	O –0.6884 3.9311 –3.6556
O -3.5117 3.9803 0.6808	O –3.4788 –3.8401 0.6992	O –4.1862 1.5487 –3.1554
O -2.6881 3.7517 -3.0245	O –2.6944 –3.7391 –3.0035	O –3.9336 3.8237 1.0579
O -4.1559 1.6068 -3.3780	O –4.1471 –1.5904 –3.3806	O 1.9377 3.8351 –3.6608
O -0.2665 3.8730 -4.0326	O –0.2830 –3.8780 –4.0431	Si –5.3623 –0.8691 1.7440
O 3.9096 3.9437 1.1758	O 3.9387 –3.9412 1.1365	Si 3.0544 –0.8501 –4.8182
Si 5.3774 -0.8009 1.8435	Si 5.3863 0.8855 1.8252	Si 3.2527 –3.2123 3.5691
Si -3.1719 -3.1719 3.6556	Si –3.2123 3.2527 3.5691	O 4.7875 1.5171 3.0978
O -4.8343 1.5664 3.1816	O 1.4299 –0.2552 –5.8159	O 4.5020 –0.7933 –4.1138
O 1.3011 -2.2738 -5.3969	O –4.8254 –1.6308 3.1790	O 3.0873 1.5904 5.0932
O 1.3390 0.3158 -5.8447	O 1.2468 2.3331 –5.4100	O –1.6712 0.2665 –5.9285
O 4.9240 -0.5609 -3.6241	O 4.9568 0.6872 –3.5796	O –1.7091 –2.3230 –5.4807
O -6.1139 -0.5609 0.7332	O –3.0696 –1.5525 5.1482	O 6.1341 –0.6922 0.6180
O -3.0784 1.6447 5.1508	O –6.1290 0.6872 0.6834	O –5.5391 0.2665 2.8700
O 5.4798 0.3398 2.9747	O 5.5846 –0.2312 2.9669	O 2.8662 –2.6262 5.0172
O -2.7854 -2.5769 5.1010	O –3.0696 2.6363 5.0487	O 2.6982 –4.7193 3.4382
O -2.6300 -4.6852 3.5456	O –2.6211 4.7496 3.5430	O –5.5012 –2.3230 2.4222
O 5.5871 -2.2485 2.5139	O 5.5252 2.3533 2.4772	O 2.5062 5.5012 2.3960
O -2.4279 5.5303 2.5165	O –2.4822 –5.4709 2.5034	O –5.7134 –0.5912 –3.0847
O -5.1198 -0.7440 -4.0300	O –5.0907 0.7466 –4.0693	O –6.4979 –0.6922 0.6180
O 6.5181 -0.5609 0.7332	O 6.5030 0.6872 0.6834	O 2.8447 –2.2978 –5.4886
O -4.7698 -3.1580 3.4749	O –4.7698 3.2970 3.1659	O 2.9521 0.2905 –5.9495
H -4.9871 2.2584 -0.4164	H –4.7202 –1.6388 1.5664	O 4.8520 –3.2073 3.3911
H 4.1811 2.4588 -1.6524	H 4.1115 –4.2767 –1.5037	H 4.7809 –1.2156 –1.8206
H 3.2777 1.7795 -4.4246	H 3.5382 –2.1417 –2.4503	H 4.6347 2.2091 –0.5002
H -4.2571 3.2282 0.9787	H –4.3132 –4.5256 0.9090	H 4.1929 3.0541 0.9145
H -3.1513 3.7936 -2.0276	H –3.0886 –3.9332 –1.9951	H –4.1860 2.6893 –1.9272
H -3.9248 1.7018 -4.4492	H –4.1370 –2.1958 –2.4623	H –1.5638 3.7191 –3.0241
H 0.6607 3.2930 -4.1504	H 0.2119 –4.7736 –3.6395	H –4.0249 1.7965 –4.2149

H 3.3596 4.8141 1.5629
H -5.4170 1.3160 4.0804
H 1.3525 -3.0416 -4.6109
H 1.6505 -0.1512 -6.7907
H 5.4644 -1.1169 -2.8439
H -6.1782 -0.3040 1.8009
H -3.1588 2.6813 5.5100
H 5.3441 1.3284 2.5119
H -3.0518 -1.5105 5.1418
H -2.4944 -5.1004 4.5551
H 5.6053 -2.1463 3.6090
H -2.2829 6.3133 1.7576
H -5.5897 -1.6050 -3.5323
H 7.3736 -1.2215 0.9376
H -5.2510 -3.2714 4.4576

H 3.8878 –3.4417 2.1152
H 1.5470 –1.2303 –5.3205
H –5.4081 –1.8812 4.0777
H 1.4176 2.2091 –6.4896
H 5.8095 0.4499 –2.9264
H –3.1500 –0.5159 5.5073
H –5.8859 1.2261 1.6111
H 5.5763 0.2502 3.9559
H –3.0982 3.4494 5.7890
H –2.3980 5.0738 4.5702
H 5.1529 3.1066 1.7673
H –2.4940 –5.3652 3.5982
H –6.0559 0.2292 –4.1728
H 7.2119 –0.0938 0.9957
H –5.3832 3.0472 4.0442

H –3.4231 4.7116 1.4591
H 2.7904 3.5978 –3.0076
H 5.3777 1.2515 3.9873
H 4.4091 –0.3269 –3.1219
H 3.1459 2.6261 5.4590
H –1.3597 –0.2004 –6.8745
H –1.6577 –3.0909 –4.6947
H 6.2163 –0.4742 1.6930
H –5.3083 1.2511 2.4372
H 3.1307 –1.5595 5.0636
H 2.5570 –5.1466 4.4420
H –5.5131 –2.2173 3.5170
H 2.1339 6.2545 1.6861
H –6.1076 –0.7853 –2.0763
H –7.3322 –1.3777 0.8278
H 2.7673 –3.0597 –4.6990
H 2.7698 –0.1784 –6.9276
H 5.3308 –3.3209 4.3749

Geometry T4
Si 0.0000 0.0000 0.0000
O 0.6228 0.1933 –1.4690
O 0.9108 0.7743 1.0762
O –1.5007 0.5823 0.0340
O –0.0328 –1.5626 0.3875
Si –3.0077 0.0278 –0.0969
Si 2.3786 0.9133 1.7283
Si 0.0114 –3.1201 –0.0157
Si 0.6114 0.0531 –3.0742
O –3.0127 –1.5714 0.0812
O 3.4953 0.7150 0.5866
O 0.6278 –3.2629 –1.4952
O 0.5495 –1.5070 –3.4644
O –0.6771 0.8110 –3.6713
O 2.5769 –0.2034 2.8700
O –3.5938 0.4143 –1.5450
O –1.4855 –3.7113 0.0105
O –3.9222 0.7036 1.0422
O 0.9310 –3.9134 1.0396
O 2.5176 2.3811 2.3803
O 1.9491 0.7150 –3.6765
Si –2.9988 –3.1694 –0.0995
Si 0.5975 –3.0734 –3.0926
O 2.4809 –2.8296 2.8752
Si 4.8330 0.0531 –0.0157
Si 2.3786 –3.9702 1.7440
Si 3.2388 –1.5411 3.4723
O 4.8216 0.1933 –1.6209
O 4.8949 –1.5070 0.3745
Si –4.1799 0.0278 –2.9931
O 3.5193 –3.7302 0.6337
Si –1.8177 0.9133 –4.8025
O –3.5938 –3.5559 –1.5450
O –3.2654 0.7036 –4.1322
O –0.7011 –3.8123 –3.6922
O –4.1749 –1.5714 –3.1711
O –3.8970 –3.8502 1.0501
O 1.9251 –3.7302 –3.7236
Si –5.3699 0.9133 1.7126
Si 3.0658 0.9133 –4.8182
Si 3.2919 3.2919 3.4565
O 4.7989 –1.6030 3.0821
O –1.5777 –0.2274 –5.9128
O 3.0986 –1.5297 5.0775
O 6.1215 0.8110 0.5813
O 4.5336 0.7743 –4.1662
O –1.7609 2.3609 –5.5069
O –5.6099 –0.2274 2.8228
O –5.4267 2.3609 2.4170
O 3.0986 2.6691 4.9256

Geometry T5
Si 0.0000 0.0000 0.0000
O –0.0193 –0.1895 –1.5974
O 1.2986 –0.7390 0.5997
O –1.3276 –0.6569 0.6311
O 0.0480 1.5664 0.3718
Si 2.4342 –0.9158 1.7257
Si –0.0193 3.1264 –0.0183
Si 0.5861 –0.0467 –3.0769
Si –2.4683 –0.8969 1.7414
O –0.0480 1.4704 3.0795
O 2.2573 0.2198 2.8517
O –0.0193 3.2666 –1.6235
O –2.3660 0.2438 2.8726
O 2.0830 –0.6379 –3.1030
O 0.6303 1.5108 –3.4801
O –2.2586 –2.3445 2.4117
O –1.3516 3.7883 0.5839
Si 1.5184 1.5184 3.4513
O 2.2952 –2.3698 2.4039
O 3.8881 –0.7769 1.0474
Si –1.6080 1.5377 3.4696
O 1.2746 3.8843 0.5787
O –3.9159 –0.8400 1.0370
O –0.3335 –0.8400 –4.1322
Si 0.5975 3.0734 –3.0926
O –4.2301 –0.1895 –1.4978
O 4.1913 –0.4825 –1.5476
O 2.1752 2.8460 2.8202
O –2.2700 2.8700 2.8674
Si 3.5963 –0.0960 –2.9931
O 0.0164 –3.2540 3.3728
O –2.9218 –0.6569 –3.7263
Si 4.7863 –0.0960 –0.1021
Si –4.8355 –0.0467 –0.0183
Si 2.4152 3.9867 1.7099
Si –2.4683 3.9867 1.7257
O 4.7724 1.5019 0.0786
O 3.6102 1.5019 –3.1737
Si –1.5828 –3.2591 3.5508
Si 1.6144 –3.2679 3.5534
O –4.8797 1.5108 0.3849
Si –1.7811 –0.8969 –4.8366
O 2.0982 3.6557 –3.1266
Si –4.2494 0.0000 –3.0952
O 3.8629 3.7770 1.0396
O 1.7078 1.5377 5.0487
O –1.7483 1.5377 5.0749
O –3.9361 3.8477 1.0736
O –0.3133 3.8477 –4.1688
O –4.2974 1.5664 –3.4670

Geometry T6
Si 0.0000 0.0000 0.0000
O –1.3323 0.6619 0.6023
O 0.0673 –1.5601 0.3902
O 0.0000 0.1402 –1.6052
O 1.2939 0.7579 0.5970
Si 2.4346 0.8602 1.7283
Si 0.0193 –3.1264 0.0183
Si –2.4490 0.8602 1.7440
Si 0.6168 –0.0531 –3.0742
O –0.0287 –1.6561 3.0978
O 2.1946 –0.2804 2.8386
O –2.2506 –0.2564 2.8857
O 0.0000 –3.3159 –1.5790
O 2.1175 0.5293 –3.1083
O 0.6497 –1.6156 –3.4618
O –1.3083 –3.7833 0.6494
O –2.3100 2.3281 2.3960
O 3.8822 0.6506 1.0579
O 2.3777 2.3079 2.4327
Si 1.5377 –1.6080 3.4696
O –3.9168 0.7213 1.0920
O 1.3179 –3.8654 0.6180
Si –1.5887 –1.5887 3.4880
O –0.2939 0.7213 –4.1505
Si 0.6054 –3.1732 –3.0585
O –4.2108 0.1402 –1.4533
O 4.2106 0.3613 –1.5293
O 0.0269 3.2717 3.0847
O 2.2767 –2.9066 2.8700
Si 3.6245 –0.0253 –2.9773
O –2.8784 0.6619 –3.6608
O –2.3466 –2.8826 2.8909
Si 4.7968 –0.0253 –0.0812
Si –4.8276 –0.0531 0.0157
Si –1.5357 3.2388 3.4723
Si 1.5844 3.2275 3.4880
Si –2.4490 –4.0233 1.7597
Si 2.4535 –4.0422 1.7440
O 4.7917 –1.6245 0.0969
O 3.6295 –1.6245 –3.1554
O –4.8604 –1.6156 0.4033
Si –1.7618 0.8602 –4.8025
Si –4.2108 0.0000 –3.0585
O 2.1023 –3.7643 –3.0847
O 1.7272 –1.5887 5.0670
O –1.7289 –1.5887 5.0932
O 3.9075 –3.9033 1.0658
O –3.8966 –3.9664 1.0553
O –4.2781 –1.5601 –3.4487
O –0.3142 –3.9664 –4.1138

O 2.5883 –5.4179 2.4144
O 2.7096 4.7926 3.4225
O –5.6869 0.5823 –3.1240
O –6.5105 0.8110 0.5813
O 2.8675 –0.2034 –5.9599
O 4.8545 3.3247 3.0690
O 2.9268 2.3811 –5.4703
H 4.8111 –0.8080 –2.0764
H 4.9041 –1.6110 1.4695
H 4.3747 –4.3908 0.8381
H –4.0067 –4.5749 –1.5110
H –1.2104 –4.3669 –2.8903
H –4.1735 –2.0506 –2.1810
H –3.8112 –3.2647 1.9773
H 2.4655 –4.2863 –2.9434
H 5.3891 –1.8685 3.9716
H –1.4607 –1.2025 –5.4173
H 3.1573 –0.4940 5.4433
H 5.8331 1.3683 1.4848
H 4.5159 1.1622 –3.1370
H –1.5901 2.2369 –6.5865
H –5.6021 0.2281 3.8241
H –5.2818 3.1439 1.6581
H 3.1367 3.4750 5.6734
H 2.6064 –5.3157 3.5094
H 2.4602 5.1124 4.4450
H –6.1501 0.6243 –2.1271
H –7.2559 0.0589 0.8792
H 2.7687 –1.1936 –5.4911
H 5.4575 3.0826 3.9565
H 2.4913 2.2955 –6.4767

O –1.9693 –2.6729 4.9989
O 2.0009 –2.6729 4.9989
O 4.4945 –0.7769 –4.1426
O –2.1373 –4.7660 3.4199
O –1.8834 0.2438 –5.9678
O 2.1563 –4.7812 3.4435
O –1.9908 –2.3445 –5.5069
O 6.2996 –0.6379 0.0079
O –6.3324 –0.6379 0.0079
O –2.3293 5.4545 2.3777
O 2.3584 5.4343 2.4144
O –5.5480 –0.7390 –3.6948
H 4.9272 1.9828 –0.8986
H 3.7715 1.7498 –4.2333
H –4.6687 2.1255 –0.5026
H 2.4720 3.7664 –2.0980
H 4.5367 3.2971 1.7646
H 1.6283 2.5719 5.4149
H –1.6903 2.5708 5.4480
H –4.6216 3.3967 1.8062
H –1.2785 3.3303 –4.2723
H –4.5681 1.6835 –4.5267
H –1.7049 –1.6062 5.0452
H 1.7345 –1.6065 5.0396
H 4.9894 –1.6725 –3.7390
H –2.2785 –5.1933 4.4236
H –2.0657 –0.2252 –6.9460
H 2.2919 –5.1964 4.4530
H –2.0682 –3.1065 –4.7174
H 6.5942 –0.6904 1.0664
H –6.6619 –0.7557 1.0507
H –2.7016 6.2078 1.6678
H 2.5033 6.2173 1.6555
H –6.0573 –1.2936 –2.8929

O –1.7289 2.6220 4.9413
O 1.7272 2.6220 4.9675
O 4.5391 0.6506 –4.1164
O –2.1180 4.7395 3.4382
O –1.9007 2.3281 –5.4545
O 2.1756 4.7244 3.4618
O –1.9601 –0.2564 –5.9442
O 6.3038 0.5293 0.0498
O –6.3282 0.5293 0.0498
O –2.2393 –5.4709 2.4301
O 2.3146 –5.4962 2.4222
O –5.5047 0.7579 –3.6556
H 4.7907 –1.8741 1.1682
H 3.6309 –2.1037 –2.1653
H –4.8653 –1.7218 1.4981
H 2.4548 –3.9159 –2.0538
H 1.6476 –0.5545 5.4332
H –1.6709 –0.5556 5.4663
H 4.6701 –4.3084 1.7471
H –4.6485 –4.4070 1.7265
H –4.2988 –2.1669 –2.5314
H –0.7841 –4.8275 –3.6161
H –1.6905 3.4304 5.6864
H 1.6980 3.4397 5.7027
H 5.4663 0.0706 –4.2342
H –2.3674 5.0594 4.4607
H –2.3362 2.2425 –6.4610
H 2.3988 5.0485 4.4890
H –2.0588 –1.2466 –5.4754
H 6.5265 0.7398 1.1062
H –6.6380 0.6838 1.0939
H –2.2211 –5.3687 3.5252
H 2.3027 –5.3905 3.5170
H –6.3784 0.5465 –3.0217

Geometry T7
Si 0.0000 0.0000 0.0000
O –1.4476 –0.2097 0.6704
O 1.1407 –0.1023 1.1312
O 0.2400 –1.1407 –1.1103
O 0.0568 1.4476 –0.7044
Si 0.8501 2.3672 –1.7597
Si –2.3622 –0.8855 1.8095
Si 2.4346 –0.8602 1.7283
Si 0.8969 –2.4683 –1.7414
O 2.3672 –2.4203 1.3381
O 2.4077 2.4114 –1.3564
O –1.7761 –0.4990 3.2575
O 0.7074 1.7618 –3.2392
O 2.4632 –2.5163 –1.3695
O –2.3571 –2.4847 1.6314
O 3.7669 –0.1983 1.1260
O 0.1579 –3.7669 –1.1417
O 2.4346 –0.7200 3.3335
O 0.7074 –2.4490 –3.3387
O –3.8692 –0.3310 1.6785
O 0.2590 3.8641 –1.7335
O 0.3171 –0.3310 4.8366
Si 4.8835 0.0000 –0.0157
Si –0.0190 –4.9025 –0.0157
Si –1.1899 –0.8855 4.7056
Si 3.9702 2.3786 –1.7440
O 4.6852 –1.1167 –1.1574
Si 2.4152 –3.9867 1.7099
O 1.1167 –4.7256 1.1103
O 4.7446 1.4678 –0.6677
Si 4.0233 –2.4490 –1.7597
O –1.4729 –4.7635 0.6625
Si –2.3710 –4.0827 1.8121
Si 1.8177 –0.9133 4.8025

Geometry T8
Si 0.0000 0.0000 0.0000
O 0.1983 –1.1167 1.1417
O 1.1167 –0.1983 –1.1417
O 0.1390 1.4678 0.6520
O –1.4678 –0.1390 –0.6520
Si 0.9133 2.3786 1.7283
Si –2.3786 –0.9133 –1.7283
Si 0.8602 –2.4490 1.7440
Si 2.4490 –0.8602 –1.7440
O 2.4759 2.4114 1.3407
O –2.4114 –2.4759 –1.3407
O 0.7200 1.7618 3.1973
O –1.7618 –0.7200 –3.1973
O 2.4203 –2.5163 1.3538
O 2.5163 –2.4203 –1.3538
O 0.1023 –3.7429 1.1470
O 3.7429 –0.1023 –1.1470
O 0.7200 –2.4490 3.3492
O 2.4490 –0.7200 –3.3492
O 0.3310 3.8793 1.6942
O –3.8793 –0.3310 –1.6942
Si 0.0000 –4.8835 0.0157
Si 4.8835 0.0000 –0.0157
O 4.6435 –1.1407 1.0946
O 1.1407 –4.6435 –1.0946
Si 4.0334 2.3672 1.7440
Si –2.3672 –4.0334 –1.7440
Si 3.9867 –2.4683 1.7257
Si 2.4683 –3.9867 –1.7257
O 4.8267 1.4476 0.6887
O –1.4476 –4.8267 –0.6887
Si 0.8602 1.7618 4.8025
Si –1.7618 –0.8602 –4.8025
O 0.1983 0.4295 5.4048

Geometry T9
Si 0.0000 0.0000 0.0000
O –0.1769 1.1356 1.1260
O –1.1356 0.1769 –1.1260
O –0.1390 –1.4539 0.6782
O 1.4539 0.1390 –0.6782
Si –0.8198 –2.3521 1.8278
Si 2.3521 0.8198 –1.8278
Si –0.9158 2.4342 1.7257
Si –2.4342 0.9158 –1.7257
O –2.4822 2.3862 1.3538
O –2.3862 2.4822 –1.3538
O –0.4333 –1.7571 3.2733
O 1.7571 0.4333 –3.2733
O –2.4178 –2.3382 1.6471
O 2.3382 2.4178 –1.6471
O –0.2590 3.7618 1.0946
O –3.7618 0.2590 –1.0946
O –0.7263 2.4535 3.3230
O –2.4535 0.7263 –3.3230
O –0.2779 –3.8654 1.7178
O 3.8654 0.2779 –1.7178
O –0.2779 0.3512 4.8287
O –0.3512 0.2779 –4.8287
Si –4.9025 0.0190 0.0157
Si –0.0190 4.9025 –0.0157
Si –0.8198 –1.1621 4.7187
Si 1.1621 0.8198 –4.7187
O –4.6928 –1.4287 0.6861
O 1.4287 4.6928 –0.6861
Si –4.0170 –2.3432 1.8252
Si 2.3432 4.0170 –1.8252
Si –4.0422 2.4535 1.7440
Si –2.4535 4.0422 –1.7440
O –4.8002 1.1596 1.1470

Si 0.8969 1.7811 –4.8366
O 0.2400 0.4535 –5.4676
O 4.1635 1.7618 –3.2130
O –1.1950 –2.4847 4.8837
Si –5.3699 –0.9133 1.7126
Si 0.8009 5.3774 –1.8435
Si 0.8501 –3.0544 –4.8182
O –1.7761 –4.4692 3.2575
O 2.4346 –4.1761 3.3073
O 4.1635 –2.4490 –3.3649
O 1.7849 –2.4759 5.1901
O –5.3370 –2.4759 1.3250
O 2.4632 1.8291 –5.2084
O 3.7429 –4.6435 1.0789
O 2.3988 5.3913 –1.6628
O 4.7812 –3.7429 –1.1627
O –2.1045 –0.2097 5.8447
O 4.5526 3.8793 –1.7099
O 0.0568 –2.1348 –5.8735
O 0.1579 3.0797 –5.4362
O –3.8843 –4.6246 1.7021
O –6.2806 –0.1390 0.6363
O 0.1200 6.2756 –0.6939
O 6.3514 –0.1390 0.6363
O 0.1200 –6.3564 –0.6939
O 2.7285 –0.1390 5.8788
O 2.4077 –3.0986 –5.2215
O 0.2590 –4.5513 –4.8444
O –5.9867 –0.7200 3.1816
O 0.4143 5.9724 –3.2890
H –0.0005 –0.2554 –4.6616
H 4.2902 0.6716 –3.1392
H –1.1960 –2.7344 5.9550
H –1.9180 –3.6262 3.9498
H 2.4279 –3.1895 3.7937
H 4.2853 –3.4821 –3.7223
H 1.7800 –2.5821 6.2849
H –5.3270 –3.0813 2.2434
H 3.0598 1.6006 –4.3129
H 4.2833 –5.1996 1.8591
H 2.6464 5.5110 –0.5977
H 4.8534 –3.6532 –0.0687
H –1.5940 0.6782 6.2459
H 4.5685 4.2430 –0.6719
H –0.9068 –2.6055 –6.1183
H –0.9271 2.9891 –5.2796
H –4.2785 –4.8187 2.7105
H –7.2458 –0.6563 0.5329
H 0.6733 7.2207 –0.5911
H 6.3336 0.2489 1.6655
H 0.1714 –7.1243 0.0921
H 2.1785 0.7315 6.2659
H 3.0072 –3.3686 –4.3396
H 0.1211 –4.9092 –3.8134
H –5.7128 0.2734 3.5665
H –0.0281 5.1769 –3.9065
O –0.4295 –0.1983 –5.4048
O 4.1761 1.7618 3.2235
O –1.7618 –4.1761 –3.2235
Si 0.8855 5.3863 1.8252
Si –5.3863 –0.8855 –1.8252
Si 0.9133 –3.0658 4.8182
Si 3.0658 –0.9133 –4.8182
O 4.1761 –2.4490 3.3230
O 2.4490 –4.1761 –3.3230
O 2.4203 1.8291 5.1927
O –1.8291 –2.4203 –5.1927
O 4.7256 –3.7669 1.1260
O 3.7669 –4.7256 –1.1260
O 2.4847 5.3913 1.6471
O –5.3913 –2.4847 –1.6471
O 0.1023 3.0557 5.3995
O –3.0557 –0.1023 –5.3995
O 4.6246 3.8641 1.7178
O –3.8641 –4.6246 –1.7178
O 0.1390 –2.1550 5.8945
O 2.1550 –0.1390 –5.8945
O 0.2097 6.3008 0.6861
O –6.3008 –0.2097 –0.6861
O 0.2097 –6.3312 0.6861
O 6.3312 –0.2097 –0.6861
O 2.4759 –3.0986 5.2058
O 3.0986 –2.4759 –5.2058
O 0.3310 –4.5665 4.8523
O 4.5665 –0.3310 –4.8523
O 0.4990 5.9724 3.2733
O –5.9724 –0.4990 –3.2733
H 0.1348 0.5143 6.4997
H 0.4247 –0.4363 –4.7538
H 4.1470 2.5795 3.9587
H –1.2923 –5.1648 –3.3337
H 4.0966 –1.4148 3.6892
H 2.4335 –5.2491 –3.5648
H 2.5214 2.0959 6.2551
H –1.8498 –3.0271 –4.2754
H 4.9921 –4.4489 1.9469
H 3.8491 –4.5076 –0.0510
H 2.9635 5.2777 2.6309
H –5.3923 –2.7344 –0.5758
H 0.8384 3.7333 5.8568
H –3.9294 –0.3138 –4.7656
H 4.8477 4.1882 2.7450
H –4.1936 –4.7424 –0.6749
H 0.7325 –1.2535 6.1066
H 1.1898 –0.6563 –5.9979
H –0.6580 5.7752 0.2607
H –5.7903 0.6782 –0.2849
H 0.2278 –6.2290 1.7812
H 7.0050 –0.6895 0.0390
H 2.5943 –2.8565 6.2722
H 3.1087 –3.0813 –4.2874
H 0.2024 –4.8863 5.8969
H 4.9403 –0.2203 –3.8237
H 0.7634 7.0391 3.3196
H –6.5533 –1.3441 –3.6712
O –1.1596 4.8002 –1.1470
Si –0.8691 1.8481 4.8025
Si –1.8481 0.8691 –4.8025
O –2.4178 –1.1760 4.8994
O 1.1760 2.4178 –4.8994
Si –0.8691 –5.3623 1.7440
Si 5.3623 0.8691 –1.7440
O –4.4035 –1.7571 3.2733
O 1.7571 4.4035 –3.2733
O –4.1825 2.4535 3.3492
O –2.4535 4.1825 –3.3492
O –2.4266 –5.3181 1.3407
O 5.3181 2.4266 –1.3407
O –2.4266 1.8039 5.2058
O –1.8039 2.4266 –5.2058
O –4.7042 3.7858 1.1417
O –3.7858 4.7042 –1.1417
O –4.5715 –3.8502 1.6942
O 3.8502 4.5715 –1.6942
O –0.1390 –2.0603 5.8683
O 2.0603 0.1390 –5.8683
O –0.0758 –6.2819 0.6887
O 6.2819 0.0758 –0.6887
O –0.0758 6.3501 0.6887
O –6.3501 0.0758 –0.6887
O –0.0758 2.7677 5.8578
O –2.7677 0.0758 –5.8578
O –0.7263 –5.9677 3.2235
O 5.9677 0.7263 –3.2235
H –2.6673 –1.0627 5.9647
H 1.3373 2.6656 –5.9589
H –4.1391 –0.6904 3.3196
H 1.1763 3.5584 –3.6712
H –4.1245 3.4867 3.7223
H –2.4535 3.1812 –3.8047
H –3.0400 –5.5678 2.2190
H 5.5291 3.0413 –2.2282
H –2.5367 2.0536 6.2714
H –1.5727 2.5216 –6.2770
H –5.8002 3.7010 1.1815
H –3.5404 5.2446 –0.2156
H –4.7127 –4.2775 2.6980
H 4.0730 4.7820 –0.6378
H –0.1849 –1.5243 6.8278
H 2.5552 –0.7567 –5.4646
H 0.3184 –7.1717 1.2014
H 6.2311 0.5752 0.2901
H 0.0691 7.1331 –0.0702
H –7.1020 –0.3648 –0.0175
H –0.6778 3.6575 6.0940
H –3.2376 –0.7852 –5.3600
H –0.7555 –5.1500 3.9587
H 6.4373 –0.2623 –3.3337

REFERENCES

[1] J. Cejka, A. Corma, S. I. Zones, Zeolites and Catalysis: Synthesis, Reactions and Applications; Wiley, New York **2010**.

[2] M. J. Antal, M. Carlsson, X. Xu, D. G. M. Anderson, *Ind*. *Eng*. *Chem*. *Res*. **1998**, *37*, 3820–3829.

[3] C. Zhao, D. M. Camaioni, J. A. Lercher, *J*. *Catal*. **2012**, *288*, 92–103.

[4] C. Zhao, Y. Kou, A. A. Lemonidou, X. Li, J. A. Lercher, *Chem*. *Commun*. **2010**, *46*, 412–414.

[5] A. Pinkert, K. N. Marsh, S. S. Pang, M. P. Staiger, *Chem*. *Rev*. **2009,** *109*, 6712–6728.

[6] R. M. Ravenelle, F. Schüssler, A. D'Amico, N. Danilina, J. A. van Bokhoven, J. A. Lercher, C. W. Jones, C. Sievers, *J*. *Phys*. *Chem*. *C* **2010,** 114, 19582–19595.

[7] A. Cizmek, B. Subotic, I. Smit, A. Tonejc, R. Aiello, F. Crea, A. Nastro, *Micropor*. *Mater*. **1997**, *8*, 159–169.

[8] T. Sano, Y. Nakajima, Z. B. Wang, Y. Kawakami, K. Soga, A. Iwasaki, *Micropor*. *Mater*. **1997**, *12*, 71–77.

[9] A. Guzman, I. Zuazo, A. Feller, R. Olindo, C. Sievers, J. A. Lercher, *Micropor*. *Mesopor*. *Mat*. **2005**, *83*, 309–318.

[10] W. Lutz, W. Gessner, R. Bertram, I. Pitsch, R. Fricke, *Micropor*. *Mater*. **1997**, *12*, 131–139.

[11] S. C. Shen, S. Kawi, *J*. *Phys*. *Chem*. *B* **1999**, *103*, 8870.

[12] R. Mokaya, *J*. *Phys*. *Chem*. *B* **2000**, *104*, 8279–8286.

[13] A. Vjunov, J. L. Fulton, T. Huthwelker, S. Pin, D. Mei, G. Schenter, N. Govind, D. M. Camaioni, J. Z. Hu, J. A. Lercher, *J*. *Am*. *Chem*. *Soc*. **2014**, *136*, 8296–8306.

[14] C. Baerlocher, L. B. McCusker, Database of Zeolite Structures, http://www.iza–structure.org/databases/

[15] J. M. Newsam, M. M. J. Treacy, W. T. Koetsier, C. B. de Gruyter, *Proc. R. Soc. Lond. A* **1988**, *420*, 375–405.

[16] T. Willhammar, X. Zhou, *Z. Kristallogr*. **2013**, *228*, 11–27.

[17] P. W. Voorhees, *J. Stat. Phys.* **1985**, *38*, 231–252.

[18] W. Ostwald, *Zeitschrift für physikalische Chemie*, **1897**, *22*, 289–330.

[19] C. S. Cundy, P. A. Cox, *Chem. Rev*. **2003**, *103*, 663–701.

[20] P. A. Wright, W. Zhou, J. Perez–Pariente, M. Arranz, *J. Am. Chem. Soc.* **2005**, *127*, 494–495.

[21] M. Mehmel, Zeitschrift für Kristallographie **1935**, 90, 35–43.

[22] P. F. Kerr, *Clays and Clay Minerals* **1952**, *1*. 19–32.

[23] Ph. Ildefonse, D. Cabaret, Ph. Sainctavit, G. Calas, A.–M. Flank, P. Lagarde, *Phys. Chem. Minerals* **1998**, *25*, 112–121.

[24] J. A. van Bokhoven, D. C. Koningsberger, P. Kunkeler, H. van Bekkum, A. P. M. Kentgens, *J. Am. Chem. Soc*. **2000**, *122*, 12842–12847.

[25] A. R. Ferreira, E. Kucukbenli, A. A. Leitao, S. de Gironcoli, *Phys. Rev. B* **2011**, *83*, 235119.

[26] J. Perez-Pariente, J. Sanz, V. Fornes, A. Corma, *J. Catal*. **1990**, 124, 217-223.

[27] C A. Fyfe, H. Strobl, G. T. Kokotailo, C. T. Pasztor, G. E. Barlow, S. Bradley, *Zeolites* **1988**, *8*, 132–136.

[28] M. A. Camblor, A. Corma, S. Valencia, *Chem. Comm*. **1996**, 2365–2366.

[29] C. A. Fyfe, Y. Feng, H. Grondey, G.T. Kokotailo, H. Gies, *Chem. Rev.* **1991**, *91,* 1525.

[30] E. Lippmaa, M. Mägi, A. Samoson, M. Tarmak, G. Engelhardt, *J. Am. Chem. Soc.* **1981**, *103*, 4992–4996.

[31] L. Čapek, J. Dědeček, B. Wichterlová, *J. Catal*. **2004**, *227*, 352–366.

[32] M. Hunger, J. Kärger, H. Pfeifer, J. Caro, B. Zibrowius, M Bülow, R. Mostowicz, *J. Chem. Soc., Faraday Trans.1* **1987**, *83*, 3459–3468.

[33] J. Jiao, W. Wang, B. Sulikowski, J. Weitkamp, M. Hunger, Micropor Mesopor Mater. **2006**, 90, 246–250.

[34] S. L. Burkett, M. E. Davis, J. Phys. Chem. **1994**, 98, 4647–4653.

[35] L.T. Zhuravlev, *Colloids Surf. A* **1993**, *74*, 71–90.

[36] E. Lippmaa, A. Samoson, V. V. Brei, Y. I. Gorlov, *Fiz. Chim*. **1981**, *259*, 403.

[37] C. A. Fyfe, G. C. Gobbi, G. J. Kennedy, *J. Am. Chem. Soc.* **1985**, *89*, 277.

[38] A. Pines, M. G. Gibby, J. S. Waugh, *J. Chem. Phys.* **1973**, *59*, 569.

[39] G. Engelhardt, U. Lohse, S. Samoson, M. Mägi, M. Tarmak, E. Lippmaa, *Zeolites* **1982**, *2*, 59–62.

[40] S. L. Burkett, M. E. Davis*, J. Phys. Chem*. **1994**, *98*, 4647–4653.

[41] W. L. Marshall, E. U. Franck, *J. Phys. Chem. Ref. Data* **1981**, *10*, 295–304.

[42] E. P. Guyer, R. H. Dauskardt, *Nature Mat.* **2004**, *3*, 53–57.

[43] S. M. Wiederhorn, S. W. Freiman, E. R. Fuller Jr., C. J. Simmons, *J. Mat. Sci*. **1982**, *17*, 3460–3478.

[44] M. Ciccotti, *J. Phys. D: Appl. Phys*. **2009**, *42(21)*, 214006/1–214006/18.

[45] R. Cook, *Nature Materials* **2004**, *3*, 15–16.

[46] T. A. Michalske, B. C. Bunker, *J. Am. Ceram. Soc*. **1993**, *76*, 2613–2618.

[47] B. K. Atkinson, *J. Geophys. Res*. **1984**, *89*, 4077–4114.

[48] W. Merlijn van Spengen, *Sensors and Actuators A* **2012**, *183*, 57–68.

[49] M. Mehmel, Zeitschrift fur Kristallographie **1935**, 90, 35–43.

Chapter 5

The impact of aqueous reaction medium on zeolite catalyzed dehydration reactions

The catalytic performance of zeolite in aqueous medium depends on a multitude of factors, such as the concentration and distribution of active sites and framework integrity. Al K–edge extended X–ray absorption fine structure and ^{27}Al MAS NMR spectroscopies in combination with DFT calculations are used to determine the distribution of tetrahedral Al sites both qualitatively and quantitatively for both parent and 48 h 160 ºC water treated HBEA catalysts. There is no evidence of Al coordination modification after aging in water. The distribution and concentration of Al T–sites, active centers for the dehydration of cyclohexanol, do not markedly impact the catalytic performance in water, because the Brønsted acidic protons are present in the form of hydrated hydronium ions and thus have very similar acid properties. The results suggest that all Brønsted acid sites are equally active in aqueous medium. The decrease of zeolite catalytic performance after water treatment is attributed to the reduced concentration of Brønsted acid sites. Increasing the stability of pore walls and decreasing the rate of Si–O–Si group hydrolysis may result in improved apparent zeolite catalytic performance in aqueous medium.

5.1 Introduction

Zeolites, microporous solid acids, are suggested as prospective catalysts in the biomass conversion field. The exceptional catalytic performance of these materials is often attributed to the pore environment of the acid sites that allows for improved stabilization of transition states.[1] The transformation of biomass–derived phenolic molecules (lignin) to diesel range hydrocarbon fuels typically requires a complex cascade of chemical reactions.[2] These reactions must be successfully performed in aqueous medium[3] due to the high water content in the feedstock material as well as its ubiquitous presence. Since the alcohol dehydration occurs at temperatures above the boiling point of water, an in–depth study of the catalytic activity as a function of zeolite framework stability is needed. While the degradation of HBEA was shown in Chapter 4 to occur *via* selective T–O–T bond hydrolysis similar to crack propagation in glass, we focus in this Chapter on understanding the performance of the Al–tetrahedral sites (Al T–sites), which are the zeolite active sites, and their behavior in hot liquid water as a function of Al concentration and distribution. The integrity of the zeolite active sites is demonstrated by using a combination of Al extended X–ray absorption fine structure (EXAFS) and magic angle spinning (MAS) nuclear magnetic resonance (NMR) spectroscopies.[4] The catalytic performance of HBEA is tested on the example of aqueous cyclohexanol dehydration following the E1–elimination mechanism,[5] which is the rate–determining step in the overall phenol hydrodeoxygenation (HDO) reaction sequence.[6]

There are several main points that are be addressed in order to substantially improve existing zeolite catalysts: 1) the effect of hot liquid water on the catalytic performance of zeolites in respect to active site integrity and 2) the influence of Al–concentration on the reaction turnover frequency (TOF). In this work we perform a systematic study of the above outlined issues and propose a model that explains the observations and results summarized here. The new insights suggest future research in the field of zeolite post–synthetic modification procedures, e.g. zeolite defect healing *via* silylation of silanol–nests, that may result in extended zeolite lifetime for catalyzed reactions in aqueous phase.

5.2 Experimental methods

5.2.1 Reagents

Cyclohexanol (Sigma–Aldrich, 99%), cyclohexene (Sigma–Aldrich, 99%, GC–grade), 1,3–dimethoxybenzene (Sigma–Aldrich, 99%), dichloromethane (Sigma–Aldrich, HPLC grade), sodium sulfate (Acros Organics, 99%, anhydrous) are used as–received without further purification.

5.2.2 Catalyst preparation

HBEA zeolites are synthesized according to the procedure reported by Derewinski and Fajula.[7] The method is briefly reviewed on the example of HBEA30 (Si/Al=15): 260.2 g tetrahethyl ammonium hydroxide (TEAOH) and 39.6 g water are mixed in a polypropylene beaker. 4.57 g sodium aluminate is then added under vigorous stirring at RT until a clear solution was obtained. 50.0 g Zeosil 175mp (silica source) (Rhone–poulenc) is slowly added to the solution. The system is aged for 24 h at RT under vigorous stirring and then the aged gel is charged into an autoclave with a Teflon liner. The synthesis is performed at 150 °C for 40 h under stirring. The synthesis time (40 h) was identical for all synthesized zeolites. Choosing the appropriate concentration of sodium aluminate in the gel controls the Si/Al ratio in the zeolite. The white product (powder) is filtered and washed with deionized water until pH = 7.5. The material is dried overnight at 80 °C and subsequently calcined at 550 °C in the flow of dry air. The calcined material is ion exchanged using a 0.1 M NH_4NO_3 solution at 80 °C for 2 h, the procedure is repeated 2 times. The zeolite in NH_3–form is treated for 8 h at 450 °C in 100 ccm nitrogen flow to obtain the H–form (HBEA).

An example of typical sample preparation *via* hot liquid water treatment: 0.5 g zeolite and 20 ml deionized water are sealed in a Teflon lined autoclave and heated for 48 h at 160 °C. The autoclave is cooled using ice/water and the samples are centrifuged and dried in vacuum for 24 h prior to storing. Prior to catalyst characterization and catalytic testing the HBEA samples are stored for 48 h in a desiccator over a saturated $Ca(NO_3)_2$ aqueous solution in order to achieve full hydration of the zeolite pores.

5.2.3 Catalyst characterization

The BET surface area and pore volume (Table 1), as well as pore size distributions were determined by N_2 adsorption–desorption isotherms measured at 77.3 K using a ASAP2020 automatic BET–Sorptometer. The total acid site concentration was determined using Temperature–programmed desorption (TPD) of NH_3. The catalysts were activated in vacuum at 723 K for 1 h with at a heating rate of 10 K min^{-1} from RT to 723 K. NH_3 was adsorbed and equilibrated (1 mbar, 373 K) for 1 h. Subsequently, the sample was outgassed for 2 h in order to remove physisorbed molecules. The sample was then heated at a rate of 10 K min^{-1} from 373 to 1033 K for NH_3–TPD and the species desorbing was detected by mass spectrometry (Pfeiffer Prisma QME 200). The concentrations of Brønsted acid sites were determined using infrared spectroscopy (IR) with pyridine as probe molecule. The catalyst samples were activated in vacuum at 723 K for 1 h with at a heating rate of 10 K min^{-1} from 423 to 723 K. Pyridine was adsorbed and equilibrated (1 mbar, 423 K) for 1 h. Subsequently, the sample was outgassed for 1 h in order to remove physisorbed molecules. The sample was then heated at a rate of 10 K min^{-1} from 423 to 723 K to allow partial pyridine desorption (removing molecules adsorbed on weak acid sites). The IR spectra are acquired at after each step using a ThermoScientific Nicolet IR spectrometer. For calibration, a standard (Zeolite HZSM–5 with Si/Al = 45, acid site concentration = 360 μmol g^{-1}) was used.

5.2.4 Catalytic testing

The catalytic testing was performed using the aqueous 0.33 M cyclohexanol dehydration at 160 °C as a test reaction. An example of a typical experiment using a zeolite catalyst: 58 mg HBEA and 80 mL 0.33 M cyclohexanol are sealed in a Hastelloy PARR reactor, pressurized to 50 bar using H_2 and stirred vigorously while heated to 160 °C. An example of a typical H_3PO_4–catalyzed experiment: 100 mL 0.02M phosphoric acid and 3.3 g cyclohexanol are sealed in a Hastelloy PARR reactor, pressurized to 50 bar using H_2 and stirred vigorously while heated to 160 °C. The reaction time is reported counting from the point when the set temperature is reached (~12 min). Upon completion the reactor is cooled using ice/water and the contents are extracted using dichloromethane. The organic phase is analyzed on an Agilent 7890A GC equipped with

HP–5MS 25–m 0.25–μm i.d. column, coupled with Agilent 5975C MS. 1,3 – dimethoxybenzene was used as internal standard for compound quantification.

5.2.5 Al K–edge XAFS

The Al K–edge XAFS experimental as well as analysis methods including DFT and MD calculations are reported in Chapter 3, sections 3.2.2, 3.2.4 and 3.2.5, respectively.

5.2.6 ^{27}Al MAS NMR

The ^{27}Al MAS NMR experimental as well as analysis methods including DFT calculations are reported in Chapter 3, sections 3.2.3 and 3.2.7, respectively.

5.2.7 X–ray diffraction (XRD)

The XRD patterns were collected following the procedure reported in Chapter 4, section 4.2.4.

5.2.8 ^{29}Si MAS NMR

The ^{29}Si MAS NMR experimental methods are reported in Chapter 4, section 4.2.5.

5.2.9 Helium ion microscopy (HIM)

The HIM images were acquired following the experimental methods reported in Chapter 4, section 4.2.6.

5.3 Results and Discussion

5.3.1 Parent HBEA catalyst properties

The HBEA catalysts used in this study are listed in Table 1. While the catalysts Si/Al ratios range from 15 to 40, the samples have comparable surface areas and pore volumes, as shown in Table 1. Although the parent HBEA catalysts have similar morphology, as determined from helium ion microscopy (HIM) images (see Figure 1–4), the particle size varies substantially and is typically related to the Si/Al ratio in the sample. Generally, the more Al is incorporated in the zeolite, the smaller the resulting particle size. As observed from HIM, the individual crystallite size depends on the Si/Al ratio and varies between ~

220 and 450 nm for the studied catalysts. Note that the individual crystallites exhibit a tendency for agglomeration, which leads to the formation of larger spherical particles. The total concentration of Brønsted acid sites (BAS) generally increases with Al–concentration in the zeolite (Table 2). A similar trend is observed for the strong BAS with the exception of HBEA52, which has 280 µmol/g strong BAS, as determined from gas phase pyridine adsorption studies.

5.3.2 Hot liquid water treated catalyst properties

The 48 h 160 ºC water treated samples are also listed in Table 1 and are marked with "w". The HIM images obtained for the water treated samples (see Figures 1–4) do not indicate substantial changes of particle morphology. Note, however, that the particles in the HIM images are better resolved in the case of the water treated HBEA samples, which is tentatively attributed to the removal and re–precipitation of silica, both dissolved from the framework and amorphous synthesis remnants, in an Ostwald ripening–like pattern reported in Chapter 4.

While the 48 h 160 ºC water treatment did not result in a significant modification of the Si/Al ratios, both the zeolite BET surface area and the pore volume have decreased by ~ 30 – 40 % compared to the parent material (Table 1). The acid properties of the HBEA samples have also changed after water treatment. Although the total concentration of acid sites as determined from NH_3–TPD increased by up to ~ 15 % in the case of HBEA30w and HBEA37w, the acid site concentration of HBEA52w and HBEA80w remained nearly identical to the parent samples.

The concentration of Brønsted acid sites, which are considered active centers for the catalytic transformations, was determined using pyridine adsorption followed by IR spectroscopy in the gas phase (Table 2). Because pyridine is a much larger molecule than ammonia and is comparable in size with cyclohexanol, pyridine adsorption probes those acid sites that are accessible during the dehydration reaction. Both the total and strong BAS concentration decreased by ~ 15 – 30 % for the water treated HBEA samples. The only exception from this observation is the HBEA37w sample, which exhibits a concentration of strong BAS approximately equal to that of the parent material. The decrease of the BET surface area and pore volume as well as an apparent decrease of the

Brønsted acid site concentration as determined from pyridine adsorption are attributed to the modification of the zeolite framework induced by the hot water treatment.

Table 1. Studied HBEA zeolite samples with the corresponding element analysis, BET and TPD characterization data.

Sample	Si/Al ratio [a]	Al concentration [a] [mol/g] ($\times 10^{-4}$)	Si concentration [a] [mol/g] ($\times 10^{-2}$)
HBEA30	15	8.9	1.3
HBEA37	18.5	7.4	1.3
HBEA52	26	5.4	1.4
HBEA80	40	3.6	1.4
HBEA30w	14.5	9.1	1.3
HBEA37w	18	7.8	1.4
HBEA52w	24	5.7	1.3
HBEA80w	40	3.6	1.4
Sample	**Surface area [b] [m^2/g]**	**Pore volume [b] [cm^3/g]**	**Total acid site concentration [c] [µmol/g]**
HBEA30	620	0.65	610
HBEA37	670	0.58	600
HBEA52	650	0.40	650
HBEA80	700	0.32	400
HBEA30w	420	0.42	730
HBEA37w	400	0.43	690
HBEA52w	360	0.23	630
HBEA80w	410	0.25	390

[a] Determined from element analysis.
[b] The measurements of micro– and mesopore surface area and volume are reported in the Appendix.
[c] Determined from NH_3–TPD.

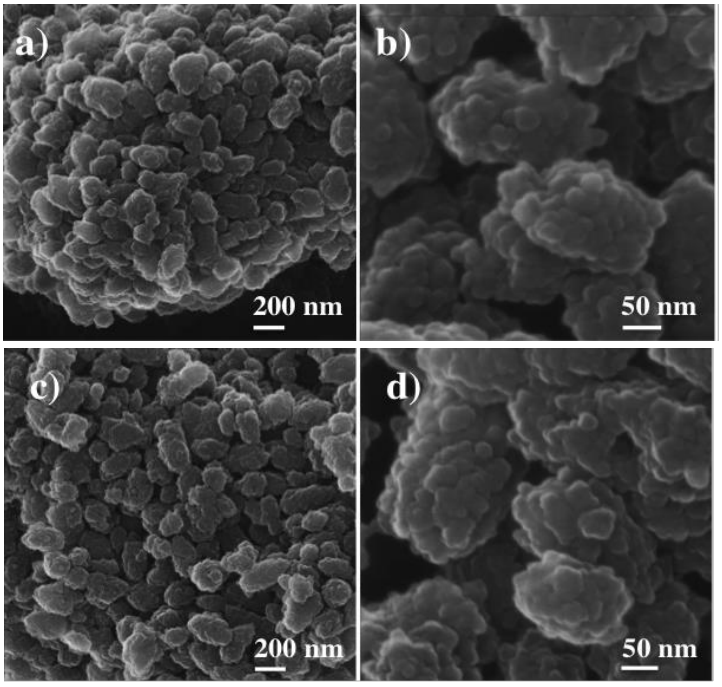

Figure 1. HIM images of the parent (a & b) and the 48 h 160 °C (c & d) water treated HBEA30 samples. The magnification is reported in the plots.

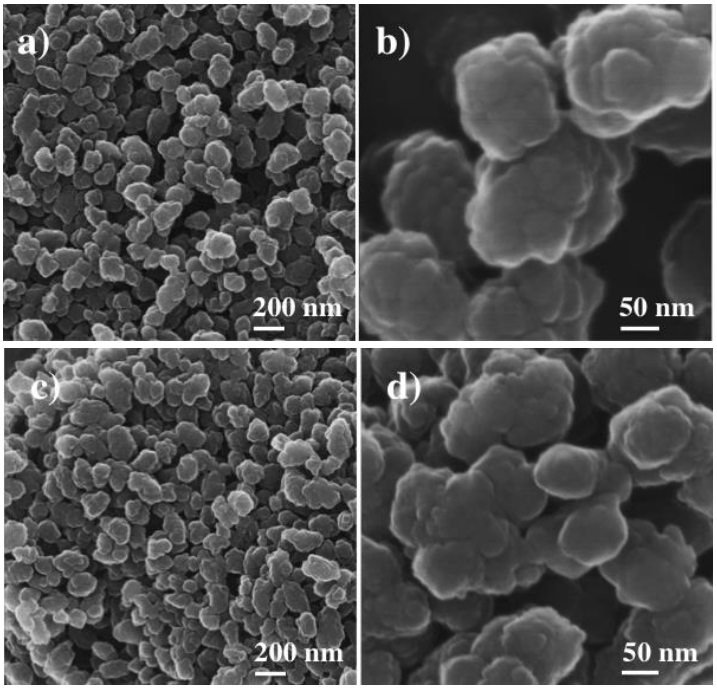

Figure 2. HIM images of the parent (a & b) and the 48 h 160 °C (c & d) water treated HBEA37 samples. The magnification is reported in the plots.

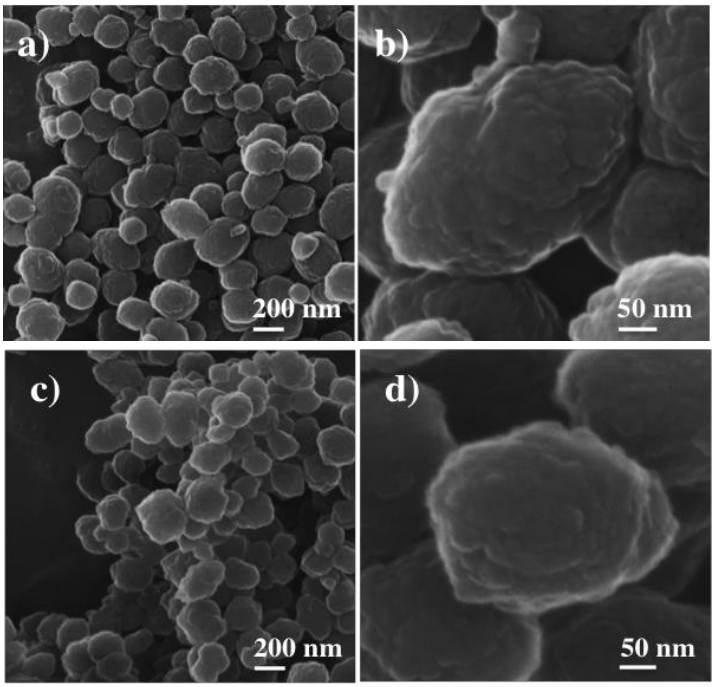

Figure 3. HIM images of the parent (a & b) and the 48 h 160 °C (c & d) water treated HBEA52 samples. The magnification is reported in the plots.

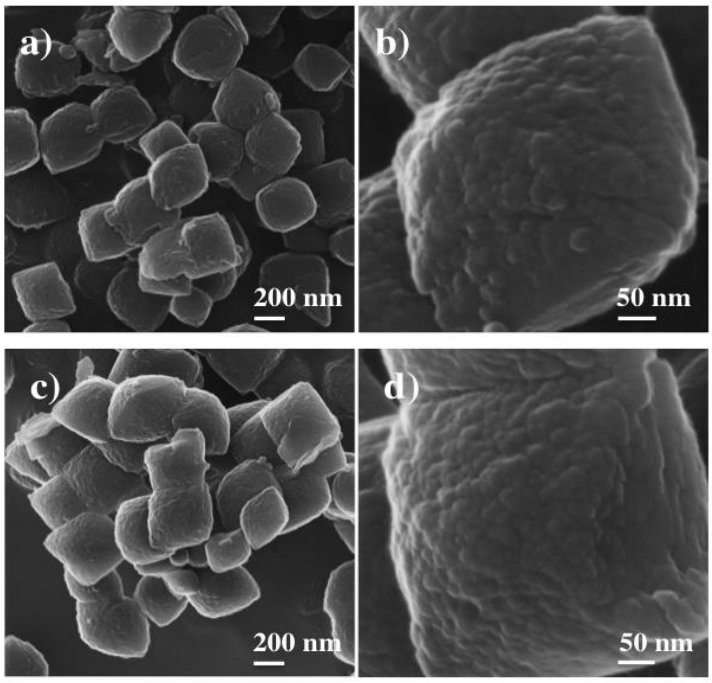

Figure 4. HIM images of the parent (a & b) and the 48 h 160 °C (c & d) water treated HBEA80 samples. The magnification is reported in the plots.

5.3.3 X–ray diffraction analysis

The XRD patterns for the parent and water treated samples are shown in Figure 5 and are used to estimate the degree of crystallinity in the HBEA polymorph intergrowth faulting region[8] that has been suggested to have the largest impact on the stability of HBEA.

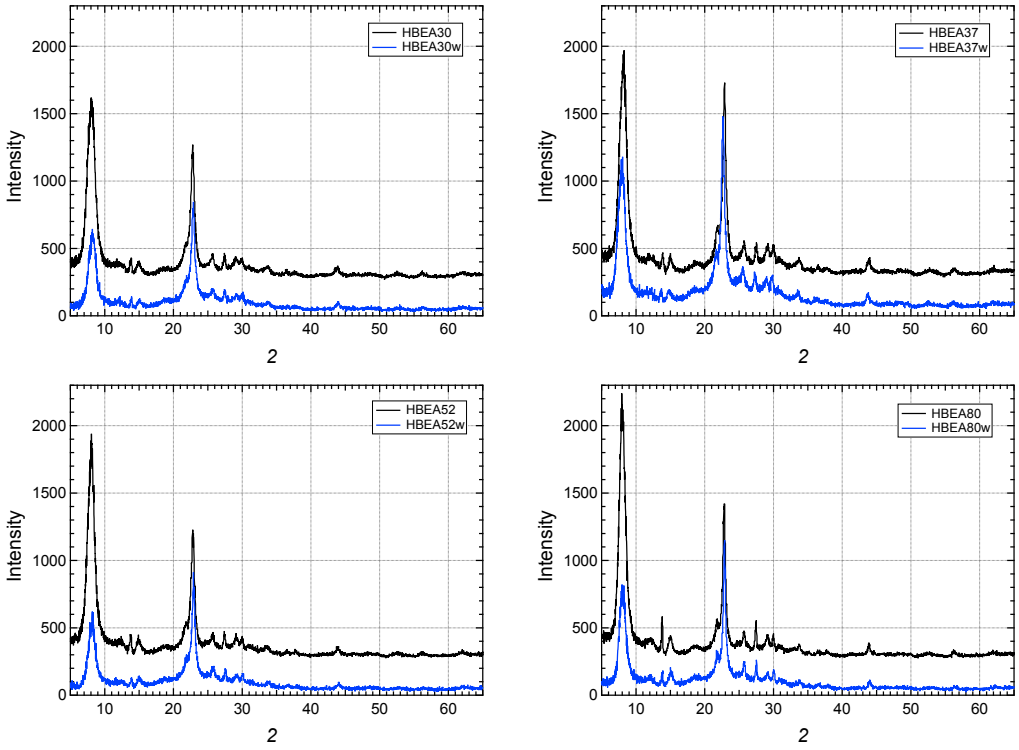

Figure 5. The plots above show the XRD patterns for the parent (black) and hot liquid water treated (blue) zeolites. The respective pairs are reported in the plot legend.

Interestingly, we find that although the XRD signal intensity at 2θ = 7.7 varies substantially for the parent HBEA30, HBEA52 and HBEA80 samples, the corresponding water treated material XRD intensity in the same region is ~ 25 % of the parent sample for these zeolites. Unlike the other catalysts, the crystallinity of HBEA37w was little changed by the water treatment. This observation is tentatively explained by the low concentration of polymorph intergrowth faults present in the parent HBEA37 sample.

Overall, the observations are in agreement with the previously proposed concept (Chapter 4) that the HBEA framework is initially degraded along polymorph intra–crystalline faults followed by the formation of an amorphous silica layer (cap) on the outer surface of the individual crystallites. This step is then followed by an internal degradation of the zeolite, which is reflected by changes in XRD intensities in a wide *2θ* – range. These changes, however, occur predominantly at higher temperatures and are thus not readily observed in this work.

5.3.4 Al XAFS analysis

The Al XANES $x\mu$E plot is shown in Figure 6a. The strong signal intensity observed at ~ 1566 eV for all samples is assigned[9] to the tetrahedral Al in the zeolite samples. The prominent tetrahedral Al feature is attributed primarily to excitations from Al 1s to a mixture of O 3p and Al 3p states.[4] There is no indication of significant amounts of 5– or 6–coordinated Al species, which are typically observed at ~ 1567.5 ev and ~ 1568 eV, respectively,[10] for both the parent and water treated samples. The Al signal intensity is slightly enhanced for all water treated samples suggesting that the overall Al concentration in the zeolites was slightly increased after the water treatment due to Si dissolution from the zeolite framework. This observation is in agreement with the changes in the HBEA Si/Al ratios determined from element analysis (Table 1).

The EXAFS Img$[\tilde{\chi}(R)]$ spectra for the parent and water treated HBEA samples are shown in Figure 6b. The parent HBEA samples appear quite similar in the Img$[\tilde{\chi}(R)]$ representation. This observation suggests that Al may be preferentially distributed among the same Sets of T–sites, but to a different extent. Since the EXAFS spectra indicate that the Al–O bond and Al–Si atom distances of the 48 h 160 ºC water treated HBEA are nearly identical to those of the parent samples, the treatment is suggested not to lead to selective Al removal from the framework.

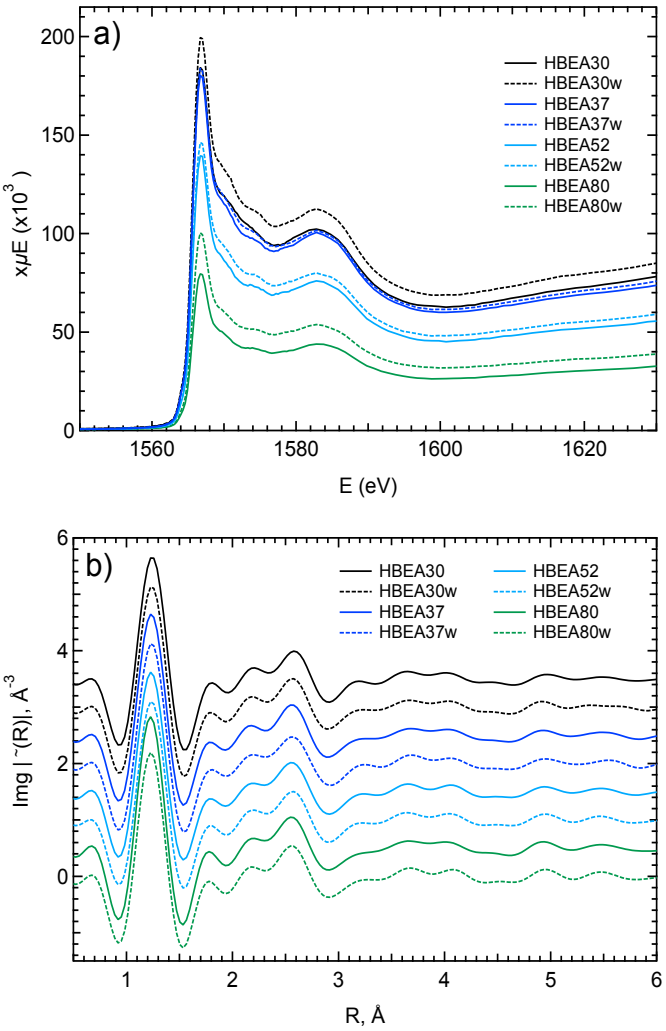

Figure 6. a) XANES $x\mu$E spectra of the parent and 48 h 160 ºC water treated HBEA samples. Note the increase in Al intensity for the water treated samples suggesting higher Al concentration in these samples. The observation is attributed to Si–removal *via* dissolution in water. b) EXAFS Img[$\tilde{\chi}(R)$] spectra for the parent and 48 h 160 ºC water treated HBEA samples. The spectra are offset (y–axis) for better visualization. The color–coding is shown in the legend.

5.3.5 ^{27}Al NMR analysis

The NMR spectra of the parent and water treated samples are shown in Figure 7a. Figure 7b shows the spectral region where tetrahedral Al signals are observed. The DFT NMR calculated chemical shifts are also reported for reference. The measured chemical shifts are in agreement with chemical shift values reported for HBEA previously.[11,12]

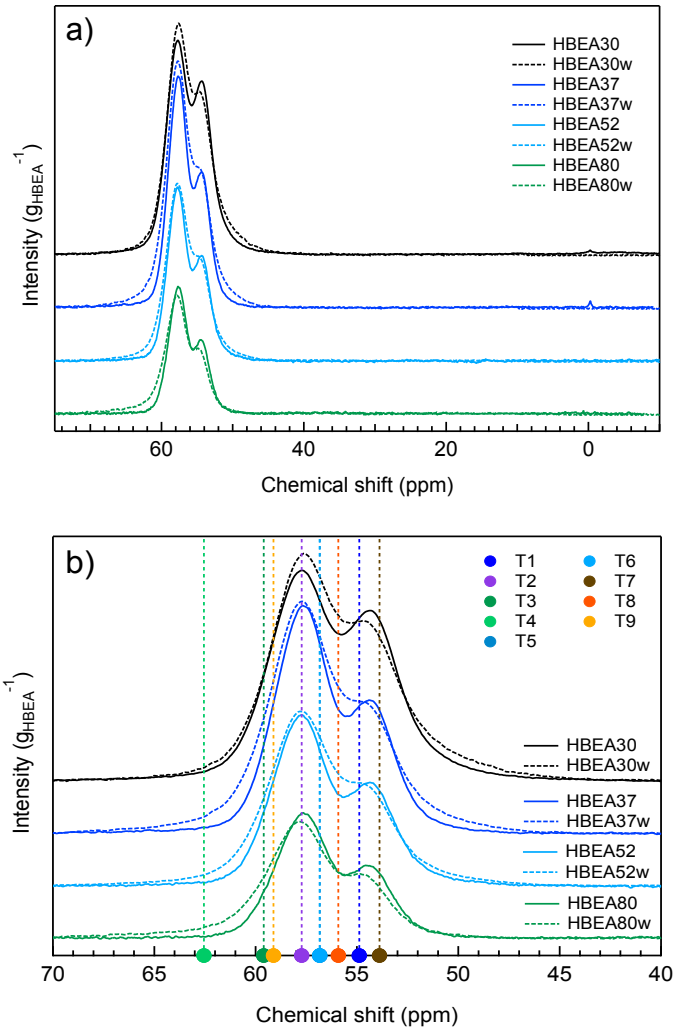

Figure 7. ^{27}Al MAS NMR spectra of the parent and 48 h 160 ºC water treated HBEA samples are shown in a). The region for the tetrahedral Al signal is shown in b). The DFT NMR chemical shifts for all 9 T–sites of HBEA are shown for reference. The color–coding is shown in the legend.

All samples exhibit almost no Al in octahedral coordination, which is typically observed in the ~ 0 ppm region.[13] The NMR region assigned to the 4–coordinated framework Al of the HBEA spans from ~ 52 – 62 ppm and has two distinct peaks at ~ 54 and ~57 ppm. There is no indication of 5–coordinated and extra–framework tetrahedral Al, which are typically observed in NMR in the regions of ~ 30 – 40 ppm[14,15] and ~ 40 – 45 ppm,[16] respectively. All of the studied HBEA samples exhibit a similar NMR peak shape and intensity. The main tetrahedral Al peak accounting for ~3/5 of the spectral intensity is observed at 57.6 ppm and the shoulder peak accounting for ~2/5 of the spectral intensity is observed at 54.3 ppm. Note that the water treatment results in two apparent changes in the NMR: 1) a minor down field shift of the peak positions and 2) a slight broadening of the peaks, which is attributed to distortions in the Si–structure in the vicinity of the Al T–sites. There is no evidence of tetrahedral Al conversion to octahedral coordination during aging in water. The NMR also confirms the determined Al concentration in the samples and is in close agreement with the Si/Al ratios reported in Table 1.

5.3.6 Al–distribution in HBEA

The distribution of Al in HBEA is determined from the combination of EXAFS and NMR supported by theory[4] and is described in detail in the experimental section in Chapter 3. Briefly, for the EXAFS analysis the 9 T–sites of HBEA are grouped in three sets (Set A (T1, T2, T5&T6), Set B (T3, T4) and Set C (T7, T8, T9)) based on geometric similarity of the T–sites. MD EXAFS spectra are calculated for a representative T–site of each set and are then used to fit the experimental spectra as a linear combination. The NMR spectra are fitted using chemical shift values for the 9 T–sites of HBEA calculated for an Al–$(OSi)_4(OH)_{12}^-$ cluster derived from the DFT optimized unit cell of the zeolite.[4] The Al distributions determined for both the parent and water treated HBEA samples are reported as fractions of total Al in the sample and are summarized in in Table A2 in the Appendix.

The Al EXAFS results indicate that the parent zeolite samples contain both Set A (T1, T2, T5, T6) and Set C (T7, T8, T9) T–sites. In all cases Al does not populate the T–sites of set B (T3, T4). The NMR results suggest that in the case of the synthesized HBEA

samples the T2 sites are predominantly (~ 60 %) populated by Al. Al is also incorporated at the T1 and T7 framework positions that demonstrate a very similar distribution of Al. Each of the two sites contains ~ 15 – 20 % of Al. T7 sites are also strongly preferred over T9 sites, both of which form six–member rings in HBEA framework. The NMR spectral fitting results indicate that Al does not populate to as significant extent the T3, T4, T5, T6 and T8 sites in the studied catalysts. The following general observations can be summarized from EXAFS and NMR results (Table A2 in the Appendix): 1) the fraction of Al in Set A T–sites increases with the increase of the Si/Al ratio at the expense of Set C T–sites and 2) T9–sites (part of Set C) are populated only in HBEA30 and HBEA37. Both these samples have a high Al–loading (a low Si/Al ratio).

In the case of the water treated samples there is no significant modification of the Al distribution compared to the respective parent zeolite as determined from EXAFS and NMR. The analysis indicates that there is neither selective Al removal nor re–distribution of Al among the zeolite T–sites. Note that the Al–distributions determined for both the parent and water treatment samples by the EXAFS and NMR are in excellent quantitative agreement and suggest a high concentration of T2 sites in all samples. We speculate that the preferential population of T2 sites by Al is due to the directing role of the template TEAOH used during synthesis of the studied HBEA catalysts. Previously the impact of the template was demonstrated on the example of ferrierite, where the Al distribution was controlled *via* a selection of appropriate organic structure directing agents (SDA) that preferentially occupy certain well defined–positions within the void volume of the zeolite framework.[17] The synthesis conditions used in this work have also resulted in the formation of isolated (determined from ^{29}Si NMR) Al T–sites. This Al distribution pattern was targeted in order to study the individual active sites and exclude the possible synergistic effects in the case of Al–pairing. In the past Dedecek et al. have shown that the sources of Si and Al as well as the synthesis temperature can affect the Al distribution and alter the pattern of the Al–O–(Si–O)$_n$–Al sequences.[18].

5.3.7 ^{29}Si MAS NMR

The acquired single pulse (SP) and cross–polarization (CP) ^{29}Si NMR spectra for the parent and water treated HBEA zeolites are shown in Figures 8 and 9, respectively. The SP NMR spectra for the parent and water treated HBEA samples are shown in Figure 8a and 8b, respectively. In the SP NMR the main peak centered at ~ –111.5 ppm is attributed to the Si Q^4 atoms.[19] Shoulder peaks left and right of the main peak are due to the distribution of NMR chemical shifts of the nine T–sites of HBEA. The signal at ~ –103 ppm[20] is assigned to the Si Q^3 [$Si(OSi)_3OAl$]. The variation of intensity for this peak is explained by the differences in the Si/Al ratios of the studied samples. The SP NMR shows that there is only a negligible amount of Si Q^2, which is typically observed at –98 ppm,[21] indicating that the amount of paired Al atoms forming an Al–O–Si–O–Al pattern is also negligible. The SP NMR spectra of the treated samples reflect the changes in the Si–O backbone of the zeolites in water. A slight decrease in signal intensity as well as broadening of the NMR spectra is observed for all samples and is attributed to the increasing number of structural defects as the zeolite framework is degraded.

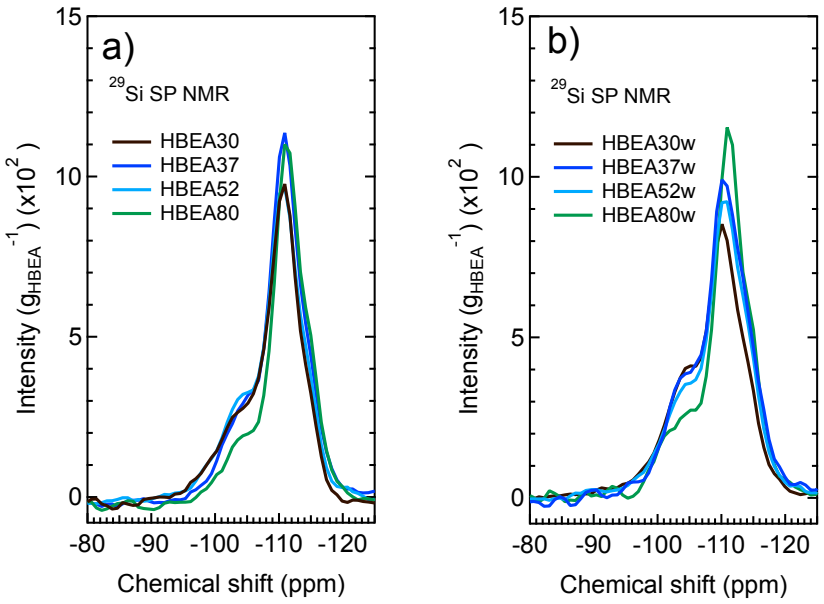

Figure 8. ^{29}Si MAS NMR single pulse (SP) spectra of the parent (a) and water treated (b) HBEA samples. The color–coding is shown in the legend.

The CP NMR spectra for the parent and water treated HBEA samples are shown in Figure 9a and 9b, respectively. The large peak at ~ –101 ppm is assigned to the $Si(OH)(OSi)_3$.[22] The Si Q^3, $Si(OSi)_3OAl$, atoms that neighbor Al T–sites are assigned to NMR signals around ~ –106 ppm.[20] The CP NMR signals from –110 to –115 ppm are assigned to the Si Q^4 atom of the zeolite.[19] The CP NMR spectra of the parent samples show as an overall trend that the signal intensity in the Si Q^3 region increases with decreasing Si/Al ratios in the sample. The higher Al concentration in HBEA leads to the formation of smaller crystallites (kinetic control during synthesis), which in turn leads to a high number of inter–crystal growth faults. These faulting regions contain a high concentration of Si–OH defect sites and Si–OH nests. The signal intensity at –101 ppm (Si Q^3 region) is markedly increased for the water treated samples, suggesting increased concentration of Si–OH groups within the lattice structure (Si–OH nests).[23]

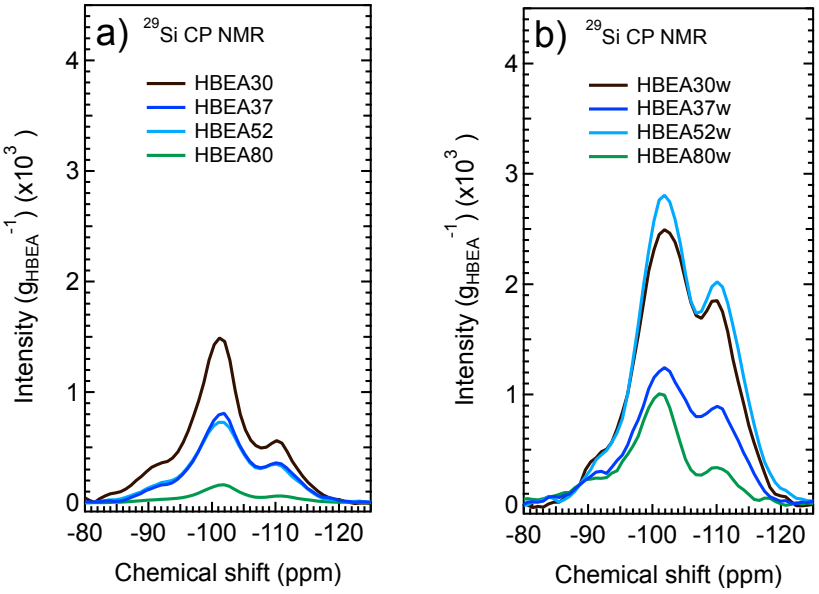

Figure 9. ^{29}Si MAS NMR cross–polarization (CP) spectra of the parent (a) and water treated (b) HBEA samples. The color–coding is shown in the legend.

While the CP NMR signal is enhanced for all water treated samples, it no longer correlates with the Al–concentration in the sample (as observed for the parent samples). Thus we speculate that the Al–concentration in HBEA alone does not direct the rate of

framework hydroxylation and that while the Al–distribution in the sample may have subtle effects on the overall framework stability, its impact is less important than the concentration of Si–OH defects that play the dominant role in the integrity of HBEA structure. The formation of surface OH–groups (typically a signal at –100 ppm)[24] cannot be unambiguously determined from the CP NMR due to substantial peak broadening. Lippmaa et al. showed that the higher chemical shift value can be related to a rearrangement in the neighboring Si–OH groups in geminal $[Si(OH)_2(OSi)_2]$ or vicinal $[(OSi)_3Si–OH\ HO–Si(OSi)_3]$ conformation.[25] As only a minor signal (by comparison) is observed at –90 ppm,[26,27] which is attributed to the Si Q^2 $[Si(OH)_2(OSi)_2]$, most Si–OH groups are suggested to be in a vicinal conformation in both the parent and water treated samples.

5.3.8 Catalytic testing

The HBEA catalytic testing is performed using the cyclohexanol dehydration reaction, which has been shown as the rate–determining step of the phenol hydrodeoxygenation sequence.[28] The mechanism of the dehydration reaction is reported in Chapter 2. While cyclohexene was observed as primary product in this reaction, dicyclohexyl ether was also formed in the initial reaction phase, however, the maximum yield was << 1 %.

The time–dependent yields of cyclohexene (%) obtained using the eight zeolite catalysts are shown in Figure 10. The corresponding rates of cyclohexene formation and turnover frequencies (TOF) are reported in Table 2. Note that both the dehydration reaction rate [mol × s^{-1} × g^{-1}] and TOF [mol × $mol_{Strong\ BAS}^{-1}$ × s^{-1}] normalized to the concentration of strong Brønsted acid sites are very similar for three of the four parent HBEA samples. Only the HBEA80 sample exhibits a slightly lower activity. However, if TOF is determined assuming all (both strong and weak BAS as determined from pyridine adsorption in the gas phase) Brønsted acid sites are equally active, then all studied catalysts exhibit identical TOF values for the dehydration reaction. There is also no direct correlation between the apparent catalytic performance of the parent HBEA and the Si/Al ratio of the zeolite. The distribution of Al among the zeolite T–sites does not markedly impact the observed reaction rates.

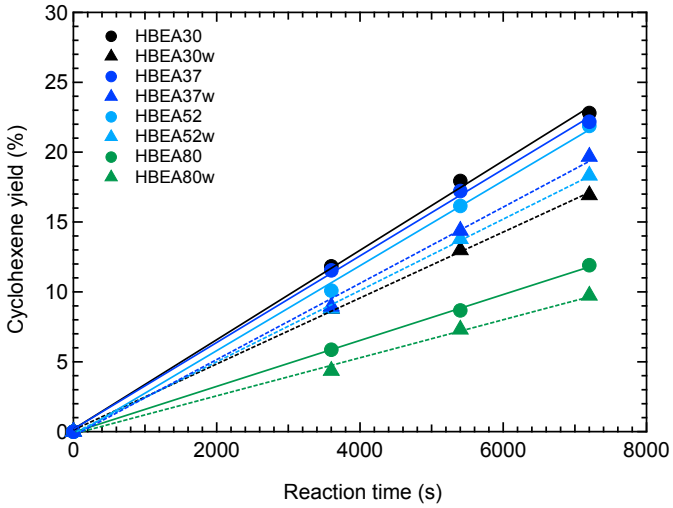

***Figure 10*.** The yield of cyclohexene is reported as a function of reaction time. The color–coding for the HBEA samples is reported in the legend.

While the rates of cyclohexene formation determined for the water treated samples are very similar, they are as much as 25 % lower than those observed for the corresponding parent HBEA. When comparing the TOF values we observe similar trends as discussed above: the reported difference in catalytic performance depends on the normalization to either to the concentration of strong or to the concentration of all BAS. In the first case the HBEA80w (the product of HBEA80 water treatment) exhibits lower TOF values compared to the other aged samples. However, the four water treated samples have TOF values identical to those of the parent HBEA when all Brønsted acid sites are assigned as catalytically active in water. Because both the tetrahedral/octahedral and the Si/Al ratios of the treated samples are very similar to the parent material, no direct correlation between Al coordination and TOF can be made for the treated samples. Similar to the parent samples, there is also no linear dependence between the catalytic performance of aged HBEA and the zeolite Si/Al ratio.

In order to better appreciate zeolite activity in water we also performed the dehydration reaction using H_3PO_4, a prototypical mineral acid catalyst for dehydration of alcohols. The rates and 1–hour cyclohexene yields are reported in Table 2. The TOF value determined for H_3PO_4 in Table 2 is based on the dissociation equilibrium estimated according to the report by Mesmer et al.,[29] which suggests that at 160 ºC for a 0.02 M

H_3PO_4 solution the concentration of protons present in the form of hydrated hydronium ions is ~ 10 % of the acid concentration. Thus, when normalized to the concentration of hydronium ions, the dehydration is approximately 20 times slower than that catalyzed by HBEA. Note that the H_3PO_4 –catalyzed dehydration is approximately 200 times slower if TOF is determined by normalizing to H_3PO_4 concentration rather than hydronium ions.

Table 2. The catalytic performance of the parent and water treated zeolite samples is tested on the cyclohexanol dehydration reaction. The rates of formation as well as TOF are reported for cyclohexene, the main dehydration product. Reaction conditions: 80 mL 0.33 M cyclohexanol + 58 mg HBEA reacting at 160 ºC.

Catalyst	Si/Al ratio [a]	Strong Brønsted acid sites [µmol/g] [b]	Total Brønsted acid sites [µmol/g] [b]	Cyclohexene yield (%) [c]
HBEA30	15.1	330	400	11.4
HBEA37	18.3	260	360	11.1
HBEA52	26.2	280	360	11.0
HBEA80	40.1	210	220	6.0
HBEA30w	14.8	230	290	8.5
HBEA37w	18.0	290	320	9.9
HBEA52w	24.0	250	300	9.2
HBEA80w	40.5	170	180	4.9
0.02M H_3PO_4	N/A	N/A	1190 [d]	19.1

Catalyst	Rate of cyclohexene formation [mol × s^{-1} × g^{-1}] (×10^{-6})	TOF normalized to strong BAS concentration [mol × $mol_{Strong\ BAS}^{-1}$ × s^{-1}] (×10^{-3})	TOF normalized to total BAS concentration [mol × $mol_{Total\ BAS}^{-1}$ × s^{-1}] (×10^{-3})
HBEA30	14.6 ± 1.0	44.5 ± 3.1	36.4 ± 2.5
HBEA37	14.1 ± 1.0	54.3 ± 3.8	39.2 ± 2.7
HBEA52	13.8 ± 1.0	49.8 ± 3.5	38.4 ± 2.7
HBEA80	7.5 ± 0.5	35.4 ± 2.5	33.9 ± 2.4
HBEA30w	10.7 ± 0.8	46.7 ± 3.3	37.0 ± 2.6
HBEA37w	12.4 ± 0.9	42.7 ± 3.0	38.8 ± 2.7
HBEA52w	11.6 ± 0.8	46.8 ± 3.3	38.7 ± 2.7
HBEA80w	6.2 ± 0.4	35.6 ± 2.5	34.4 ± 2.4
0.02M H_3PO_4	0.7 ± 0.05	N/A	1.7 ± 0.1

[a] Determined from element analysis; [b] BAS concentration is determined from pyridine adsorption measurements, the accuracy is estimated at ±10%; [c] Determined yield for the 1 h reaction; [d] Acid site concentration estimate is reported in µmol(H^+)/g(added H_3PO_4). The estimate is based on H_3PO_4 dissociation equilibrium reported by Mesmer et al.[29]

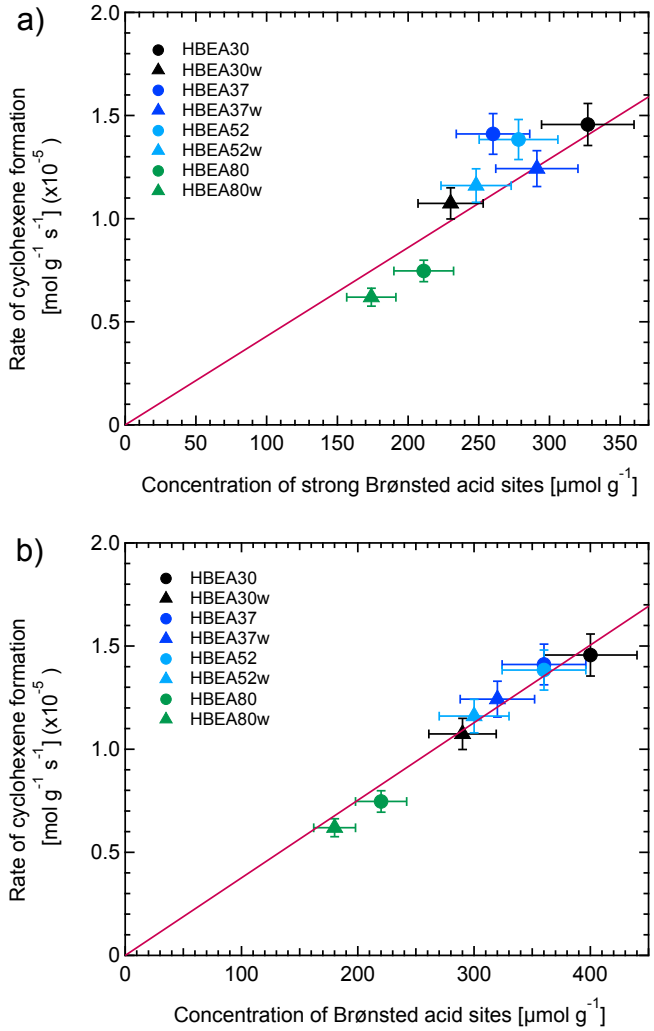

Figure 11. The rate of cyclohexene formation is reported as a function of the concentration of a) strong BAS and b) total BAS determined by pyridine adsorption. The color–coding for the HBEA samples is reported in the legend.

Figure 11a shows that while the observed rate of cyclohexene formation correlates with the concentration of strong Brønsted acid sites (BAS) in the catalyst, this correlation is improved substantially if weak BAS are included (see Figure 11b). We suggest that all Brønsted acid sites exhibit similar activity in aqueous medium, because in the presence of water zeolite protons are present in the form of hydrated H_3O^+ ions.[30] This in turn implies that the intrinsic acid site strength and catalytic performance must be largely independent

of both the Al position in the framework and the acid strength determined in the gas phase by pyridine adsorption.

The aging of HBEA in water prior to catalytic testing results is an alteration of the zeolite performance due to T–O–T hydrolysis during lattice degradation resulting in a decrease of both pore volume and BET surface as well as a decrease in long–range order in the lattice (XRD). Because the zeolite active sites, Al T–sites, retain geometry after water treatment (EXAFS), the observed rates and turnover frequencies for olefin formation should not decrease unless the catalytic performance is dependent on the zeolite pore environment[31] and its ability to stabilize transition states and intermediates.[32] Minor differences in zeolite catalytic activity (TOF normalized to BAS concentration) observed in this work are attributed to the stability of the HBEA catalysts in water.

A possible solution for improving zeolite catalytic performance in water may be achieved by decreasing the concentration of surface silanol–sites as well as silanol–nests, which have been proposed as reactive centers for the framework decomposition.[33] We suggest future work toward increasing HBEA framework stability *via* post–synthetic treatment of zeolite, e.g. curing of Si–OH to form a hydrophobic particle surface.[34]

5.4 Conclusions

The impact of Al T–site concentration on aqueous phase catalysis was studied on the example of cyclohexanol dehydration reaction. The zeolite TOF in aqueous medium is proportional to the total concentration of Brønsted acid sites. Both strong and weak BAS, as determined from gas phase adsorption of pyridine, are equally active in water, because the Brønsted acid protons are dissociated in the zeolite pores and present as hydrated hydronium ions. The apparent catalytic performance of HBEA is suggested to depend on the stability of the zeolite framework, which is readily hydrolyzed in the presence of liquid water leading to a reduction of the active site concentration. Further work toward decreasing the rate of hydrolysis of T–O–T groups by lowering the Si–OH group concentration either by design or post–synthetic treatment may result in extended lifetime and higher apparent catalytic performance of zeolites in water.

5.5 Acknowledgements

B. W. Arey (PNNL) is acknowledged for HIM measurements, T. Huthwelker for support during Al XAFS measurements at the Swiss Light Source (PSI, Switzerland), J. Z. Hu and S. D. Burton (PNNL) for support during NMR experiments. This work was supported by the U. S. Department of Energy (DOE), Office of Basic Energy Sciences, Division of Chemical Sciences, Geosciences & Biosciences.

5.6 Appendix

5.6.1 BET Surface area and pore volume measurements

The micro– and mesopore BET surface area measurement results are reported in Table A1. The distribution of micro– and mesopores in the size range of 1.7–20 nm is shown in Figure A1.

Table A1. The measured BET surface area and pore volume for the studied HBEA zeolites.

Sample	Si/Al	Total pore area [m^2/g]	Mesopore surface area [m^2/g]	Micropore surface area [m^2/g]
HBEA30	15	624	186	438
HBEA37	18.5	666	152	514
HBEA52	26	650	80	570
HBEA80	40	697	98	599
HBEA30w	14.5	417	87	330
HBEA37w	18	401	80	321
HBEA52w	24	355	54	301
HBEA80w	40	408	94	314

Sample	Total pore volume [cm^3/g]	Mesopore volume [cm^3/g]	Micropore volume [cm^3/g]
HBEA30	0.65	0.50	0.15
HBEA37	0.58	0.40	0.18
HBEA52	0.40	0.20	0.20
HBEA80	0.32	0.08	0.24
HBEA30w	0.42	0.32	0.10
HBEA37w	0.43	0.33	0.10
HBEA52w	0.23	0.14	0.09
HBEA80w	0.25	0.13	0.12

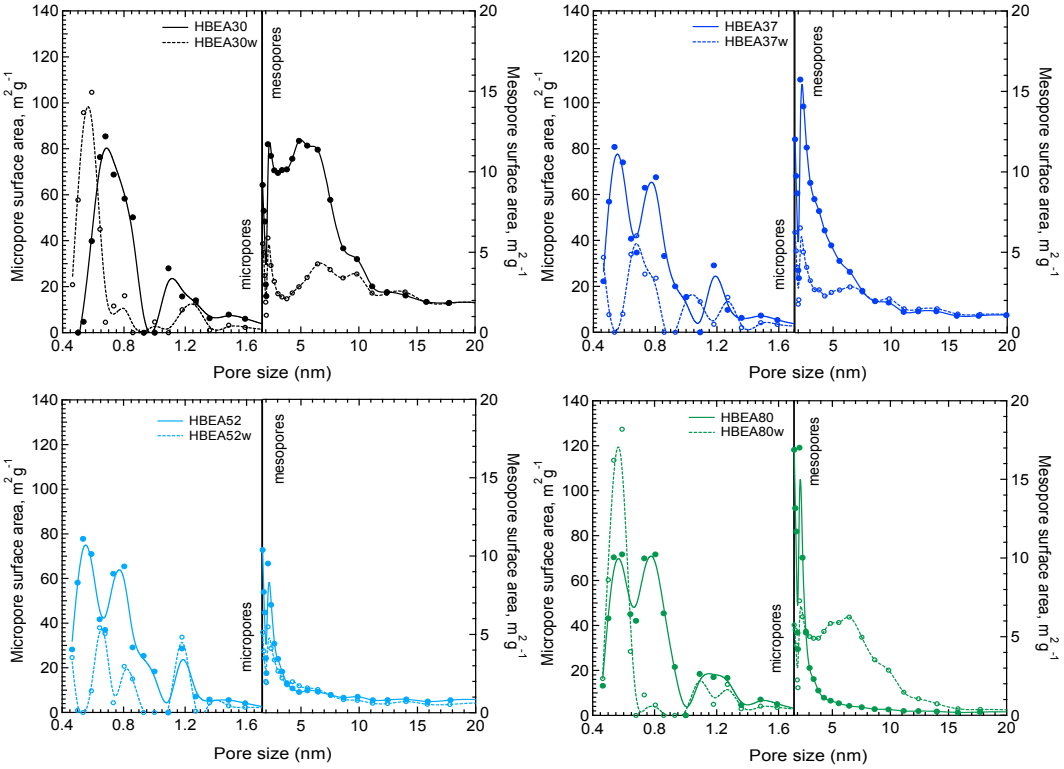

Figure A1. The distribution of micro– and mesopore BET surface area measured for the parent and water treated HBEA catalysts are shown. The color–coding is reported in the legend. The markers indicate measured points. The lines are a spline fit to the experimental data.

5.6.2 Al distribution from DFT NMR and EXAFS

The NMR spectra measured for the parent samples were fitted using the chemical shift values for individual T–sites determined from DFT NMR calculations. The method and ^{27}Al DFT NMR chemical shifts were reported previously in detail in *J. Am. Chem. Soc*. **2014,** *136*, 8296–8306. The fitted NMR spectra are shown in Figure A2. The Al distribution determined from NMR and EXAFS is reported in Table A2. Note that the two independent techniques are in excellent quantitative agreement.

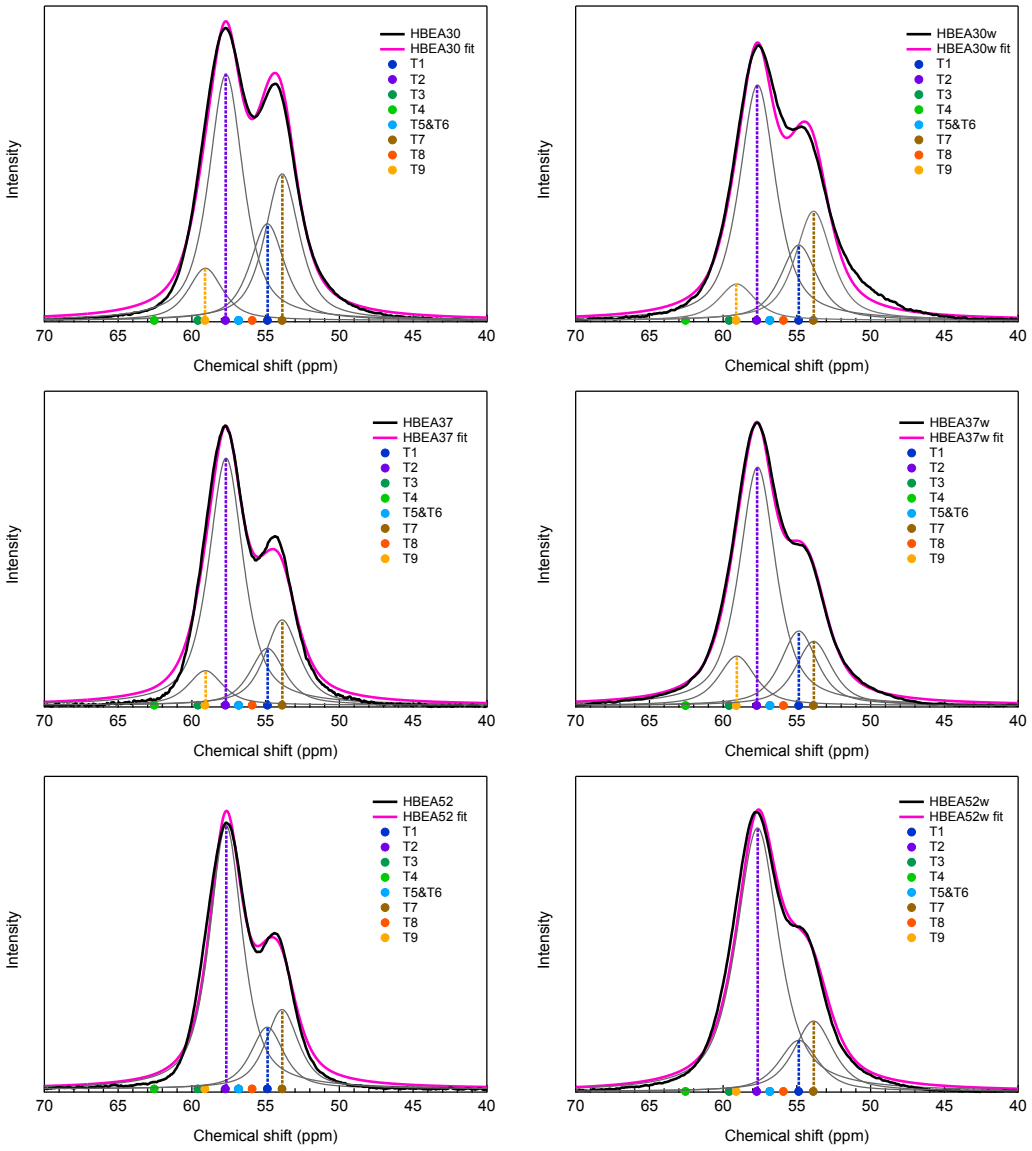

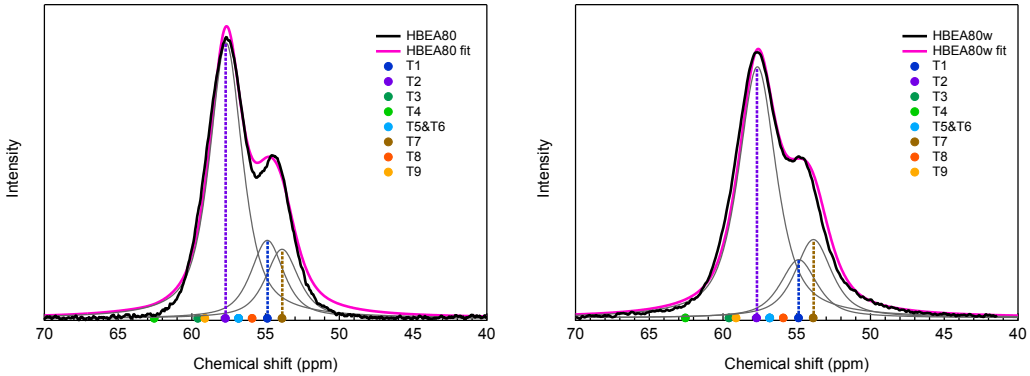

Figure A2. The ^{27}Al MAS NMR spectral regions containing the tetrahedral Al features (40–70 ppm) for the parent and water treated HBEA samples are shown. Measured spectrum (black), the least square fit (magenta) and individual T–site contributions to the spectra (grey) are shown. The 9 T–sites of HBEA are shown as markers (dots). The color–coding is reported in the legend. Note that the DFT NMR chemical shifts for T5– and T6–sites are nearly identical and overlap in this projection.

Table A2. Al T–site distribution determined for the parent and water treated HBEA zeolites from EXAFS and NMR.

HBEA30 EXAFS grouped T–sites	Distribution [a]		HBEA30 NMR T–sites (fraction)	HBEA30w EXAFS grouped T–sites	Distribution [a]		HBEA30w NMR T–sites (fraction)
	via EXAFS	*via* NMR			*via* EXAFS	*via* NMR	
Set A (T1, 2, 5, 6)	0.66	0.63	1 (0.18), 2 (0.45), 5+6 (0)	Set A (T1, 2, 5, 6)	0.71	0.71	1 (0.19), 2 (0.52), 5+6 (0)
Set B (T3, 4)	0	0	3 (0), 4 (0)	Set B (T3, 4)	0	0	3 (0), 4 (0)
Set C (T7, 8, 9)	0.34	0.36	7 (0.27), 8 (0), 9 (0.09)	Set C (T7, 8, 9)	0.25	0.27	7 (0.21), 8 (0), 9 (0.06)
AlO_6^- (octahedral)	0	0.01	AlO_6^- (octahedral)	AlO_6^- (octahedral)	0.04	0.02	AlO_6^- (octahedral)
HBEA37 EXAFS grouped T–sites	Distribution [a]		HBEA37 NMR T–sites (fraction)	HBEA37w EXAFS grouped T–sites	Distribution [a]		HBEA37w NMR T–sites (fraction)
	via EXAFS	*via* NMR			*via* EXAFS	*via* NMR	
Set A (T1, 2, 5, 6)	0.75	0.72	1 (0.14), 2 (0.58), 5+6 (0)	Set A (T1, 2, 5, 6)	0.78	0.72	1 (0.17), 2 (0.55), 5+6 (0)
Set B (T3, 4)	0	0	3 (0), 4 (0)	Set B (T3, 4)	0	0	3 (0), 4 (0)
Set C (T7, 8, 9)	0.25	0.28	7 (0.20), 8 (0), 9 (0.08)	Set C (T7, 8, 9)	0.19	0.26	7 (0.16), 8 (0), 9 (0.10)
AlO_6^- (octahedral)	0	0	AlO_6^- (octahedral)	AlO_6^- (octahedral)	0.03	0.02	AlO_6^- (octahedral)
HBEA52 EXAFS grouped T–sites	Distribution [a]		HBEA52 NMR T–sites (fraction)	HBEA52w EXAFS grouped T–sites	Distribution [a]		HBEA52w NMR T–sites (fraction)
	via EXAFS	*via* NMR			*via* EXAFS	*via* NMR	
Set A (T1, 2, 5, 6)	0.79	0.80	1 (0.15), 2 (0.65), 5+6 (0)	Set A (T1, 2, 5, 6)	0.77	0.80	1 (0.12), 2 (0.68), 5+6 (0)
Set B (T3, 4)	0	0	3 (0), 4 (0)	Set B (T3, 4)	0	0	3 (0), 4 (0)
Set C (T7, 8, 9)	0.21	0.20	7 (0.20), 8 (0), 9 (0)	Set C (T7, 8, 9)	0.21	0.18	7 (0.18), 8 (0), 9 (0)
AlO_6^- (octahedral)	0	0	AlO_6^- (octahedral)	AlO_6^- (octahedral)	0.02	0.02	AlO_6^- (octahedral)
HBEA80 EXAFS grouped T–sites	Distribution [a]		HBEA80 NMR T–sites (fraction)	HBEA80w EXAFS grouped T–sites	Distribution [a]		HBEA80w NMR T–sites (fraction)
	via EXAFS	*via* NMR			*via* EXAFS	*via* NMR	
Set A (T1, 2, 5, 6)	0.80	0.83	1 (0.18), 2 (0.65), 5+6 (0)	Set A (T1, 2, 5, 6)	0.76	0.79	1 (0.14), 2 (0.65), 5+6 (0)
Set B (T3, 4)	0	0	3 (0), 4 (0)	Set B (T3, 4)	0	0	3 (0), 4 (0)
Set C (T7, 8, 9)	0.20	0.16	7 (0.16), 8 (0), 9 (0)	Set C (T7, 8, 9)	0.24	0.20	7 (0.20), 8 (0), 9 (0)
AlO_6^- (octahedral)	0	0.01	AlO_6^- (octahedral)	AlO_6^- (octahedral)	0	0.01	AlO_6^- (octahedral)

[a] The estimated errors are ± 10% by EXAFS and NMR.

REFERENCES

[1] M. J. Antal, M. Carlsson, X. Xu, D. G. M. Anderson, *Ind. Eng. Chem. Res.* **1998**, *37*, 3820–3829.

[2] C. Zhao, J. A. Lercher, *Angew. Chem. Int. Ed.* **2012**, *51*, 5935–5940.

[3] A. Pinkert, K. N. Marsh, S. S. Pang, M. P. Staiger, *Chem. Rev.* **2009,** *109*, 6712–6728.

[4] A. Vjunov, J. L. Fulton, T. Huthwelker, S. Pin, D. Mei, G. Schenter, N. Govind, D. M. Camaioni, J. Z. Hu, J. A. Lercher, *J. Am. Chem. Soc.* **2014,** *136*, 8296–8306**.**

[5] A. Vjunov, M. Y. Hu, J. Feng, D. M. Camaioni, D. Mei, J. Z. Hu, C. Zhao, J. A. Lercher, *Angew. Chem. Int. Ed.* **2014**, *53*, 479–482.

[6] C. Zhao, Y. Kou, A. A. Lemonidou, X. Li, J. A. Lercher, *Chem. Commun.* **2010**, *46*, 412–414.

[7] M. A. Derewinski, F. Fajula, *Appl. Catal. A:General* **1994**, *108*, 53–61.

[8] P. A. Wright, W. Zhou, J. Perez–Pariente, M. Arranz, *J. Am. Chem. Soc.* **2005**, *127*, 494–495.

[9] J. A. van Bokhoven, H. Sambe, D. E. Ramaker, D. C. Koningsberger, *J. Phys. Chem. B* **1999**, *103*, 7557–7564.

[10] D. Li, G. M. Bancroft, M. E. Fleet, X. H. Feng, Y. Pan, *Am. Miner.* **1995**, *80*, 432–440.

[11] J. A. van Bokhoven, A. M. J. van der Berden, D. C. Koningsberger, *J. Am. Chem. Soc.* **2003**, *125*, 7435–7442.

[12] S. M. Maier, A. Jentys, J. A Lercher, *J. Phys. Chem. C* **2011**, *115*, 8005–8011.

[13] J. A. van Bokhoven, D. C. Koningsberger, P. Kunkeler, H. van Bekkum, A. P. M. Kentgens, *J. Am. Chem. Soc.* **2000**, *122*, 12842–12847.

[14] F. Deng, Y. Yue, C. Ye, *J. Phys. Chem. B* **1998**, *102*, 5252–5256.

[15] M. Hunger, G. Engelhardt, J. Weitkamp, *Microporous Mater.* **1995**, *3*, 497.

[16] J. Perez–Pariente, J. Sanz, V. Fornes, A. Corma, *J. Catal.* **1990**, *124*, 217–223.

[17] A. B. Pinar, L. Gomez–Hortguela, L. B. McCusker, J. Perez–Pariente, *J. Chem. Mat.* **2013**, *25*, 3654–3661.

[18] V. Gabova, J. Dedecek, J. Cejka, *Chem. Commun.* **2003**, 1196.

[19] E. Lippmaa, M. Mägi, A. Samoson, M. Tarmak, G. Engelhardt, *J. Am. Chem. Soc.* **1981**, *103*, 4992–4996.

[20] L. Čapek, J. Dědeček, B. Wichterlová, *J. Catal.* **2004**, *227*, 352–366.

[21] C. A. Fyfe, Y. Feng, H. Grondey, G.T. Kokotailo, H. Gies, *Chem. Rev.* **1991**, *91*, 1525.

[22] M. Hunger, J. Kärger, H. Pfeifer, J. Caro, B. Zibrowius, M Bülow, R. Mostowicz, *J. Chem. Soc., Faraday Trans.1* **1987**, *83*, 3459–3468.

[23] L.T. Zhuravlev, *Colloids Surf. A* **1993**, *74*, 71–90.

[24] G. Engelhardt, U. Lohse, S. Samoson, M. Mägi, M. Tarmak, E. Lippmaa, *Zeolites* **1982**, *2*, 59–62.

[25] E. Lippmaa, A. Samoson, V. V. Brei, Y. I. Gorlov, *Fiz. Chim*. **1981**, *259*, 403.

[26] C. A. Fyfe, G. C. Gobbi, G. J. Kennedy, *J. Am. Chem. Soc.* **1985**, *89*, 277.

[27] A. Pines, M. G. Gibby, J. S. Waugh, *J. Chem. Phys.* **1973**, *59*, 569.

[28] J. He, C. Zhao, J. A. Lercher, *J. Am. Chem. Soc*., **2012**, *134*, 20768–20775.

[29] R. E. Mesmer, C. F. Jr. Baes, *J. Solution Chem*. **1974**, *3*, 307–322.

[30] A. Corma, A. Lopez Agudo, V. Fornes, *J. Chem. Soc., Chem. Commun.* **1983**, 942–944.

[31] E. G. Derouane, *J. Catal*. **1986**, *100*, 541.

[32] M. Brändle, J. Sauer, *J. Am. Chem. Soc*. **1998**, *120*, 1556-1570.

[33] R. M. Ravenelle, F. Schüssler, A. D'Amico, N. Danilina, J. A. van Bokhoven, J. A. Lercher, C. W. Jones, C. Sievers, *J. Phys. Chem. C* **2010,** 114, 19582–19595.

[34] P. A. Zapata, J. Faria, M. P. Ruiz, R. E. Jentoft, D. E. Resasco, *J. Am. Chem. Soc*. **2012**, *134*, 8570–8578.

Chapter 6

Summary and conclusions

The goal of this dissertation is to provide better understanding of the rate–determining cycloalkanol dehydration step as part of the hydrodeoxygenation sequence of biomass–derived phenolics to diesel range alkanes. Presented work focuses on a fundamental study of cyclohexanol dehydration in aqueous phase. Water is the solvent of choice, because of its ubiquitous presence in the biomass feedstock. The acid catalyzed dehydration reaction is performed using zeolite catalysts. Thus the distribution of active sites and their integrity in the course of the reaction as well as the modification of the zeolite framework in hot water are specifically explored in this work.

The fundamental study of the reaction mechanism and the zeolite catalyst are achieved by combining kinetic measurements with in situ NMR spectroscopy to qualitatively and quantitatively describe the complex solid–liquid–gas reaction. The cyclohexanol dehydration in water is reversible and follows the E1 mechanism that includes the protonation of the alcohol followed by water elimination leading to the formation of a carbenium ion, which yields cyclohexene as primary product upon deprotonation. The protonated alcohol species can also react with another cyclohexanol molecule to form dicyclohexyl ether, the C–O alkylation product. A further alkylation reaction leading to the C–C coupling product is observed as the reaction approaches equilibrium. The formation of cyclohexyl–1–cyclohexene is promoted with the increase of the olefin concentration that facilitates the nucleophilic addition of cyclohexene to the carbenium ion.

The nature of the zeolite active sites is studied by using a combination of X–ray absorption and NMR spectroscopies supported with ab initio computational models that enable quantitative analysis of the spectral data. The method allows a first of a kind analysis of the zeolite structure up to 6 Å from the absorbing tetrahedral Al site (Al T–site) that forms the zeolite active site. Spectroscopic evidence is presented suggesting that the Brønsted acidic protons compensating the zeolite lattice charges are present in the form of mobile hydrated hydronium ions. In this work we quantitatively determine the Al–distribution for zeolites HBEA150 and HBEA25, which differ substantially both from one another and the populations predicted from thermodynamic evaluation of Al T–sites. This indicates that the location of Al in a zeolite lattice is controlled by synthesis kinetics. Although the impact of synthesis conditions on Al populations in

HBEA is not studied in detail, the presented analytical method demonstrates potential to explore the nature of the zeolite active sites in a depth and detail, which were not available hitherto.

Since the studied dehydration reaction is performed in aqueous medium, this dissertation also addresses the influence of water on both the zeolite framework stability and the integrity of the catalytically active Al T–sites. The experimental results suggest that the degradation of HBEA occurs primarily *via* gradual hydrolysis of Si–O–Si groups leading to the formation of Si–OH groups, which is initiated by selective conversion of strained siloxane bonds and silanol groups at lattice mismatch positions introduced by polymorph–intergrowth faults. The hydrolysis pathway is similar to that of crack formation and propagation in glass. This first step is followed by the formation of smaller crystalline blocks that form amorphous silica outer–shells from the re–precipitation of the hydrolyzed Si–material. In the final step the Si–O–Si groups of the 6 member rings in these microcrystalline domains are selectively cleaved leading to complete framework deconstruction to amorphous silica and alumina. While the crystallinity of the zeolite is completely disrupted, the local structure, including the Al–O–Si angles and bond distances, about the Al T–sites remains mostly intact. Although presented work does not focus on exploring the impact of lattice structures on the stability in water, it appears evident that the local strain, concentration of Si–OH groups and specific incorporation of heteroatoms will greatly affect the zeolite framework integrity in aqueous medium.

The final addressed issue is the impact of the concentration and distribution of Al T–sites in a zeolite on the catalyst activity in the dehydration reaction. The turnover frequency is proportional to the concentration of strong Brønsted acid sites in the zeolite and the catalytic performance is structure–independent with respect to Al T–site population. While the acid sites are largely unaltered in the presence of hot water, the apparent activity of HBEA is suggested to be dependent on accessibility of reactants to the Al T–sites. Current results suggest that a possible path toward efficient catalytic performance of zeolites in aqueous medium is the reduction of Si–OH concentration in the framework *via* post–synthetic treatment with silylating reagents, e.g. trimethylsilyl chloride.

Curriculum vitae

Aleksei Vjunov was born on June 28th, 1988 in Tallinn, Estonia. After completing his high school education in 2006, he was matriculated into the Department of Chemistry at the Technische Universität München (Munich, Germany), where he received his B.Sc. degree in Chemistry in March 2010. Aleksei went on to continue his education at the Technische Universität München and in September 2011 he earned his M.Sc. in Chemistry under the supervision of Prof. Dr. Bernhard Rieger with the thesis titled "*Design and Synthesis of Functionalized MOF Systems*". The M.Sc. thesis experimental work was performed at Fudan University (Shanghai, PR China) under collaboration with Prof. Dr. Guoxin Jin. In February 2012 Aleksei was enrolled as Ph.D. student at the Technische Universität München in the group of Prof. Dr. Johannes A. Lercher. The Ph.D. thesis experimental work was performed at the Pacific Northwest National Laboratory (Richland, WA, USA). Recent research is focused on fundamental understanding of elementary steps in hydrodeoxygenation of biomass including mechanistic reaction pathway, zeolite active site and framework stability studies.

List of publications

1. Following Solid Acid Catalyzed Reactions by MAS NMR Spectroscopy in Liquid Phase – Zeolite Catalyzed Conversion of Cyclohexanol in Water, A. Vjunov, M. Y. Hu, J. Feng, D. M. Camaioni, D. Mei, J. Z. Hu, C. Zhao, J. A. Lercher, *Angew. Chem. Int. Ed.* **2014**, *53*, 479–482.

2. Quantitatively Probing the Al Distribution in Zeolites, A. Vjunov, J. L. Fulton, T. Huthwelker, S. Pin, D. Mei, G. Schenter, N. Govind, D. M. Camaioni, J. Z. Hu, J. A. Lercher, *J. Am. Chem. Soc.* **2014,** *136*, 8296–8306**.**

3. The Impact of Aqueous Medium on Zeolite Framework Integrity, A. Vjunov, J. L. Fulton, D. M. Camaioni, J. Z. Hu, Sarah D. Burton, J. A. Lercher, submitted to *J. Am. Chem. Soc.*

4. Novel Glucose and Cellulose Derived Ni/C-SO_3H Catalysts for Liquid Phase Phenol Hydrodeoxygenation, S. Kasakov, C. Zhao, E. Barath, Z. Chase, J. L. Fulton, D. M. Camaioni, A. Vjunov, J. A. Lercher, accepted to *Chem. Eur. J.*

5. The Impact of aqueous reaction medium on zeolite catalyzed reactions, A. Vjunov, M. A. Derewinski, J. L. Fulton, D. M. Camaioni, J. A. Lercher, in preparation for *J. Am. Chem. Soc.*

6. Impact of Ni/ZrO_2 Support Properties on Stearic Acid Hydrodeoxygenation, S. Foraita, J. L. Fulton, Z. A. Chase, A. Vjunov, M. Balasubramanian, E. Barath, D. M. Camaioni, C. Zhao, J. A. Lercher, accepted to *Chem. Eur. J.*

7. State of Supported Nanoparticle Ni during Catalysis in Aqueous Media, Z. A. Chase, A. Vjunov, J. L. Fulton, D. M. Camaioni, M. Balasubramanian, H. Shi, Y. Wang, J. A. Lercher, submitted to *J. Phys. Chem. Lett.*

8. Electronic and chemical state of aluminum from the single– (K) and double–electron excitation ($KL_{II\&III}$, KL_I) XANES spectra of α–alumina, sodium aluminate, aqueous $Al^{3+}\cdot(H_2O)_6$, and aqueous $Al(OH)_4^-$, J. L. Fulton, N. Govind, T. Huthwelker, E. J. Bylaska, A. Vjunov, S. Pin, T. D. Smurthwaite, submitted to *J. Phys. Chem. B*

9. Towards a better understanding of activity enhancement in steamed MFI–type zeolites for alkane cracking, N. Xue, S. Schallmoser, A. Vjunov, J. L. Fulton, D. M. Camaioni, O. Gobin, L. Peng, J. A. Lercher, in preparation for *J. Catal.*

List of presentations

1. Effect of hot liquid water on the HBEA zeolite framework (oral presentation). A. Vjunov, J. L. Fulton, D. M. Camaioni, M. Derewisnki, J. A. Lercher, ACS 2014 fall national meeting, San Francisco, CA, USA

2. Impact of zeolite stability in aqueous phase catalysis (oral presentation). A. Vjunov, J. L. Fulton, D. M. Camaioni, M. Derewisnki, J. A. Lercher, ACS 2014 fall national meeting, San Francisco, CA, USA

3. Biomass Conversion: Novel Analytical Methods and Techniques (oral presentation). A. Vjunov, D. M. Camaioni, J. L. Fulton, D. Mei, J. Z. Hu, J. A. Lercher, AIChE 2014 spring national meeting, New Orleans, LA, USA

4. Distribution of Al^{3+} in HBEA zeolite (oral presentation). A. Vjunov, J. L. Fulton, T. Huthwelker, S. Pin, D. Mei, G. Schenter, N. Govind, D. M. Camaioni, J. Z. Hu, J. A. Lercher, ACS **2014** spring national meeting, Dallas, TX, USA

5. Reaction of Cyclohexanol on HBEA in Liquid Water (oral presentation). A. Vjunov, M. Y. Hu, J. Feng, D. M. Camaioni, D. Mei, J. Z. Hu, C. Zhao, J. A. Lercher, 23rd NAM meeting **2013**, Louisville, KY, USA